A. Zakery
S. R. Elliott

SPRINGER SERIES IN OPTICAL SCIENCES 135

Springer

Springer Series in
# OPTICAL SCIENCES 135

*founded by H.K.V. Lotsch*

Springer Series in

# OPTICAL SCIENCES

The Springer Series in Optical Sciences, under the leadership of Editor-in-Chief *William T. Rhodes*, Georgia Institute of Technology, USA, provides an expanding selection of research monographs in all major areas of optics: lasers and quantum optics, ultrafast phenomena, optical spectroscopy techniques, optoelectronics, quantum information, information optics, applied laser technology, industrial applications, and other topics of contemporary interest.
With this broad coverage of topics, the series is of use to all research scientists and engineers who need up-to-date reference books.

The editors encourage prospective authors to correspond with them in advance of submitting a manuscript. Submission of manuscripts should be made to the Editor-in-Chief or one of the Editors. See also www.springeronline.com/series/624

A. Zakery S.R. Elliott

# Optical Nonlinearities in Chalcogenide Glasses and their Applications

With 92 Figures, 14 in Color and 18 Tables

Springer

Dr. A. Zakery
Shiraz University, College of Sciences, Department of Physics
Golestan Avenue, Shiraz 71454, Iran
E-mail: zakeri@susc.ac.ir

Professor Dr. S.R. Elliott
University of Cambridge, Department of Chemistry
Lensfield Road, Cambridge CB2 1EW, UK
mail: sre1@cam.ac.uk

ISSN 0342-4111

ISBN-10 3-540-71066-3 Springer Berlin Heidelberg New York

ISBN-13 978-3-540-71066-0 Springer Berlin Heidelberg New York

Library of Congress Control Number: 2007923601



Typesetting by SPi using Springer LaTeX macro package
Cover: eStudio Calamar Steinen

Printed on acid-free paper SPIN: 11495802 56/3180/SPI 5 4 3 2 1 0

# Preface

Photonics, which uses photons for information and image processing, is labeled as one of the technologies of the 21st century, for which nonlinear optical processes provide the key functions of frequency conversion and optical switching.

Chalcogenide glasses are based on the chalcogen elements S, Se, and Te. These glasses are formed by the addition of other elements such as Ge, As, Sb, Ga, etc. These glasses are low-phonon energy materials and are generally transparent from the visible to infrared. Chalcogenide glasses can be doped by rare-earth elements such as Er, Nd, Pr, etc., and hence numerous applications of active optical devices have been proposed. These glasses are optically highly nonlinear and could therefore be useful for all-optical switching.

This book is a review of recent progress in the science and technology of chalcogenide glasses, with an emphasis on their nonlinear optical properties, for graduate students, practising engineers and scientists from a wide multidisciplinary area such as physics, chemistry, electrical engineering and material science. Since the interest in this area is growing worldwide, a book dealing with this subject will be of great value to researchers of varied backgrounds.

Chalcogenide glasses and their electronic, structural, and photoinduced properties are introduced. Techniques to characterize the linear and nonlinear optical properties of these glasses are introduced and used to measure the optical constants of chalcogenide glasses in the form of bulk, thin film and fiber. The possibilities of fabricating passive and active devices are presented. A novel application of chalcogenide glasses, namely all-optical switching for the fabrication of efficient femtosecond switches, is introduced. Finally other applications of chalcogenide glasses, such as optical limiting, second-harmonic generation, fabrication of rib and ridge waveguides and of fiber gratings, optical regenerators and the possibility of using these glasses in all-optical nonlinear integrated circuits and the possibility of enhancing optical nonlinearities by inclusion of nanometals, are discussed in some detail.

We wish to express gratitude to our families and especially to our wives Susan and Penny who, in spite of their own professional schedules, have

provided valuable support and understanding for this project. We would also like to thank many of our colleagues and students from whom we benefited very much from their collaboration. A.Z. would also like to thank the Royal Society of London for providing support for a short visit to Cambridge which helped to collect part of the literature materials in an early phase of the writing of this book.

Shiraz and Cambridge *A. Zakery*
April 2007 *S.R. Elliott*

# Contents

# 1

# An Introduction to Chalcogenide Glasses

## 1.1 Introduction

Chalcogenide glasses are based on the chalcogen elements S, Se, and Te. These glasses are formed by the addition of other elements such as Ge, As, Sb, Ga, etc. They are low-phonon-energy materials and are generally transparent from the visible up to the infrared. Chalcogenide glasses can be doped by rare-earth elements, such as Er, Nd, Pr, etc., and hence numerous applications of active optical devices have been proposed. Since chalcogenide-glass fibers transmit in the IR, there are numerous potential applications in the civil, medical, and military areas. Passive applications utilize chalcogenide fibers as a light conduit from one location to another point without changing the optical properties, other than those due to scattering, absorption, and reflection.

These glasses are optically highly nonlinear and could therefore be useful for all-optical switching (AOS). Chalcogenide glasses are sensitive to the absorption of electromagnetic radiation and show a variety of photoinduced effects as a result of illumination. Various models have been put forward to explain these effects, which can be used to fabricate diffractive, waveguide and fiber structures. For recent reviews, see [1–4]. Next-generation devices for telecommunication and related applications will rely on the development of materials which possess optimized physical properties that are compatible with packaging requirements for systems in planar or fiber form. This allows suitable integration to existing fiber-based applications, and hence requires appropriate consideration as to material choice, stability, and long-term aging behavior.

## 1.2 Structure of Chalcogenide Glasses

Solids are a particular state of condensed matter characterized by strong interactions between the constituent particles (atoms, molecules). Solids can be found or prepared either in an ordered (crystalline) state or in a disordered (noncrystalline) state. While the ordered state of a solid is limited to only

a few structural forms, a disordered material is neither unique nor clearly defined. An ideal crystal corresponds to a regular arrangement of atoms in a lattice with well-defined symmetry, and a structural unit called the unit cell can be defined. Translation of the unit cell along the three coordinate axes reproduces the whole assembly of atoms. A real crystal does not exhibit perfect periodicity in space and contains various kinds of imperfections or defects. Solids which lack the periodicity of the atoms are called noncrystalline solids or amorphous, vitreous or glassy solids. While crystals possess long-range order (LRO), in amorphous materials short-range order (SRO) still exists. Although the first and second nearest-neighbor coordination shells are well-defined, atoms in the third coordination sphere start to become uncorrelated with those in the first one. In other words, the limit of short- and medium-range order is the first 3–4 interatomic distances. The price to be paid for the loss of LRO is the appearance of fluctuations in angles and distances between the bonds. The ideal noncrystalline network is difficult to define. Particularly, different thermal treatments lead to various noncrystalline arrangements of atoms. A continuous random network [5] might be considered to be an ideal noncrystalline network for covalent solids.

The structure of chalcogenide glasses, however, cannot be described by means of a continuous random network which is isotropic in three dimensions, as in the case of amorphous silicon for example. $As_2S_3$, $As_2Se_3$, $GeS_2$, and $GeSe_2$ can be locally layer-like, while pure S and Se are chain like. For all these materials, there is considerable flexibility of the structure as a result of the weak van der Waal's bonding between layers or chains [6], so that changes in the structure can be relatively easily accommodated.

Raman (or inelastic) scattering of light in a material yields structural and dynamic information on a molecular level. The nondestructive nature of the probe, and flexibility in sampling arrangements, has opened up many potentially new areas where Raman measurements have proven valuable [7,8]. Near-infrared (NIR) Raman spectroscopy can be used in the analysis of materials which are strongly absorbing in the visible. A distinct advantage over the more conventional approach using the visible part of the spectrum as the excitation wavelength is the ability to obtain the Raman spectrum of photosensitive compounds without interference from photoreactions caused by the probe beam. In As–S–Se chalcogenide glasses, shifting the excitation wavelength to 840 nm (typically below the band gap) allows one to obtain high-quality Raman spectra without material modification. Raman spectroscopy can be extremely powerful in the microstructural analysis of single and multilayer waveguide devices [9]. Here, the material of interest is made in the form of a slab waveguide, thereby significantly increasing both the scattering volume and the electric-field intensity within the film. Raman scattering in the NIR can be excited with 840 nm radiation from a tunable Ti:sapphire laser (30–50 mW). The dominant feature in binary sulfide and selenide compounds are bands at 345 $cm^{-1}$($As_{40}S_{60}$) and 230 $cm^{-1}$ ($As_{40}Se_{60}$), respectively, [10] (see Fig. 1.1).

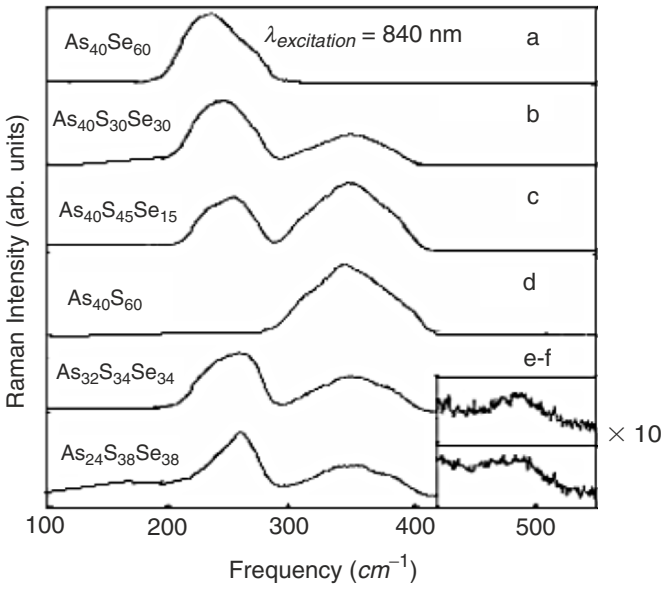


**Fig. 1.1.** Raman spectra of bulk glasses obtained with near-infrared excitation ($\lambda = 840\,\text{nm}$) as a function of compositional variation. Spectral resolution is $1.5\,\text{cm}^{-1}$ (after [10])

A strong broad band is seen which is attributed to the antisymmetric As–(S,Se)–As stretching vibration in $As(S, Se)_3$ pyramidal units. In ternary compounds with a S/Se = 1 molecular ratio and decreasing As content, a progressive decrease in the intensity of these broad bands is observed, indicative of a decrease in the number of As-containing pyramidal sites. New bands appearing around $255\,\text{cm}^{-1}$ and 440–$480\,\text{cm}^{-1}$ form in chalcogen-rich glasses, and are attributed to Se–Se homopolar bonds. These units serve as chalcogen chains connecting the remaining pyramidal units. The small numbers of S–S bonds, indicated by a weak band near $495\,\text{cm}^{-1}$, for equal concentrations of S and Se suggests that S stays with the remaining pyramids and that it is the Se which dominates the connecting chain units. Deviations from bulk glass properties in fibers and films are observed. The extent of such compositional variation, and the resulting structural units formed, varies with the specific fiber or film-processing technique used. Neutron-scattering and X-ray diffraction studies on bulk sulfide and selenide glasses and their thin films [11] have shown variations in structural units on the intermediate-range order scale. Depending on processing conditions, polymeric cages (based on $As_4S_4$ units) or less connected groups of As–S pyramidal units, were observed. Furthermore, these units are much more metastable and can be structurally modified or eliminated with postdeposition processing. Waveguide Raman spectroscopy (WRS) has been applied to the structural characterization of chalcogenide

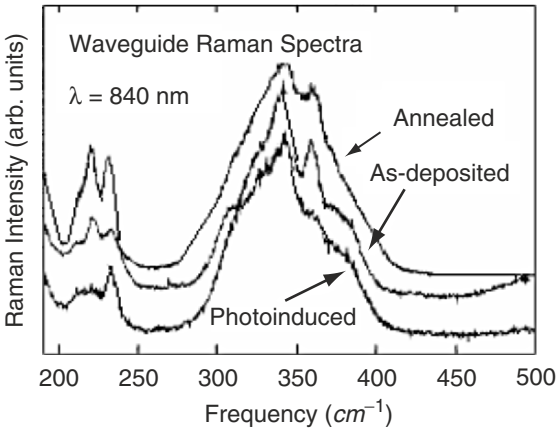


**Fig. 1.2.** Variation in waveguide Raman spectra for a fresh, annealed, and photostructurally modified $As_2S_3$ channel waveguide (exposure $\lambda = 514.5\,nm$). Excitation wavelength was 840 nm (after [10])

glasses [12, 13]. The excitation beam (840 nm) was launched into the end face of an $As_2S_3$ channel waveguide at various lateral positions. Although the $As_2S_3$ film had a thickness of just 1.5 µm, the high signal-to-noise ratio achieved by guided-mode excitation was evident and low-frequency Raman peaks were well separated from interfering Rayleigh scattering. In comparison with the bulk, new substructures appeared in the film spectra as compared with the broad features of the bulk spectra (see Fig. 1.2).

These differences in the spectra from the bulk are due to different (molecular) arrangements of the constituent atoms within the films. These sharp, molecular-signature features were confirmed not to be due to crystallinity within the film, but most likely result from the formation of as-deposited $As_4S_4$ units [11, 14]. Rutherford backscattering spectroscopy (RBS) is an analytical tool that gives very useful information regarding compositional and structural analysis of films, as well as a precise measurement of the film thickness. Results obtained showed no apparent variation in composition and small (less than 10%) density variation in single-layer $As_2S_3$ films [15]. Multilayer films, whose thickness can be measured using SEM images, display compositional and density modifications associated with the annealing process. Film ageing was investigated in films after almost a year. Stoichiometric and thickness modifications, caused by ageing, were observed in unannealed structures [15]. No apparent changes were detected in annealed films. The RBS data shows that the ratio of the sulfur-to-arsenic concentration increases during the annealing process. This suggests that the sulfur is not evaporating during annealing. However, SEM shows a modification in the layer thickness for the multilayer structure. This result implies that the molecules in the films are rearranging. NIR Raman results complement this conclusion.

Chalcogenide glasses seem to experience slight modifications with time, under standard conditions (i.e. room temperature). However, these structural modifications or relaxation in the molecular structure of the films are less apparent in annealed structures, which suggests that annealed films are fairly stable in time. Seal et al. [16] have used X-ray photoelectron spectroscopy (XPS) to study the resulting chemical composition of $As_2S_3$ at the film surface as compared to the parent bulk glass and the corresponding variation in the nature of chemical bonds and electronic structure. $Ar^+$-ion sputtering converts the amorphous phase into a crystalline phase as the binding energy of the As peak increases from 42.7 to 43.8 eV [16]. Inference of the crystalline phase in the sputtered region is based on the fact that 99.99% pure melted $As_2S_3$ glass has a similar binding energy to that seen for As in its crystalline form. It was found that laser irradiation induces structural and chemical changes in the sample, as can be seen from the change in the As/S ratio with illumination. Polarization direction, vertical and circular polarization were found to induce an As-deficient structure and horizontal polarization was found to make the system As-rich [16]. It was also found that, when films are illuminated, some non-bridging S atoms were observed but no nonbridging atoms appeared to be created when the sample was sputtered with an $Ar^+$ beam [16]. EXAFS studies [17] have shown that there is chemical disorder in the structural network of GaLaS thin films, although chemical ordering is predominant in bulk GaLaS glass. EXAFS results show that gallium is always fourfold coordinated in the GLS network. Both Ga–Ga and S–S bonds occur in GLS thin-film samples but the lanthanum atoms remain eightfold coordinated by sulfur alone. The bond lengths were the same as those found in bulk glass. Although the nearest-neighbor environment is well-defined, there is considerable bond-angle variation, and hence a wide variation in second-neighbor distances. Benazeth et al. [18] also studied the structure of bulk GLS glasses using EXAFS at the gallium K edge and lanthanum $L_3$ edge. Their results show that gallium atoms in the glass exist in tetrahedral networks of $GaS_4$, and the Ga–S distances in the glasses are identical to those existing in the crystalline form of $Ga_2S_3$. The gallium and sulfur environment in crystalline $Ga_2S_3$ is such that two of the three sulfur atoms are linked to three gallium atoms and the third sulfur atom is linked to two gallium atoms. The bonds that link two of the three sulfur atoms to three gallium atoms consist of two covalent bonds and a third dative bond, while the third sulfur atom linked to two gallium atoms represents the bridging atom. The addition of $La_2S_3$ brings in an additional $S^{2-}$ anion that results in modification of the dative bond of the trigonally coordinated sulfur atom. The dative bond is broken and the $S^{2-}$ anion provided by the modifying rare-earth sulfide helps in restoring and maintaining the tetrahedral environment of $GaS_4$, at the same time creating a negative site for the $La^{3+}$ cation. Lucazeau et al. [19] studied the structure of these glasses using Raman spectroscopy. The Raman spectra of the glasses and of similar crystalline phases were compared and spectral differences were found between the two glassy and crystalline states. This has been interpreted in

terms of structural modification of the short-range periodicity around the Ga atoms, although there was no conclusive evidence.

## 1.3 Electronic Properties of Chalcogenide Glasses

Chalcogenide glasses can be characterized as being variously covalent, metallic, and ionic. In covalent chalcogenide glasses such as Se and $As_2S_3$, the so-called 8-$N$ rule applies to the coordination number of the constituent atoms, e.g. the coordination number of chalcogens is generally 2 since the total number of valence electrons is $N = 6$. The magnitude of the band gap is 1–3 eV depending on the composition, the band gap increasing in the series Te → Se → S. Electrical conduction in many chalcogenide glasses is governed by holes. Accordingly, these glasses can be regarded as amorphous semiconductors. However, in a glass containing large amounts of Te, the band gap decreases (∼1 eV), and the metallic character increases. Moreover, in glasses such as Ag–As(Ge)–S, the coordination number of S is demonstrated to be 3–4 [20], and ionic conduction of $Ag^+$ governs the electrical conductivity. So these glasses can be considered as ionic glasses or ion-conducting amorphous semiconductors.

### 1.3.1 Electronic States in Chalcogenide Glasses

If we compare the optical properties of crystalline and amorphous $As_2S_3$ and $As_2Se_3$, we see that the effect of disorder on the electronic structure is relatively small; the optical absorption edges (band gaps) are very similar. The major difference between crystalline and amorphous solids lies in a higher density of traps and a larger energy distribution of the trapping levels in the amorphous solid. The electrical band gap for $As_2Se_3$ is 1.1 eV in comparison to 1.9 eV for the optical gap. The optical gap is therefore approximately double the electrical gap, which indicates that the Fermi level is situated near the middle of the mobility gap (the energy interval between the demarcation levels between localized and extended states in valence and conduction bands). In a chalcogen, e.g. selenium, the four 4p electrons occupy two bonding orbitals representing covalent bonding and one orbital named a lone-pair orbital, which does not participate in the covalent bonding. The p electrons give rise to strong covalent bonds. Lone-pair electrons determine the dihedral angles and, being the uppermost electrons in the valence band, play an important role in defining the energy bands.

Various experimental techniques have been used to determine the density of localized states in the gap. It was concluded from transient photocurrent-decay measurements that the density of tail states decreases exponentially and does not have any defined structure [21]. It is now generally believed that, on top of a featureless distribution of states in the tails, a structured density of states exists, attributed to valence alternation pairs (VAPs)) [22]. For arsenic

triselenide, time-of-flight and transient photoconductivity measurements suggest a feature located 0.6 eV above the valence band edge which dominates the transport. There has been some controversy in the literature related to the sign of the correlation energy in amorphous selenium. While Kastner et al. [23] originally assumed a negative correlation energy, early theoretical work [24] indicated that, in fact, the correlation energy in a-Se should be positive, i.e. spin pairing at coordination defects would be energetically unfavorable. Recently, it was demonstrated by Kolobov et al. [25], using light-induced ESR, that the correlation energy was indeed negative. Popescu [26] has stated that in amorphous selenium the defect states $C_3^+$ (where C stands for chalcogen and the superscript and subscript gives the charge and coordination, respectively) give rise to discrete traps situated at around 0.33 eV below the bottom of the conduction band and they control the electron mobility. The $C_1^-$ defect states are situated at 0.17 eV above the top of the valence band and control the hole concentration. Both types of traps are distorted by trapping of the charge carriers, and, as a consequence, their energies do not correspond to that found from light-absorption experiments and charge-carrier generation.

Tanaka has recently proposed [27,28] a model of a realistic density of states based on several experimental results (Fig. 1.3a). Spatial potential fluctuations and the atomic structure in $As_2S_3$ are shown schematically in Fig. 1.3b, c, respectively. In this model, it is assumed that the Urbach edge arises from fluctuations of the van der Waal's type interlayer bonds and/or disordered interactions among the intralayer lone-pair electrons. The weak absorption tail in this model is ascribed to transitions involving antibonding states of As–As wrong bonds, which can produce unoccupied deep states below the conduction band. Electronic excitations can generate localized holes in the valence-band edge and delocalized electrons in the conduction band. The other possibility is generation of delocalized holes in the valence band and localized electrons in the conduction-band tail. Excited carriers are immediately ($\approx 10^{-12}$ s) trapped into the localized states.

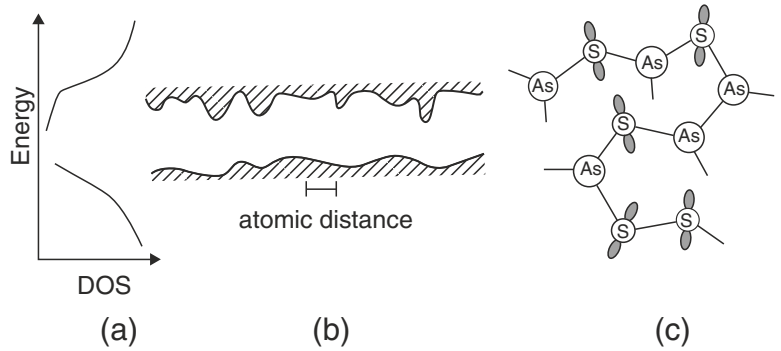


**Fig. 1.3.** (**a**) Density of states, (**b**) the spatial potential fluctuations and (**c**) the corresponding atomic structure proposed for $As_2S_3$ glass (after [20])

### 1.3.2 Measurements of the Absorption Coefficient and the Optical Gap

The optical absorption edge in amorphous semiconductors is generally not as steep as that in crystalline semiconductors. In general, the absorption spectrum $\alpha(\hbar\omega)$ can be divided into three parts [29] (see Fig. 1.4). For $\alpha \geq 10^4 \mathrm{cm}^{-1}$, the spectrum shows a square-root dependence, $\alpha\hbar\omega \propto (\hbar\omega - E_\mathrm{g}^\mathrm{T})^{1/2}$.

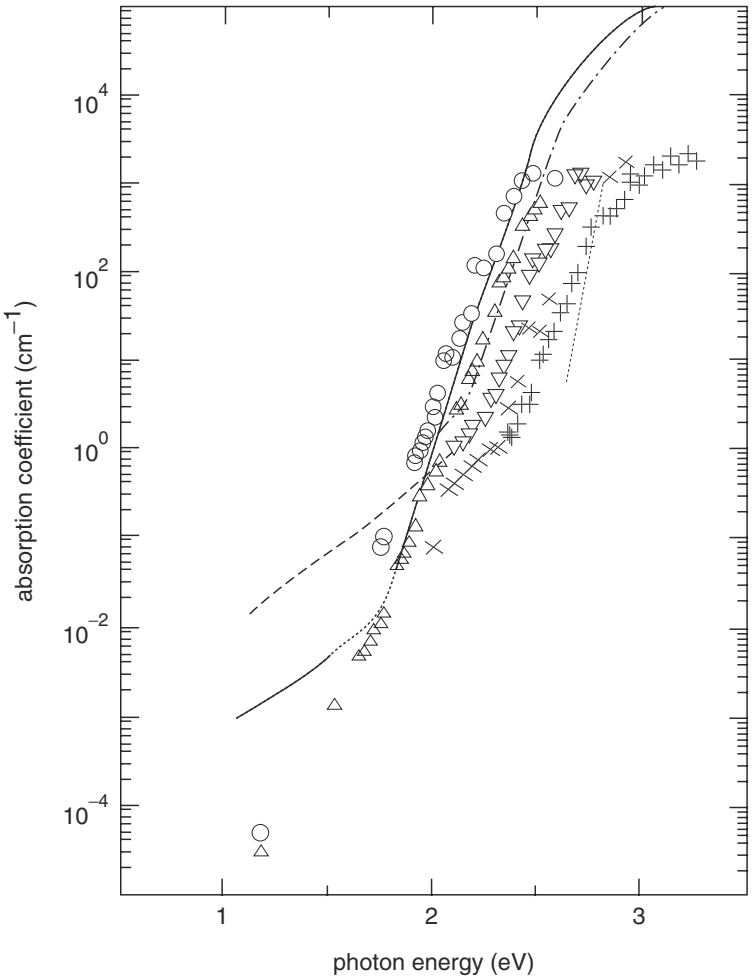


**Fig. 1.4.** Optical absorption edges in $As_2S_3$ glasses at different temperatures. The two lines (*solid* and *dashed*) show absorption spectra for different samples at 300 K. Spectra at 175 K(*plus*), 200 K (*times*), 250 K (*downtriangle*), 300 K (*triangle*), and 400 K (*circle*) have been obtained under $10^5$ V cm$^{-1}$ using the constant-photocurrent method. Also shown are spectra at 10 K for $As_2S_3$ glass (*dot-dashed line*) and for a crystalline sample (*dotted line*) (after [30])

For $10^4 \geq \alpha \geq 10^0\,\mathrm{cm}^{-1}$, the so-called Urbach edge with the form of $\alpha \propto \exp(\hbar\omega/E_\mathrm{U})$ appears. For $\alpha \leq 10^0\,\mathrm{cm}^{-1}$, a weak-absorption tail with $\alpha \propto \exp(\hbar\omega/E_\mathrm{W})$ exists. In the above, $E_\mathrm{g}^\mathrm{T}$ represents the optical ($T$auc) gap. In $As_2S_3$ glass at room temperature, for example, $E_\mathrm{g}^\mathrm{T} = 2.36\,\mathrm{eV}$, $E_\mathrm{U} \approx 50\,\mathrm{meV}$, and $E_\mathrm{W} \approx 250\,\mathrm{meV}$ [29–31]. It should be noted that the mobility gap, which can be evaluated from photoconduction spectra, appears to be located at ≈2.5 eV [30, 32].

The absorption coefficient, $\alpha$, of chalcogenide films has been measured using several techniques for as-deposited, annealed, and photodarkened films, as well as in fabricated waveguides. At short wavelengths, where the absorption is high, a conventional spectrophotometer could be used, with corrections for reflection losses using the method described in [33]. At wavelengths beyond the band edge, however, the absorption is too small for this technique to be useful. Photothermal deflection spectroscopy (PDS) has therefore been used [31] to measure the relative absorption coefficient in the long-wavelength region. To calibrate the PDS data, absorption values from the spectrophotometer and the PDS are overlapped in the region of moderate absorption just beyond the band edge, where both give an accurate measurement. In addition, optical loss can be determined at spot wavelengths from propagation measurements made in slab waveguides.

For these measurements [34], films deposited onto oxidized Si wafers were placed in a prism coupler, and the lowest-order slab waveguide mode was excited. Some radiation was scattered from the surface of the sample and could be detected using a cooled CCD camera. At wavelengths close to the absorption edge (633 nm), the decay of the intensity with distance was assumed to be dominated by film absorption, and hence the absorption coefficient for the film could be determined and used to calibrate the PDS data. The results of PDS measurements showed that as-deposited $As_2S_3$ films have losses below $0.1\,\mathrm{dB\,cm}^{-1}$ across the telecommunications band at 1,300 and 1,550 nm [34]. Films that were 2.5 μm thick were used for single-mode waveguide fabrication using a direct-writing system. To assess the losses in fabricated waveguides, it was found possible to image the light scattered from the waveguides and to monitor the decay of the power in the waveguide as a function of distance using an IR-sensitive video camera. Light from laser-diode sources at 780, 1,300, and 1,550 nm was end-coupled into the waveguides using a microscope lens for these measurements. The losses obtained in this way were $\sim 0.4\,\mathrm{dB\,cm}^{-1}$ at 780 nm, $\sim 0.24\,\mathrm{dB\,cm}^{-1}$ at 1,300 nm, and $0.2\,\mathrm{dB\,cm}^{-1}$ at 1,550 nm [34]. These values are in good agreement with those obtained from the PDS measurements. The output from the waveguides was imaged with a microscope objective onto a video camera. The waveguides were single mode at 1,300 nm and 1,550 nm.

Band theory for crystalline semiconductors suggests that the absorption coefficient for indirect transitions can be written as

$$\alpha = \mathrm{const} \times M^2 \frac{(h\nu - E_\mathrm{g})^2}{h\nu} \tag{1.1}$$

**Table 1.1.** Optical gap for evaporated films (after [35])

| composition | $E_g(eV)$ |
|---|---|
| $As_2S_3$ | 2.26 |
| $As_3Se_{97}$ | 1.935 |
| $As_{22}Se_{78}$ | 1.872 |
| $As_{41}Se_{59}$ | 1.79 |
| $As_{39}Se_{61}$ | 1.79 |
| $Ge_9As_{25}Se_{66}$ | 1.922 |
| $Ge_5As_{35}Se_{60}$ | 1.828 |
| $Ge_2As_{40}Se_{58}$ | 1.783 |

The optical gap for $As_2S_3$ is for PLD deposited films [34]

**Table 1.2.** Optical gap for some bulk chalcogenide glasses (after [36])

| glass | $E_g(eV)$ |
|---|---|
| $Ge_{25}Se_{75}$ | 2.07 |
| $Ge_{25}Se_{65}Te_{10}$ | 1.73 |
| $Ge_{28}Se_{60}Sb_{12}$ | 1.8 |
| $As_2Se_3$ | 1.77 |
| $As_2S_3$ | 2.4 |

The optical gap for $As_2S_3$ is taken from [37]

where $M$ is the matrix element of the optical transition and $E_g$ is the band gap energy.

The absorption in many amorphous semiconductors is observed to obey this relation above the exponential Urbach edge. If $M$ is constant, plotting $(\alpha h\nu)^{1/2}$ versus $h\nu$ should result in a straight line. The optical gap, $E_g$, is obtained from the intersection of this line with the energy axis. The value obtained for the optical gap of pulse laser deposited (PLD) a-$As_2S_3$ film was $E_g = 2.26 \pm 0.02$ eV [34]. This value is slightly lower than that of 2.36 eV found for thermally evaporated $As_2S_3$ films, most probably due to illumination of the films during the laser-deposition process. Table 1.1 shows the results of optical-gap measurements for evaporated chalcogenide films, while the optical gaps of some chalcogenide glasses are shown in Table 1.2.

## 1.4 Chalcogenide Glasses for Near-Infrared Optics

A range of optical functions can be realized in these glasses, including optical amplification and emission at telecommunication wavelengths by rare-earth (e.g., Pr and Er) dopants, fabrication of waveguides (channel, self-written, femtosecond written), that can laterally or vertically couple light to various locations within a planar structure, and gratings (relief and phase) that can spectrally filter or modulate light. Diffraction gratings have been fabricated

in chalcogenide glasses using the photoinduced effects that they exhibit. Both photodarkening [38] and the metal-photodissolution effect [40] (especially of silver) have been used to fabricate transmissive gratings, especially for use at IR wavelengths. A variety of techniques have been used to fabricate these gratings, including holographic, mask exposure, or etching methods. These gratings can be used as efficient beam combiners, couplers and have significant applications in monochromators, laser-tuning devices, shapers, optical-fiber couplers, etc. For instance, gratings have been written holographically in sputtered $Ge_{10}As_{40}S_{25}Se_{25}$ films with 514.5 nm light from an Ar-ion laser and probed with a 670 nm diode laser [38]. The probe was highly attenuated to avoid influencing the photodarkening process. The first-order efficiency of Raman–Nath diffraction for a probe beam tuned to the Bragg condition was used to measure a refractive-index change of $\Delta n = 0.001$ for a written intensity of $100\,\mathrm{mW\,cm^2}$. Slinger et al. [39] recorded volume holographic gratings in evaporated $As_{40}S_{60}$ films in which silver was photodissolved. They measured the angular response of the gratings, and replay was made in air using light of wavelength 632.8 nm from a helium–neon laser. Typical Bragg behavior was observed and the diffraction efficiency in the first-order diffracted beams reached a maximum of 9% near the Bragg angle. A photolithographic technique has been used [40] to fabricate surface-relief gratings in a bi-layer structure consisting of a 0.8 µm a-$As_{30}S_{70}$ film and an under-layer of Ag of 0.14 µm thickness. Thin gratings produced by mask exposure showed Raman–Nath type diffractive behavior and, when replayed at 632.8 nm, first-order diffraction efficiencies of up to 10% were measured. First- and second-order Bragg reflectors at telecommunication wavelengths (1.5 µm) have been fabricated in single-mode monolayer ($As_2S_3$) and multilayer (As–S–Se/As–S) chalcogenide glass planar waveguides with near-band gap illumination using an interferometric technique [41]. Reflectivities as high as 90% near 1.55 µm, and refractive-index modulations up to $3 \times 10^{-4}$ were achieved. The volume photodarkening effect is the principal mechanism involved in the formation of the Bragg gratings. The stability and high efficiency of these gratings make them potentially useful as wavelength-selection elements, and add-drop filters for WDM networks [41].

Richardson et al. [42] have written permanent waveguides in both bulk and film of $As_2S_3$ glasses [43]. Using a train of 850 nm femtosecond laser pulses, they measured both the induced index variation and structural changes induced through the photomodification. The refractive-index variation between the waveguide (exposed region of the glass sample) and the cladding (unexposed region) was evaluated following waveguide writing. An induced index change of $\Delta n = -0.04$ was associated with the formation of a 9 mm diameter circular waveguide formed by moving the sample through a well-characterized focal region [41]. A key finding of the study defined the structural mechanism associated with the writing process in the $As_2S_3$ material. The concurrent destruction of As–S bonds within the glass network and the associated formation of As–As bonds during the bulk material

modification was quantified by a two-dimensional micro-Raman analysis (excitation with $\lambda \approx 752\,nm$).

Optical amplification at 1.083 µm in neodymium-doped chalcogenide fibers was observed [44] in a glass composition of Ge–As–Ga–Sb–S. A maximum internal gain of 6.8 dB was achieved for a pump power of 180 mW. The first amplified spontaneous emission in a chalcogenide glass fiber has also been reported [44]. Laser action in a rare-earth-doped GaLaS chalcogenide glass has been demonstrated, showing that this class of glasses is suitable for active applications, such as amplifiers and lasers [45]. A neodymium-doped GaLaS glass laser has been operated under continuous-wave conditions at a wavelength of 1.08 µm when pumped with a Ti:Sapphire laser at either 0.815 or 0.890 µm [45]. The reasonably low laser threshold indicated acceptable glass losses, but the laser performance was worse in comparison with conventional Nd-lasers. The original application of GaLaS glass was as a practical and efficient 1.3 µm optical fiber amplifier.

The ability to move and manipulate light without using costly and delicate articulated arms and mirrors is a common requirement for several applications, e.g., laser surgery. Power handling of GaLaS fibers has been assessed by coupling to an Nd:YAG laser operating at 1,064 nm. A total of 5 W of power was guided through a core of about 150 µm with no apparent laser damage [46].

## 1.5 Chalcogenide Glasses for Mid-IR and Far-IR Applications

A selenide glass has been developed that can be doped with rare-earth ions and is stable against crystallization during fiberization [47]. The glass is based on GeAsGaSe and can be doped with $Pr^{3+}$ and $Dy^{3+}$ for near- and mid-IR applications. The doped glasses have been fiberized with core-only losses of $0.8\,dB\,m^{-1}$ at 6 µm and $1.5\,dB\,m^{-1}$ at 2.5 µm. Single-mode fibers have been drawn with a measured core loss of $3\,dB\,m^{-1}$ at 1.55 µm.

$Pr^{3+}$ incorporation has been investigated and mid-IR emission in the 3–5 µm region has been observed. Schweizer et al. [48] have found that the absorption spectrum of a 9.7 mol% $Er^{3+}$-doped GaLaS glass showed excellent rare-earth solubility and the potential for high doping concentrations and hence short devices; this represents a major advantage of GaLaS glass compared with conventional chalcogenide glasses, which suffer from very low rare-earth solubilities. Values obtained for branching ratios of 1% for both the 3.6 and 4.5 µm transitions, with measured lifetimes of 100 and 590 µs and cross-sections of $0.43 \times 10^{-20}$ and $0.25 \times 10^{-20}\,cm^2$, were in good agreement with the results of [49], respectively, in an $Er^{3+}$-doped barium indium gallium germanium sulfide glass. The radiative properties of $Er^{3+}$-doped Ga–La–S lend themselves to applications. Radiation at 2 µm has application in LIDAR systems, radiation at 2.75 µm coincides with a strong water absorption

in tissue and is used for medical applications, the 3.6 μm transition could be useful for $H_2S$, NO, and $SO_2$ (remote) sensing and the 4.5 μm transition could find use in CO and $O_3$ gas sensors when tuned to 4.7 μm. High-power CO and $CO_2$ lasers operating at 5.4 and 10.6 μm, respectively, are available and are used for industrial welding and cutting. Transmitting the laser power through fibers enables remote operation to take place. Te-based fibers have demonstrated output powers of 10.7 W for 19.4 W launched power (efficiency = 55.2%) at 10.6 μm [50]. The fibers possessed an antireflection (AR) coating and were cooled with water to prevent thermal lensing caused by an increase in absorption coefficient with temperature ($d\alpha/dT$) and an increase in refractive index with temperature ($dn/dT$). On the other hand, arsenic sulfide-based fibers have demonstrated 85 W output power for 169 W launched power (efficiency = 50.3%) without the need for cooling and AR coatings [51]. Unlike the Te-based glasses, arsenic sulfide-based glasses have smaller values of $d\alpha/dT$ and $dn/dT$ . Typically, the fiber diameters are usually in excess of 500 μm for high-power laser delivery to reduce the power density. However, small core diameter (<200 μm) fibers have demonstrated a tolerance to power densities of 125 kW cm$^{-2}$ at 5.4 μm and 54 kW cm$^{-2}$ at 10.6 μm without damage [52]. The arsenic sulfide fibers transmit in the 2–5 μm region and can be used for transmission of laser power in this region for military applications, such as in infrared countermeasures and laser threat-warning systems [53]. The output power versus input power for a sulfide fiber using a pulsed laser operating in the 2–5 μm region has been measured [54]. The average power was about 2.69 W, but the peak power was 26.9 kW which corresponds to the largest input power density, 1.07 GW cm$^{-2}$, without fiber damage for $\leq 1.5 \times 10^7$ pulses [54]. This threshold of about 3.0 GW cm$^2$ is due to dielectric breakdown at the surface. Recent efforts have considered delivery of energy from a medical free-electron laser (MFEL) operating between 2 and 10 μm through chalcogenide fibers [55]. The MFEL can emit more than 10 MW of power in a femtosecond pulse, which relates to an average power of greater than 10 W. It has been shown [2, 56] that surgery at 6.45 μm based on cleaving of protein bonds is more efficient and leads to less denatured tissue and scarring than with conventional Er:YAG lasers operating at 2.94 μm based on OH absorption [2, 56].

Chalcogenide fibers are well-suited for chemical-sensing applications, since most molecular species vibrate in the infrared region. Chalcogenide fibers can be used in fiber-optic chemical-sensor systems for quantitative remote detection and identification, as well as detecting chemicals in mixtures. Different sensing techniques including attenuated total reflectance (ATR) [57–59], diffuse reflectance, and absorption spectroscopy [60–62] have been introduced. Numerous systems have been studied which include oil, freon, soap, paints, polymer-curing reactions, glucose/water, benzene and derivatives, chlorinated hydrocarbons, alcohols, carboxylic acids, aqueous acids, perfumes, and pharmaceutical products.

For example, a fiber-optic dipstick probe could monitor the quality of engine oil and, consequently, save large amounts of money in preventing unnecessary oil changes in the military and civil sector. A fiber optic-based reflectance probe has been used to detect contaminants in soil [63]. Detection limits of 130 ppm of marine diesel fuel in sea sand have been demonstrated using a 20-meter length of cable. A chalcogenide-fiber ATR probe has been used to show the spectral differences between various tissues and organs in biomedical samples. IR spectra in the region of 2–10 μm for various organs/tissues from a dead chicken, as well as from the liver of an anaesthetized sheep [55], have been recorded. Chalcogenide fibers can be utilized to generate a biomedical database for medical diagnostics, such as tissue evaluation and early detection of cancer [64].

Ueda et al. [65] have used As–S fibers with a Teflon cladding to measure temperature increases of up to 200°C on the surface layer of ceramic plates during grinding. Chalcogenide fibers have also been used for thermal imaging [66]. Saito et al. [67] recorded the image of an electric iron at 773 K through a 1,000 fiber bundle, and Nishi et al. [68] fabricated a flexible fiber bundle containing 8400 Teflon-coated fibers and recorded the thermal image of an operating integrated circuit in the 3–5.4 μm region. Hyperspectral imaging can be exploited by coupling coherent fiber bundles to focal-plane array (FPA) detectors based on InSb (2–5.4 μm) detectors. Focal-plane array detectors are extremely sensitive and can be used for performing both spatial and spectral analyses in the infrared [69].

A $10 \times 10$ bundle of $As_2S_3$ fibers with a Teflon cladding was reformatted to a $1 \times 100$ array and the output analysed using a grating spectrometer [70]. High-quality single-mode and multimode chalcogenide fibers have been used to demonstrate 100 nm resolution for both topographic and spectroscopic analyses of polycrystalline diamond [71]. The material that is most widely used in fiber optics is currently silica, which provides a transmission window that extends to only about 2 microns. With their high glass-transition temperature, GaLaS glasses offer the potential for greater power handling capacity. Lasers with emission wavelengths around 2.9 microns are widely used in surgery. This wavelength corresponds to the strongest absorption band of water and thus bio-tissues, allowing a host of medical applications [72].

## 1.6 Bulk Chalcogenide Glasses, Composition, and Optical Constants

In order to synthesize chalcogenide glasses, the appropriate chemical elements (e.g., 99.999% pure), in the quantities required for producing the desired composition, are placed in a pre-cleaned quartz ampoule. After evacuating the residual gases to a pressure of $10^{-5}$ Torr, the ampoule is sealed under vacuum and placed in a furnace, where melting of the components takes place at

temperatures between 600°C and 970°C (depending on composition). In order to achieve good homogenization of the chalcogenide glasses and to produce glasses with uniform composition, the furnace can be slowly rocked during the time the ampoule is at high temperature. The ampoule is cooled down to 350–400°C at a rate of $\sim$100°C h$^{-1}$. At this temperature, the ampoule containing the synthesized material is left in air or is cooled rapidly in cold water. Whereas most chalcogenides are melted in sealed ampoules containing the required amounts of elemental precursors, gallium lanthanum sulfides are melted from prepared batches of $Ga_2S_3$, $La_2S_3$, and $La_2O_3$. Batches of powders are placed in a vitreous carbon crucible and melted in a tube furnace at 1,150°C for typically 24 h, depending on the batch size. The molten $Ga_2S_3$ fluxes the lanthanum precursors, incorporating them into the liquid at temperatures much lower than their melting point. After quenching the resulting melt, the glasses are then annealed near the glass-transition temperature. The composition of bulk glasses can be determined in a scanning electron microscope with an X-ray microanalyzer [73]. The mean data for the element content in a selection of the bulk glasses, including some of those exhibiting the greatest changes in optical properties, has been presented [74]. It was shown that the compositions of bulk glasses were generally within $\sim$1 at.% of the expected compositions. Some crystalline phases were observed in $As_{45}S_{55}$ and also in the Ge–S–Tl bulk glasses (C–$As_4S_4$ and $\alpha$-$GeS_2$, respectively). The binary gallium lanthanum sulfide system has a maximum stability for a gallium-to-lanthanum ratio of 70:30 [75]. Glass formation extends from about 60:40 to 80:20 for this two-component glass. Through the addition of a third or fourth component to the basic GLS glass, a wide range of modified compositions with varying properties can be realized. A wide range of modifiers have been tested. This was originally motivated by the quest for glass stabilizers, additional components that would improve the thermal characteristics of the glass and thus aid fiber drawing. The majority of attention has focused on the addition of oxides, in particular, lanthanum oxide in GLS glass. It is now believed that a small percentage, typically 1–2 weight percent of lanthanum oxide, is essential for glass stability. The addition of oxide radically improves the thermal stability of the glass but at the expense of its phonon energy and thus of the potential for active optical applications.

Different techniques have been used to measure the optical constants of chalcogenide glasses. For bulk samples, normally an optical transmission curve of the sample at different thicknesses, together with reflection data, is needed to calculate both the dispersion and the absorption characteristics of the sample [76,77]. Table 1.3 summarizes, for some of the glass systems examined [78], the optical band gap energy and the refractive index as measured in the mid-infrared.

Tables 1.4–1.7 show the results of refractive-index measurements for some other chalcogenide systems examined at different wavelengths using various methods.

**Table 1.3.** Optical band gap and refractive index measured at 10.6 μm for several chalcogenide glass compositions (after [78])

| nominal composition (mol%) | $E_g(eV)$ | n |
|---|---|---|
| $As_{40}S_{40}Se_{20}$ | 1.70 | 2.47 |
| $As_{24}S_{38}Se_{38}$ | 1.67 | 2.32 |
| $As_{37}S_{56}Se_7$ | 1.79 | 2.43 |
| $Ge_{30}As_{11}Se_{49}Te_{10}$ | 1.22 | 2.50 |
| $Ge_{17}As_{18}S_{26}Se_{39}$ | 1.64 | 2.41 |
| $As_{30}Se_{63}Sb_4Sn_3$ | 1.28 | 2.80 |
| $Ge_{28}Sb_{12}Se_{60}$ | 1.39 | 2.60 |
| $Ge_{25}Ga_5S_{70}$ | 2.38 | $\sim 2$ |
| $Ga_{28}La_{12}S_{60}$ | 2.38 | 2.50 |
| $Ga_{24}La_{10}S_{60}Ce_6$ | 2.17 | 2.54 |

**Table 1.4.** Optical properties of $GeS_2$-based glasses measured using ellipsometry (after [79])

| composition (mol%) | $n$ at 633 nm |
|---|---|
| $x = 0$ | 2.01 |
| $x = 10$ | 2.15 |
| $x = 20$ | 2.21 |
| $x = 30$ | 2.25 |
| 5-a: $(100 - x)GeS_2 - xGa_2S_3$ glasses | |
| composition (mol%) | n at 633 nm |
| $x = 0$ | 2.25 |
| $x = 10$ | 2.20 |
| $x = 15$ | 2.17 |
| $x = 20$ | 2.14 |
| 5-b: $70GeS_2 - (30 - x)Ga_2S_3 - x$CdS glasses | |
| composition (mol%) | $n$ at 633 nm |
| $x = 0$ | 2.01 |
| $x = 10$ | 2.12 |
| $x = 20$ | 2.15 |
| $x = 30$ | 2.17 |
| $x = 40$ | 2.19 |
| 5-c: $(100 - x)GeS_2 - x[0.5Ga_2S_3 - 0.5$CdS] glasses | |

**Table 1.5.** Optical properties of $Ge_{10}As_{10}Se_{80-x}Te_x$ glasses: $n_s$, values measured using the cut-back method; $n_E$, values measured using ellipsometry (after [80])

| glasses | $n_s$ at 1,550 nm | $n_E$ at 1,550 nm | $n_s$ at 1,050 nm | $n_E$ at 1,050 nm |
|---|---|---|---|---|
| x = 0 | 2.58 | 2.52 | 2.66 | 2.56 |
| x = 10 | 2.74 | 2.60 | 2.82 | 2.63 |
| $x = 15$ | 2.80 | 2.69 | 2.90 | 2.75 |
| $x = 20$ | 2.90 | 2.73 | 2.95 | 2.81 |

**Table 1.6.** Optical properties of some chalcogenide glasses (after [81])

| glass | $n$ at 1.55 µm | $\lambda_{\text{gap}}$ (µm) |
|---|---|---|
| $As_{40}S_{60}$ | 2.45 | 0.52 |
| $As_{40}S_{50}Se_{10}$ | 2.49 | 0.55 |
| $As_{40}S_{40}Se_{20}$ | 2.55 | 0.59 |
| $As_{40}S_{30}Se_{30}$ | 2.62 | 0.62 |
| $As_{40}S_{20}Se_{40}$ | 2.70 | 0.64 |
| $As_{40}S_{10}Se_{50}$ | 2.76 | 0.67 |
| $As_{40}Se_{60}$ | 2.81 | 0.70 |
| $As_{39}Se_{61}$ | 2.81 | 0.70 |
| $As_{40}Se_{55}Cu_5$ | 2.93 | 0.79 |
| $As_{25}S_{55}Te_{20}$ | 2.52 | 0.79 |

**Table 1.7.** Optical properties of $GeS_2$-based glasses (after [82])

| Glass | $n$ at 633 nm |
|---|---|
| $(GeS_2)_{85}(Ga_2S_3)_{15}$ | 1.9940 |
| $(GeS_2)_{85}(Ga_2S_3)_{11}(CsI)_4$ | 2.1600 |
| $(GeS_2)_{75}(Ga_2S_3)_{10}(CsI)_{10}(Ag_2S)_5$ | 2.1445 |

## 1.7 Chalcogenide Thin Films and Comparison with the Bulk

As the properties of a glass are a function of its thermal history, it is not unexpected that films or fibers may have properties that vary from those seen in their melt-derived bulk analogues. Films can be deposited, by thermal evaporation of their parent bulk glasses, onto room-temperature, pre-cleaned substrates under a vacuum of nominally between $10^{-5}-10^{-7}$ Torr. Glassy films prepared by this technique have been confirmed to be amorphous in nature and can vary in composition from the parent bulk by less than 5 at.% [79]. The refractive index can be obtained using transmission-curve or prism-coupling techniques [83] or a grating-coupling technique [84].

The absorption coefficient and the band gap can be calculated using transmission data. PDS has been used [31] to measure low values of the optical absorption coefficient of chalcogenide glasses in the form of thick samples, as well as films. PDS has been applied to optical-absorption measurements in, for example, $As_2S_3$ and As–S glasses [31]. This spectroscopic method has been demonstrated to be suitable for the evaluation of low absorption in thin samples, although its accuracy is affected by light scattering. For $As_2S_3$, as-evaporated films have a higher residual absorption than that of the bulk. As compared with changes in bulk-glass refractive indices, in the As–S–Se system, the film indices exhibited slightly larger variations with composition. This variation may be attributable to subtle compositional variations and the higher cooling rate with which the film structure assembles from the vapor

phase. The ability for molecular species to occur in the vapor phase [11] would give rise to a notably more ordered, connected molecular structure as compared with systems where little or no molecular ordering is believed to occur (e.g., in ternary As–S–Se glasses). Annealing of as-deposited films results in a further increase in refractive index and density, as the frozen network structure relaxes and further polymerizes.

Up to now, thermal evaporation and sputtering have been used to produce chalcogenide amorphous thin films. A significant problem encountered with these films is associated with the need to anneal them before light exposure for waveguide writing. In general, their thermal-expansion coefficient is much larger than common substrate materials, such as fused silica or silicon, leading to cracking or film lift off during or after annealing. While rapid thermal annealing [38] has proven a useful approach to minimize these problems, any deposition process that removes the need for annealing would have a significant advantage. Pulsed-laser deposition (PLD) is another technique for depositing chalcogenide films. A well-known advantage of the PLD technique is that it can accurately transfer the stoichiometry of a multicomponent target to a film deposited on a substrate. This is particularly important in materials containing weakly bonded volatile components such as sulfur, where thermal evaporation often results in marked changes in stoichiometry. In addition, PLD can result in bombardment of the substrate by relatively high-energy ions or neutral species, and this assists in densification of the film in a way analogous to the use of ion bombardment during sputtering. It is possible, therefore, for PLD to produce high-quality films that do not require annealing, as is generally essential for thermally evaporated films. A disadvantage of the conventional PLD process, which uses high-energy ($\sim$1 J), low-repetition rate (10–100 Hz) nanosecond laser pulses, is the production of particulates that can lead to high scattering losses in the films. It has been previously shown that the problem of particulates produced by conventional PLD can be eliminated by using an ultrafast PLD process that employs short ($<$50 ps), low-energy ($\sim\mu$J), high-repetition-rate ($10^5$–$10^8$ Hz) pulse trains [85, 86]; indeed, it was possible to produce high optical quality $As_2S_3$ chalcogenide glass films using ultrafast PLD [87]. The surface quality of the deposited films was almost down to the atomic level, with an rms roughness of the order of 0.42 nm. The resulting films were highly photosensitive and could be used without thermal annealing for waveguide fabrication using the photodarkening process. The prism-coupling technique [34] was used to measure the refractive index at 632.8, 810, and 1,064 nm for films deposited onto fused-silica microscope slides or onto silicon wafers covered by an oxidized layer 2.4 $\mu$m thick. During these measurements, the ability of the films to act as waveguides could also be assessed from propagation of the excited slab waveguide modes. In general, rather poor propagation was observed at 633 nm due to strong absorption (10–20 dB cm$^{-1}$) of the films due to the proximity of the band edge, whilst at longer wavelengths the losses were relatively low (a few dB cm$^{-1}$ or lower). The beams propagating in

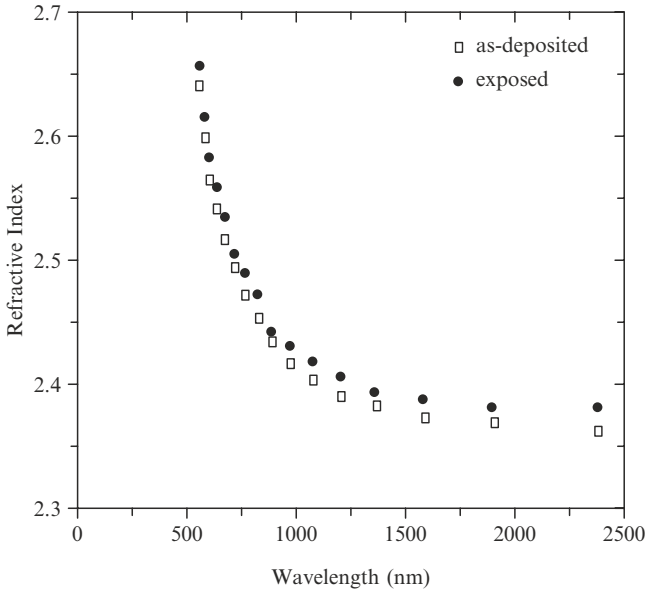


**Fig. 1.5.** Refractive index of MLQS $As_2S_3$ films versus wavelength. Samples were exposed by a green laser beam and the illumination intensity was 10 mW $mm^{-2}$ (after [88])

the planar slabs could be discerned from scattering of the propagating light, indicating that scattering centers had not been totally eliminated. In order to characterize more broadly the refractive indices of the films, a transmissivity measurement was performed using a spectrophotometer. The dispersion characteristics of the material were extracted from interference fringes present on the transmission curve, via the Swanepoel technique [77]. Figure 1.5 shows a typical spectral dependence of the refractive index for one of the mode-locked Q-switched (MLQS) films. The results were reproducible to 0.01 over different deposition runs. Similar results were obtained for the films deposited using a purely mode-locked (PML) laser ($\lambda = 532\,nm$), although the as-deposited refractive index was generally about 0.01 lower than (MLQS) deposited films.

In order to examine the effect of laser exposure on these films, an area of a few $cm^2$ of the sample was scanned with a 514.5 nm, cw laser beam (the illumination intensity was 10 mW $mm^{-2}$) with a total fluence of 1,000 mJ $mm^{-2}$. Refractive indices of the illuminated area were again measured using the above techniques. Figure 1.5 shows also the spectral dependence of the refractive index of the illuminated area. In this case, a significant difference in the exposure characteristics was observed for the MLQS films compared with the PML films. In the former case, a photoinduced change of $\Delta n_{\mathrm{MLQS}} \approx +0.01$ in refractive index was measured over the whole wavelength range,

whilst in the latter, the index change was much bigger $\Delta n_{\mathrm{PML}} \approx +0.04$. In both cases, the index change could, in principle, be exploited for waveguide fabrication. In order to prepare a film with the lowest number of scattering centers, extensive work on the effects of annealing of these films was carried out [88]. Normally, annealing removes all stress and strain in films and hence produces a more relaxed glass structure for device fabrication. Figure 1.6 shows the index change as a result of annealing of MLQS films in a nitrogen environment. As can be seen, a change of refractive index up to 0.04 was observed as a result of annealing of films at 150°C. No detectable change in composition was observed for the films when annealed up to 150°C.

Tables 1.8 and 1.9 summarize the result of optical-constant measurements for chalcogenide films prepared by different deposition techniques and under different heat-treatment procedures, while Figs. 1.7 and 1.8 show results of optical-constant measurements versus wavelength for $Ge_xSb_yTe_z$ films [89].

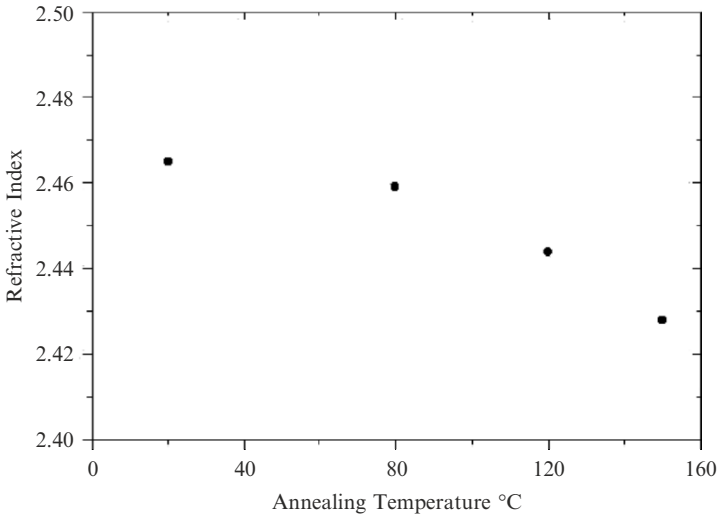


**Fig. 1.6.** Effect of annealing on the refractive index of an $As_2S_3$ film measured at 810 nm (after [88])

**Table 1.8.** Optical constants of thin $Ge_xSb_yTe_z$ films (after [89])

| material | deposition method | $n$ at 635 nm | $k$ at 635 nm | $n$ at 650 nm | $k$ at 650 nm | $n$ at 780 nm | $k$ at 780 nm | $n$ at 830 nm | $k$ at 830 nm |
|---|---|---|---|---|---|---|---|---|---|
| $Ge_8Sb_{23}Te_{59}$ | evap. | 4.38 | 2.27 | 4.43 | 2.22 | 4.83 | 1.77 | 4.92 | 1.58 |
| $Ge_{14}Sb_{28}Te_{58}$ | sputt. | 4.39 | 2.08 | 4.46 | 2.04 | 4.77 | 1.65 | 4.80 | 1.47 |
| $Ge_{22}Sb_{22}Te_{56}$ | sputt. | 4.31 | 1.90 | 4.36 | 1.85 | 4.62 | 1.46 | 4.72 | 1.3 |

**Table 1.9.** Optical constants of evaporated chalcogenide films (after [10])

| composition | $n$ at 1.53 µm | $n$ at 1.55 µm | film status |
|---|---|---|---|
| $As_{40}S_{60}$ | 2.4035 | 2.4050 | annealed |
| $As_{40}S_{60}$ | 2.3439 | 2.3439 | not annealed |
| $As_{36}S_{59}Se_{15}$ | 2.4707 | 2.4636 | annealed |
| $As_{40}S_{45}Se_{15}$ | 2.4139 | 2.4098 | not annealed |
| $As_{39}S_{29}Se_{32}$ | 2.5727 | 2.5709 | annealed |
| $As_{40}S_{30}Se_{30}$ | 2.5074 | 2.4949 | not annealed |
| $As_{40}S_{14}Se_{46}$ | 2.6750 | 2.6766 | annealed |
| $As_{40}S_{15}Se_{45}$ | 2.6239 | 2.6270 | not annealed |
| $As_{40}Se_{60}$ | 2.8318 | 2.8318 | annealed |
| $As_{40}Se_{60}$ | 2.7842 | 2.7707 | not annealed |
| $As_{32}S_{34}Se_{34}$ | 2.5400 | 2.5414 | annealed |
| $As_{32}S_{34}Se_{34}$ | 2.5050 | 2.5041 | not annealed |
| $As_{24}S_{38}Se_{38}$ | 2.4666 | 2.4650 | annealed |
| $As_{24}S_{38}Se_{38}$ | 2.4445 | 2.4445 | not annealed |
| $As_{18}S_{41}Se_{41}$ | 2.3764 | 2.3745 | annealed |
| $As_{18}S_{41}Se_{41}$ | 2.3691 | 2.3673 | not annealed |

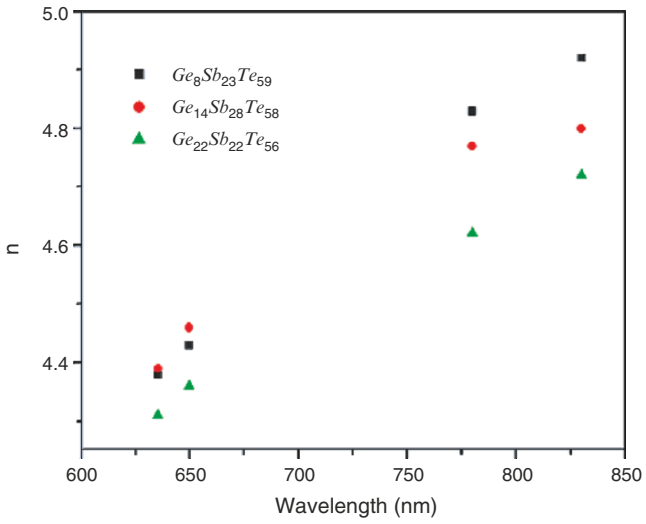


**Fig. 1.7.** Variation of refractive index $n$ versus wavelength for $Ge_xSb_yTe_z$ films [89]

## 1.8 Photoinduced Changes in Chalcogenide Glasses

### 1.8.1 Photoinduced Phenomena

At least seven distinct photoinduced phenomena are exhibited by amorphous chalcogenides [90, 91]. These include photocrystallization or (amorphization),

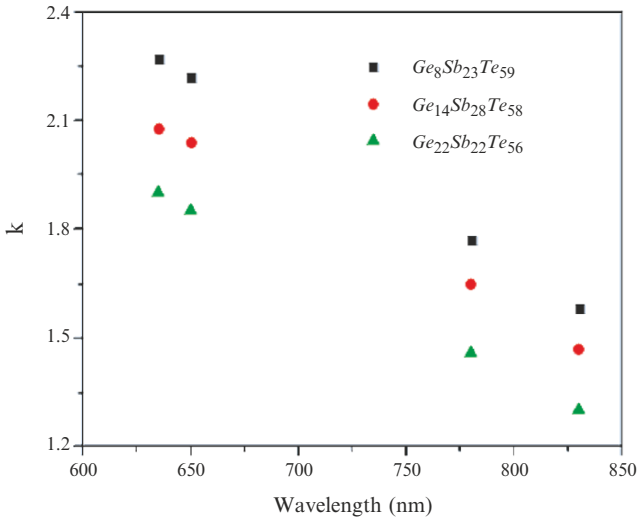


**Fig. 1.8.** Variation of extinction coefficient $k$ versus wavelength for $Ge_xSb_yTe_z$ films [89]

photopolymerization, photodecomposition, photocontraction or expansion, photovaporization, photodissolution of metals such as Ag into the chalcogenide, and light-induced change in local atomic configuration. These changes are accompanied by changes in the optical constants, i.e., changes in the electronic band gap, refractive index and optical absorption coefficient. X-ray studies of volume expansion are shown in Fig. 1.9 [92]. We see in the upper pattern that the first sharp diffraction peak is located at a wavenumber-transfer value of $Q \sim 1.2\,\text{Å}^{-1}$. The lower curve shows the intensity difference between the annealed and illuminated states, with positive difference values indicating a decrease in the X-ray intensity with illumination. The results show that the peak intensity decreases with illumination. In addition, the peak broadens asymmetrically. This asymmetric change can be interpreted as a manifestation of interlayer cracking [92]. In distorted layer structures (as a result of illumination) with a typical interlayer distance of ∼0.5 nm, in a few places the interlayer distance becomes as wide as ∼1 nm.

These light-induced changes are favored in chalcogenide glasses due to their structural flexibility (low coordination of chalcogens) and also due to their high-lying lone-pair p states in the valence band. Annealing chalcogenide glasses can affect the photoinduced changes. In particular, irreversible effects occur in as-deposited films, while reversible effects occur in well-annealed films as well as bulk glasses. Changes in local atomic structure are observed on illumination with light having a photon energy near the optical band gap of the chalcogenide. Although light-induced effects can also be observed at longer wavelengths, they generally necessitate much higher intensities.

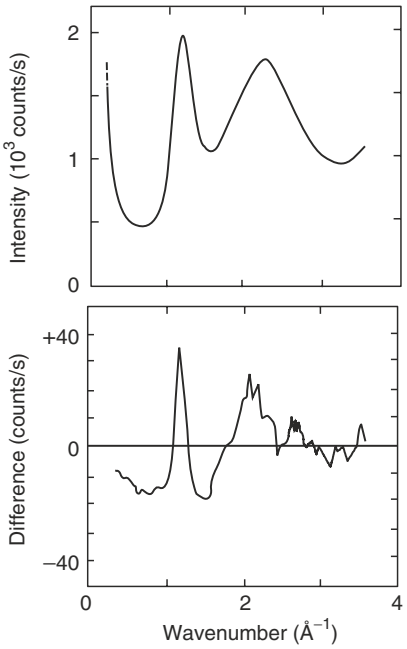


**Fig. 1.9.** An X-ray diffraction pattern of $As_2S_3$ glass (*top*) and the intensity change (*bottom*) induced by band gap illumination. A positive difference means an intensity reduction upon illumination (after [20, 92])



Photodarkening is sensitive to hydrostatic pressure, and it can be thermally erased by annealing near the glass-transition temperature. Photoinduced anisotropy (PA) is induced [3] when the glass or film is exposed to linearly polarized light and can be removed by exposure to unpolarized light or thermal annealing. When chalcogenide glasses are exposed to short laser pulses, large Kerr-type nonlinearities are induced. Photoinduced stable second-harmonic generation has also been reported in chalcogenide glasses [93]. These photoinduced effects can be used for the fabrication of devices such as gratings, waveguides, etc. (see Chaps. 1 and 7).

### 1.8.2 Exposure Characteristics

In order to explore the utility of photodarkening for device applications, a map of variation of intensity versus exposure for $As_2S_3$ films deposited by PLD has been measured [88]. Photodarkening was measured by monitoring the change in the transmission of a sample with time during illumination. Figure 1.10 shows a typical curve of transmissivity at 514.5 nm versus time. As is evident, the transmission of the sample decreases with time, approaching

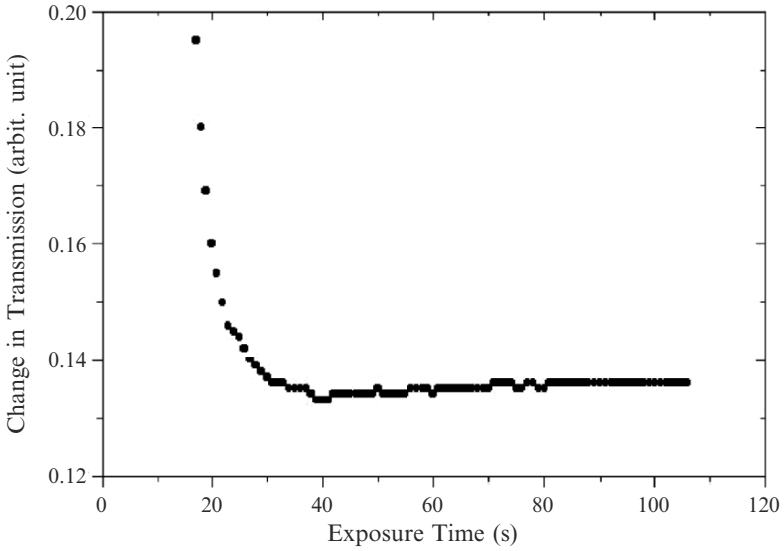


**Fig. 1.10.** Change of optical transmission of a 2 μm thick $As_2S_3$ film versus time during photodarkening at 514.5 nm. Illumination intensity of the green light was 30 mW mm$^{-2}$; the value 0.2 corresponds to 20% transmission (after [88])

a saturation point for long exposures. In order to see whether darkening is reversible or permanent, annealing at 150°C for 2 h under a nitrogen flow was performed after sample exposure. Annealing at this temperature allowed for maximum index change. It should be emphasized here that all the exposure measurements were obtained at a time for which maximum darkening had occurred (when the transmission of the sample had reached the saturation value). Figure 1.11 shows the result of intensity change versus exposure for $As_2S_3$ films [88]. As is seen, the exposure map divides into three distinctly different regions.

These results are very similar to those reported by the Laval group [94], although the latter films seem to be slightly less sensitive. This could be explained as partly due to a different composition of films used in [88] and partly to the fact that the films had been illuminated during the deposition in the PLD chamber. When using photodarkening to write waveguides using a laser, it is important to know the damage threshold corresponding to the intensity when the film starts to be ablated/melted off the substrate. This threshold was found to be $\approx 7,100$ mW mm$^{-2}$ for PLD $As_2S_3$ films at 514.5 nm [88].

As a result, from Fig. 1.11 one can see that permanent photodarkening can be achieved at waveguide writing speeds of $>100$ μm s$^{-1}$ at a subdamage irradiance of 5,600 mW mm$^{-2}$. On the basis of these results, Zakery [88] assembled a laser-writing system to fabricate channel waveguides about 3 μm wide. The

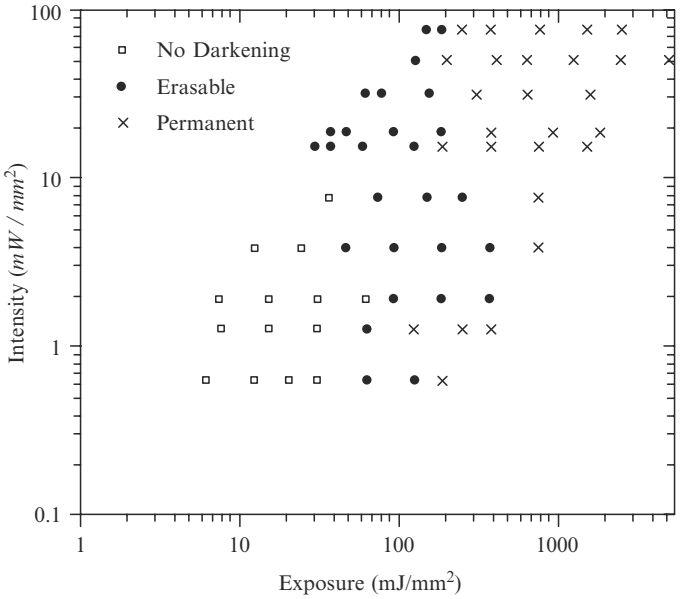


**Fig. 1.11.** Darkening map of films as a function of both intensity and exposure for a 4 µm thick sample irradiated at 514.5 nm with an argon laser and subsequently annealed at 150°C for 2 h [ after 88]

514.5 nm green line of an argon laser was attenuated by passing through a neutral-density filter and then expanded by a pinhole. The expanded output was then focused on the sample using a 10× objective. PLD $As_2S_3$ films were deposited on a silicon wafer with an overlayer of 2.4 µm $SiO_2$. As-deposited $As_2S_3$ films with thicknesses up to 2 µm were used in which channel waveguides were fabricated.

### 1.8.3 Measurements of the Propagation Losses by a Prism Coupler

Measurements of waveguiding can be performed [88] using a prism coupler. An $As_2S_3$ film deposited with a $SiO_2$ overlayer, pressed against a high refractive-index prism ($n = 2.8659$ at 632.8 nm), can be rotated to find angular positions at which coupling into a waveguide mode is possible. It is possible to observe the propagation of guided light by detecting the light scattered from the sample with a CCD camera and the propagation loss can be calculated using the output intensity versus the propagation distance. The camera measured propagation distances of 4–5 cm at 632.8 nm. The results of loss measurements by the prism coupler are also shown in Fig. 1.12. The direct beam of an argon laser (green line) was used to expose an area of $5 \times 1$ cm on the sample and this

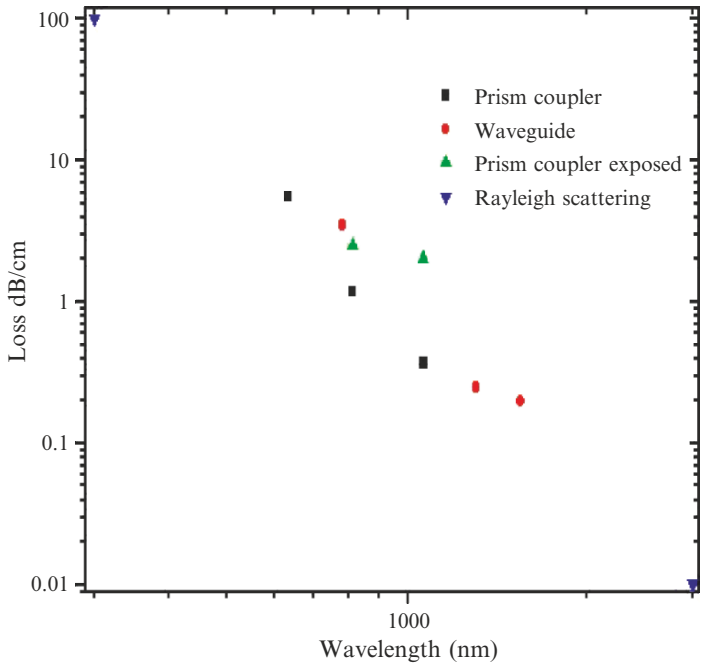


**Fig. 1.12.** Propagation loss versus wavelength for a 3 µm channel waveguide fabricated in PLD $As_2S_3$ films. Prism coupler corresponds to loss measurements using a prism-coupling technique described in the text, while waveguide corresponds to loss measurements in a fabricated waveguide. Prism-coupler exposed refers to the case where the sample was exposed prior to loss measurements (after [88])

exposed region was also used in propagation-loss measurements. Figure 1.12 shows losses of between 5 and 8 dB $cm^{-1}$ measured at 632.8 nm.

Measured losses at 810 nm are between 1 and 2 dB $cm^{-1}$, while at 1,064 nm losses of between 0.3 and 0.7 dB $cm^{-1}$ were measured for as-deposited films. For exposed samples, measured losses were between 1 and 2 dB $cm^{-1}$ in the wavelength region of 780–1,064 nm [88].

### 1.8.4 Measurements of Propagation Losses in Laser-Written Waveguides

$As_2S_3$ films of up to 2 µm thickness were used for waveguide fabrication. Channel waveguides of 5 cm length and 3 µm width were written (using the direct laser writing set up described earlier) in these films. Light from different laser-diode sources at 780, 1,300, and 1,550 nm were used for these measurements. The output of the laser source was butt coupled to the film via a fiber of 5 µm diameter and the guided light through the waveguide was then coupled to a microscope objective and collected by a CCD camera. Figure 1.13 shows the

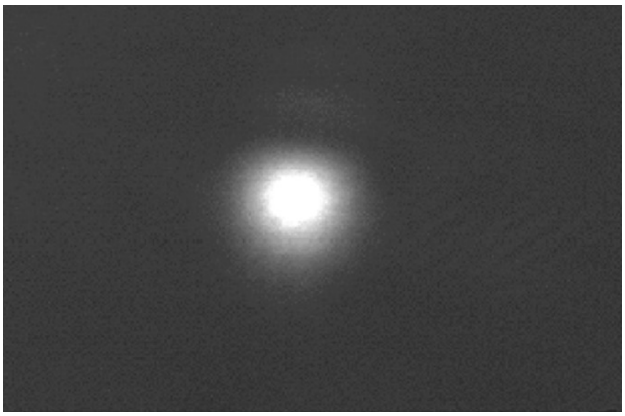

**Fig. 1.13.** Near-field image of the output of a single-mode photoinduced channel waveguide made in an $As_2S_3$ film measured at 780 nm (after [88])

near-field image of the output of a photoinduced channel waveguide written in these PLD films. Results of loss measurements for waveguides written in $As_2S_3$ films are also shown in Fig. 1.12. Losses lower than $0.3\,\mathrm{dB\,cm^{-1}}$ were measured at 1,550 nm.

## 1.9 Summary

Chalcogenide glasses are low-phonon-energy materials and are generally transparent from the visible to the infrared. Doping chalcogenide glasses by rare-earth elements has opened up numerous applications of active optical devices. Because of their large nonlinearities, chalcogenide glasses are promising candidates for AOS applications. The structure of chalcogenide glasses cannot be described by means of a continuous random network, but can be rather layer-like, as for example in $As_2S_3$, and chain-like, as in pure S or Se. Flexibility of their structures, as a result of the van der Waal's bonding between layers allows for easily accommodation of changes in their structures. Various structural techniques such as NIR Raman spectroscopy, RBS, WRS, and EXAFS have been used to probe different structural units present in chalcogenide glasses. Different techniques have been employed to determine the density of localized states in the gap and it is now generally believed that on top of a featureless distribution of states in the tails, a structured density of defect states exists, attributed to VAPs. It could be said that well-defined states exist in the gap of chalcogenide glasses. The absorption coefficient, $\alpha$, of films has been measured using several techniques, such as with a conventional spectrophotometer in the visible region and PDS for wavelengths beyond the band edge. The results of PDS measurements have shown that as-deposited films have losses below $0.1\,\mathrm{dB\,cm^{-1}}$ across the telecommunica-

tion band. The optical gap obtained from the analysis of the data shows that chalcogenide glasses have optical gaps ∼2–3 eV. Various photoinduced effects, such as photodarkening, the metal-photodissolution effect and PA, have been used to fabricate devices such as gratings, waveguides, Bragg gratings, etc. Doping chalcogenide glasses with rare-earth elements has allowed the possibility of using these glasses for active applications such as amplifiers and lasers. Since chalcogenide glass fibers transmit in the IR, there are numerous potential applications in the civil, medical and military areas. Chalcogenide fibers are well-suited for chemical-sensor applications, such as fiber-optic chemical-sensor systems for quantitative remote detection and identification as well as detecting chemicals in mixtures. Different techniques have been used to measure the optical constants of chalcogenide glasses and films, such as optical transmission and reflection, ellipsometry, prism coupling, etc. While, up to now, evaporated and sputtered films have been used for producing films of chalcogenide glasses, pulsed laser-deposition of these films has proved useful. These PLD films have a stoichiometry similar to their parent materials and do not need annealing after deposition. They have been used in fabricating many devices, such as waveguides, fiber Bragg gratings, nonlinear directional couplers, etc. using light-induced photostructural changes. Results of loss measurements in laser-written waveguides show that losses lower than 0.3 dB $cm^{-1}$ at 1,550 nm are found for a typical chalcogenide glass such as $As_2S_3$.

# 2

# Basic Concepts of Nonlinear Optics

## 2.1 Polarization

When an electric field is applied to a dielectric medium (of overall neutral electric charge), a separation of bound charges is induced, as illustrated in Fig. 2.1. This separation of charge results in a collection of induced dipole moments $\mu^{(\sim)}$, which, as designated, may be rapidly oscillating if the applied field is also oscillating. The tilde symbol denotes a quantity which is varying rapidly with time.

The electrical polarization is defined as the net average dipole moment per unit volume and is given by:

$$P^{(\sim)} = N\langle\mu^{(\sim)}\rangle, \tag{2.1}$$

where $N$ is the number of microscopic dipoles per unit volume, and the angular brackets indicate an ensemble average over all the dipoles in the medium.

Any permanent dipoles within the medium will be ignored, since they do not oscillate at optical frequencies and hence do not radiate electromagnetic waves.

To an excellent approximation, at low light-intensity levels, the polarization is linearly proportional to the applied field: This is the regime of linear optics.

The spatially local, steady-state electric polarization response, for frequencies far removed from any material resonance, may then be written as:

$$P_{\mathrm{L}}^{(\sim)} = \varepsilon_0 \chi^{(1)} \cdot E^{(\sim)}, \tag{2.2}$$

where the subscript L signifies a linear polarization, $\varepsilon_0$ is the electrical permittivity of free space, and $\chi^{(1)}$ is the linear dielectric response tensor. In general, the relation between $P^{(\sim)}$ and $E^{(\sim)}$ is tensorial, and (2.2) can also be written as

$$P_{\mathrm{L},i}^{(\sim)} = \varepsilon_0 \sum_j {\chi_{ij}}^{(1)} E_j^{(\sim)}, \tag{2.3}$$

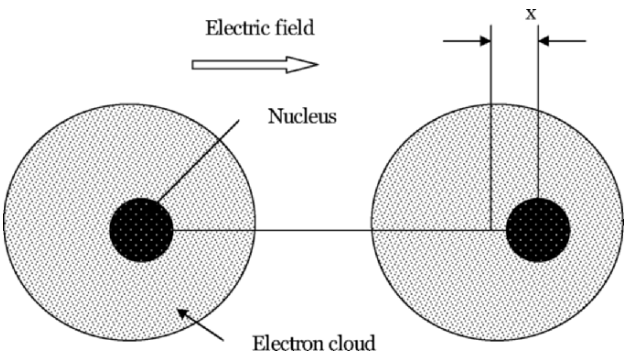


**Fig. 2.1.** Schematic illustration of the electronic polarization of an atom (ion) relative to the nucleus under the influence of an external field $E$

where the subscript $i$ signifies the $i$th Cartesian coordinate ($i = x, y, z$), and the sum is over $j = x, y, z$. The tensor $\chi^{(1)}$ thus has nine components. In an isotropic medium, there is only one independent nonzero component, and the dielectric response is written as the scalar quantity $\chi^{(1)}$.

## 2.2 Wave Equation

For the majority of situations considered in nonlinear optics, it can be assumed that there is no macroscopic magnetization in the dielectric medium (no microscopic magnetic dipoles). The medium is also electrically neutral and nonconducting, so that no free charge or current density exists. Under these conditions, the wave equation describing the propagation of the vector electric field is given by:

$$\nabla \times \nabla \times E^{(\sim)} + \frac{1}{c^2}\frac{\partial^2 E^{(\sim)}}{\partial t^2} = -\frac{k}{c^2}\frac{\partial^2 P^{(\sim)}}{\partial t^2} \ , \tag{2.4}$$

where $c$ is the speed of light in a vacuum and $k$ is a constant depending on the system of units used, e.g.,

$$k = (\varepsilon_0)^{-1}. \qquad \text{(SI)} \tag{2.5}$$

When the light intensity is sufficiently high (e.g., from a laser), a small additional polarization will appear, so that the total polarization can be written as

$$P^{(\sim)} = P_{\mathrm{L}}^{(\sim)} + P_{\mathrm{NL}}^{(\sim)}, \tag{2.6}$$

where $P_{\mathrm{NL}}^{(\sim)}$ is a nonlinear function of the applied field. Substituting this expression into (2.4) and using (2.2), the wave equation becomes

$$\nabla \times \nabla \times E^{(\sim)} + \frac{1}{c^2}\kappa\frac{\partial^2 E^{(\sim)}}{\partial t^2} = -\frac{k}{c^2}\frac{\partial^2 P_{\mathrm{NL}}^{(\sim)}}{\partial t^2} \ , \tag{2.7}$$

where $\kappa = \varepsilon/\varepsilon_0$ (SI) is the linear dielectric tensor with tensor component

$$\kappa_{ij} = \left(\delta_{ij} + \chi_{ij}^{(1)}\right) \qquad \text{(SI)}. \tag{2.8}$$

For most situations in nonlinear optics, the total electric field can be considered to be a superposition of quasimonochromatic waves. The total field is then written as:

$$E^{(\sim)}(r,t) = \sum_{\mu} \widehat{e}_{\mu} A_{\mu}(r,t) \exp[\mathrm{i}(k_{\mu} \cdot r - \omega_{\mu} t] + \text{c.c.}, \tag{2.9}$$

where the sum is over an integer number $\mu$, of waves of frequencies $\omega_{\mu}$ and wave vectors $k_{\mu}$, $\hat{e}_{\mu}$ is a unit vector representing the polarization of the wave, $A_{\mu}(r,t)$ is the complex field amplitude and c.c. denotes the complex conjugate.

For the typical case when the nonlinear polarization represents a small perturbation to the total polarization, it can also be written as:

$$P_{\mathrm{NL}}^{(\sim)}(r,t) = \sum_{\mu} P_{\mathrm{NL}_{\mu}}(r,t) \exp(-\mathrm{i}\omega_{\mu} t) + \text{c.c.}, \tag{2.10}$$

where $P_{\mathrm{NL}_{\mu}}(r,t)$ is a slowly time-varying (compared to the rapidly oscillating part of the wave) complex polarization amplitude. Then, by the linearity of the wave equation, each frequency component (Fourier component) of the total field also satisfies (2.7), with the corresponding frequency component of the nonlinear polarization appearing on the right-hand side of the equation. In relations between Fourier components of the polarization and field, the Fourier transform of the fully time-dependent dielectric response is used, which is in general a complex function of frequency. This quantity is called the electric susceptibility tensor. The dielectric constant is then also a complex function of frequency. Under usual conditions, the left-hand side of (2.7) can be simplified. To an excellent approximation in homogeneous media,

$$\nabla \times \nabla \times E^{(\sim)} \cong -\nabla^2 E^{(\sim)}, \tag{2.11}$$

where $\nabla^2$ is the Laplacian operator.

### 2.2.1 Linear Optics

In the linear optical regime, the nonlinear part of the polarization may be neglected. The wave equation, (2.7), then becomes a homogeneous differential equation. Its solutions are given in the form of:

$$E^{(\sim)}(r,t) = \hat{e} A(r,t) \exp[\mathrm{i}(kz - \omega t)] + \text{c.c.} \tag{2.12}$$

The polarization of the wave (i.e., the direction of the electric-field vector) is given by the unit vector $\hat{e}$. When this vector is real, the wave is said to be plane polarized. A complex unit vector implies that the wave is elliptically polarized.

### Isotropic Media

In an isotropic medium, the approximation given in (2.11) is exact for a plane wave, and the susceptibility is a scalar quantity. The latter will be a complex function of frequency, in general, and can be written as:

$$\chi^{(1)} = \chi_{\mathrm{R}}^{(1)} + \mathrm{i}\chi_{\mathrm{I}}^{(1)}, \tag{2.13}$$

where the subscripts R and I signify real and imaginary parts, respectively. The dielectric constant is also complex, and has the form:

$$\sqrt{\frac{\varepsilon(\omega)}{\varepsilon_0}} = n(\omega) + \mathrm{i}\frac{\alpha(\omega)}{4\pi} \ . \tag{2.14}$$

In (2.14), $n(\omega)$ is the refractive index given by:

$$n(\omega) = \sqrt{1 + \chi_{\mathrm{R}}^{(1)}(\omega)}, \tag{2.15}$$

and $\alpha(\omega)$ is the intensity absorption coefficient, given by:

$$\alpha(\omega) = \frac{\omega\chi_{\mathrm{I}}^{(1)}(\omega)}{n(\omega)c}. \tag{2.16}$$

The plane-wave solution to the wave equation then has the form:

$$E^{(\sim)}(z,t) = \hat{e}A_0 \exp(-\alpha z/2) \exp[\mathrm{i}(kz - \omega t)] + \mathrm{c.c.}, \tag{2.17}$$

where $A_0$ is the amplitude of the wave at $z$ =0 and the wave vector obeys the dispersion relation given by:

$$k(\omega) = n(\omega)\omega/c \tag{2.18}$$

The wave thus travels with a phase velocity $\nu_{\mathrm{p}} = c/n$. In isotropic media, the electric-field vector is always perpendicular to the wave vector, and the phase velocity of the wave is independent of the direction of propagation. Since detectors cannot respond to the rapidly varying optical frequency, the quantity measured experimentally is the time-averaged field flux, where the average is over several optical cycles. The quantity of interest then is the optical intensity (or irradiance), which is related to the field amplitude by:

$$I(z,t) = 2\varepsilon_0 nc \left|A(z,t)\right|^2 . \tag{2.19}$$

In a cw laser beam of finite cross-sectional area, the optical power is typically measured and is related to the intensity by

$$P = \int\limits_A I \mathrm{d}A, \tag{2.20}$$

where the integral is over the area, $A$, of the beam, not to be confused with the complex field amplitude.

For a $\mathrm{TEM}_{00}$ Gaussian beam, the relationship at the beam waist is

$$P = \frac{\pi\omega_0^2}{2} I_0, \tag{2.21}$$

where $I_0$ is the peak on-axis intensity of the Gaussian beam.

### Anisotropic Media

In anisotropic media, the situation is not so simple. Generally, the electric-field vector is not perpendicular to the wave vector (direction of propagation). However, the displacement vector $D^{(\sim)}$, defined by:

$$D^{(\sim)} = \varepsilon \cdot E^{(\sim)} + P^{(\sim)} \tag{2.22}$$

is orthogonal to the wave vector $k$ (see Fig. 2.2). In any anisotropic medium, two independent orthogonally polarized $D^{(\sim)}$-waves can propagate with different phase velocities. The problem in the optics of anisotropic media is to find the polarizations of these modes and their corresponding phase velocities. It can be shown that the linear dielectric constant is a symmetric tensor ($\varepsilon_{ij} = \varepsilon_{ji}$) [95]. By the laws of linear algebra, an orthogonal coordinate system can be found in which this tensor is diagonal ($\varepsilon_{ij} = \varepsilon_{ii}\delta_{ij}$, where $\delta_{ij}$ is given in (2.8)). The axes of this system are called the principal axes, and the corresponding diagonal elements of the dielectric tensor are called the principal dielectric constants of the medium. These are designated $\varepsilon_{XX}, \varepsilon_{YY}, \varepsilon_{ZZ}$, where the upper-case subscript symbols are used to signify the principal axes. Similarly, the principal refractive indices are found to be

$$n_{ii} = (\varepsilon_{ii}/\varepsilon_0)^{1/2}. \tag{2.23}$$

The phase velocity for a wave polarized along the $i$th principal axis is $\nu_{\mathrm{p}i} = c/n_{ii}$.

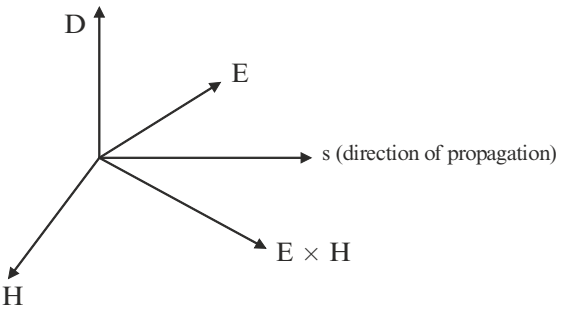


**Fig. 2.2.** The relative orientation of $E$ (electric field), $D$ (displacement vector), $H$ (magnetic field), $s$ (direction of propagation), and the Poynting vector $E \times H$, in an anisotropic crystal. The vectors $D$, $E$, $s$, and $E \times H$ lie in a single plane

If the dielectric tensor elements are complex, then the principal refractive indices are related to the real part of the square root given above in (2.23). The imaginary part of the square root is related to the principal values of absorption coefficients $\alpha_{ii}$ analogous to the scalar quantity given by (2.16). This polarization-dependent, propagation-direction dependent absorption is called pleochromism [96]. Often, these principal quantities are written with a single rather than a double subscript. In general, $n_X \neq n_Y \neq n_Z$. Such a medium is called biaxial. A great simplification occurs when two of the principal indices are equal, for example, $n_X = n_Y \neq n_Z$. This type of medium is called uniaxial. There is a single axis of symmetry taken to be the $z$-axis, which is called the optic axis. When light propagates along this axis, its phase velocity is independent of polarization. The following designation is made: $n_X = n_Y = n^{\mathrm{o}}$ and $n_Z = n^{\mathrm{e}}$, where the symbol o stands for ordinary and the symbol e for extraordinary waves. Uniaxial media are said to be birefringent, exhibiting double refraction. The birefringence of the medium is given by $\Delta n = n^{\mathrm{e}} - n^{\mathrm{o}}$. Many useful transparent crystals in nonlinear optics have a very small birefringence ($|\Delta n| \ll 1$). In these types of materials, $E^{(\sim)}$ and $D^{(\sim)}$ are nearly parallel and can be treated as such for most practical situations. One of the independent propagation modes in uniaxial media has its polarization orthogonal to the optic axis and thus has a phase velocity given by $\nu_{\mathrm{p}} = c/n$. This is called the ordinary wave. The extraordinary wave will have a component of its polarization along the optic axis, and its phase velocity will be given by $\nu_{\mathrm{p}} = c/n^{\mathrm{e}}(\theta)$, where $\theta$ is the direction of propagation of the extraordinary wave with respect to the optic axis, and

$$\frac{1}{[n^{\mathrm{e}}(\theta)]^2} = \frac{\cos^2\theta}{(n^{\mathrm{o}})^2} + \frac{\sin^2\theta}{(n^{\mathrm{e}})^2} \ . \tag{2.24}$$

General methods for determining the orthogonal polarizations of the $D^{(\sim)}$-waves and the corresponding phase velocities for any uniaxial crystal by use of the so-called optical indicatrix are found in several books [95–97]. For biaxial media, the phase velocities of the two allowed modes of propagation are determined by solving the Fresnel equation [95–97]:

$$\frac{\sin^2\theta\cos^2\phi}{(n)^{-2} - (n_X)^{-2}} + \frac{\sin^2\theta\sin^2\phi}{(n)^{-2} - (n_Y)^{-2}} + \frac{\cos^2\theta}{(n)^{-2} - (n_Z)^{-2}} = 0 \ , \tag{2.25}$$

where $\theta$ and $\phi$ are the spherical angles describing the direction of propagation with respect to the principal axes. Generally, this equation must be solved numerically for the two independent values of the refractive index.

### 2.2.2 Nonlinear Optics

In the nonlinear-optics regime, the nonlinear part of the polarization can no longer be ignored. The nonlinear polarization in (2.4) serves as a source for the generation of new waves, and the wave equation becomes an inhomogeneous

differential equation. Hence an expression for $P_{\mathrm{NL}}$ is required. This quantity can be expressed as a power-series expansion in the applied fields.

### Nonlinear Susceptibilities

It is assumed that the nonlinear polarization can be written as:

$$P_{\mathrm{NL}}^{(\sim)} = P^{(\sim)(2)} + P^{(\sim)(3)} + \cdots , \tag{2.26}$$

where

$$P^{(\sim)(2)} = \varepsilon_0 \chi^{(2)} : E^{(\sim)} E^{(\sim)} \tag{2.27}$$

$$P^{(\sim)(3)} = \varepsilon_0 \chi^{(3)} : E^{(\sim)} E^{(\sim)} E^{(\sim)}$$

$$\vdots$$

etc.

These expressions are given in SI units. It is important to note that the field in the equations above is the total applied field, which can be a superposition of many fields of different frequencies. $\chi^{(n)}$ is the $n$th-order dielectric response and is a tensor of rank $n+1$. When the total field is expanded in terms of its Fourier components, then the nonlinear polarization will consist of several terms oscillating at various combination frequencies. For example, if the total field consists of two waves oscillating at frequencies $\omega_1$ and $\omega_2$, the second-order nonlinear polarization will have components oscillating at $2\omega_1$, $2\omega_2$, $\omega_1 + \omega_2$, $\omega_1 - \omega_2$, and zero-frequency dc terms. It is common to write the Fourier components of the nonlinear polarization in the following way. Consider a second-order polarization oscillating at $\omega_3$ due to the presence of fields oscillating at frequencies $\omega_1$ and $\omega_2$, with $\omega_3 = \omega_1 + \omega_2$. Then the $i$th cartesian component of the complex polarization amplitude is expressed as

$$P_i^{(2)}(\omega_3) = \varepsilon_0 D^{(2)} \sum_{j,k} {\chi_{ijk}}^{(2)}(-\omega_3; \omega_1, \omega_2) E_j(\omega_1) E_k(\omega_2), \tag{2.28}$$

where $D^{(2)} = 2$ for distinguishable fields, and ${\chi_{ijk}}^{(2)}(-\omega_3; \omega_1, \omega_2)$ is the second-order (complex) Fourier-transformed dielectric response, or the second-order susceptibility. The form of (2.28) allows for the possibility that the frequencies $\omega_1$ and $\omega_2$ are equal, or equal in magnitude and opposite in sign. In this case, there may actually be only one field present, and the degeneracy factor $D^{(2)}$ takes this into account. It should be noted, however, that the value of the degeneracy factor depends on whether the fields are physically distinguishable, or not. Two fields with the same frequency will be physically distinguishable if they travel in different directions, for example. Also, the negative frequency part of the real field is considered to be distinguishable from the positive frequency part, i.e., they have different frequencies. For negative

frequencies, it is important to note that $E(-\omega) = E^*(\omega)$, since the rapidly varying field is a real mathematical quantity. Thus, for example, if $\omega_1 = \omega$ and $\omega_2 = -\omega$, then the second-order polarization would be written as

$$P_i^{(2)}(0) = 2\varepsilon_0 \sum_{j,k} {\chi_{ijk}}^{(2)}(0;\omega,-\omega)E_j(\omega){E_k}^*(\omega). \tag{2.29}$$

This polarization drives the phenomenon known as optical rectification, wherein an intense optical wave creates a dc polarization in a nonlinear medium. This notation is easily extended to higher orders. When three frequencies, $\omega_1, \omega_2, \omega_3$, are present, the third-order polarization at $\omega_4 = \omega_1 + \omega_2 + \omega_3$ is given by

$${P_i}^{(3)}(\omega_4) = \varepsilon_0 D^{(3)} \sum_{jkl} {\chi_{ijkl}}^{(3)}(-\omega_4;\omega_1,\omega_2,\omega_3)E_j(\omega_1)E_k(\omega_2)E_l(\omega_3). \tag{2.30}$$

This form of the third-order polarization allows for various combination frequencies even when only two fields are present, such as $\omega_1 + 2\omega_2$, or $2\omega_1 - \omega_2$, etc.

The degeneracy factor is just due to the number of different ways in which the products of the field's Fourier components appear in the expansion of the total field to some power. For example, there is only one way that the product for the frequency $3\omega_1$ appears: $E(\omega_1)E(\omega_1)E(\omega_1)$. However, there are three different ways that the product for the frequency $2\omega_1 - \omega_2$ appears: $E(\omega_1)E(\omega_1)E^*(\omega_2)$, $E(\omega_1)E^*(\omega_2)E(\omega_1)$, and $E^*(\omega_2)E(\omega_1)E(\omega_1)$.

### Symmetry Relations of the Nonlinear Susceptibility

The first symmetry apparent from the form of (2.29) and (2.30) is due to the lack of difference physically in which order the product of the field amplitude is given. Thus an interchange in the order of the product $E_j(\omega_1)E_k(\omega_2)$ [i.e., $E_j(\omega_1)E_k(\omega_2) \leftrightarrow E_k(\omega_2)E_j(\omega_1)$] will not affect the value or the sign of the $i$th component of the nonlinear polarization. The nonlinear susceptibility should reflect this symmetry. But note that in the above interchange, both frequencies and subscripts for the Cartesian coordinates are interchanged simultaneously. This is important since, for example, exchanging the product $E_x(\omega_1)E_y(\omega_2)$ with the product $E_x(\omega_2)E_y(\omega_1)$ could change the nonlinear polarization, especially, for example, if the two fields are orthogonally polarized. Thus the symmetry property is expressed as (for third-order susceptibilities)

$$\begin{aligned} {\chi_{ijkl}}^{(3)}(-\omega_4;\omega_1,\omega_2,\omega_3) &= {\chi_{ikjl}}^{(3)}(-\omega_4;\omega_2,\omega_1,\omega_3) \\ &= {\chi_{ilkj}}^{(3)}(-\omega_4;\omega_3,\omega_2,\omega_1) = \text{etc.} \end{aligned}$$

In other words, if any of the subscripts $(jkl)$ are permuted, then the susceptibility will remain unchanged as long as the corresponding set of subscripts

(123) are also permuted. This holds even if any of the frequencies are negative. Note that this does not hold for the subscript pair $(i, 4)$. The same relation holds for second-order and can be generalized to any order. This is called intrinsic permutation symmetry and is the underlying reason why the nonlinear polarization can be written compactly in terms of a degeneracy factor as in (2.29) and (2.30).

There is another notation that is used in second-order nonlinear optics. Often the susceptibility is represented as the so-called $d$-coefficient, where $d$ is a tensor given by:

$$d_{ijk} = \frac{1}{2}\chi_{ijk}{}^{(2)}. \tag{2.31}$$

Furthermore, the intrinsic permutation symmetry is used to contract the last two subscripts and write $d_{ijk} \rightarrow d_{il}$. The subscripts are then written as numbers instead of letters using the scheme

$$\begin{aligned} xx \qquad & l = 1, \\ yy \qquad & 2, \\ zz \qquad & 3, \\ yz = zy \qquad & 4, \\ xz = zx \qquad & 5, \\ xy = yx \qquad & 6. \end{aligned} \tag{2.32}$$

For example, $d_{xyz} = d_{xzy} = d_{14}$ and $d_{zxx} = d_{31}$, etc.

The utility of the notation is that the $d$-coefficients can be expressed as elements of a $3\times6$ matrix rather than a $3\times3\times3$ tensor. To use these coefficients in the nonlinear polarization of (2.29), the substitution $\chi_{ijk} \rightarrow 2d_{il}$ needs to be made.

## 2.3 The Harmonic Oscillator Model in Linear Optics

An instructive way to visualize the optical properties of a medium is to consider it as an assembly of forced harmonic oscillators, according to the model due to Lorentz. The bonding of electrons to the nuclei is approximated by that of charged particles attached to nuclei by springs. To simplify the discussion, the interactions are assumed to be isotropic and vector notation will not be used. The force $F_E$ exerted on an electron of charge $e$ by the electric field $E$ is then given by:

$$F_E = eE. \tag{2.33}$$

The bond, approximated as a spring, will exert a restoring force on the electron given by:

$$F_{\mathrm{R}} = -m{\omega_0}^2 x, \tag{2.34}$$

where $m$ is the mass of the electron, $x$ is the displacement from the equilibrium position, and $\omega_0$ is the natural frequency of the oscillation and is equal to the square root of the ratio of the elastic constant to the mass, $m$. Newton's second law states that the sum of the forces acting on a particle of mass $m$ and charge $e$ equals the mass times the acceleration. Hence, the equation of motion is

$$eE - m{\omega_0}^2 x = m\frac{\mathrm{d}^2 x}{\mathrm{d}t^2}. \tag{2.35}$$

Providing for damping of the oscillation by adding a term proportional to the velocity, and rearranging, gives the familiar equation of motion:

$$\frac{\mathrm{d}^2 x}{\mathrm{d}t^2} + 2\Gamma\frac{\mathrm{d}x}{\mathrm{d}t} + {\omega_0}^2 x = -\frac{e}{m}E, \tag{2.36}$$

where $\Gamma$ is the damping constant.

We now consider the action of an oscillating electric field of a plane wave on the harmonic oscillator. The solution of the differential equation, ignoring transient terms, then yields the following expression for the displacement $x$, where c.c. again denotes the complex conjugate:

$$x = -\frac{e}{m}E\frac{\mathrm{e}^{\mathrm{i}\omega t}}{{\omega_0}^2 - 2\mathrm{i}\Gamma\omega - \omega^2} + \text{c.c.} \tag{2.37}$$

Inspection of (2.37) suggests a sinusoidal behavior in time with increasing displacement as the frequency of the field approaches the natural frequency of the oscillator. The following expression for the polarization can be obtained:

$$P = \frac{Ne^2}{m}\frac{1}{{\omega_0}^2 - 2\mathrm{i}\Gamma\omega - \omega^2}E(\omega)\mathrm{e}^{\mathrm{i}\omega t} + \text{c.c.}. \tag{2.38}$$

This expression shows that the induced polarization is proportional to the amplitude of the electric field and has the same frequency dependence. One can use the expression for polarization to describe the linear optical phenomena that it would exhibit. As the electromagnetic wave propagates through the medium, the electrons surrounding the nuclei (here approximated as harmonic oscillators) are polarized and these oscillating dipoles act as new sources of radiation.

The frequency of the radiated wave is identical to the incident wave, but its phase lags behind the incident wave by a time determined by the natural frequency of the oscillator. If the wave encounters $N$ oscillators as it passes through the medium, it will accumulate a phase delay proportional to $N$ and will appear to have been delayed relative to a parallel wave that had traveled an identical distance, but in a vacuum.

As discussed above, the ratio between $c$, the velocity of light in a vacuum, and the apparent velocity in the medium, or phase velocity $v$, is the refractive index of the material. The use of the relationships between the refractive index, dielectric constant, and $\chi^{(1)}$ and the polarization leads to

$$n^2 = \varepsilon = 1 + 4\pi\chi^{(1)} = 1 + \frac{Ne^2}{m}\frac{4\pi}{\omega_0^2 - 2\mathrm{i}\omega - \omega^2}. \tag{2.39}$$

When $N$ is small enough, the absolute value of the second term on the right-hand side is small compared with unity. A good approximation (using a Binomial series expansion) to $n$ then is the right-hand side of (2.39) with the second term divided by 2. The real ($n$) and imaginary ($k$) parts are then given by

$$\mathrm{Re}(n) = 1 - \frac{Ne^2}{m}\frac{2\pi(\omega^2 - {\omega_0}^2)}{m(\omega^2 - {\omega_0}^2)^2 + (2\Gamma\omega)^2} \tag{2.40}$$

and

$$\mathrm{Im}(n) = \frac{Ne^2}{m}\frac{4\pi\gamma\omega}{(\omega^2 - {\omega_0}^2)^2 + (2\Gamma\omega)^2}. \tag{2.41}$$

The behavior of these expressions is shown schematically in Fig. 2.3, where the real and imaginary parts of the refractive index corresponding to dispersion and absorption are plotted as a function of frequency in the region of an optical transition at $\omega_0$. The familiar dispersion in the refractive index that occurs in the wavelength region below an optical transition is a manifestation of this behavior. Near the peak of the absorption, the refractive index decreases rapidly and begins to increase again slowly on the high-energy side of the transition. This relatively simplistic treatment has illustrated some of the important linear properties exhibited by many different materials. It should be emphasized that the understanding and control of linear optical properties are extremely important to the observation and practical utility of nonlinear optical properties.

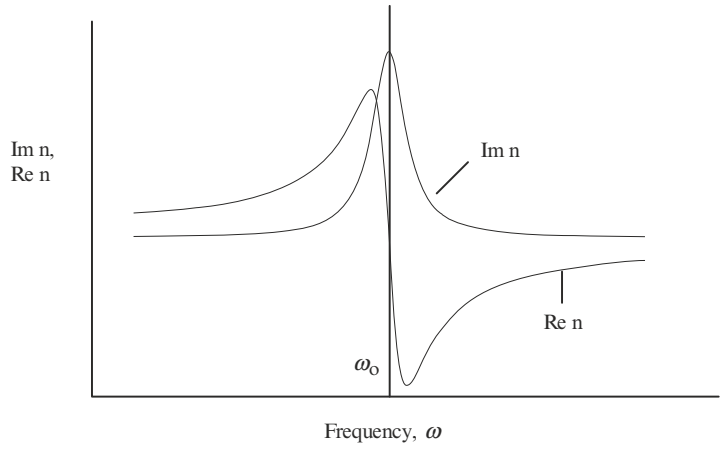


**Fig. 2.3.** The real and imaginary parts of the refractive index for the Lorentz (harmonic) oscillator with frequency $\omega$, which illustrate anomalous dispersion and absorption near $\omega = \omega_0$

## 2.4 The Anharmonic Oscillator Model in Nonlinear Optics

At the most fundamental level, the nonlinear optical response of a medium can be related to the deviation of electronic displacement from harmonic behavior in a relatively straightforward and similar manner to the harmonic-oscillator treatment for linear optics. The occurrence of nonlinear optical properties can be visualized by introducing anharmonic terms, such as $ax^2$ for second-order effects and $bx^3$ for third-order effects, into (2.36):

$$\frac{\mathrm{d}^2x}{\mathrm{d}t^2} + 2\Gamma\frac{\mathrm{d}x}{\mathrm{d}t} + {\omega_0}^2x + ax^2 = -\frac{e}{m}E. \tag{2.42}$$

In this equation, we have assumed that the applied electric field is given by $E(t)$, that there is a damping force of the form $-2\Gamma(\mathrm{d}x/\mathrm{d}t)$, and the restoring force is given by:

$$F_{\text{restoring}} = m\left(-\omega_0^2x - ax^2\right),$$

where $a$ is a parameter that characterizes the strength of the nonlinearity.

We can understand the nature of this form of restoring force by noting that it corresponds to a potential-energy function of the form

$$U = -\int F_{\text{restoring}}\mathrm{d}x = m\left(\frac{1}{2}\omega_0^2x^2 + \frac{1}{3}ax^3\right). \tag{2.43}$$

Here, the first term corresponds to a harmonic potential and the second term corresponds to an anharmonic correction term, as illustrated in Fig. 2.4. This model corresponds to the physical situation of electrons in real materials, because the actual potential well that the electron feels is not perfectly parabolic. The present model can describe only noncentrosymmetric media, because we have assumed that the potential-energy function contains both even and odd powers of $x$.

The addition of the anharmonic term prevents a straightforward solution of the equation in a manner similar to that for (2.36). The usual course of action is to assume that the anharmonic contribution to the polarization is small compared to the harmonic or linear term and to approximate the solution as a power series in the displacement $x$. Considering the first two terms in the expansion, we can write

$$x = x_1 + x_2. \tag{2.44}$$

The solution for the first term $x_1$ is exactly as obtained in (2.37) for the linear case. The solution for the second term is obtained by approximating $ax^2$ in (2.42) by $ax_1^2$, which linearizes the equation and leads to a straightforward solution in terms of a component at frequency $2\omega$ and another at zero frequency (or dc). This solution is of the form

$$x_2 = x_2(2\omega) + x_2(0) + \text{c.c.}, \tag{2.45}$$

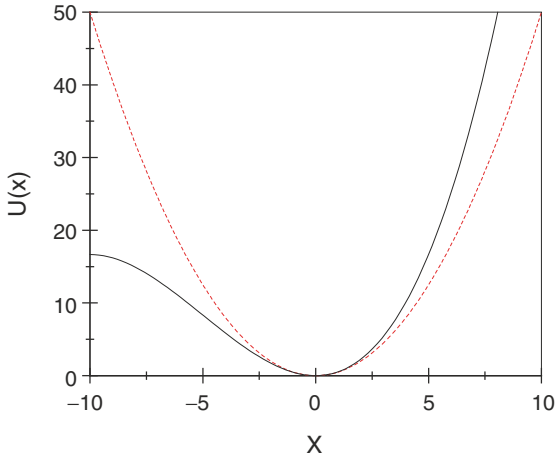


**Fig. 2.4.** Potential-energy function for a noncentrosymmetric medium. The *dashed parabola curve* is the harmonic potential and the *solid curve* is the actual potential

where

$$x_2(2\omega) = -a\left(\frac{e}{m}\right)^2 E^2(\omega)\frac{\mathrm{e}^{\mathrm{i}2\omega t}}{({\omega_0}^2 - 2\mathrm{i}\Gamma\omega - \omega^2)({\omega_0}^2 - 4\mathrm{i}\Gamma\omega - 4\omega^2)} + \text{c.c.} \tag{2.46}$$

and

$$x_2(0) = -2a\left(\frac{e}{m}\right)^2 \frac{E(\omega)}{{\omega_0}^2}\frac{1}{({\omega_0}^2 - 2\mathrm{i}\Gamma\omega - \omega^2)} + \text{c.c.} \tag{2.47}$$

The first term in (2.45) shows the response of the oscillator at $2\omega$ and leads to the phenomenon of second-harmonic generation. The second term shows that the nonlinear response leads to a dc polarization or displacement in the equilibrium position of the oscillator. Substituting these results into the equation

$$P = -Ner, \tag{2.48}$$

where $r$ is the field-induced displacement, leads directly to expressions for the nonlinear polarizations at the corresponding frequencies and to the susceptibility functions commonly used to describe the response to the field:

$$P_{\mathrm{NL}} = -Ne[x_2(2\omega) + x_2(0)], \tag{2.49}$$

$$\chi^{(2)}(2\omega) = \frac{Nex_2(2\omega)}{E(\omega)^2}, \tag{2.50}$$

$$\chi^2(0) = \frac{Nex_2(0)}{E(\omega)^2}. \tag{2.51}$$

If we were to generalize the analysis by considering that the polarizing field contained frequency components at arbitrary frequencies $\omega_1$ and $\omega_2$, terms

would appear in (2.45) with frequency arguments of the type $x_2(\omega_1+\omega_2)$ and $x_2(\omega_1-\omega_2)$ at the sum and difference frequencies that, through Maxwell's equation, are the source of new electromagnetic fields at those frequencies. By adding the next higher-order anharmonic term to (2.42), and engaging in a similar iterative process to obtain solutions, we would find terms containing up to three frequency components, leading to a variety of third-order processes including third-harmonic generation and four-wave mixing processes $\chi^{(3)}(-\omega;\omega,-\omega,\omega)$, which are discussed in detail in later chapters.

## 2.5 Properties of Anisotropic Media

In the discussion of the harmonic oscillator and anharmonic oscillator models, we assumed that the interactions were isotropic and, as a result, the induced polarization was parallel to the field and was related to it by a proportionality constant. However, most materials in nonlinear optics are not isotropic. Examples are organic crystals and polymer chains in a solid that are often oriented other than randomly and the exact nature of their orientational distribution will determine their response. For this reason, the proportionality factors (susceptibilities) are tensor quantities. One manifestation of anisotropy in a medium is that the dielectric constant $\varepsilon_{ij}$, which relates the electric field and the dielectric displacement, is a second-rank tensor quantity. We can write all the components of the dielectric-displacement vector in terms of the tensor elements $\varepsilon_{ij}$ and the components of the electric-field vector in an arbitrary coordinate system:

$$\begin{aligned} D_x &= \varepsilon_{11}E_x + \varepsilon_{12}E_y + \varepsilon_{13}E_z, \\ D_y &= \varepsilon_{21}E_x + \varepsilon_{22}E_y + \varepsilon_{23}E_z, \\ D_z &= \varepsilon_{31}E_x + \varepsilon_{32}E_y + \varepsilon_{33}E_z. \end{aligned} \tag{2.52}$$

We can find a suitable rotation of the coordinate system to diagonalize $\varepsilon$ so that

$$\begin{aligned} D_x &= \varepsilon_x E_x, \\ D_y &= \varepsilon_y E_y, \\ D_z &= \varepsilon_z E_z, \end{aligned} \tag{2.53}$$

where $\varepsilon_x, \varepsilon_y, \varepsilon_z$ are referred to as the principal dielectric axes of the medium.

One interesting consequence of dielectric anisotropy in crystals is the phenomenon of birefringence. We consider a uniaxial crystal with $n_x = n_y \neq n_z$ and a light wave propagating along the $x$-axis with the electric field polarized in the $z$ direction. The propagation constant $k_z$ will be determined from

$$k_z = \frac{\omega}{c} n_z, \tag{2.54}$$

and $n_z = \sqrt{\varepsilon_z}$. Another wave with $y$ polarization propagating along the $x$-axis would have a different propagation constant $k_y$. A phase lag is accumulated and causes the resultant electric field to rotate as it propagates, resulting in elliptically polarized light. A further consequence of birefringence is that the flow of energy does not occur normal to the wave front, as is the case for an isotropic medium. In the nonlinear process of second-harmonic generation, where the flow of power from the fundamental to the harmonic beam is dependent on the spatial overlap of the polarization wave propagating with wave vector $k_\omega$ and the electric field propagating with $k_{2\omega}$, the nonparallel nature of $E_{2\omega} \times H$ and $S$ (the direction of power flow), places a fundamental limitation on the distance over which the interaction can be maintained and hence the efficiency of harmonic generation (walk-off phenomenon).

## 2.6 Second-Harmonic Generation

In this section, a mathematical description of the process of second-harmonic generation, shown in Fig. 2.5, is presented. By assuming that the medium is lossless both at the fundamental frequency $\omega_1$ and at the second-harmonic frequency $\omega_2 = 2\omega_1$, the nonlinear susceptibility obeys the condition of full permutation symmetry.

We take the total electric field within the nonlinear medium to be given by:

$$E(z,t) = E_1(z,t) + E_2(z,t), \tag{2.55}$$

$$\text{where } E_j(z,t) = E_j(z)\mathrm{e}^{-\mathrm{i}\omega t} + \text{c.c., and } E_j(z) = A_j(z)\mathrm{e}^{\mathrm{i}k_j z}. \tag{2.56}$$

We assume that each frequency component of the electric field obeys the driven wave equation:

$$\partial^2 E_j/\partial z^2 - \frac{\varepsilon^{(1)}(\omega_j)}{c^2}\partial^2 E_j/\partial t^2 = \frac{4\pi}{c^2}\frac{\partial^2 P_j}{\partial t^2}. \tag{2.57}$$

The nonlinear polarization is represented by

$$P^{\mathrm{NL}}(z,t) = P_1(z,t) + P_2(z,t), \tag{2.58}$$

with $P_j(z,t) = P_j(z)\mathrm{e}^{-\mathrm{i}\omega_j t} + \text{c.c.}$, where $j$=1, 2.

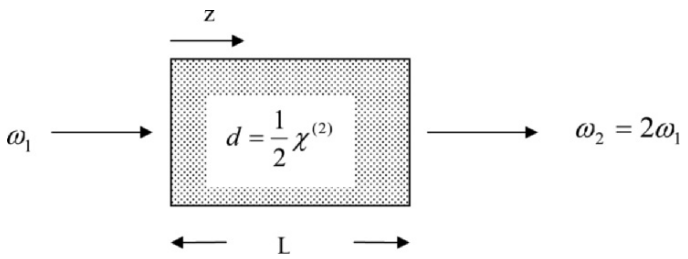


**Fig. 2.5.** Schematic illustration of second-harmonic generation

The expressions for $P_j$ are given [98], by

$$P_1(z) = 4\mathrm{d}E_2{E_1}^* = 4\mathrm{d}A_2{A_1}^*\mathrm{e}^{\mathrm{i}(k_2-k_1)z} \tag{2.59a}$$

and

$$P_2(z) = 2\mathrm{d}{E_1}^2 = 2\mathrm{d}{A_1}^2\mathrm{e}^{2\mathrm{i}k_1 z}. \tag{2.59b}$$

If one obtains coupled-amplitude equations for the two frequency components, we find that

$$\frac{\mathrm{d}A_1}{\mathrm{d}z} = \frac{8\pi\mathrm{i}{\omega_1}^2 d}{k_1 c^2}A_2{A_1}^*\mathrm{e}^{-\mathrm{i}\Delta k z} \tag{2.60a}$$

and

$$\frac{\mathrm{d}A_2}{\mathrm{d}z} = \frac{4\pi\mathrm{i}{\omega_2}^2 d}{k_2 c^2}{A_1}^2\mathrm{e}^{\mathrm{i}\Delta k z}, \tag{2.60b}$$

where $\Delta k = 2k_1 - k_2$.

In the undepleted-pump approximation (i.e., $A_1$ constant), (2.60b) can be integrated to obtain an expression for the spatial dependence of the second-harmonic field amplitude. The above pair of coupled equations must be solved simultaneously to obtain the amplitude of the fundamental and the second-harmonic waves. We examine the solution to these expressions in the small-signal or low-conversion limit. We note that the power per unit area ($P^\omega$) for frequency $\omega$ in a material of refractive index $n$ is

$$P^\omega = \frac{cn}{8\pi}EE^*. \tag{2.61}$$

The solution to (2.60a) and (2.60b) leads to an expression for the power-conversion efficiency $\eta$ in the small-conversion limit:

$$\eta = \frac{512\pi^5 d^2 l^2 P_\omega}{n_{2\omega}n_\omega^2\lambda^2 c}\left(\frac{\sin x}{x}\right)^2, \tag{2.62}$$

where $x = \Delta k l/2$, $d$ is in MKS units and $P_\omega$ is in watts. The term $(\sin x/x)^2$ oscillates between one and zero, depending on the degree of phase mismatch. If $\Delta k = 0$, then $(\sin x/x)^2 = 1$ and the conversion efficiency depends only on the square of the interaction length, the square of the nonlinear coefficient $d^2$ and the incident power. As significant power is accumulated in the harmonic wave, (2.60a) predicts some type of saturation behavior or steady-state condition since the amplitude and hence the power is gradually decreasing. If phase mismatch occurs, power is readily transferred from the harmonic to the fundamental wave.

## 2.7 Self-Phase Modulation and Soliton Generation

Self-phase modulation is the change in the phase of an optical pulse due to the nonlinearity of the refractive index of the material medium. We consider the propagation of the optical pulse:

$$E(z,t) = A(z,t)\mathrm{e}^{\mathrm{i}(k_0 z-\omega_0 t)} + \text{c.c.} \tag{2.63}$$

through a medium characterized by a nonlinear refractive index:

$$n(t) = n_0 + n_2 I(t). \tag{2.64}$$

We assume that the medium can respond almost instantaneously to the pulse intensity and we also assume that no reshaping of the optical pulse can occur within the medium. The effect of the medium is to change the phase of the transmitted signal by:

$$\Phi_{\mathrm{NL}}(t) = -n_2 I(t)\omega_0 L/c. \tag{2.65}$$

As a result, the spectrum of the transmitted pulse will be modified and typically will be broader than that of the incident pulse. It is possible to describe the spectral content of the transmitted pulse by introducing the concept of the instantaneous frequency $\omega(t)$ of the pulse by

$$\omega(t) = \omega_0 + \delta\omega(t), \tag{2.66}$$

where

$$\delta\omega(t) = \mathrm{d}\Phi_{\mathrm{NL}}(t)/\mathrm{d}t \tag{2.67}$$

denotes the variation of the instantaneous frequency.

If we consider the pulse shape $I(t) = I_0(t)\ \mathrm{sech}^2(t/\tau_0)$, the nonlinear phase shift is given by:

$$\Phi_{\mathrm{NL}}(t) = -n_2 \frac{\omega_0}{c} L I_0\ \mathrm{sech}^2(t/\tau_0), \tag{2.68}$$

and the change in instantaneous frequency is given by:

$$\delta\omega(t) = 2n_2 \frac{\omega_0}{c\tau_0} L I_0\ \mathrm{sech}^2(t/\tau_0)\ \tanh(t/\tau_0). \tag{2.69}$$

Under the assumption that $n_2$ is positive, the leading edge of the pulse is shifted to lower frequencies and the trailing edge is shifted to higher frequencies (see Fig. 2.6). The maximum value of the frequency shift will be of the order of

$$\delta\omega_{\max} \approx \frac{\Delta\Phi_{\mathrm{NL}}^{\max}}{\tau_0},\ \text{where}\ \Delta\Phi_{\mathrm{NL}}^{\max} \approx n_2 \frac{\omega_0}{c} I_0 L. \tag{2.70}$$

We expect that spectral broadening due to self-phase modulation will be important whenever $\delta\omega_{\max}$ exceeds the spectral width of the incident pulse. We thus expect self-phase modulation to be important whenever $\Delta\Phi_{\mathrm{NL}}^{\max} \geq 2\pi$.

### 2.7.1 Optical Solitons

It is possible for the effects of group-velocity dispersion to compensate for the effects of self-phase modulation. Under appropriate circumstances, the degree of compensation can be complete, and the optical pulse can propagate as a "soliton" through a dispersive, nonlinear optical medium with

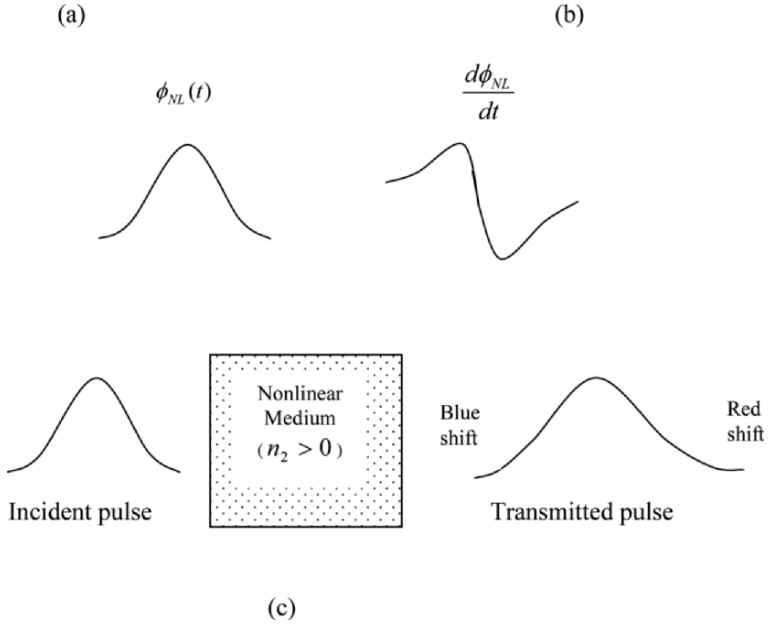


**Fig. 2.6.** (**a**) Intensity of incident pulse versus time. (**b**) Change in instantaneous frequency of the transmitted pulse, $\delta\omega(t)$, versus time. (**c**) Experimental arrangement to observe self-phase modulation. $\Phi_{\mathrm{NL}}$ is the nonlinear phase shift experienced by the pulse upon propagation

an invariant shape. As an example of a soliton, we should note that the nonlinear Schrödinger equation, which describes the propagation of optical pulses through dispersive, nonlinear optical media, governs a pulse whose amplitude is of the form:

$$A_{\mathrm{s}}(z,t) = A_{\mathrm{s}}^{0}\ \mathrm{sech}(t/t_0)\mathrm{e}^{\mathrm{i}kz}, \tag{2.71}$$

where the pulse amplitude $A_{\mathrm{s}}^{0}$ and pulse width $\tau_0$ must be related according to:

$$\left|A_{\mathrm{s}}^{0}\right|^2 = \frac{-k_2}{\gamma\tau_0^2} = \frac{-2\pi k_2}{n_0 n_2 \omega \tau_0^2},$$

and where $k = -k_2/2\tau_0^2$ represents the phase shift experienced by the pulse upon propagation. In fact, $k_2$ and $\gamma$ must have opposite signs in order for the group-velocity dispersion to compensate for self-phase modulation. One circumstance under which $k_2$ and $\gamma$ have opposite signs occurs is in fused-silica optical fibers.

Here, the nonlinearity in the refractive index occurs as the result of electronic polarization, and $n_2$ is consequently positive. The group-velocity dispersion parameter $k_2$ is positive for visible light, but becomes negative

for wavelengths longer than 1.3 μm. Optical solitons of this sort have been observed by Mollenauer et al. [99].

### 2.7.2 Mechanisms of Nonlinearity

Some of the physical processes that can produce a nonlinear change in refractive index are listed in Table 2.1, along with typical values of $n_2$, of $\chi^{(3)}$ and of the characteristic time scale for the nonlinear process to develop.

#### Nonresonant Electronic Nonlinearities

Nonresonant electronic nonlinearities occur as the result of the nonlinear response of bound electrons on an applied optical field. This nonlinearity is not particularly large ($\chi^{(3)} \approx 1.4 \times 10^{-22}\,\mathrm{m^2\,V^{-2}}$) but is of considerable importance because of its presence in all dielectric materials. Larger values, as large as $\chi^{(3)} \approx 1.4 \times 10^{-17}\,\mathrm{m^2\,V^{-2}}$, due to the response of delocalized $\pi$ electrons in some organic nonlinear optical materials (such as polydiacetylene) have also been reported [100]. Nonresonant electronic nonlinearities are extremely fast, with a typical time constant $\tau \approx 10^{-16}\,\mathrm{s}$.

#### Nonlinearities Due to Molecular Orientation

Organic liquids that are composed of anisotropic molecules (molecules having an anisotropic polarizability tensor) typically possess a large value of $n_2$. The origin of this nonlinearity lies in the tendency of molecules to become aligned (Fig. 2.7) in the electric field of an applied optical wave. As a result, the optical wave experiences a modified value of the refractive index because the average polarizability per molecule has been changed by the molecular alignment.

**Table 2.1.** Typical values of the nonlinear refractive index

| mechanism | $n_2(\mathrm{m^2\,W^{-1}})$ | $\chi^3_{1111}(\mathrm{m^2\,V^{-2}})$ | resonant time(s) |
|---|---|---|---|
| molecular orientation | $10^{-18}$ | $1.40 \times 10^{-20}$ | $10^{-12}$ |
| electronic polarization | $10^{-20}$ | $1.40 \times 10^{-22}$ | $10^{-15}$ |
| electrostriction | $10^{-18}$ | $1.40 \times 10^{-20}$ | $10^{-9}$ |
| saturated atomic absorption | $10^{-14}$ | $1.40 \times 10^{-16}$ | $10^{-8}$ |
| thermal effects | $10^{-10}$ | $1.40 \times 10^{-12}$ | $10^{-3}$ |
| photorefractive effect | large | large | (intensity-dependent) |

The photorefractive effect often leads to a very strong nonlinear response. This response usually cannot be described in terms of a $\chi^{(3)}$ nonlinear susceptibility, because the nonlinear polarization does not depend on the applied field strength in the same manner as the other mechanisms listed (after [98])

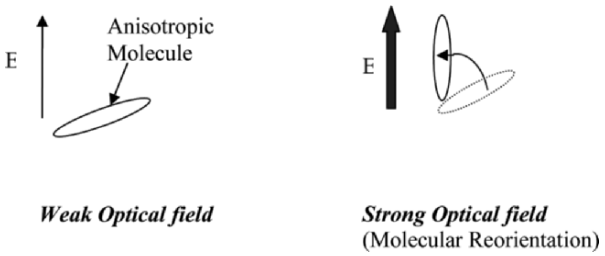


**Fig. 2.7.** Anisotropic molecular reorientation by a strong electric field. When a strong field is applied to such a system, the induced dipole moments of the molecules experience a torque attempting to align the most polarizable axis with the applied field

We can quote some numerical values appropriate to the case of carbon disulfide. The maximum possible value of $\delta n$ is 0.58, which corresponds to complete alignment of the molecules. For a field strength of $E \approx 3 \times 10^9\,\mathrm{V\,m^{-1}}$, the value of $n_2$ is $3 \times 10^{-18}\,\mathrm{m^2\,W^{-1}}$.

### Electrostriction

Electrostriction is the tendency of materials to become compressed in the presence of an electric field. The compressibility is approximately equal to $10^{-9}\,\mathrm{m^2\,N^{-1}}$ for $CS_2$ and is of the same order of magnitude for all condensed matter. We thus obtain $\chi^{(3)} \approx 2.8 \times 10^{-21}\,\mathrm{m^2\,V^{-2}}$ for condensed matter. For gases at atmospheric pressure, $\chi^{(3)}$ of the order of $1.4 \times 10^{-23}\,\mathrm{m^2\,V^{-2}}$ is obtained. The value of $\chi^{(3)}$ resulting from electrostriction is usually not large in comparison with other types of optical nonlinearities. However, electrostriction provides the nonlinear coupling that leads to stimulated Brillouin scattering, which can be an extremely strong effect.

## 2.7.3 Optical Phase Conjugation

Optical phase conjugation is a process that can be used to remove effects of aberrations from certain types of optical systems. While, for an optical wave falling at normal incidence onto an ordinary metallic mirror, the most advanced portion of the incident wave front remains the most advanced after reflection, for a phase-conjugate mirror (PCM), the most advanced portion turns into the most retarded portion in the reflection process (Fig. 2.8).

In the phase-conjugation process, the generated wave front exactly replicates the incident wave front but propagates in the opposite direction. It is sometimes referred to as the generation of a time-reversed wave front. The process of phase conjugation can be understood by a mathematical description of the process. If the incident wave on the PCM is

$$\widetilde{E}_\mathrm{s}(r,t) = E_\mathrm{s}(r)\mathrm{e}^{-\mathrm{i}\omega t} + \mathrm{c.c.}, \tag{2.72}$$

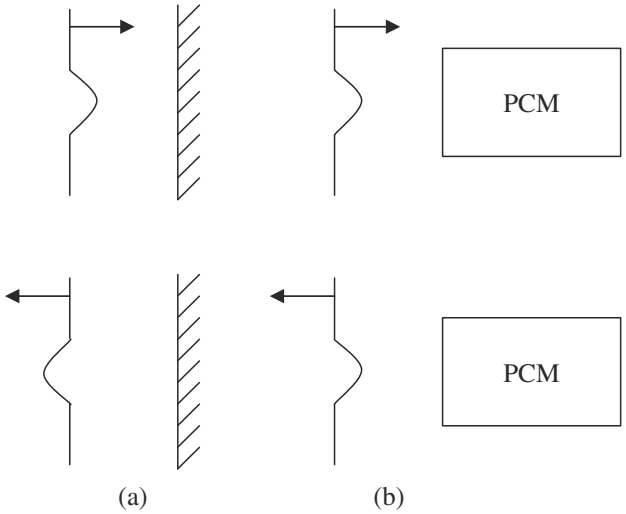


**Fig. 2.8.** Reflection from (**a**) an ordinary mirror, (**b**) a phase-conjugate mirror (PCM)

the reflected wave (the phase-conjugate wave) produced can be described by

$$E_{\mathrm{c}}(r,t) = rE_{\mathrm{s}}^{*}(r)\mathrm{e}^{-\mathrm{i}\omega t} + \text{c.c.}, \tag{2.73}$$

where $r$ represents the amplitude reflection coefficient of the mirror. The significance of replacing $E_{\mathrm{s}}(r)$ by ${E_{\mathrm{s}}}^{*}(r)$ in the reflection process can be understood if we write

$$E_{\mathrm{s}}(r) = \hat{\varepsilon}_{\mathrm{s}} A_{\mathrm{s}}(r)\mathrm{e}^{\mathrm{i}K_{\mathrm{s}}\cdot r}, \tag{2.74}$$

where $\hat{\varepsilon}_{\mathrm{s}}$ is the polarization unit vector, $A_{\mathrm{s}}(r)$ the slowly varying field amplitude, and $k_{\mathrm{s}}$ the wavevector of the incident light. So the complex conjugate of $E_{\mathrm{s}}(r)$ is

$$E_{\mathrm{s}}^{*}(r) = \hat{\varepsilon}_{\mathrm{s}}^{*} \cdot A_{\mathrm{s}}^{*}(r)\mathrm{e}^{-\mathrm{i}k_{\mathrm{s}}\cdot r}. \tag{2.75}$$

Right-hand circularly polarized light remains right-hand circularly polarized on reflection from a phase-conjugate mirror rather than being converted into left-hand circularly polarized light, as in the case of reflection at normal incidence from a metallic mirror. Moreover, each ray of the incident beam is precisely reflected back onto itself.

We further can show that

$$E_{\mathrm{c}}(r,t) = rE_{\mathrm{s}}(r,-t). \tag{2.76}$$

This result shows that the phase-conjugation process can be thought of as the generation of a time-reversed wave front.

It has been shown [101, 102] that the phase conjugate of an incident wave can be created by the process of degenerate four-wave mixing (DFWM). It has also been shown that a phase-conjugate mirror can be used for aberration correction in optical systems [98, 103] (see Fig. 2.9).

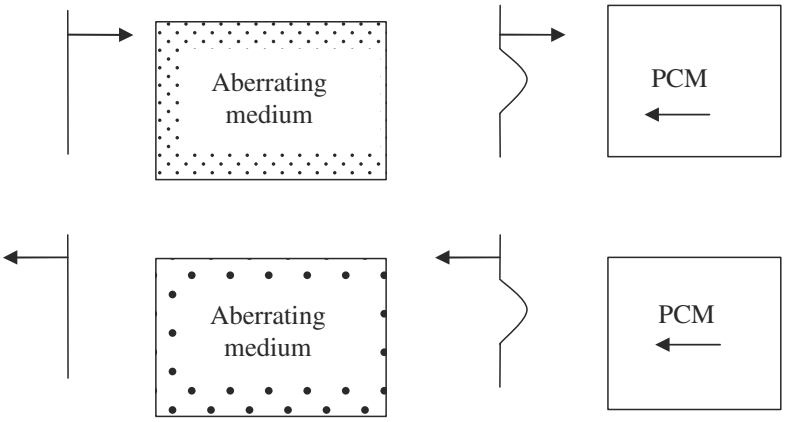


**Fig. 2.9.** Aberration correction by optical phase conjugation. An initially plane wave front becomes distorted when leaving the aberrating medium. This aberrated wave front is allowed to fall onto a phase-conjugate mirror. As a result, when this wave front passes through the aberrating medium again, an undistorted output plane wave will emerge

### 2.7.4 Optical Bistability

Certain nonlinear optical systems can possess more than one output for a given input state. Optical bistability refers to the situation in which two different output intensities are possible for a given input intensity. Optically bistable devices can be used as a switch for use in optical communication and in optical computing. A bistable optical device can be described as consisting of a nonlinear medium placed inside a Fabry–Perot resonator. If $A_1$ denotes the field amplitude of the incident wave, it can be shown that $A_2$, the amplitude of the forward-going wave within the interferometer, is

$$A_2 = \frac{\tau A_1}{1 - \rho^2 \mathrm{e}^{2\mathrm{i}kl - \alpha d}}, \tag{2.77}$$

where $\tau$ is the amplitude transmission, $\rho$ is the amplitude reflectance, and $\alpha$ is the absorption coefficient. If $k$ the propagation constant, or $\alpha$, is a sufficiently nonlinear function of the light intensity within the interferometer, this equation predicts bistability in the intensity of the transmitted wave (see Fig. 2.10). If we assume that the absorption coefficient obeys the relation valid for a two-level saturable absorber

$$\alpha = \frac{\alpha_0}{1 + I/I_\mathrm{s}}, \tag{2.78}$$

and by introducing $C = R\alpha l/1 - R$, it can be shown that

$$I_1 = TI_2 \left(1 + \frac{C_0}{1 + 2I_2/I_\mathrm{s}}\right)^2, \tag{2.79}$$

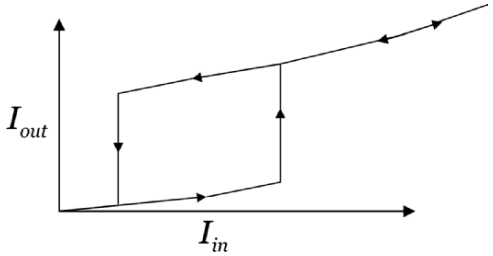


**Fig. 2.10.** Typical input-versus-output characteristics of a bistable optical device

where

$$C_0 = R\alpha_0 l/(1-R) \text{ and } T = (\tau)^2. \tag{2.80}$$

### 2.7.5 Stimulated Raman Scattering

In the spontaneous Raman effect, a beam of light illuminates a material sample and the scattered light is observed spectroscopically. In general, the scattered light contains frequencies shifted to lower frequencies (Stokes components) and those shifted to higher frequencies (anti-Stokes components). The spontaneous Raman process described is typically a rather weak process. Even for condensed matter, the scattering cross-section per unit volume for Raman Stokes scattering is only about $10^{-6}\,\mathrm{Cm}^{-1}$. However, under excitation by an intense laser beam, highly efficient scattering can occur as a result of the stimulated Raman scattering process. Typically 10% or more of the energy of the incident laser beam is often converted into the Stokes frequency. While the spontaneous process leads to nearly isotropic emission, the stimulated process leads to emission in a narrow cone in the forward and backward directions. The Stokes intensity is seen to grow exponentially with propagation distance through the medium according to

$$m_\mathrm{s}(z) = m_\mathrm{s}(0)\mathrm{e}^{Gz}, \tag{2.81}$$

where $m_\mathrm{s}(0)$ denotes the photon occupation number associated with the Stokes field at the input to the Raman medium and $G$ is the Raman-gain coefficient. It can be shown that the Raman-gain coefficient can be expressed as

$$G = \frac{N\pi^2 c^3 m_\mathrm{L}}{V\omega_\mathrm{s}^2 b n^3}(\partial\sigma/\partial\omega)_0, \tag{2.82}$$

where $N$ is the number density of molecules, $V$ denotes the volume of the region in which the modes are defined, $(\partial\sigma/\partial\omega)_0$ is the spectral density of the scattering cross-section at the line center, $\omega_\mathrm{s}$ is the Stokes frequency, $m_\mathrm{L}$ is the mean number of photons per mode in the laser radiation and $b$ is a geometrical factor that accounts for the fact that the angular distribution of the scattered radiation may be nonuniform and hence the scattering rate in the different Stokes modes may be different.

**Table 2.2.** Stimulated Raman scattering parameters for various materials [104,105]

| substance | frequency shift $\nu_0(\mathrm{cm}^{-1})$ | linewidth $\Delta\nu(\mathrm{cm}^{-1})$ | gain factor $G/I_1(\mathrm{m\,GW}^{-1})$ |
|---|---|---|---|
| liquid $O_2$ | 1552 | 0.117 | $(14.5\pm4)\times10^{-2}$ |
| $CS_2$ | 655.6 | 0.50 | $24\times10^{-2}$ |
| $LiTaO_3$ | 201 | 22 | $4.4\times10^{-2}$ |
| $SiO_2$ | 467 | – | $0.8\times10^{-2}$ |
| $O_2$ gas | 1555 | – | $0.016\times10^{-2}$ |

Properties of stimulated Raman scattering for several materials are given in Kaiser and Maier [104] and Simon and Tittel [105], and are shown in Table 2.2. The gain factor is measured at 694 nm.

### 2.7.6 Third-Harmonic Generation

The theoretical description of third-harmonic generation follows a treatment similar to second-harmonic generation. The starting point is the wave equation for propagation of a plane-wave electric field in a nonlinear medium (2.2–2.8), but now with the inclusion of the $\chi^{(3)}$ term. The solution of the resulting coupled amplitude equations, under the assumption of low conversion, leads to an expression for the efficiency of the generated third harmonic [106]:

$$\eta = \frac{576\pi^6}{n(3\omega)n^3(\omega)\lambda^2c^2}\left|\chi^{(3)}(-3\omega;\omega,\omega,\omega)\right|^2 I_\omega^2 L^2 \frac{\mathrm{Sin}^2(\Delta kL/2)}{(\Delta kL/2)^2}, \tag{2.83}$$

where $L$ is the interaction length and $n(3\omega)$ and $n(\omega)$ are refractive indices at frequencies $3\omega$ and $\omega$ and $\Delta k = 3k_1 - k_3$ defines the wavevector mismatch between the incident fundamental and generated third-harmonic wave. In the derivation of the above equation, it has been assumed that the incident field remains undepleted in the interaction with the medium. $\Delta k$ is given by:

$$\Delta k = \frac{6\pi(n_{3\omega} - n_\omega)}{\lambda}. \tag{2.84}$$

As seen from the expression for $\eta$, the intensity of the third-harmonic generation depends on the wavevector mismatch $\Delta k$ which is shown in Fig. 2.11. $I_{3\omega}$ shows a symmetric damped oscillatory behavior about $\Delta k = 0$. These oscillations result when the harmonic field gets out of phase with the polarization that drives it as the waves propagate through the medium.

In anisotropic media, it is possible to take advantage of the normal birefringence to achieve phase matching in the process of third-harmonic generation. In this case, we should have

$$n_\mathrm{e}(3\omega) = n_\mathrm{o}(\omega), \tag{2.85}$$

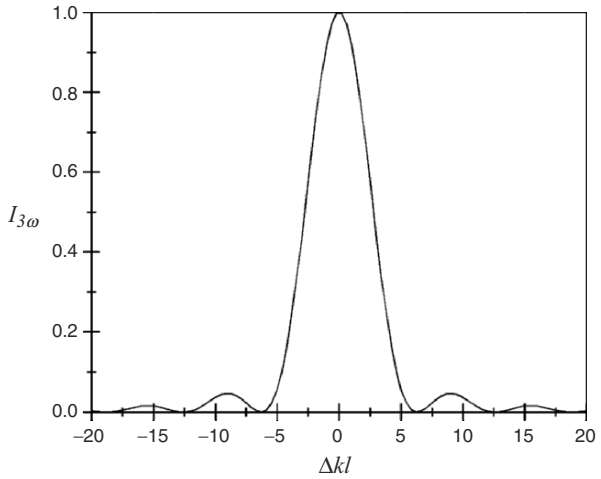


**Fig. 2.11.** Third-harmonic intensity $I_{3\omega}$ in arbitrary units, plotted as a function of $\Delta kl$, for a finite wavevector mismatch $\Delta k = 3k_1 - k_3$

where e and o refer to extraordinary and ordinary rays, respectively. However, in practice, phase matching for the third-harmonic generation in a crystal is very hard to achieve due to the widely different frequency values of the fundamental and the third-harmonic waves.

One can optimize third-harmonic generation by adjusting the interaction length. The harmonic intensity oscillates as the interaction length is changed (either by rotation of the sample, as in the Maker-fringe method, or by translation of a wedge-shape sample, as in the wedge-fringe method [107]). It should be mentioned that harmonic generation is derived from nonlinear interactions which are viewed as instantaneous. Such coherent nonlinearities are derived only from those electronic interactions that do not depend on the population of the excited state. Dynamic nonlinearities are not probed by third-harmonic generation. However, if the fundamental and/or the third-harmonic frequency is near one-photon, two-photon, or three-photon absorption bands of the material, the susceptibility $\chi^{(3)}$ is resonantly enhanced due to dispersion effects.

# 3

# Experimental Techniques to Measure Nonlinear Optical Constants

## 3.1 Introduction

Different techniques have been used to characterize the nonlinear optical constants of materials (e.g., the nonlinear refractive index, $n_2$, and the two-photon absorption coefficient, $\beta$). In what follows, the relevant techniques used to obtain the nonlinear optical constants of chalcogenide glasses, fibers, and films are introduced in some detail.

## 3.2 Degenerate Four-Wave Mixing

In this process, three coherent waves of the same frequency are incident on a nonlinear medium and, as a result of their interaction, a fourth wave (the conjugate) is generated. The strength of this phase-conjugate wave is dependent on a coupling coefficient $\kappa$ that is proportional to the effective $\chi^{(3)}$ for the interaction. Hence measurements of the phase-conjugate intensity can yield $\chi^{(3)}$ tensor components of the medium. Both backward and forward Degenerate Four-Wave Mixing (DFWM) geometries can be employed. Figure 3.1 illustrates the backward geometry. The forward geometry will have many of the same features, other than the directions of the various beams. In the backward geometry, two strong pump beams, the forward and the backward pump, are counter-propagating and a third wave, the probe beam, is incident at some angle $\theta$ to the direction of the forward pump.

The conjugate beam is generated in the process and propagates in the counter direction to the probe beam. As a result of the interaction of these waves, a third-order polarization oscillating at the same frequency $\omega$ is generated:

$$P_{\mathrm{c}}{}^{(3)} = 6\varepsilon_0 \chi^{(3)}_{\mathrm{eff}} A_{\mathrm{f}} A_{\mathrm{b}} A^*_{\mathrm{p}} \exp[\mathrm{i}(K_{\mathrm{f}} + K_{\mathrm{b}} - K_{\mathrm{p}}) \cdot r], \tag{3.1}$$

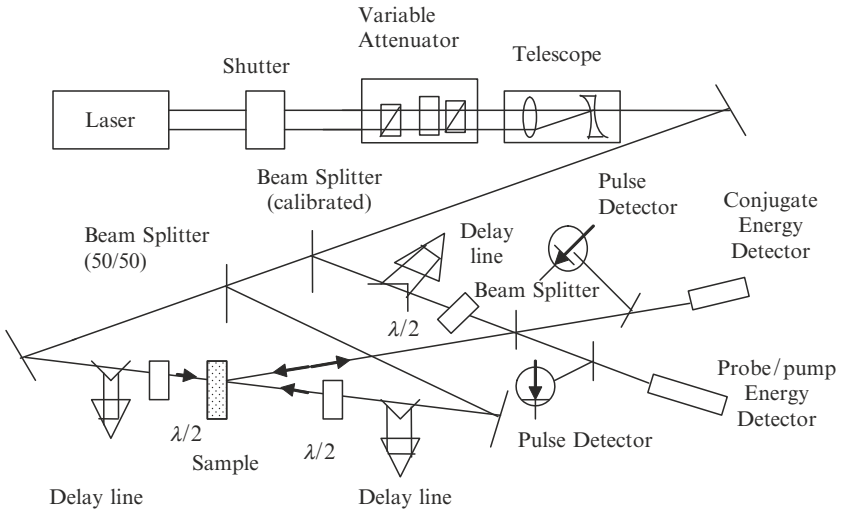


**Fig. 3.1.** Schematic diagram of a degenerate four-wave mixing experiment in the backward geometry (redrawn from [108])



where

$$\chi^{(3)}_{\text{eff}} = e^{\wedge}_{\text{c}} \cdot \chi^{(3)}(-\omega;\omega,\omega,-\omega) : e^{\wedge}_{\text{f}} e^{\wedge}_{\text{b}} e^{\wedge *}_{\text{p}}, \tag{3.2}$$

Because $K_{\text{f}} = -K_{\text{b}}$ and $K_{\text{p}} = K_{\text{c}}$, the DFWM process is automatically phase matched.

The third-order polarization couples the four waves. The wave equation employing the slowly varying amplitude approximation yields the spatial evolution of the waves in this process. In the so-called nondepleted pump regime, $A_{\text{f}}$ and $A_{\text{b}}$ are approximately constant through the medium. The equations for the probe and conjugate waves are given by [108]:

$$\frac{\mathrm{d}A_{\text{p}}}{\mathrm{d}z} = \mathrm{i}\kappa A^*_{\text{c}} \tag{3.3}$$

and

$$\frac{\mathrm{d}A^*_{\text{c}}}{\mathrm{d}z} = \mathrm{i}\kappa^* A_{\text{p}}, \tag{3.4}$$

where

$$\kappa = \frac{3\omega}{n_0 c}\chi^{(3)}_{\text{eff}} A_{\text{f}} A_{\text{b}} \tag{3.5}$$

is the coupling coefficient. By considering $\theta$ to be small and using the usual boundary conditions ($A_{\text{p}}(0) \neq 0$ and $A_{\text{c}}(L) = 0$), the solutions to the coupled wave equations are given by:

$$A_{\mathrm{p}}(z) = \frac{\cos[|\kappa|\,(z-L)]}{\cos(|\kappa|\,L)} A_{\mathrm{p}}(0) \tag{3.6}$$

$$A_{\mathrm{c}}(z) = -\mathrm{i}\frac{\kappa\,\sin[|\kappa(z-L)|]}{|\kappa|\,\cos(|\kappa L)|} A_{\mathrm{p}}^{*}(0). \tag{3.7}$$

The DFWM process can also be understood by using the general picture of a laser-induced grating [110]. We can imagine that the interaction of two coherent beams in a material gives rise to a modulation of the refractive index, which is effectively a diffraction grating. In the case of a backward-wave DFWM geometry, there are three different gratings formed by each two-beam pair, but only two of these gratings generate phase-matched conjugate signals. We can express the nonlinear polarization in terms of three contributions due to these three gratings. The first term describes the grating formed by the forward pump beam $I_{\mathrm{f}}$ and the probe beam $I_{\mathrm{p}}$; the signal is produced by phase-matched Bragg diffraction of the backward beam $I_{\mathrm{b}}$. The second term shows the grating formed by the backward pump beam $I_{\mathrm{b}}$ and the probe beam $I_{\mathrm{p}}$; the signal is produced by phase-matched Bragg diffraction of the forward beam $I_{\mathrm{f}}$. The last term describes a standing-wave grating formed by the two pump beams $I_{\mathrm{f}}$ and $I_{\mathrm{b}}$. It has a temporal oscillation frequency of $2\omega$ because it contains the pump-field product $E_{\mathrm{f}} \cdot E_{\mathrm{b}}$. This grating makes a dominant contribution if the frequency of the optical waves approaches a two-photon resonance of the medium (i.e. if the medium absorbs at $2\omega$).

In relative measurements, the same measurement as described above is performed on a standard third-order nonlinear material under the same conditions as those of the sample. To within a proportionality constant, that is the same in both measurements of the sample and of the standard, the conjugate reflectance data can be fitted to a formula of the form

$$R = aP_{\mathrm{pump}}^{2}, \tag{3.8}$$

where $P_{\mathrm{pump}}$ is the average pump power. Once both the sample and reference data have been fitted to a formula of the above form, the sample susceptibility is given by

$$\chi_{\mathrm{eff}}^{(3)} = \left(\frac{n_0}{n_{\mathrm{ref}}}\right)^{2} \left(\frac{L_{\mathrm{ref}}}{L}\right) \left(\frac{a}{a_{\mathrm{ref}}}\right)^{1/2} \chi_{\mathrm{ref}}^{(3)}. \tag{3.9}$$

Using the boxcar forward geometry (Fig. 3.2) [108, 111–113] for thin films allows one to monitor two signals, that is generated as the result of phase-matched interaction of the three incident beams and one of the nonphase-matched signals generated by the film.

A typical result of DFWM for an $As_{20}S_{80}$ bulk sample is shown in Fig. 3.3.

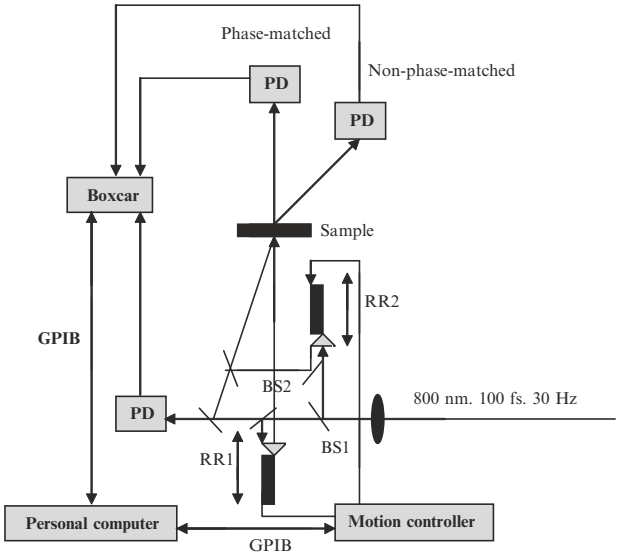


**Fig. 3.2.** A scheme of a forward DFWM set up using the BOXCAR geometry, showing phase-matched and non phase-matched signal detection. PD, photodiode; RR, retro-reflector; BS, beam splitter; GPIB, data collection bus (redrawn from [109])

Reprinted from A. Samoc, M. Samoc, M. Woodruff and B. Luther-Davies, "Poly (p-phenylenevinylene): An Attractive Material for Photonic Applications" in Photonic Polymer Systems, D.L. Wise, G.E. Wnek, D.J. Trantolo, T.M. Cooper, J.D. Gresser (Eds.) Marcel Dekker, New York (1998), © (1998), with permission from Taylor & Francis, a division of informa plc

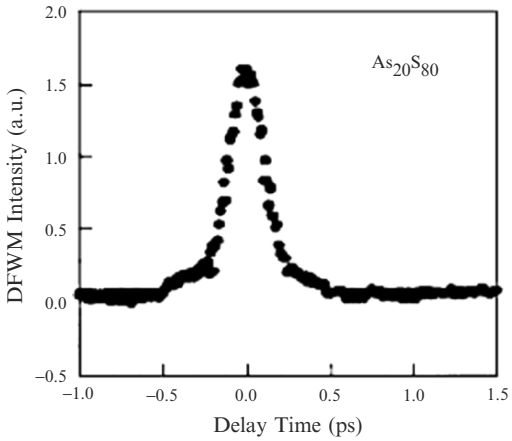


**Fig. 3.3.** DFWM intensity as a function of the delay time for an $As_{20}S_{80}$ bulk sample. This fast response behavior without any slow relaxation is characteristic of the electric polarization effect (after [114])

Reprinted from H. Kanbara, S. Fujiwara, K. Tanaka, H. Nasu, K. Hirao, Appl. Phys. Lett. **70**, 1925 (1997), © (1997) with permission from the American Institute of Physics

## 3.3 Nearly Degenerate Three-wave Mixing

This technique is a form of four-wave mixing in which two of the waves are derived from the same beam. A strong pump beam with a frequency $\omega$ interacts with a weak probe beam with a frequency $\omega - \Delta\omega$ to produce a new wave at $2\omega - (\omega - \Delta\omega) = \omega + \Delta\omega$, where $\Delta\omega \ll \omega$ . Under these conditions,

$$\chi^{(3)}_{xxxx}(-\omega;\omega,\omega,-\omega) \cong \chi^{(3)}_{xxxx}(-\omega-\Delta\omega;\omega,\omega,-\omega+\Delta\omega), \tag{3.10}$$

where the latter susceptibility is that governing the three-wave mixing process.

The intensity of the newly generated wave is proportional to the absolute square of the susceptibility in (3.10). Thus, a measurement of this intensity provides a measure of the susceptibility, which is related to the degenerate form of $\chi^{(3)}$ through the approximate relationship of (3.10). The advantage of this technique is that it is nearly phase matched for forward collinear propagation of all three waves. This greatly simplifies the beam alignment in the experiment. The disadvantage is that waves of nearly equal frequency must be separated to measure the newly generated wave intensity.

Adair et al. [115] developed this technique for a relatively rapid assessment of glass hosts for laser media. They determined that the approximate relationship in (3.10) will hold for frequency shifts up to $\Delta\omega \approx 60\,\mathrm{cm}^{-1}$. Under normal conditions, this will result in a small phase mismatch. The phase-matching diagram for the nearly degenerate three-wave mixing process is shown in Fig. 3.4. The phase mismatch $\Delta k$ is given by

$$\Delta k \approx -\left[2\left(\frac{\mathrm{d}n}{\mathrm{d}\omega}\right)_{\omega} + \omega\left(\frac{\mathrm{d}^2 n}{\mathrm{d}\omega^2}\right)_{\omega}\right]\frac{(\Delta\omega)^2}{c}. \tag{3.11}$$

The generated signal intensity at $\omega + \Delta\omega$ is given by

$$I_{+} \propto \frac{1}{n_0^4}\left|\chi^{(3)}_{xxxx}(-\omega-\Delta\omega;\omega,\omega,-\omega+\Delta\omega)\right|^2 I_{\mathrm{p}}^2 I_{-} L^2, \tag{3.12}$$

where $I_{+(-)}$ is the intensity of the upshifted (downshifted) frequency, and $I_{\mathrm{p}}$ is the pump intensity. By measuring intensities for both the sample and a


**Fig. 3.4.** Phase-matching diagram for a nearly degenerate three-wave mixing process

reference material, one can compute the sample susceptibility from:

$$\chi^{(3)}_{xxxx} = \left(\frac{n}{n_{\rm ref}}\right)^2 \frac{L_{\rm ref}}{L} \left(\frac{1-R_{\rm ref}}{1-R}\right)^2 \left(\frac{I^-_+}{I^{\rm ref}_+}\right)^{1/2} [\chi^{(3)}_{xxxx}]_{\rm ref}, \qquad (3.13)$$

where $R = [(1-n)/(1+n)]^2$ is the Fresnel reflectance of the sample or reference ($R_{\rm ref}$) material. A schematic diagram of the experiment is shown in Fig. 3.5. The pump beam is the fundamental from an Nd:YAG laser at 1.064 μm, while the other wavelength at 1.071 μm is obtained by Raman-shifting the output of a dye laser (0.567 μm) pumped by the second harmonic of the Nd:YAG laser. The two beams are combined by beam splitters and adjusted

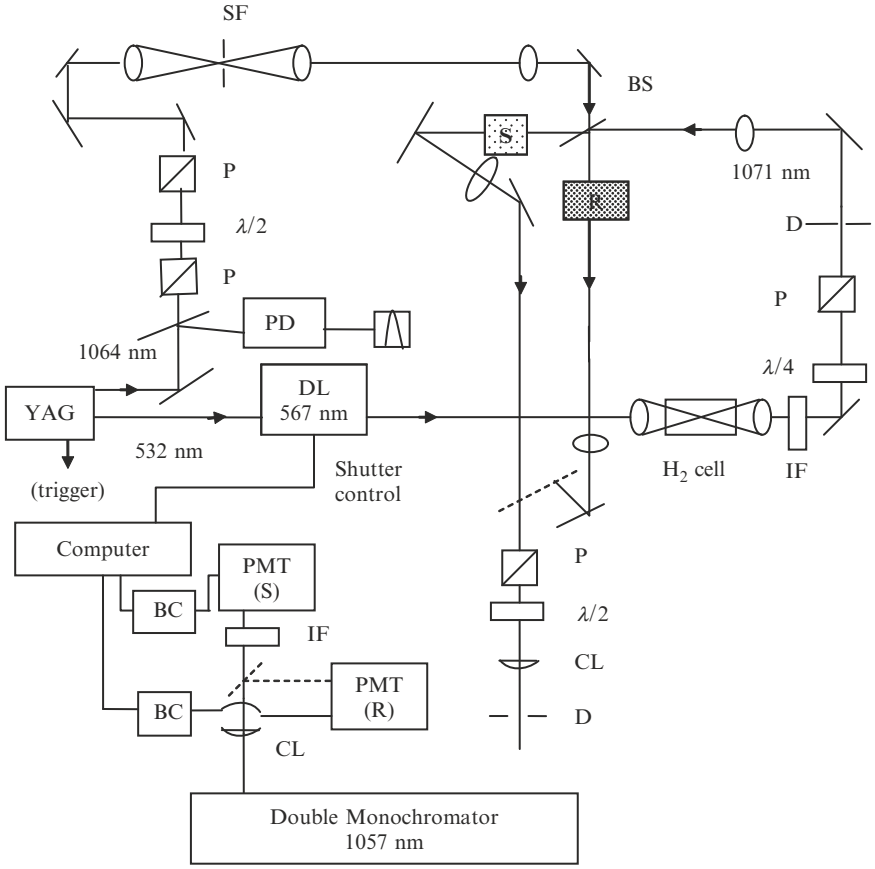


**Fig. 3.5.** Schematic diagram of a nearly degenerate three-wave mixing experiment. The two wavelengths are from an Nd:YAG laser and the Raman-shifted ($H_2$ cell) output of a dye laser. The sample and reference are labeled by S and R, respectively (redrawn from [115])

to overlap spatially and temporally. The sample and reference are irradiated simultaneously in separate paths. The two generated signal beams are then vertically separated and passed through a double monochromator. The output signals are physically separated and detected by PMTs connected to boxcar integrators for signal averaging. Averages of the signal intensity from both the sample and the reference are then used in (3.13) to compute the sample susceptibility.

## 3.4 Z-Scan

Self-focusing of an intense Gaussian beam in a nonlinear medium results in beam distortion, which can be measured. The $n_2$ value of the medium can be extracted from this distortion. The Z-scan technique developed by Sheik-bahae et al. [116] is a sensitive self-focusing measurement technique that is based on focusing a laser beam through a thin sample (see Fig. 3.6).

The light transmitted by a small aperture in the far field is then detected. The far-field aperture transmittance is measured for a constant laser input as the sample is scanned along the z-direction through the focus of the lens. Hence, the measurement method has come to be known as the Z-scan method. The principle of Z-scan can be understood as follows. Imagine a material with positive $n_2$ far from the focus of a lens. The transmitted intensity through the sample is small and, since the sample is thin, it remains approximately constant with the distance. As the sample is brought nearer the focus, the

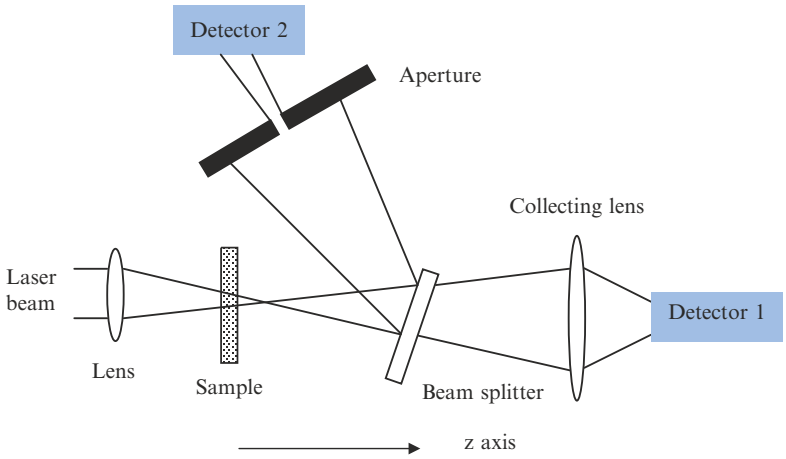


**Fig. 3.6.** Schematic illustration of simultaneous closed-aperture and open-aperture Z-scan measurements. The transmitted beam is split after the sample; the first detector measures the open-aperture transmittance, and detector 2 measures the closed-aperture transmittance as a function of the sample position (redrawn from [117])

intensity is high enough to produce a positive lensing effect. When the sample is scanned, for $z<0$ distances (before the focus), this lensing effect causes the beam to come closer to the focus and as a result diverges more rapidly in the far field. The result is that the aperture transmittance decreases. For $z>0$ (after the focus), however, the positive lensing causes the beam divergence to decrease, resulting in an increased aperture transmittance. The lens has little effect on the beam near $z=0$, and the aperture transmittance returns to its low-intensity value. The net Z-scan yields an s-shaped transmittance curve (see Figs. 3.7 and 3.8).

A material with a negative $n_2$ will produce a similar curve, but with the peak and valley reversed about $z=0$. The basis of the Z-scan technique is the fact that the aperture transmittance as a function of sample position depends on the magnitude and sign of $n_2$. The nonlinear medium impresses a phase distortion on the electric field of the transmitted light. The value of $n_2$ can be extracted using the computed aperture transmittance. Among several advantages of the Z-scan technique is its simplicity, and being a single- beam technique, there are no difficult alignment problems other than keeping the beam centered on the aperture. It can be used to determine both the magnitude and sign of $n_2$. The sign is obvious from the shape of the transmittance curve. Unlike most DFWM methods, the Z-scan can determine both the real and the imaginary parts of $\chi^{(3)}$.

The Z-scan technique is also highly sensitive, capable of resolving a phase distortion of $\approx\lambda/300$ [108] in samples of high optical quality. Among the disadvantages of the technique is the requirement of a high-quality Gaussian

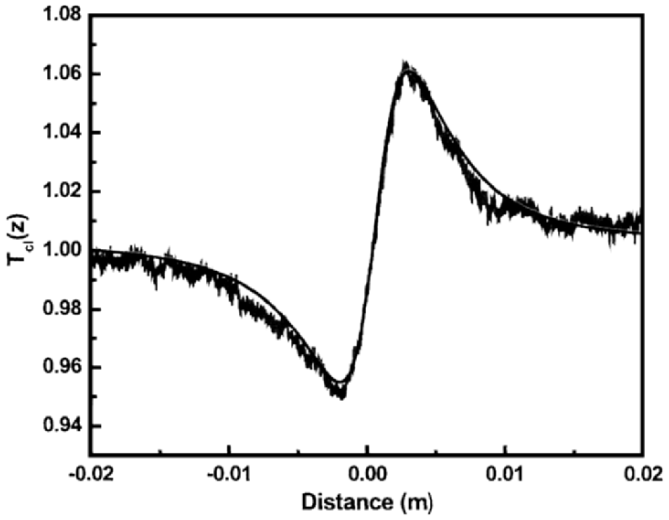


**Fig. 3.7.** Transmission versus position, z, for a closed- aperture scan of $Ge_{33}As_{12}Se_{55}$ at an intensity of $0.16\,\mathrm{GW\,cm^{-2}}$ (after [118])

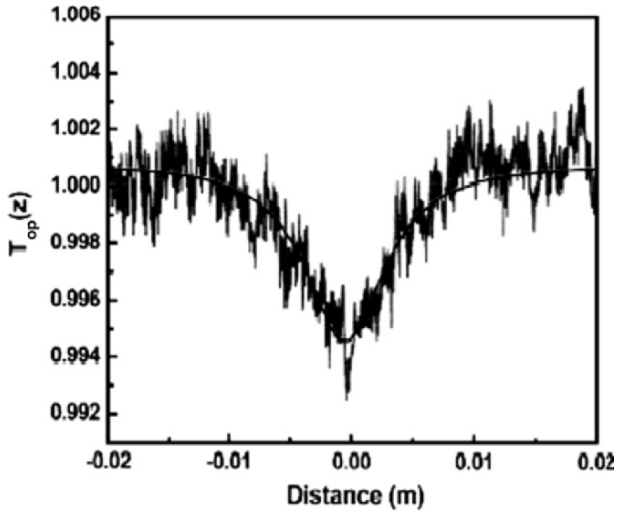


**Fig. 3.8.** Transmission versus position, z, for an open-aperture scan of $Ge_{33}As_{12}Se_{55}$ at an intensity of $0.16\,GW\,cm^{-2}$ (after [118])

$TEM_{00}$ beam for absolute measurements. Effects such as sample distortion and tilting of the sample during translation can cause beam deflection and hence cause unwanted fluctuations in the detected signal.

## 3.5 Third-Harmonic Generation

Generally, one utilizes a Q-switched pulse Nd:YAG laser for this technique, which provides nanosecond pulses at low repetition rates (10–30 Hz). After proper selection of wavelength and polarization, the laser beam is divided into two parts, one being used to generate the third harmonic in the sample and the other to generate the third harmonic in a reference (see Fig. 3.9).

Fused silica glass is generally taken as the reference. The third-harmonic generation (THG) susceptibility is determined from the following relation.

$$\chi^{(3)}(\mathrm{THG}) = \left(\frac{n+1}{n_\mathrm{s}+1}\right)^4 \frac{l_\mathrm{c.s}}{l_\mathrm{c}} \left(\frac{I_{3\omega}}{I_{3\omega,\mathrm{s}}}\right)^{1/2} \chi_\mathrm{s}^{(3)}(\mathrm{THG}). \tag{3.14}$$

Here $n$ is the refractive index, $l_\mathrm{c}$ is the coherence length, and $I_{3\omega}$ is the TH intensity. The suffix s means the standard medium. For nonphase-matched THG, one uses the Maker fringe method in which the path length of the sample is varied and the third-harmonic signal is monitored as a function of the interaction length to obtain the fringes. From the fringes, one determines the coherence length for the sample. Since all media, including air, show third-order nonlinear effects, one has to be extremely careful in third-harmonic

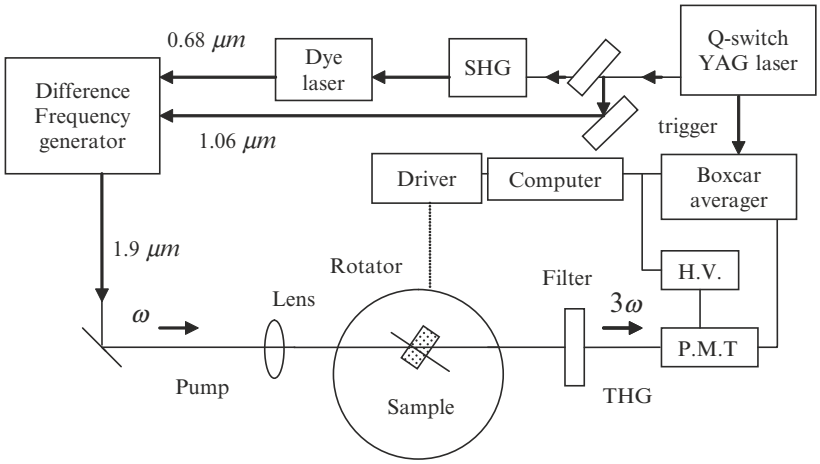


**Fig. 3.9.** Schematic illustration of the equipment for measurement of third-harmonic generation. SHG, second harmonic generation; THG, third harmonic generation; P.M.T, photomultiplier tube; H.V., high voltage (redrawn from [119])

measurements. Contributions from air and the walls of the cell (the latter in the case of liquid samples) may even be dominant, especially with samples having low values of $\chi^{(3)}$. The resulting harmonic field is equal to the sum of contributions from consecutive nonlinear media. The advantage of the THG technique is that it probes purely electronic nonlinearity. Therefore, orientational and thermal effects, as well as other dynamic nonlinearities derived from resonant excitations, are eliminated. The disadvantage of the technique is that very large resonant dynamic nonlinearities cannot be probed by this method. The THG method does not provide any information on the time response of optical nonlinearity.

## 3.6 Optical Kerr Gate and Ellipse Rotation

### 3.6.1 Optical Kerr Gate

In this method, an intense linearly polarized light pulse traveling through an optically isotropic $\chi^{(3)}$ medium induces optical birefringence using the optical Kerr effect. A linearly polarized weaker probe pulse is utilized to obtain the birefringence $\delta n = \delta n_{\parallel} - \delta n_{\perp}$. One can obtain $\chi^{(3)}$ from $\delta n$. The time evolution of the birefringence, and hence the response time of $\chi^{(3)}$, can be probed by delaying the probe beam with respect to the pump beam. A suitable Kerr-gate experiment is shown in Fig. 3.10 [120]. A picosecond pulse of appropriate wavelength is divided in two parts: a strong ($100\,\mathrm{MW\,cm^{-2}}$) pump pulse and

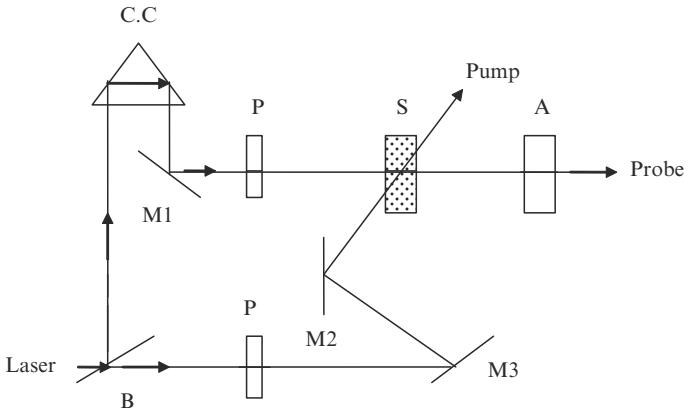


**Fig. 3.10.** Schematic of the Kerr-gate experimental arrangement. A, analyzer; P, polarizer; S, sample; M, mirrors; B, beam splitter; C.C., corner cube for optical delay (redrawn from [120])

a weak probe pulse that undergoes a variable delay. The two beams make an angle (usually 45°) with each other. The analyzer measures the transmitted probe beam as a function of the delay time between the probe and pump pulses. The signal $I_t(\tau)$ transmitted by the analyzer, for a time delay $\tau$, is given by:

$$I_t(\tau) = \int_{-\infty}^{+\infty} \langle E^2_{\text{probe}}(t - t_{\text{D}})\rangle \, \sin^2\left[\frac{\delta\phi(t)}{2}\right] \mathrm{d}t. \tag{3.15}$$

Here $E_{\text{probe}}$ is the electric field of the probe beam and $\delta\phi$ is the phase retardation of the probe beam due to induced birefringence given by

$$\delta\phi(t) = \frac{2\pi l}{\lambda}\delta n(t), \tag{3.16}$$

where $l$ is the sample path length, $\lambda$ is the wavelength of the probe beam, and $\delta n(t)$ is the induced refractive-index change written as

$$\delta n(t) = n_2^f \langle E_1^2(t)\rangle + \sum_i \frac{n_{2i}^s}{\tau_i} \int_{-\infty}^{t} \langle E_1^2(t')\rangle \, \exp\left(-\frac{t - t'}{\tau_i}\right)\mathrm{d}t'. \tag{3.17}$$

Here, $n_2^f$ is the intensity-dependent refractive index due to the rapidly responding electronic $\chi^{(3)}$. The second term consists of various slowly responding nonlinearities with response time $\tau_i$.

In the case of nonresonant electronic nonlinearity

$$\delta n = n_2 I_{\text{pump}}. \tag{3.18}$$

If $\delta n$ is substituted in (3.16), the peak value of the phase retardation $\delta\phi$ is obtained from

$$\delta\phi = \frac{2\pi l}{\lambda} n_2 I_{\text{pump}}. \tag{3.19}$$

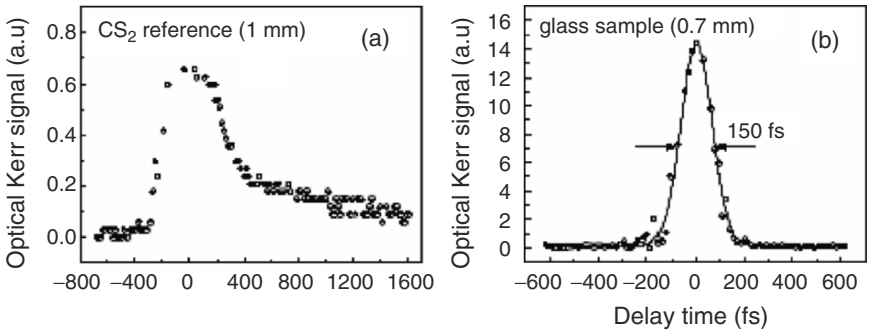


**Fig. 3.11.** Time-resolved optical Kerr signals at 820 nm. (**a**) Standard $CS_2$ reference medium. (**b**) The $90GeS_2 - 5Ga_2S_3 - 5CdS$ (in mol.%) chalcogenide glass sample. Dots show the experimental data and *solid curve* indicates the Gaussian fit (after [121])



From a measurement of the peak value of the transmitted probe signal $I_s$, one can obtain $\delta\phi$ and hence $n_2$, which is related to $\chi^{(3)}$ by

$$n_2 = \frac{12\pi}{n_0}(\chi^{(3)}_{1111} - \chi^{(3)}_{1122}). \tag{3.20}$$

At a wavelength far from resonance and for an isotropic medium, a purely electronic nonlinearity leads to $\chi^{(3)}_{1122} = \frac{1}{3}\chi^{(3)}_{1111}$ and hence the measurement of $n_2$ yields a direct determination of $\chi^{(3)}_{1111}$.

A typical optical Kerr-gate result for a $90GeS_2 - 5Ga_2S_3 - 5CdS$ sample is shown in Fig. 3.11.

### 3.6.2 Ellipse Rotation

If a single optical beam is incident on an isotropic nonlinear medium, for both linearly and circularly polarized light, the third-order polarization has the same vector character as the applied field. Thus, the induced birefringence produces no change in the polarization state of the optical field. When an elliptically polarized wave induces a nonlinear polarization that mixes the left- and right-hand circularly polarized components of the wave, an induced circular birefringence $\Delta n_c$ is formed and is given by

$$\Delta n_c = -\frac{3\chi^{(3)}_{xyyx}}{n_0}\left(|E_+|^2 - |E_-|^2\right), \tag{3.21}$$

where $E_+$ and $E_-$ are the complex field amplitudes of the left- and right-hand circularly polarized components, respectively, of the elliptically polarized

wave. The circular birefringence produces a rotation of the polarization ellipse (ellipse axes) through an angle $\theta$, given by

$$\theta_{\mathrm{c}} = \frac{\pi \Delta n_{\mathrm{c}} L}{\lambda}. \tag{3.22}$$

A measurement of this rotation angle gives a measure of the $\chi^{(3)}_{xyyx}$ tensor component of the medium.

## 3.7 Self-Phase Modulation

An intense pulse propagating through a nonlinear medium acquires an additional phase due to the nonlinear index of refraction, $n_2$. The self-induced phase is time dependent if the pulse intensity is time dependent. The nonlinear phase shift can be written as

$$\phi_{\mathrm{NL}}(t) = -\frac{\omega_0}{c} n_2^I I(t) L, \tag{3.23}$$

where $\omega_0$ is the pulse center frequency and $L$ is the medium thickness. An instantaneous frequency shift is introduced:

$$\delta\omega(t) = \mathrm{d}\phi_{\mathrm{NL}}/\mathrm{d}t. \tag{3.24}$$

The frequency shift near the peak of the pulse is zero. The leading edge is red-shifted while the trailing edge is blue-shifted. If the bandwidth of the pulse is $\tau_0^{-1}$, self-phase modulation becomes important when $\Delta\phi_{\max} \geq 2\pi$, where $\Delta\phi_{\max}$ is the maximum phase shift. For light with a wavelength 1 μm propagating through a medium of length 1 cm with $n_2^I \approx 10^{-18}\,\mathrm{m^2\,W^{-1}}$, a peak intensity of $>10\,\mathrm{GW\,cm^{-2}}$ is needed, which means pulses of picosecond width and shorter are required. A self-modulated pulse has a broadened spectrum of frequencies. If the medium has group-velocity dispersion (for ultrashort pulses), then the pulse will also spread in time [122]. Applications of self-phase modulation include super-continuum generation [123] and pulse compression [122]. A mode-locked Nd:YAG laser is normally used as the light source [124] (see Fig. 3.12).

The temporal-pulse profile is monitored with a pin-photodiode and a sampling oscilloscope. The laser beam is focused into the fiber with an objective lens. Spectral broadening of the output is analyzed using an optical spectrometer. The $n_2$ value can be estimated from the following equation:

$$\Delta\nu^2 = \Delta\nu_0^2 \left(1 + \frac{4}{3\sqrt{3}} \gamma^2 P^2\right), \tag{3.25}$$

where

$$\gamma = \frac{2\pi n_2}{\lambda A_{\mathrm{eff}}} Z_{\mathrm{eff}} \tag{3.26}$$

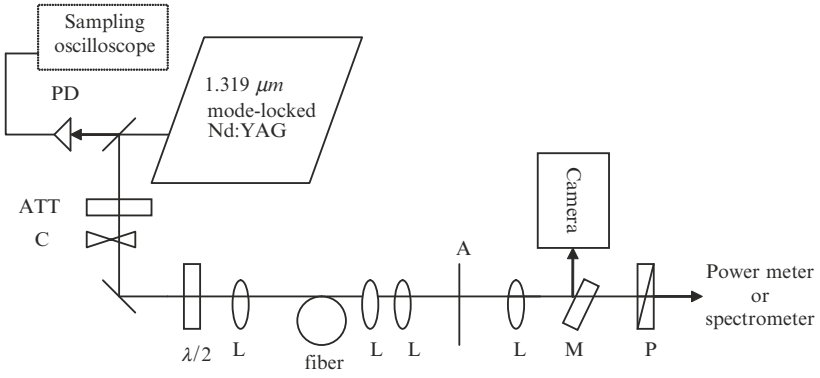


**Fig. 3.12.** Schematic diagram of the experimental set up. PD, pin-photodiode; ATT, attenuator; C, chopper; $\lambda/2$, half-wave plate; L, lens; A, variable aperture; M, glass plate; P, polarizer (redrawn from [124])



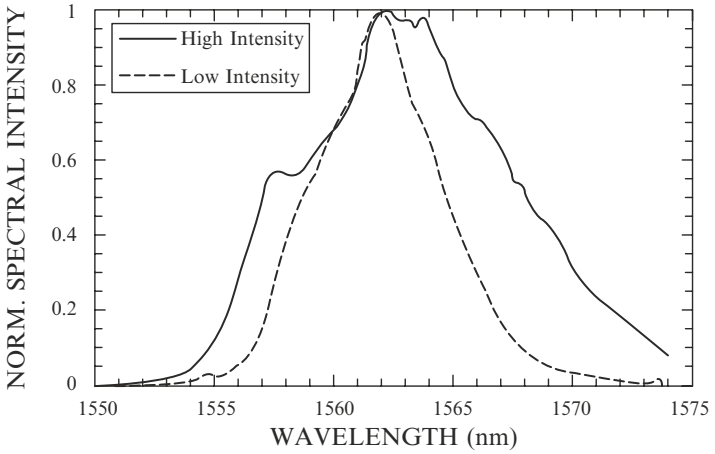


**Fig. 3.13.** Self-phase modulation spectrum at the output of an $As_2S_3$ waveguide. The *solid* and *dashed lines* are for high and low input intensity, respectively (after [125])



and

$$Z_{\text{eff}} = \frac{1}{\alpha}[1 - \exp(-\alpha L)]. \tag{3.27}$$

Here, $\Delta\nu_0$ is the initial spectral width, $P$ is the input peak power, $\lambda$ is the wavelength, $A_{\text{eff}}$ is the effective core area, $Z_{\text{eff}}$ is the effective length, $\alpha$ is

the loss coefficient, and $L$ is the fiber length. A typical result of self-phase modulation for an $As_2S_3$ waveguide is shown in Fig. 3.13.

## 3.8 Spectrally Resolved Two-Beam Coupling

Spectrally resolved two-beam coupling (SRTBC) is a two-beam technique and it utilizes the modulation of the probe-pulse spectrum due to the nonlinear phase shift induced by the pump [126]. SRTBC provides the sign and magnitude of the real and imaginary parts of the third-order susceptibility (nonlinear refraction and nonlinear absorption) along with their dynamics. This technique is based on a standard pump-probe setup with the addition of a monochromator to analyze spectrally the energy content of the probe beam (see Fig. 3.14).

The presence of a strong pump pulse can change the index of refraction and absorption coefficient of a material. When the weak probe beam passes through the medium, it acquires a frequency shift and may experience nonlinear absorption. These changes in the probe beam are detected by measuring the energy of the beam in a narrow spectral band selected by the monochromator as a function of the time delay between the arrival of the pump and probe pulses. One can extract the nonlinear index of refraction and two-photon absorption coefficient from these data. Since the experiment monitors changes in the spectrum, the signal is derivative-like; an index change with a Gaussian temporal envelope will produce a bimodal signal. The TPA signal is superimposed on this and is directly proportional to the energy loss. The advantage of the technique is detection far away from the center wavelength. At this wavelength, the intensity of the beam is much smaller than at the center of the spectrum, but the nonlinear modulation is relatively larger. Nonlinear phase shifts as small as $10^{-6}$ rad can be detected. The time resolution and sensitivity of the technique is such that in the case of fused silica, which has among the smallest known nonlinearity, the nuclear contribution, which is only a fraction

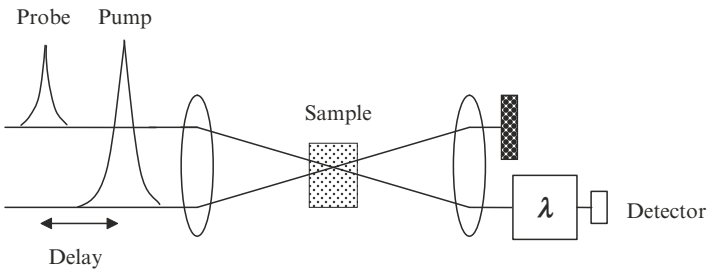


**Fig. 3.14.** Schematic diagram of the experimental set-up for a spectrally resolved two-beam coupling (SRTBC) technique. $\lambda$ represents the monochromator

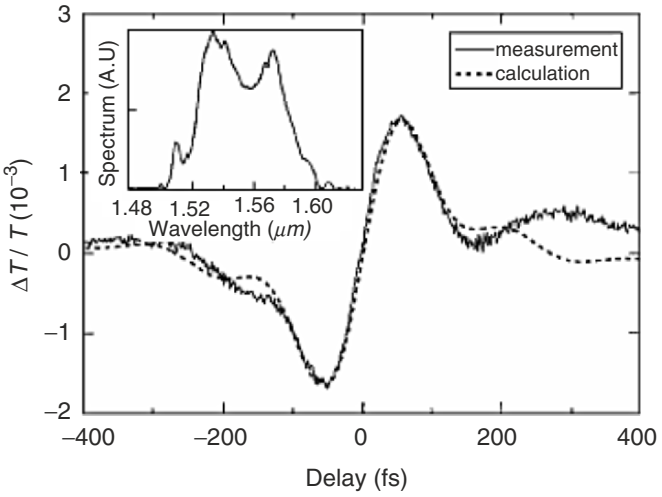


**Fig. 3.15.** Representative SRTBC signal obtained with an Er-doped fiber laser at 1.25 μm (EDFL). The calculated signal is derived from a zero-phase Fourier transform of the laser spectrum (*inset*). The difference between measurement and calculation for positive delay is due to the nuclear contribution to the nonlinearity (after [128])

of the total nonlinearity, is clearly resolved [127]. A typical result of SRTBC is shown in Fig. 3.15.

## 3.9 Mach-Zehnder Interferometry

The experimental set up is shown in Fig. 3.16. As is seen, the first arm of a Mach-Zehnder interferometer is used as the reference beam $I_1(r)$. The second arm $I_2(r)$ is used as the probe beam. The nonlinear medium (NS) is illuminated by a pump beam focused by means of the lens $L_1$. At the output of the set-up, the interferometer pattern intensity $I_{\mathrm{NL}}(r)$ is recorded on a CCD camera placed in a $O(x, y)$ plane perpendicular to the light-propagation axis. Rectilinear fringes are obtained by adjusting the interferometer. The intensity at the output is given by

$$I_{\mathrm{NL}}(r) = I_1(r) + I_2(r) \cdot T(r)^2 + 2T(r)\sqrt{I_1 I_2}\,\cos[\phi_L + \phi_{\mathrm{NL}}(r)], \qquad (3.28)$$

where $\phi_L$ is the linear phase difference between the interferometer arms. Local fringe alterations occur in a small region of the interference pattern. These local alterations are due to a local displacement of fringes attributed to the nonlinear dephasing $\phi_{\mathrm{NL}}(r)$ and a local modification in the fringe visibility attributed to the amplitude nonlinear transmission $T(r)$. A numerical spatial Fourier transform (FT) is performed on the acquired image $I_{\mathrm{NL}}(r)$. The FT

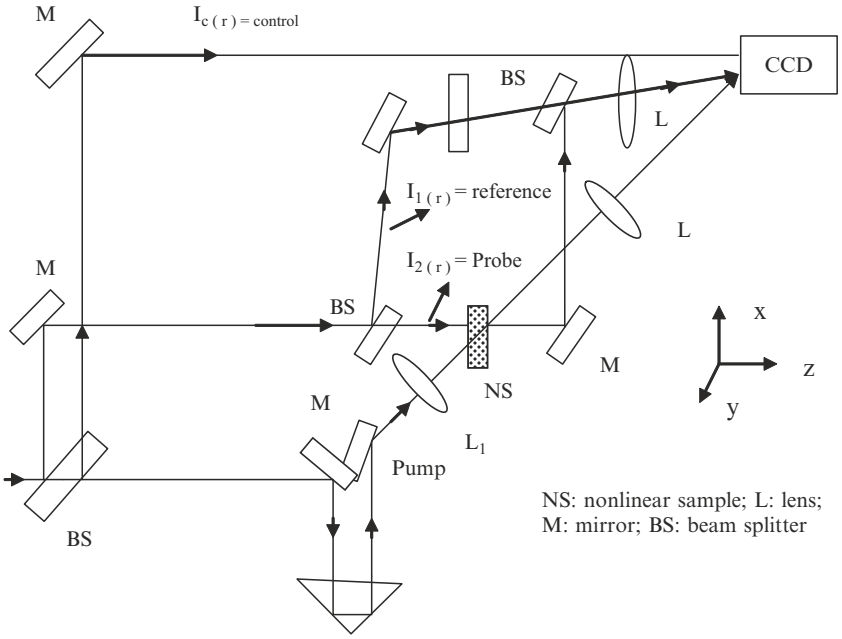


**Fig. 3.16.** Set-up for Mach-Zehnder interferometry measurements (redrawn from [129, 130])

of the cosine function (representing the rectilinear fringes) in the third term of (3.28) consists of two Dirac delta functions far enough from the origin (location of the FT of the first and second terms in (3.3)–(3.28) in the Fourier plane), convoluting a complex function that contains the information about the nonlinearities.

By considering the part of the spectrum around one of these delta functions and performing an inverse FT on this part, the quantities $T$ and $\phi_{\mathrm{NL}}$ as functions of the radial coordinate $r$ are extracted. In order to extract the information related to the nonlinearities, a linear fringe pattern is obtained by placing the sample in the interferometer but the pump beam is switched off. In this case, the nonlinearities are negligible, which allows one to measure the linear response of the sample. By comparing the linear and the nonlinear fringe patterns, one is able to get spatially resolved information on the nonlinearities. The nonlinear dephasing allows one to find a nonlinear index assuming a purely third-order nonlinearity.

$$\phi_{\mathrm{NL}}(r) = kLn_2 I_{\mathrm{eff}}(r), \tag{3.29}$$

with

$$I_{\mathrm{eff}}(r) = \frac{1}{\beta L} \ln[1 + q(r)], \tag{3.30}$$

where $I_{\text{eff}}$ is the effective pump intensity inside the nonlinear medium, $k$ is the wave vector, $L$ is the sample length, $\beta$ is the two-photon absorption coefficient and $q(r) = \beta L_{\text{eff}}(r)$ with $L_{\text{eff}} = \frac{(1-\mathrm{e}^{-\alpha L})}{\alpha}$. $I(r)$ is the incident pump-intensity distribution and $\alpha$ is the linear absorption coefficient. The two-photon absorption coefficient $\beta$ is deduced from the amplitude transmittance as

$$T(r) = (\mathrm{e}^{\alpha L}[1 + q(r)])^{1/2}. \tag{3.31}$$

Figure 3.17 shows a typical result of Mach-Zehnder interferometry for an $As_2S_3$ sample.

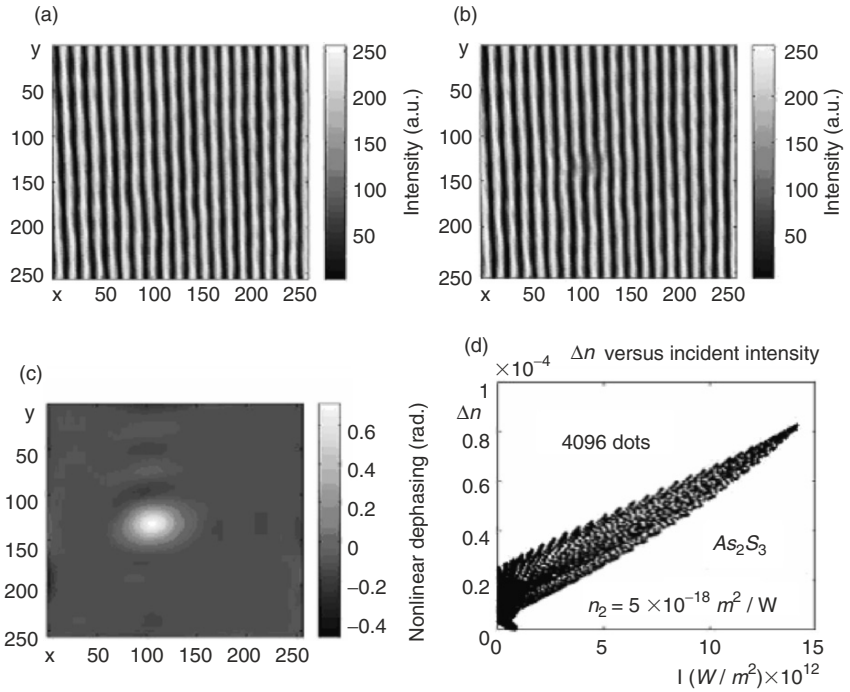


**Fig. 3.17.** Experimental acquisition and numerical processing in the presence of a chalcogenide glass $As_2S_3$(1.8 mm thick) at $\lambda = 1064\,\text{nm}$. $X$ and $y$ are graduated in pixels. The control and the pump beams are not shown in the figure. (**a**) The fringe pattern without the incident pump beam. The fringes that appear in this figure are due to interference between reference and probe beams. (**b**) Local alteration of the previous fringe pattern in the presence of the incident pump beam inducing nonlinear dephasing. (**c**) Result of the numerical processing giving an image of the nonlinear dephasing when the two experimental acquisitions shown in (**a**) and (**b**) are taken into account. (**d**) Plot of $\Delta n(x, y)$ versus $I(x, y)$. The $n_2$ measurement is given by the slope of the linear regression line calculated over 4096 pixels in the image (after [129])

## 3.10 Summary

Different techniques have been introduced, which allow measurements of the nonlinear optical constants ($n_2$ and $\beta$) of bulk/film samples. While DFWM allows determination of $n_2$ only, Z-scan can be used to obtain both $n_2$ and $\beta$ of samples. Moreover, this single-beam technique allows determination of the sign of $n_2$. THG is a technique that probes purely electronic nonlinearity but does not provide any information on the time response of optical nonlinearity. An intense pulse propagating through a nonlinear medium acquires an additional phase due to the nonlinear index of refraction. By monitoring the temporal-pulse profile, and analyzing the spectral broadening of the output due to self-phase modulation, the $n_2$ value of the sample can be estimated. SRTBC is a two-beam technique that provides the sign and magnitude of the real and imaginary parts of the third-order susceptibility along with their dynamics. Finally, Mach-Zehnder interferometry allows one to determine both $n_2$ and $\beta$. When the nonlinear medium is illuminated by a focused pump beam, local fringe alterations occur in a small region of the interference pattern. These local alterations are due to the nonlinear dephasing $\phi_{\mathrm{NL}}(r)$ and the amplitude nonlinear transmittance $T(r)$. The quantities $T$ and $\phi_{\mathrm{NL}}$ as functions of the radial coordinate $r$ are extracted. The nonlinear dephasing allows determination of the nonlinear index, while the two-photon absorption coefficient $\beta$ is deduced from the amplitude transmittance.

# 4

# Measurement of Nonlinear Optical Constants

## 4.1 Measurements of Nonlinear Refractive Index $n_2$

Different techniques, such as two-photon absorption spectroscopy [131], degenerate four-wave mixing (DFWM), Z-scan [132, 133], third-harmonic generation (THG), optical Kerr-shutter (OKS) [134], and self-phase modulation (SPM), have been used to measure the nonlinear refractive index, as well as the nonlinear absorption coefficient, of chalcogenide glasses. The nonlinear refractive index $n_2$ of $As_2S_3$ glass fiber was first measured directly by a spectrum-broadening experiment at a wavelength of 1.3 µm [135]. The $n_2$ value was also measured by a Kerr-shutter (Fig. 4.1) experiment at 1.3 µm [136]. In the optical Kerr effect, the nonlinear phase shift induced by an intense, high-power, pump beam is used to change the transmission of a weak signal through a nonlinear medium. The operating principle of a Kerr-shutter can be explained in the following way. The pump and signal beams are linearly polarized at the fiber input with a 45° angle between their directions of polarization. A gate pulse induces a phase-shift difference between two signal components whose polarization is parallel and perpendicular to that of the gate. When the phase-shift difference reaches $\pi$, the polarization of the signal is switched by 90°. The $n_2$ values obtained were $1.7 \times 10^{-14}\,\mathrm{cm^2\,W^{-1}}$ and $4 \times 10^{-14}\,\mathrm{cm^2\,W^{-1}}$, respectively. The difference may be due to an increase in the transmission loss caused by a higher average power in the spectrum-broadening experiment.

Other Kerr-shutter experiments at 1.55 µm resulted in $n_2 = 2 \times 10^{-14}\,\mathrm{cm^2\,W^{-1}}$. There is a possibility that the $n_2$ value depends on the wavelength because of the two-photon resonance near 1.3 µm [138]. So, it was confirmed that $As_2S_3$ glass possesses a $n_2$ value about two orders of magnitude greater than silica ($n_2 = 3 \times 10^{-16}\,\mathrm{cm^2\,W^{-1}}$). The $\chi^{(3)}$ value obtained for the Kerr-shutter experiment at 1.3 µm was $1.4 \times 10^{-19}\,\mathrm{m^2\,V^{-2}}$ and was in good agreement with the value of $1.01 \times 10^{-19}\,\mathrm{m^2\,V^{-2}}$ measured in a THG experiment at 2 µm [139]. Third-order optical nonlinear susceptibilities $\chi^{(3)}$ of some high-refractive-index chalcogenide glasses were evaluated from

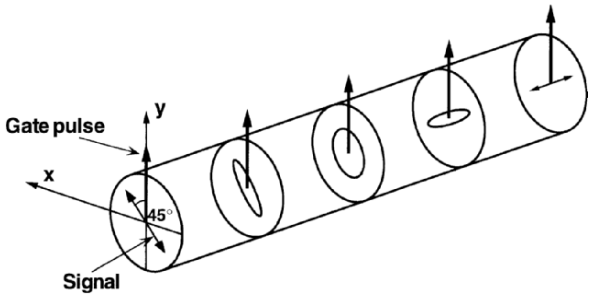


**Fig. 4.1.** Principle of an OKS (after [137])



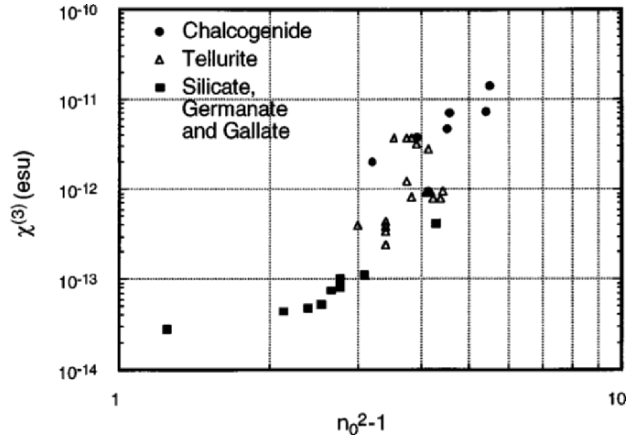


**Fig. 4.2.** Relationship between linear and third-order optical susceptibilities (after [137])



THG [139]. Compared with oxide glasses, whose $\chi^{(3)}$ was known, $\chi^{(3)}$ values of chalcogenide glasses were higher by an order of magnitude. The highest $\chi^{(3)}$ (for a composition of $As_{40}S_{57}Se_3$) is $1.96 \times 10^{-19} m^2\,V^{-2}$, being comparable with those of high-$\chi^{(3)}$ organic compounds (see Fig. 4.2). It was found [133] that $\chi^{(3)}$ generally increased with increasing density of the chalcogenide glasses. The real part of $\chi^{(3)}$ of binary and ternary glasses is plotted against $E_g$ and $n$ in Fig. 4.3. Re $\chi^{(3)}$ increases monotonically with decreasing $E_g$ and increasing $n$. A similar relation holds between Im $\chi^{(3)}$ and $E_g$ and $n$. As a result, the $\chi^{(3)}$ of binary and ternary glasses derived from the Z-scan method increases monotonically with decreasing $E_g$ and increasing $n$. This agrees well with the dependence of $\chi^{(3)}$ on $E_g$ and $n$ measured by THG [140]. It should be mentioned here that we have tried to give $\chi^{(3)}$ values in MKS units

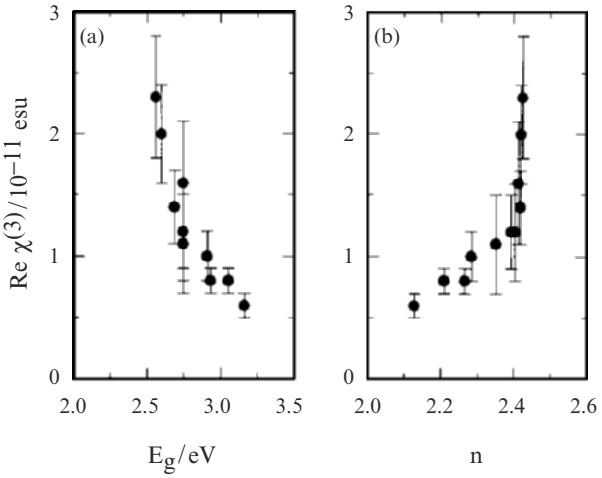


**Fig. 4.3.** The real part of $\chi^{(3)}$ of binary $La_2S_3$–$Ga_2S_3$ and ternary MS–$La_2S_3$–$Ga_2S_3$ glasses plotted against (**a**) $E_g$ and (**b**) $n$, (MS = $Ag_2S$ and $Na_2S$) (after [133])

throughout the text whenever possible. In the literature, however, $\chi^{(3)}$ values are normally given in Gaussian or (esu) units. The nonlinear susceptibilities in these two systems of units are related by

$$\chi^{(3)}(\text{MKS}) = \frac{4\pi}{(3\times 10^4)^2}\chi^{(3)}(\text{Gaussian}) = 1.40\times 10^{-8}\chi^{(3)}(\text{Gaussian}),$$

where the unit of $\chi^{(3)}$ in the MKS system of units is $\text{m}^2\,\text{V}^{-2}$.

Harbold et al. [141] have found that chalcogenide glasses in the As–S–Se system simultaneously exhibit a large nonlinear index of refraction and a figure of merit (FOM = $n_2/\beta\lambda$) that satisfies a standard criterion for all-optical switches (AOSs) [142]. They found that in samples with a FOM >5, nonlinear phase shifts of $\pi$ rad can be produced without damage for intensities of $\leq$200 MW cm$^{-2}$. They observed that the FOM increases substantially near $h\nu/E_{\text{gap}} \approx 0.45$, as is qualitatively expected when the absorption edge is not infinitely sharp. Their experiments confirm that the nonlinearities are determined largely by the abundance of the most polarizable constituent, in this case selenium. In particular, $As_{40}Se_{60}$ exhibits high values of $n_2$ and FOM ($2.3\times10^{-17}$ m$^2$ W$^{-1}$ and 11, respectively) and is thus quite promising for AOS use at 1.55 µm. A monotonic increase in $n_2$ with progressive replacement of S by Se in the sulfoselenide glasses, and the gradual removal of Se at fixed Ge:As ratio from the selenide glasses, is observed [143]. As shown in Fig. 4.4, $n_2$ increases faster than $\beta$ for photon energies just below the half gap. The FOM (Fig. 4.5) depends on the proximity of the frequency of the light to the two-photon absorption (TPA) edge and the peak at $h\nu/E_{\text{gap}} \approx 0.45$ occurs when nonlinear refraction increases more rapidly than TPA with normalized photon energy. Quemard et al. [144] suggest that the concentration

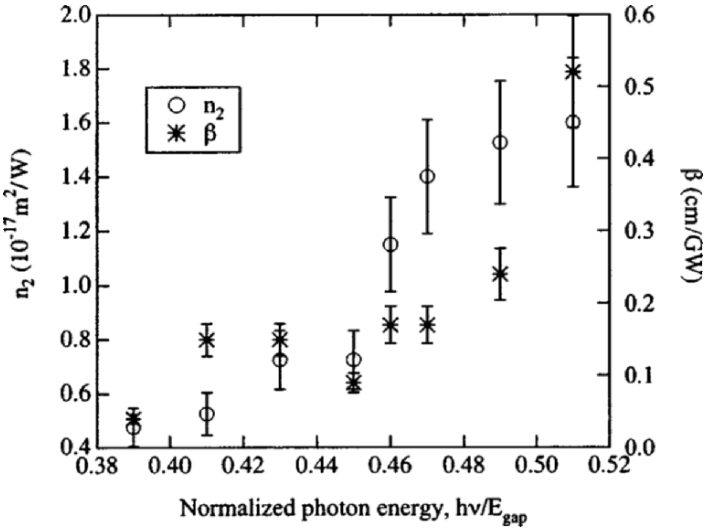


**Fig. 4.4.** Variation of $n_2$ and $\beta$, the TPA coefficient, with normalized photon energy in the Ge–As–S–Se system (after [143])

Reprinted from J.M. Harbold, F.O. Ilday, F.W. Wise, and B.G. Aitken, IEEE Photon. Technol. Lett. **14**, 822 (2002), © (2002) with permission from IEEE

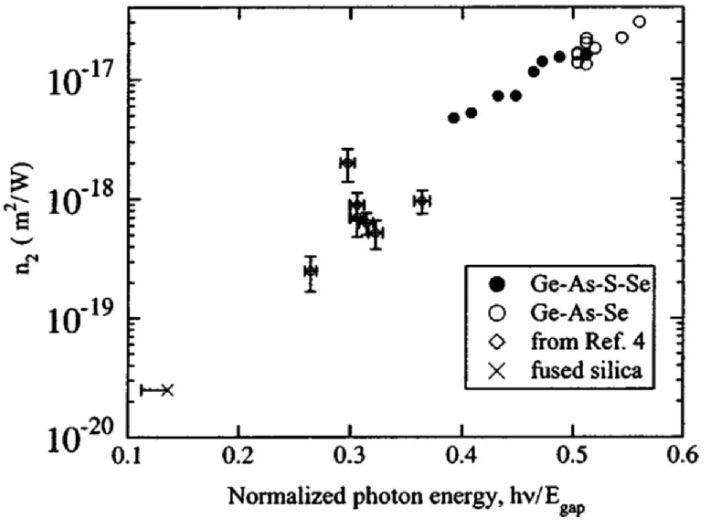


**Fig. 4.5.** Variation of $n_2$ with normalized photon energy in the selenide, sulfoselenide, sulfide, and heavy-metal-doped oxide systems, all at 1.25 µm (after [3]). Fused silica is also shown for comparison. Glasses in [4] in the inset belong to Ge–Se and Ge–Se–As systems

Reprinted from J.M. Harbold, F.O. Ilday, F.W. Wise, and B.G. Aitken, IEEE Photon. Technol. Lett. **14**, 822 (2002), © (2002) with permission from IEEE

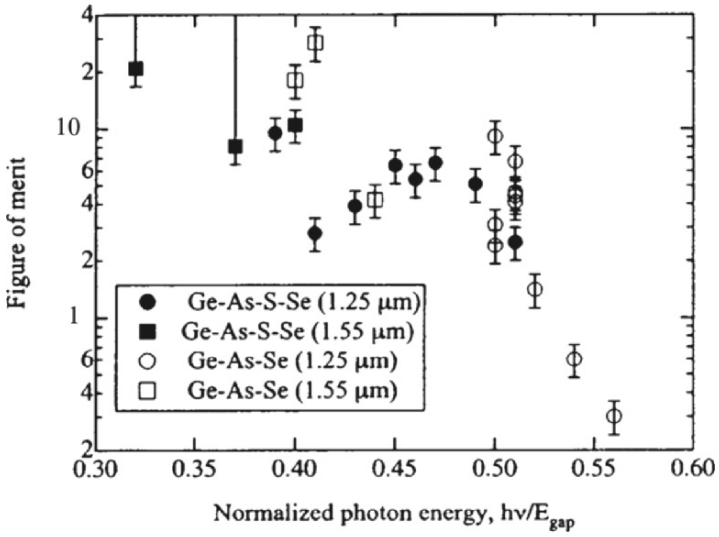


**Fig. 4.6.** Variation in the FOM with normalized photon energy in the Ge–As–Se and Ge–As–S–Se systems. Two femtosecond laser sources at 1.25 and 1.55 μm were used in nonlinear measurements using SRTBC (after [143])

Reprinted from J.M. Harbold, F.O. Ilday, F.W. Wise, and B.G. Aitken, IEEE Photon. Technol. Lett. **14**, 822 (2002), © (2002) with permission from IEEE

of electron lone pairs is the dominant factor in achieving large nonlinearities, and it has recently been confirmed that $n_2$ increases with the most polarizable constituent (in this case, selenium) in As–S–Se glasses [141]. It should be noted that a change in the electron lone-pair concentration modifies the energy gap so it is impossible to determine whether a corresponding change in the nonlinearity is due to lone pairs or resonant enhancement. However, Harbold et al [143] found no systematic increase of $n_2$ with increasing Se content and hence lone-pair concentration. Overall, they found that $n_2$ increases as the band gap decreases in the selenide and sulfoselenide glass systems. It can be said that the general trend in the nonlinearity is accounted for by the normalized photon energy (Fig. 4.6). So, when designing an AOS at a given wavelength, one would choose a glass with $h\nu/E_{\text{gap}} \approx 0.45$ in order to achieve both a large $n_2$ and large FOM.

Kosa et al. [145] measured the third-order nonlinear optical response of silver-doped and undoped $As_2S_3$ at a wavelength of 1.064 μm. A single-beam (Z-scan) technique was used for the measurement, which allowed them to separate the refractive and absorptive contribution to the signal at this wavelength. They observed that silver doping changes the sign of the refractive nonlinearity and it was also found that $n_2$ increased by almost a factor of 80 relative to the undoped material. Third-order nonlinear optical properties of chalcogenide glasses were investigated by Kanbara et al. [132] through THG, OKS, and DFWM measurements. They examined the dependence of the THG

susceptibility on the absorption edge (for glasses in As–S–Se and Ge–As–S systems), showing that the susceptibility rapidly increased as the absorption edge red shifted. To within experimental errors, the THG susceptibility compared well with the OKS susceptibility. The DFWM experiment pointed out that an ultrafast response time of less than a picosecond was attainable with the chalcogenide glass.

The Z-scan measurements were performed on germanium arsenic selenide films of 2 µm thickness [146]. 100-fs pulses with energies in the range of 0.1–0.5 µJ were used. In most measurements, the focused spot size was in the range of 20–40 µm, which resulted in maximum light intensities in the range of 10–150 GW cm$^{-2}$. A simple arrangement allowed the open-aperture Z-scan and the closed-aperture Z-scan to be recorded simultaneously. The Z-scans obtained were analyzed with expressions derived by Sheik-Bahae et al. [138] to yield the real part of the nonlinear phase shift $\Delta\phi_{\text{real}}$ induced by the third-order nonlinearity and the $T_{\text{t}}$ factor (defined here as $T_{\text{t}} = 4\pi\Delta\phi_{\text{imag.}}/\Delta\phi_{\text{real}}$) for a given sample. This analysis was performed by comparing the shapes of closed- and open-aperture scans with those computed theoretically. Roughly speaking, the amplitude of a closed-aperture Z-scan (i.e., the peak-to-valley difference in transmission values) is proportional to the real part of the nonlinear phase shift $\Delta\phi_{\text{real}}$, whereas the asymmetry of a closed-aperture scan depends on the $T_{\text{t}}$ factor (for $T_{\text{t}} = 0$, the scan is essentially S-shaped and symmetric). The imaginary part of the nonlinear phase shift $\Delta\phi_{\text{imag.}}$ can be obtained either from the asymmetry of the closed-aperture scan (with $\Delta\phi_{\text{imag.}} = \Delta\phi_{\text{real}}/4\pi$) or from the depth of a dip in the open-aperture scan that is directly related to the value of $\Delta\phi_{\text{imag.}}$.

Figure 4.7 shows examples of closed- and open-aperture scans for a germanium arsenic selenide film.

The relation between the nonlinear phase shift and the nonlinear refractive index can be written as

$$\Delta\phi = 2\pi n_2 I L_{\text{eff}}/\lambda, \tag{4.1}$$

where $I$ is the light intensity, $L_{\text{eff}}$ is the effective sample thickness (e.g., corrected for one-photon absorption, $L_{\text{eff}} = (1 - \text{e}^{-\alpha L})/\alpha$, and $\alpha$ is the linear absorption coefficient).

Knowledge of the light intensity can be used for conversion from phase-shift values to the nonlinearity values. It is, however, more convenient to perform the measurements in a relative manner. They therefore calibrated the values of the NLO parameters by performing measurements of the nonlinear phase shift for a fused silica plate for which a value $n_2 = 2\times10^{-16}\text{cm}^2\,\text{W}^{-1}$ was assumed. The thickness of the fused silica substrate was 1 mm. The sign of $n_2$ deduced from Z-scan measurements was positive. Their results show that the nonlinear response of $Ge_{33}As_{12}Se_{55}$ is dominated by an induced absorption effect. The value of the real part of the nonlinearity is $\text{Re}(n_2) \approx 2.2 \times 10^{-13}\,\text{cm}^2\,\text{W}^{-1}$ and its imaginary part is characterized by a nonlinear absorption coefficient $\beta_2 = 5.6 \times 10^{-8}\,\text{cm}\,\text{W}^{-1}$. It should be mentioned that Z-scan measurements on $As_2S_3$ films did not yield reliable signals, and hence Z-scan measurements

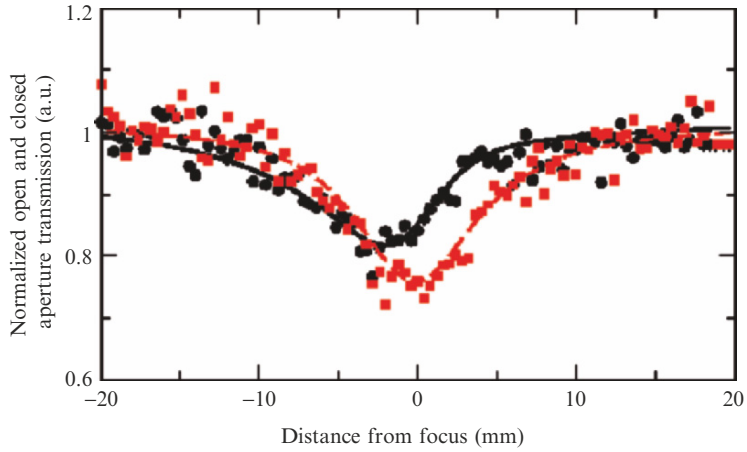


**Fig. 4.7.** Open (*squares*) and closed (*circles*) aperture Z-scan results obtained on a 2 µm $Ge_{33}As_{12}Se_{55}$ film on a 1 mm silica substrate. The lines are results of numerical fitting. The spot size was 32 µm, $\mathrm{Re}(\Delta\phi) = 0.36$ rad, $T_t = 12$. The results show that the nonlinear response of GeAsSe is dominated by an induced absorption effect. By calibrating the Z-scans against silica, one can calculate the real and imaginary parts of the nonlinearity. The real part of the nonlinearity is approximately $\mathrm{Re}(n_2) = 2.2 \times 10^{-13}\,\mathrm{cm}^2\,\mathrm{W}^{-1}$ and the imaginary part of the nonlinearity is characterized by a nonlinear absorption coefficient $\beta_2 = 5.6 \times 10^{-8}\,\mathrm{cm\,W}^{-1}$ (after [146])

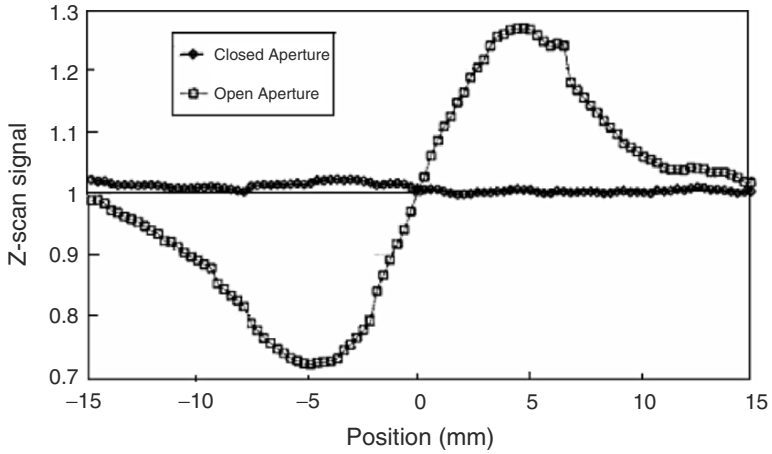


**Fig. 4.8.** Open- and closed-aperture Z-scan signals from a 2-mm-thick bulk sample of $As_2S_3$ glass measured at 1,550 nm. Note the absence of any nonlinear absorption in the open-aperture scan (after [147])

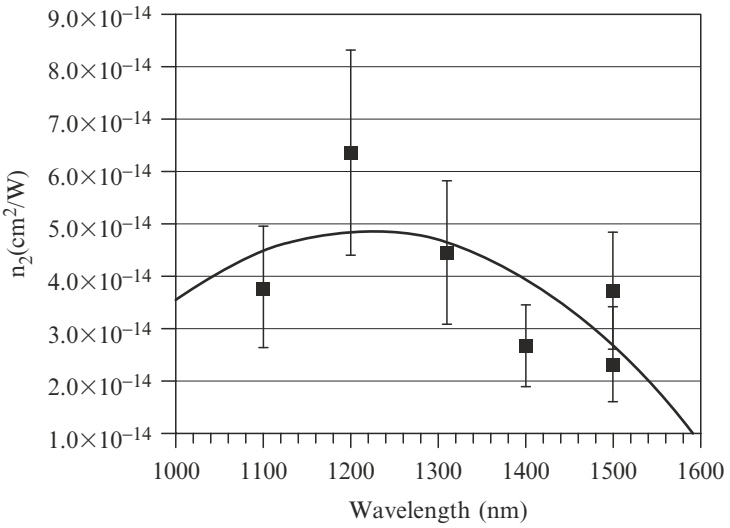


**Fig. 4.9.** Nonlinear refractive-index versus wavelength for $As_2S_3$ glass (after [147])

for the case of $As_2S_3$ were performed using glass disks [147]. Figure 4.8 shows the results of one such Z-scan measurement.

Zakery et al. [147] have used Z-scan measurements to find the variation of nonlinearity $n_2$ with wavelength for $As_2S_3$ glass. The values varied slightly with wavelength, reaching a maximum for wavelengths around 1,300 nm ($200 \times n_2$ (silica)) and decreasing to around $100 \times n_2$ (silica) at 1,500 nm (Fig. 4.9).

Figure 4.10 shows an example of a nonphase-matched DFWM signal obtained for intensities in the range of 1–60 GW cm$^{-2}$ [148]. These measurements were made using a femtosecond laser with hundred-femtosecond pulses. The energy per pulse was up to 35 µJ and the spot size on the sample was approximately 200 µm. $As_2S_3$ films up to 4 µm thick were used in these measurements. Normally two signals were monitored. One was generated as a result of phase-matched interaction of the three incident beams and the other was one of the nonphase-matched signals generated mostly by the arsenic sulfide film. The signals recorded at lower intensities show essentially only the instantaneous response similar to that obtained from the bare silica substrate. A very weak tail of the signal appears at high intensities, probably due to the formation of permanent gratings that are gradually formed in the material that distort the background signal.

Figure 4.11 shows a comparison of the power dependence of the phase-matched and nonphase-matched DFWM signal for a 4 µm thick film. As expected for Kerr nonlinearity, the dependences are roughly cubic. The modulus of the nonlinear refractive index of films was calculated from a comparison of the DFWM signals with those for bare silica substrates. The modulus of $n_2$ was found from the above measurements to be $2.7 \times 10^{-14}$cm$^2$ W$^{-1}$ at 800 nm, which was in good agreement with literature data.

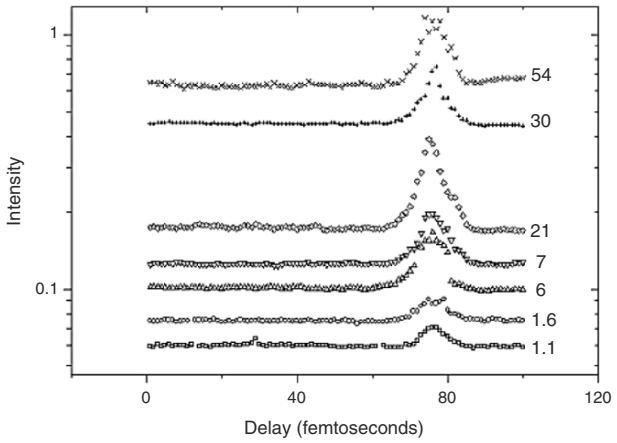


**Fig. 4.10.** Degenerate four-wave mixed (DFWM) signal versus the delay time for an $As_2S_3$ film. The numbers on the graphs correspond to the input pulse intensities (in $GW\,cm^{-2}$) (after [148])

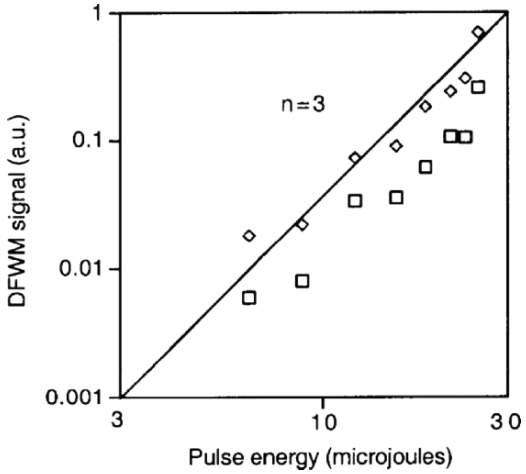


**Fig. 4.11.** Double-logarithmic plot of power dependencies of the DFWM signals (diamonds, phase matched; squares, nonphase matched) from a 4-μm thick $As_2S_3$ film. The line shows a theoretical cubic dependence (after [147])

Bindra et al. [149] have used Z-scan measurements at 1,550 nm and obtained $n_2$ values of $18 \times 10^{-19}\,m^2\,W^{-1}$, $9.2 \times 10^{-19}\,m^2\,W^{-1}$, and $3.8 \times 10^{-19}\,m^2\,W^{-1}$ for $As_2S_3$, $GeS_2$, and $TeO_2$, respectively. Smektala et al. [150] have used Z-scan measurements at 1.06 μm and found that the nonlinear refraction properties found for $As_2S_3$ were consistent with the literature. Moreover, a nonlinear refractive index four times that of $As_2S_3$ has been measured for a bulk $Ge_{10}As_{10}Se_{80}$ sample.

Nonlinear optical properties of As–S–Se chalcogenide glasses were measured [151] by the Z-scan technique at 1.6 μm, and values of $n_2$ up to 400 times that for silica were observed. Such large values of $n_2$ for glasses with small As/(S + Se) molar ratios are correlated with the presence of covalent, homopolar Se–Se bonds in the glass structure as identified by Raman spectroscopy, and cannot be attributed to any red shift in the absorption edge or to a resonant effect. Spalter et al. [152] have tested the ability of $Ge_{25}Se_{75}$ chalcogenide films for ultrafast AOS and investigated nonlinear pulse propagation in their photodarkened samples. Nearly transform limited, 270-fs pulses were coupled into the carefully cleaved guides. Pulse energies ranged up to 1.04 nJ in front of the input facet at a repetition rate of 13.5 MHz. The overall input-to-output transmission was 13%. Pulse spectra were measured with an optical spectrum analyzer.

The results for $Ge_{25}Se_{75}$ indicate that, at low energies, the output spectrum is identical to the input spectrum. Increasing the energy results in significant spectral broadening, as well as in an oscillating structure, as expected from SPM. By comparing their spectrum to numerical simulations, they inferred a peak nonlinear phase shift of $3.5\pi$, from which a value of $n_2 \approx 1.5 \times 10^{-14}\,\mathrm{cm^2\,W^{-1}}$ (58 times the value for silica) was obtained, which agreed well with independent Z-scan measurements. The nonlinear refractive index $n_2$ of binary $La_2S_3$–$Ga_2S_3$ and ternary MS–$La_2S_3$–$Ga_2S_3$ (MS=$Ag_2S$ and $Na_2S$) glasses were measured at 532 nm by the Z-scan method [133]. The $n_2$ of the glasses increased with increasing $La_2S_3$ content in the binary glasses, or decreased with the addition of $Ag_2S$ or $Na_2S$, respectively, in the ternary glasses. These results qualitatively agree with measurements by the THG method.

An optical power limiter utilizing the TPA phenomena acts as a protective element to restrict the irradiance of light pulses upon sensitive optical components, or as a regulator to smooth optical transients. Because the $La_2S_3$–$Ga_2S_3$ glasses possess large $\beta$ values at 532 nm, they could be promising materials for use as optical power-limiting materials. Figure 4.12 shows the result of the output transmittance versus the input intensity. The *open circles* represent the experimental data. The *broken line* is the hypothetical linear relation between $I_{\mathrm{out}}$ and $I_{\mathrm{in}}$ when TPA is not present. As seen in Fig. 4.12, the experimentally transmitted intensity was suppressed below the broken line due to the power-limiting effect of TPA. The *solid line* in Fig. 4.12 is the theoretical prediction using $\beta = 41.3\,\mathrm{cm\,GW^{-1}}$ [133].

Lenz et al. [142] have measured $n_2$ using Z-scan experiments at 1.5 μm for a number of chalcogenide compositions. Their results indicate that values of $n_2$ 500 times that of silica for $As_2S_3$ glasses are possible. Based on their results, and assuming a 1 pJ, 1 ps pulse and an effective mode area of $1\,\mu\mathrm{m}^2$, resulting in a peak intensity of $100\,\mathrm{MW\,cm^{-2}}$, would require a 5–8 cm long device for AOS applications. They assert that the above numbers indicate that small, integrated devices are possible and can be combined with existing silicon optical-bench technology.

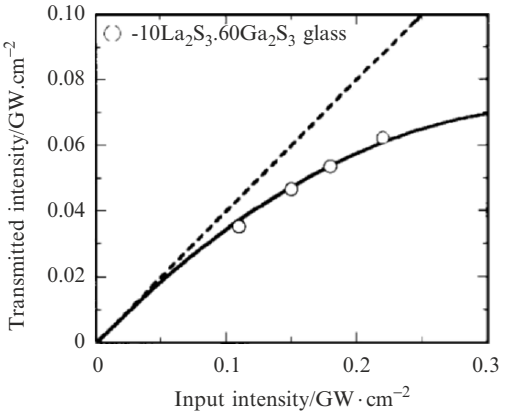


**Fig. 4.12.** Optical-limiting behavior for $40La_2S_3.60Ga_2S_3$ glass of thickness 0.1039 cm. The *open circles* represent the experimental data, the *solid line* is the theoretical curve and the *broken line* is what is expected in the absence of TPA (after [133])

Bulk chalcogenide glasses spanning a range of compositions have been measured for their nonlinear index of refraction $n_2$ at 1.3 and 1.55 μm using the Z-scan technique [153]. The figure of merit $T(T = \beta\lambda/n_2)$ was calculated for each glass and used as an indication of potential of these glasses for all-optical switching applications. SPM measurements for the $As_{40}S_{60}$ samples were performed using an additive pulse mode-locked color-center laser producing 500 fs pulses. The SPM was estimated at $\pi/2$ assuming a 500 W peak power in the waveguide, suggesting a value of $n_2 = 8 \pm 4 \times 10^{-15}\,\mathrm{cm^2\,W^{-1}}$, which is within the error of the Z-scan measurements.

Smolorz et al. [154] presented measurements of third-order optical nonlinearities in heavy-metal oxide (containing Ga, La, Bi, Pb) and sulfide glasses, using Z-scan and spectrally resolved two-beam coupling (SRTBC) techniques. The nonlinear index of refraction was found to increase with the sulfide content, and the nuclear contribution to the nonlinearity was found to be approximately constant at $(15 \pm 3)\%$. The largest nonresonant nonlinear index of refraction occurs in $35La_2S_3.65Ga_2S_3$, which is 30 times larger than the nonlinear index of refraction of fused silica.

Petkov et al. [155] have developed a formula for predicting the nonlinear refractive index $n_2$ for chalcogenide glasses from the dispersion of $n$, and which enables $n_2$ to be related to structural parameters. Using the various formulae and the measured values of $n$, $n_2$ values for these materials have been predicted. The results [156] indicate that glasses with compositions near $As_{42}S_{58}$ or $As_2S_3Tl_{0.13}$ may, after UV exposure, exhibit significantly (about 25%) larger values of $n_2$ than as-deposited $As_{40}S_{60}$.

Third- and second-order nonlinear optical properties of chalcogenide glasses in the (Ge–Se–S–As) system have been studied [157]. The Z-scan and

Mach-Zehnder interferometry measurements of the nonlinear refractive-index $n_2$ performed at 1,064 nm are in good agreement. The evaluation of the nonlinear refractive-index values has been correlated to the structure of the glasses, more particularly in the case of binary Ge–Se glasses when $n_2$ is a function of the length of selenium chains in the glass. Third-order nonlinearities as high as $24 \times 10^{-18}\,\mathrm{m^2\,W^{-1}}$ (850 times the nonlinearity of silica glass) have been obtained [157].

The third-order nonlinear susceptibility $\chi^{(3)}$ of homogeneous glasses has been studied by Nasu et al. [158]. $\chi^{(3)}$ roughly depends on the refractive index but is not uniquely determined. The largest $\chi^{(3)}$ among the homogeneous glasses is $1.96 \times 10^{-19}\,\mathrm{m^2\,V^{-2}}$ for As–S–Se glasses, being almost $10^3$ times larger than that of silica.

Boudebs [159] has investigated both experimentally and theoretically the optical nonlinearities of two chalcogenide glasses ($As_2Se_3$ and $As_2S_3$). Experimental data given by the spatially resolved Mach-Zehnder technique clearly indicate that the samples used in their experiments cannot be described with the usual third-order nonlinear theory. Consequently, they have constructed a model based on the existence of both a cubic and quintic nonlinear index. The evolution of the resulting nonlinear index coefficient as a function of the intensity is in good agreement with the experimental data. A fit allowed the determination of values of the nonlinear index coefficients. In particular, a negative quintic nonlinear index coefficient has been demonstrated.

Rangel Rojo et al. [160] report a study of the third-order optical nonlinearities of amorphous selenium using picosecond pulses at 1.064 µm, from a mode-locked Nd:YAG laser. The Z-scan technique was used to resolve the absorptive and refractive contributions to the nonlinear response of the material, including their sign. The chosen wavelength lies to the lower photon energy side of the absorption edge for the material studied; the interaction is therefore nonresonant and electronic in origin. They measured $n_2 = -0.06\,\mathrm{cm^2\,GW^{-1}}$ (3 orders of magnitude larger than for $As_2S_3$ and $Ge_{33}As_{12}Se_{55}$), with negligible TPA.

Kim et al. [161] deposited thin films of $As_2Se_3$ glass by thermal evaporation. These films were found to have significantly large third-order nonlinear coefficients at the wavelength of 633 nm. The self-focusing effect results in a reduced beam size, as confirmed by a laser beam profiler. This indicates that thin-film $As_2Se_3$ is a strong candidate for reducing the laser-beam spot size and thus can enhance the density of phase-change optical disks.

Wang et al. [156] report measurements of third-order optical nonlinearity of $90GeS_2$–$5GeS_3$–5CdS (in mole%) chalcogenide glass using the femtosecond time-resolved optical Kerr-gate technique at 820 nm. The third-order nonlinear susceptibility was estimated to be as large as $1.4 \times 10^{-20}\,\mathrm{m^2\,V^{-2}}$. The full width at half maximum of the Kerr signal was 150 fs, implying that the sample had a response faster than 120 fs. Its response was dominantly assigned to the ultra-fast distortion of the electron cloud.

Munzar et al. [162] have prepared amorphous $Ge_xS_{1-x}$ films by thermal evaporation. Using Miller's generalized rule ($\chi^{(3)}(\omega_4, \omega_3, \omega_2, \omega_1) = A\chi^{(1)}(\omega_4)\chi^{(1)}(\omega_3)\chi^{(1)}(\omega_2)\chi^{(1)}(\omega_1)$, where $\omega_4 = \omega_1 + \omega_2 + \omega_3$ and $A$ is a quantity that is assumed to be frequency independent and nearly the same for all materials [163]), values of the third-order nonlinear susceptibility were estimated. They report a value of $6.72 \times 10^{-21}\,\mathrm{m^2\,V^{-2}}$ for the composition $x = 0.36$.

Kobayashi et al. [164] have carried out THG measurements and optical Kerr-shutter operation using $As_2S_3$ glass. The value of $\chi^{(3)}$ for the $As_2S_3$ glass obtained by THG at the fundamental wavelength of 2.1 µm was $1.4 \times 10^{-19}\,\mathrm{m^2\,V^{-2}}$ (300 times that for silica glass). THG measurements also showed the spectra of $\chi^{(3)}$, which becomes larger at shorter wavelengths where the TH wave is absorbed, which indicates the three-photon resonance effect. Operation of an OKS using this glass has achieved a large value of $n_2 = 6.8 \times 10^{-18}\mathrm{m^2\,W^{-1}}$. The dependence of the output power on the gate light power has also been measured. The efficiency is affected by the gate-light absorption, the TPA, and the loss, which is thought to be due to excited carriers. The values of $n_2$ obtained from the Kerr-shutter operation agree with the values estimated from THG measurements.

Petkov et al. [165] have used a semi-classical model of the simple harmonic oscillator given by Boling et al. [166]. They derived a relation between the nonlinear refractive index $n_2$, the resonance frequency, $\omega_0$, and the product $NS$ ($N$ is the density of polarizable ions and $S$ is the oscillator strength). They showed that $\omega_0$ and $NS$ could be related to the parameter $n_\mathrm{d}$, and the Abbe number $\nu_\mathrm{d} = (n_\mathrm{d} - 1)/(n_\mathrm{f} - n_\mathrm{c})$, where $n_\mathrm{d}, n_\mathrm{f}$, and $n_\mathrm{c}$ are the linear refractive indices at the following standard wavelengths $\lambda_\mathrm{f} = 486.13\,\mathrm{nm}$ and $\lambda_\mathrm{d} = 587.56\,\mathrm{nm}$, and $\lambda_\mathrm{c} = 656.27\,\mathrm{nm}$. Boling et al. [166] derived two formulae for predicting $n_2$ to an accuracy of ∼20% or better using the values of the linear refractive index, $n$. However, it is difficult to find $\nu_\mathrm{d}$ and $n_\mathrm{d}$ values for IR-transmitting glasses, such as chalcogenide glasses, since they are relatively absorbing in the visible. A better fit is obtained by fitting the complete dispersion curves of these materials using the Wemple–Di Domenico model [167] and then Boling's formula. Using the parameters $E_0$, the oscillator energy, and $E_\mathrm{d}$, the dispersion energy, the following expression for $n_2$ could be used:

$$n_2 = \sqrt{3} g S (n^2 + 2)^{1.5} (n^2 - 1)^2 \hbar^2 e^2 / 12\, nm\, E_\mathrm{d} E_0^2, \tag{4.2}$$

where $n$ is the linear refractive index at long wavelengths, $S$ the oscillator strength, $\hbar$ is Planck's constant divided by $2\pi$, $g$ is the anharmonicity parameter, $e$ and $m$ are the electron charge and mass, respectively. Values of $n_2$ before and after exposure of thin As–S and As–S–Tl films to UV illumination were compared. It was found that $n_2$ increases with increasing As content in the films (unexposed and exposed), passing through a maximum for the composition $As_{42}S_{58}$ [165]. This correlates with the data obtained for $n_\mathrm{c}$. The nonlinear index for unexposed thin As–S–Tl films increases with increasing Tl content. $n_2$ also increases after illumination.

Ganeev et al. [168] presented the characterization of nonlinear optical parameters of chalcogenide films $\{As_2S_3, As_{20}S_{80}, 2As_2S_3/As_2Se_3, 3As_2S_3/As_2Se_3\}$. $2As_2S_3/As_2Se_3$ represents a multilayered film structure in which the thickness of the $As_2S_3$ layer is twice that of the $As_2Se_3$ layer. They measured nonlinear refractive indices and TPA coefficients using the Z-scan method at the wavelength of an Nd:YAG laser at 1,064 nm and its second harmonic at 532 nm.

Ganeev et al. [169] have investigated the properties of $As_2S_3$ and CdS nanoparticle aqueous solutions prepared by laser ablation. Nonlinear optical characteristics of these solutions were studied by the Z-scan technique using an Nd:YAG laser and its second harmonic ($\lambda = 532\,\text{nm}, t_\text{p} = 55\,\text{ps}$). Nonlinear refractive indices, nonlinear absorption coefficients, and third-order nonlinear susceptibilities of these solutions were measured. It was shown that nonlinear refractive indices of $As_2S_3$ and CdS nanoparticles decreased with a growth in laser intensity. High nonlinear optical susceptibilities of such structures were attributed to size-related effects. A value of $n_2$ for CdS solution was calculated to be $\sim 0.86 \times 10^{-19}\,\text{m}^2\,\text{W}^{-1}$ at an intensity of $3.9 \times 10^9\,\text{W}\,\text{cm}^{-2}$. For $As_2S_3$ solution, a value of $n_2 = 1.46 \times 10^{-18}\,\text{m}^2\,\text{W}^{-1}$ was calculated at an intensity of $2.94 \times 10^9\,\text{W}\,\text{cm}^{-2}$.

Tichy et al. [170] have used parameters of the Wemple–DiDomenico single-oscillator model for the linear refractive-index dispersion and Miller's rule and estimated the values of the third-order nonlinear optical susceptibility for several amorphous chalcogenide thin films. Estimated values are large (up to $\chi^{(3)} = 1.05 \times 10^{-19}\,\text{m}^2\,\text{V}^{-2}$ for $Ge_2As_{40}Se_{58}$ thin films) and are comparable with $\chi^{(3)}$ values observed for other chalcogenide systems [139].

Cherukulappurath et al. [171] have investigated nonlinear coefficients of chalcogenide glasses containing different amount of tellurium ($Ge_{10}As_{10}Se_{80-x}Te_x,\ x = 0, 10, 15, 20$). A comparison of the measurements of the nonlinear coefficient obtained by Z-scan with values given by other methods show that the agreement is good at the same incident intensity. It was seen that the nonlinear refraction coefficients measured were among the largest values reported for chalcogenide glasses ($n_2 \sim 20 \times 10^{-18}\,\text{m}^2\,\text{W}^{-1}$). Furthermore, they found that the addition of tellurium does not enhance significantly the nonlinear refraction coefficient.

Ogusu et al. [172] have prepared $Ag_x(As_{0.4}Se_{0.6})_{100-x}$ glasses and measured their nonlinear optical properties at 1.05 μm (see Fig. 4.13). The measured nonlinear refractive index of the glass with $x = 20$ at.% is approximately 2–4 times as large as that of $As_2Se_3$ glass and ranges from 2,000 to 27,000 times as large as that of fused silica, depending on the incident intensity.

Although the figure of merit $F (F = 2\lambda\beta/n_2)$ of the samples tested at 1.05 μm does not satisfy the standard criterion ($F < 1$), it can be expected to decrease at the telecommunication wavelengths of 1.3 and 1.55 μm. It should be noted that the design of an efficient switch requires that the nonlinear absorption per unit nonlinear refractive index be small. Specifically, for a Mach-Zehnder-based AOS, a FOM $< 1$ is necessary.

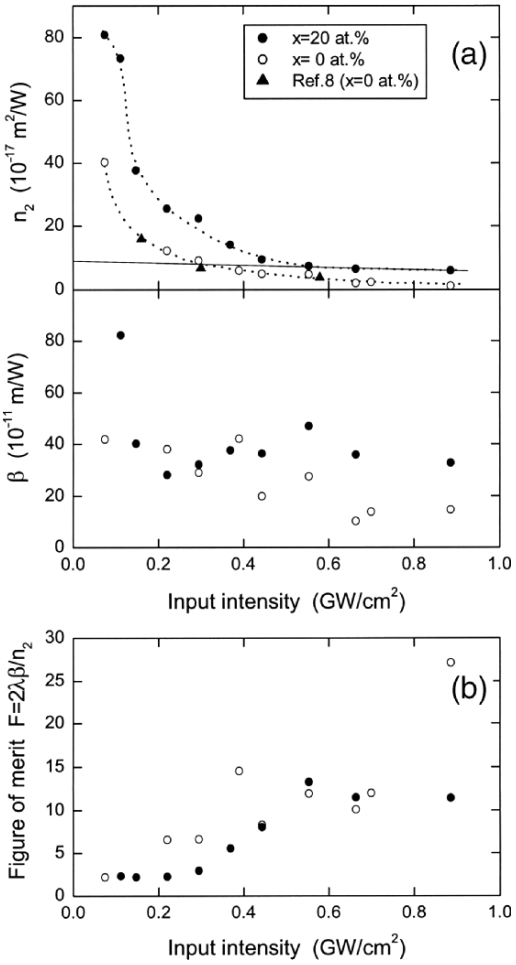


**Fig. 4.13.** (**a**) Dependence of nonlinear optical properties ($n_2$ and $\beta$) on input intensity for $Ag_x(As_{0.4}Se_{0.6})_{100-x}$ glasses and for Ag content $x = 0$ and $x = 20$ at.%. Experimental data from [173] are shown for comparison. (**b**) Calculated figure of merit $F = 2\lambda\beta/n_2$ as a function of the input intensity (after [172]). Ref. 8 in the inset to Fig. 4.13(a) corresponds to [173]

Troles et al. [174] have studied glass formation in a new chalcohalogenide system based on As, Sb, Bi, S, Pb, and I. Wide vitreous regions have been identified, both in the ternary $As_2S_3$–$Sb_2S_3$–$PbI_2$ system and in the quaternary $As_2S_3$–$Sb_2S_3$–$Bi_2S_3$–$PbI_2$ system. Because of the richness of these new glasses in highly polarizable elements, they are of interest for the implementation of highly nonlinear optical properties. To explore the potential of chalcogenide glasses for ultra-fast optical applications, the nonlinear refractive indices of different compositions were measured. Nonlinear measurements have been performed through a pump/probe experiment using a Mach-Zehnder

interferometer coupled to a CCD camera. The measured values are as high as $16 \times 10^{-18}\,\mathrm{m^2\,W^{-1}}$ for the nonlinear refractive index.

Kwak et al. [175] have extended the conventional Z-scan theory by employing an aberration-free approximation of a Gaussian beam through a nonlinear medium and derived a simple analytical formula for Z-scan transmittance, including the effects of both nonlinear absorption and nonlinear refraction, which could be applicable to samples with large nonlinear phase shifts. They verified their extended Z-scan model in a $As_2S_3$ thin film by measuring the Z-scan transmittance with both open and closed apertures. The nonlinear refractive index measured was $7.6 \times 10^{-15}\,\mathrm{cm^2\,W^{-1}}$ at sub-band gap 633 nm illumination.

Slusher et al. [176] have studied third-order Kerr nonlinearities in high-purity $As_2Se_3$ optical fibers for wavelengths near 1.55 μm. Kerr nonlinear coefficients were measured to be nearly 1,000 times higher than those for silica fibers. In pulsed mode, nonlinear phase shifts near $1.2\,\pi$ rad were measured in fibers only 85 cm long, with peak pulse powers near 3 W. However, there are nonlinear losses near 20% for nonlinear phase shifts near $\pi$.

A summary of the results of measurements of nonlinearity using various techniques is shown in Table 4.1, where $n_2$, $\beta$, and FOM values for different chalcogenide glasses are presented.

**Table 4.1.** Nonlinear optical constants of chalcogenide glasses (after [177])

| composition | $n_2$ ($\mathrm{cm^2\,W^{-1}}$) | $\beta$ ($\mathrm{cm\,W^{-1}}$) | $F = n_2/\beta\lambda$ | measurement method | band gap (nm) | reference |
|---|---|---|---|---|---|---|
| $As_2S_3$ | $2.7 \times 10^{-14}$ | – | – | DFWM | | [147,148] |
| $As_2S_3$ | $2.5 \times 10^{-14}$ | $2 \times 10^{-9}$ | | Z-scan | 604 | [150] |
| $As_2S_3$ | $0.9 \times 10^{-14}$ | – | – | THG | | [164] |
| $As_2S_3$ | $1.4 \times 10^{-13}$ | $0.26 \times 10^{-9}$ | 5 | Z-scan | | [146] |
| GeAsSe | $2 \times 10^{-13}$ | – | – | DFWM | 766 | [146] |
| GeAsSe | $2.2 \times 10^{-13}$ | $5.6 \times 10^{-8}$ | – | Z-scan | 766 | [146] |
| $GeSe_4$ | $8 \times 10^{-14}$ | $0.5 \times 10^{-9}$ | – | Z-scan | 746 | [150] |
| $Ge_{10}As_{10}Se_{80}$ | $10.2 \times 10^{-14}$ | $10 \times 10^{-9}$ | – | Z-scan | – | [150] |
| $Ge_{25}Se_{75}$ | $3.1 \times 10^{-14}$ | – | 2 | Z-scan | – | [142] |
| $Ge_{25}Se_{65}Te_{10}$ | $7.3 \times 10^{-14}$ | – | 1 | Z-scan | – | [142] |
| $Ge_{28}Se_{60}Sb_{12}$ | $11.3 \times 10^{-14}$ | – | 3 | – | – | [142] |
| $As_2Se_3$ | $12.2 \times 10^{-14}$ | – | 2 | – | – | [142] |
| $As_2S_3$ | $4 \times 10^{-15}$ at 1.55 μm | $0.03 \times 10^{-9}$ | – | Z-scan | – | [153] |
| $As_{24}S_{38}Se_{38}$ | $17.5 \times 10^{-15}$ | $<0.05\times10^{-9}$ | – | Z-scan | – | [153] |
| $Ge_{30}As_{11}Se_{49}Te_{10}$ | $11 \times 10^{-15}$ | $0.16 \times 10^{-9}$ | – | Z-scan | – | [153] |
| $Ge_{25}Ga_5S_{70}$ | – | $<0.02\times10^{-9}$ | – | Z-scan | – | [153] |
| $Ga_{28}La_{12}S_{60}$ | – | $<0.03\times10^{-9}$ | – | Z-scan | – | [153] |
| $Ag_2As_{39}S_{59}$ | $-102 \times 10^{-13}$ | $99.5 \times 10^{-9}$ | 0.96 | Z-scan | – | [145] |
| $As_2Se_3$ | $2.3 \times 10^{-13}$ | $0.14 \times 10^{-9}$ | 11 | SRTBC | 700 | [178] |

Reprinted from A. Zakery, S.R. Elliott, J. Non-Cryst. Solids, 330 (2003) 1, © (2003), with permission from Elsevier

## 4.2 Measurements of Nonlinear Absorption Coefficient $\beta$

Tanaka [179] has demonstrated that the two-photon absorption spectrum of $As_2S_3$ glass has an exponential form, which is qualitatively the same as that in $SiO_2$. These exponential spectra imply that the two-photon process is resonantly enhanced by gap states, which cause residual (weak) absorption tails. The reason why the chalcogenide glass exhibits greater nonlinear refractivity can be ascribed to the smaller band gap energy and detailed electronic structure may play a secondary role. Jha et al. [180] have presented data for the two-photon absorption coefficient for a family of chalcogenide glass systems. A value of $0.03\,\mathrm{cm\,W^{-1}}$ at 1,550 nm for the $As_{40}S_{60}$ composition was reported [153].

Asobe et al. [181] have studied the third-order nonlinear optical properties of $As_2S_3$-based glass fibers at a wavelength of around 1.55 µm. The two-photon absorption (TPA) coefficient was estimated to be $\alpha_2 = 6.2 \times 10^{-15}\,\mathrm{m\,W^{-1}}$ through a transmittance-change measurement.

Sanchez et al. [182] have investigated both theoretically and experimentally two- and three-photon absorption in $As_2Se_3$ chalcogenide glass. An approximate closed-form expression has been established for the effective TPA coefficient.

$$\beta_{\mathrm{eff}} = \beta - \frac{\gamma\alpha}{\beta} + \frac{\gamma(\alpha+\beta I_0)}{\beta^2 I_0 L_{\mathrm{eff}}}\log[1+\beta I_0 L_{\mathrm{eff}}], \tag{4.3}$$

where $\alpha$ is the linear absorption coefficient, $\beta$ is the two-photon absorption coefficient, $\gamma$ is the three-photon absorption coefficient, $L_{\mathrm{eff}} = \frac{1-\mathrm{e}^{-\alpha L}}{\alpha}$, and $I_0$ is the incident intensity.

This coefficient is not a simple linear function of the incident intensity. Indeed, it depends on the effective intensity in the presence of TPA, which is a nonlinear function of the incident intensity. Theoretical results have been found to be in good agreement with the experimental data. They have determined the values of two- and three-photon absorption coefficients. A value of $8.8\,\mathrm{cm\,GW^{-1}}$ was obtained for the TPA coefficient of $As_2Se_3$ glass.

Tanaka [179] has investigated high-purity glasses of $As_2S_3$ that were prepared by a conventional melt-quenching technique. One- and two-photon absorption spectra were evaluated for these samples. Two-photon absorption coefficients $\beta(h\nu)$ were determined using monochromatic light pulses with a width of ∼5 ns, which were obtained from an optical parametric oscillator pumped by the third harmonic of an Nd:YAG laser [131]. Special attention was paid so that the spectra were not affected by photodarkening in $As_2S_3$ [183, 184]. It was mentioned that a temperature rise caused by light pulses can be neglected under their experimental conditions.

From the spectrum of TPA, it seems that this spectrum appears at $\sim E_{\mathrm{g}}/2$, ($E_{\mathrm{g}} \sim 2.4\,\mathrm{eV}$), which is a common behavior in semiconductors. $\beta(h\nu)$ is approximately proportional to $\exp(h\nu/E_{\mathrm{B}})$, where $E_{\mathrm{B}} \approx 150\,\mathrm{meV}$. It should be mentioned here that, in the experimental region investigated

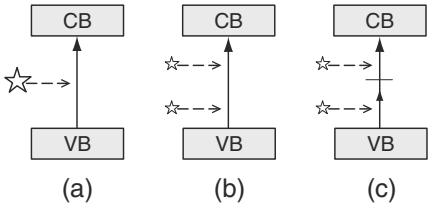


**Fig. 4.14.** Schematic illustrations of (**a**) one-photon absorption, (**b**) TPA, and (**c**) two-step absorption in insulators. CB and VB denote conduction band and valence band, respectively, and the horizontal bar in (**c**) represents a gap state (after [179])



($h\nu = 0.9$–$2.2\,\mathrm{eV}$), the results for $h\nu \geq 2\,\mathrm{eV}$ have been affected by the two-step absorption [131]. Optical transitions at around the absorption edge occur, in general, from the valence-band top to the conduction-band bottom (Fig. 4.14).

In $As_2S_3$, and also in $SiO_2$, this transition occurs from lone-pair p electrons of S or O atoms to antibonding states of As–S or Si–O (or hybridized 3p and 3d states of Si) [183,184,188]. The gap states, which appear as the one-photon absorption tails at $\sim E_g/2$, may act as resonant intermediate states in the two-photon absorption processes. It is asserted that chalcogenide glasses exhibit greater nonlinear refractivity than silica because of their smaller band-gap energies. Detailed electronic structures may play secondary roles. Sheik-Bahai et al. [186,189] have demonstrated for many crystals with $E_g - 1 \sim 10\,\mathrm{eV}$ that, when the spectral dependence is normalized, an intrinsic material dependence appears as a universal line, in which $n_0 n_2$ is proportional to $E_g^{-4}$. As shown in Fig. 4.15, this line is also applicable to typical chalcogenide glasses and $SiO_2$ as well [149, 174, 180, 185], despite the accuracy being worse than the case for crystals [186, 189], which may be partly due to experimental reliability and gap states existing in glassy materials. So it can be said that optical properties in chalcogenide and oxide glasses behave in a unified way. The relatively small band gap in chalcogenide glasses leads to appreciable absorption in the infrared, which may be unfavorable for optical applications. Nevertheless the large chalcogen mass means that the long-$\lambda$ cutoff of the transmission window is bigger than oxides. Figure 4.15 also shows that the Moss rule [186] $n^4 E_g = 77$ approximately holds in these glasses.

Ganeev et al. [168] have used the normalized transmittance for the open-aperture Z-scan to calculate $\beta$ values of chalcogenide glasses. The measured $\beta$ values of chalcogenide films, $As_{20}S_{80}$($\beta = 3 \times 10^{-6}\,\mathrm{cm\,W^{-1}}$, $\lambda = 532\,\mathrm{nm}$, $I_0 = 4 \times 10^8\,\mathrm{W\,cm^{-2}}$) and $3As_2S_3/As_2Se_3$($\beta = 10^{-7}\,\mathrm{cm\,W^{-1}}$, $\lambda = 1,064\,\mathrm{nm}$, $I_0 = 3 \times 10^8\,\mathrm{W\,cm^{-2}}$) show that some thin chalcogenide films possess large nonlinear absorption coefficients. The experimental results of optical limiting, due to TPA, show a 25-fold optical limiting in the case of $As_2S_3$.

The open-aperture Z-scan scheme was used for the investigation of nonlinear absorption of aqueous colloidal solutions of $As_2S_3$ and CdS nanoparticles

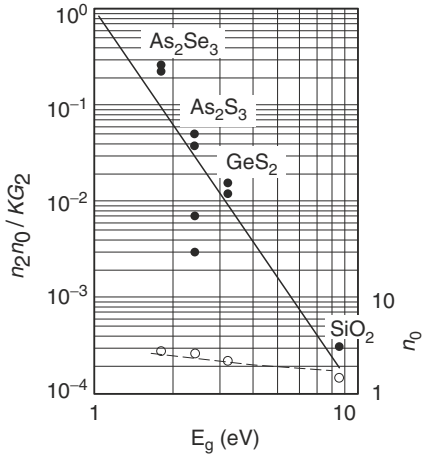


**Fig. 4.15.** Relation between the nonlinear refractive index $n_2(\bullet)$ and the band gap energy $E_g$ in some chalcogenide glasses and $SiO_2$ [149, 174, 180, 185], where $n_0$ is the linear refractive index, and a constant $K$ and a spectral factor $G_2$ are defined following Sheik-Bahae et al. [186]. The *solid line* is a universal line ($n_0 n_2 = KG(\hbar\omega/E_g){E_g}^{-4}$) employed in [186], where $K$ is a material-independent constant and $G(\hbar\omega/E_g)$ represents a universal spectral dependence. The Moss rule [187], $n_0^4 E_g \approx 77$ is also shown by a *dashed line* (after [179])

Reprinted from Keiji Tanaka, J. Non-Cryst. Solids 338–340 (2004) 534, © (2004), with permission from Elsevier

**Table 4.2.** Nonlinear optical properties at 1.06 μm for different tellurium-containing chalcogenide glasses (after [190])

| glass composition | $\langle\beta_{\text{eff}}\rangle$ (cm GW$^{-1}$) | $\beta$ (cm GW$^{-1}$) | $\gamma$ (cm$^3$ GW$^{-2}$) |
|---|---|---|---|
| $Ge_{10}As_{10}Se_{80}$ | 1.8 | 1.2 | 0.25 |
| $Ge_{10}As_{10}Se_{70}Te_{10}$ | 5.0 | 7.1 | −1.7 |
| $Ge_{10}As_{10}Se_{65}Te_{15}$ | 6.3 | 7.5 | −1.2 |
| $Ge_{10}As_{10}Se_{60}Te_{20}$ | 9.6 | 18.7 | −12 |

[169] (see Sect. 4.2). Chalcogenide CdS and $As_2S_3$ thin films were used for comparison with CdS and $As_2S_3$ nanoparticle solutions. Ganeev et al. obtained $\beta$ values of $6 \times 10^{-10}$ and $2.9 \times 10^{-10}$ cm W$^{-1}$ for $As_2S_3$ and CdS solutions, respectively, at 532 nm.

Boudebs et al. [190] have used the Z-scan technique to measure nonlinear optical constants of different chalcogenide systems (Table 4.2). The evolution of these nonlinear quantities is also given. A quasi-linear dependence of $\langle\beta_{\text{eff}}\rangle$ with $h\nu/E_g$ is noted due to an opposite variation of $\beta$, the two-photon absorption coefficient and the third-order nonlinear coefficient $\gamma$. The same kind of linear behavior of $\langle\beta_{\text{eff}}\rangle$ has been observed in other selenium-based chalcogenide glasses for photon energies below half the band gap [191]. This could explain the

decrease of $\langle\beta_{\text{eff}}\rangle$ with incident intensity and appears mathematically by the presence of a negative coefficient in the third-order coefficient $\gamma$ to compensate this loss of absorption. For optical-limiting applications, a high tellurium concentration is required. Compared to $As_2Se_3$ chalcogenide glasses ($\langle\beta_{\text{eff}}\rangle = 5\,\text{cm}\,\text{GW}^{-1}$) [192], the mean value of the nonlinear absorption coefficient $\langle\beta_{\text{eff}}\rangle$ obtained for $Ge_{10}As_{10}Se_{60}Te_{20}$ is approximately two times larger. A closed-form relation has been derived [192] for the effective TPA coefficient, improving the simple linear relation that has been used up to now.

Ogusu et al. [172] have used the Z-scan technique to measure the two-photon absorption coefficient $\beta$ of Ag-doped As–Se glasses ($Ag_x(As_{0.4}Se_{0.6})_{100-x}$). They have found that, for both $x = 0$ and 20%, the sign of $\beta$ is positive. $\beta$ decreases with increasing incident optical intensity for $x = 0$ at.%, as observed for $As_2S_3$ glass [150]. However, for $x = 20$ at.% the $\beta$ value does not depend on the input intensity, except for weak intensities ($I < 0.15\,\text{GW}\,\text{cm}^{-2}$).

Measurements of $n_2$, the nonlinear refractive index, and $\alpha_2$, the TPA coefficient, were carried out [153] at 1.3 and 1.55 µm using a passively mode-locked, 10 Hz doubled Nd:YAG laser pumping a LBO optical parametric generator-amplifier (OPG-OPA) assembly. The resulting pulse width was 20 ps and had peak intensities up to $50\,\text{GW}\,\text{cm}^{-2}$. The pulses were not transform-limited; however, it was asserted that this fact did not influence the measurements due to negligible dispersion of the material. The measured $\beta$ values for the range of compositions studied were $<0.01\,\text{cm}\,\text{GW}^{-1}$ (the lowest) and $0.17\,\text{cm}\,\text{GW}^{-1}$ (the highest) for $As_{40}S_{40}Se_{20}$ and $As_{30}S_{11}Se_{49}Te_{10}$, respectively.

Nonlinear measurements have been performed through a pump/probe experiment using a Mach-Zehnder interferometer coupled to a CCD camera [174]. Troles et al. have obtained values of the TPA coefficient in a new chalcohalogenide system based on As, Sb, Bi, S, Pb, and I (see Sect. 4.2). The lowest value of $\beta = 0.9 \pm 0.23\,\text{cm}\,\text{GW}^{-1}$ was obtained for $(PbI_2)_{20}(As_2S_3)_{50}(Sb_2S_3)_{30}$, while the highest value obtained was $\beta = 5.7 \pm 1.4\,\text{cm}\,\text{GW}^{-1}$ for the $(PbI_2)_{30}(As_2S_3)_{30}(Sb_2S_3)_{30}(Bi_2S_3)_{10}$ composition.

Kwak et al. [175] have extended the conventional Z-scan theory by employing an aberration-free approximation of a Gaussian beam through a nonlinear medium and derived a simple analytical formula for Z-scan transmittance, including the effects of both nonlinear absorption and nonlinear refraction, which could be applicable to the sample with large nonlinear phase shifts. The nonlinear absorption coefficient $\beta$ measured with sub-band gap 633 nm illumination was $1.6\,\text{cm}\,\text{W}^{-1}$ for an $As_2S_3$ thin film.

## 4.3 Determination of Three Photon-Absorption and Multiphoton Absorption

Sanchez et al. [182] have obtained the three-photon absorption coefficient in $As_2Se_3$ chalcogenide glass at $\lambda = 1.064\,\mu\text{m}$. Based on a fit of experimental data to the theoretical model for the variation of the effective TPA coefficient

versus the incident intensity (see Sect. 4.2), a value of $-2.8\,\mathrm{cm^3\,GW^{-2}}$ was obtained for the three-photon absorption coefficient. Observation of four- and five photon absorption in chalcogenide glasses at the telecommunication wavelengths ($\lambda = 1.3$ and $1.55\,\mu\mathrm{m}$) is reported by Bindra et al. [149]. They have reported dominant four/five photon absorption in $TeO_2$ or $GeS_2$ glasses and three-photon absorption in $As_2S_3$ chalcogenide glasses. They assert that the large nonlinear refractive indices, coupled with the absence of photodarkening, make these materials attractive for optical-switching and the multiphoton absorption should not affect the optical-switching performance.

## 4.4 Second-Harmonic Generation, Phase Conjugation, Self-Phase Modulation, etc.

Haro-Poniatowski et al. [193] have presented experimental results of phase conjugation (PC) via DFWM in amorphous Se, $Ge_{10}Se_{90}$, and $Te_7Se_{93}$ chalcogenide thin films. Simultaneously to the PC signal, a laser-induced grating was formed. The obtained gratings were subsequently analyzed in a scanning force microscope. It was found that the relief of the grating, as well as the pc efficiency, exhibited a maximum for a particular irradiation pump intensity. These maxima occurred at different pump intensities, contrary to what would be expected. Moreover, they found that the relief at the surface was not solely responsible for the observed phenomena; recording effects in the bulk of the material could also occur, contributing to the diffraction efficiency of the grating. Various methods have been developed to characterize the third-order response of nonlinear materials. However, these methods require several laser shots to produce one measured value of the nonlinear refractive index $n_2$. Monteil et al. [194] reported a powerful technique to measure the third-order susceptibility. The technique is based on a pump/probe experiment using a Mach-Zehnder interferometer combined with a CCD camera where only one laser shot in the material was needed to obtain a great number of measurements. A new numerical treatment permits both the characterization of poor optical quality samples and an increase of the precision of the measurements. Chalcogenide glasses ($As_2S_3$, $GeSe_6$, $GeSe_4$, and $Ge_{11}As_{11}Se_{78}$) were characterized using thermal poling and optically assisted poling [195] to induce a second-order nonlinear susceptibility $\chi^{(2)}$ in $As_2S_3$ chalcogenide glasses. $As_2S_3$ films of $\approx 4\,\mu\mathrm{m}$ thickness were deposited on transparent ITO electrodes that were previously deposited onto BK7 borosilicate plates. Thermal poling was performed by heating the sample to $\approx 70^\circ\mathrm{C}$ for 1 hr and by simultaneously applying 150 V across the electrodes. The optically assisted poling was achieved using an argon laser (both 488 and 514 nm) and the beam was defocused onto the sample. The total fluence and intensity were equal to $5\,\mathrm{J\,mm^{-2}}$ and $2.5\,\mathrm{mW\,mm^{-2}}$, respectively. The optically assisted poling was carried out by applying 100 V for half an hour across the electrodes as the sample was irradiated. After the exposure, a change in the color of the poled

region was observed due to the photosensitivity of the $As_2S_3$ to exposure to near band-gap illumination. A Maker-fringe experiment with a pump wavelength of $\lambda = 1,550\,\text{nm}$ was used to measure the magnitude of the induced $\chi^{(2)}$. The peak power of the second-harmonic wave generated in the sample as a function of the incident angle of the pump laser beam was recorded. The repetition rate of the pump laser was 10 Hz and the average pulse duration was ≈10 ns. Values of $\chi_{333}$ of $As_2S_3$ samples were found to be between 0.6 and $26\,\text{pm}\,\text{V}^{-1}$. The second-order nonlinearity, $\chi^{(2)}$, is observable in strongly electrically polarized $TeO_2$-based bulk glasses [159]. A 4 kV dc voltage was applied to the glass plate at 200°C in an electric furnace in air, and then the plate was cooled to room temperature. The SHG was measured using the Maker fringe method. Nasu et al. [159] have also observed that the SHG in $SiO_2$ glasses is dependent on the OH concentration and increases with an increase in OH concentration. It is asserted that the OH in $SiO_2$ glasses induces an asymmetrical electron distribution around Si. Likewise, the network-forming glass $TeO_2$ includes a lone pair of Te electrons in the $TeO_4$ trigonal bipyramid structure [196]. The first evaluation of $n_2$ in an $As_2S_3$ chalcogenide glass fiber has been reported [135] from spectral broadening due to SPM. A 1.45 m long single-mode fiber with a $As_{38}S_{62}$ core and $As_{37.4}S_{62.6}$ cladding was prepared. The effective core area was $24.6\,\mu\text{m}^2$. A mode-locked Nd:YAG laser operating at a wavelength of 1.319 μm was used as the light source. The temporal-pulse profile was monitored with a pin-photodiode and a sampling oscilloscope. The pulse width and repetition rate were 178 ps and 100 MHz, respectively. Spectral broadening of the light output was analyzed using an optical spectrometer. The relations given in Sect. 3.7 were used to calculate the $n_2$ value. The obtained value of $n_2$ was $1.7 \times 10^{-14}\,\text{cm}^2\,\text{W}^{-1}$, which was in good agreement with the $\chi^{(3)}$ value from the THG experiment.

Qiu et al. [197] have optically encoded SHG in $Ge_{20}As_{20}S_{60}$ glass by use of nanosecond laser pulses at wavelengths of 1.064 μm and 532 nm. Their experiments showed that the magnitude of SHG in this glass is $10^4$ times larger than in a telluride glass with a composition of $15Nb_2O_5.85TeO_2$. Figure 4.16 shows a tensor curve for the x component of the SHG signal (a nonlinear coupling between the two orthogonally polarized components of an optical wave changes the refractive index by different amounts for the two components, and hence different nonlinear phases are developed for different components). The intensity of SHG was strongest when the polarization of the probe light (or the readout beam) was parallel to the polarization direction of the laser beams for optical poling.

Moreover, they observed (Fig. 4.17) that there was no apparent decay of photoinduced SHG in the $Ge_{20}As_{20}S_{60}$ glass at room temperature, while glasses based on $Bi_2O_3$ and $TeO_2$ showed a rapid decay in the intensity of photoinduced SHG. Chalcogenide glasses exhibit excellent photoinduced SHG properties in both conversion efficiency and stability. They assert that their results demonstrated the possibility of increasing the SHG conversion efficiency and stability by selecting only the proper glass composition.

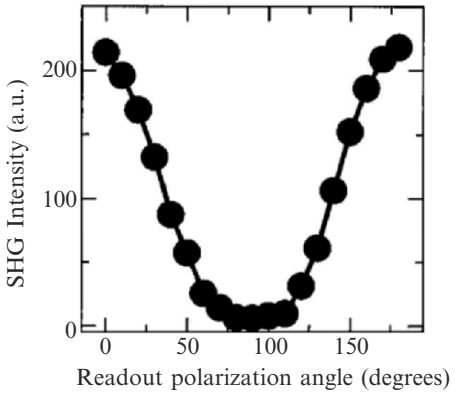


**Fig. 4.16.** $x$ component of SHG versus readout polarization for $Ge_{20}As_{20}S_{60}$ glass (after [197])

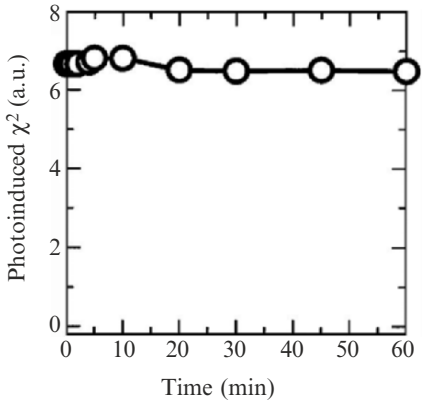


**Fig. 4.17.** Decay of the photoinduced $\chi^{(2)}$ for $Ge_{20}As_{20}S_{60}$ glass under irradiation of the $\omega$ preparation light. The intensity and the repetition rate of the $\omega$ preparation light were kept at $1\,\mathrm{GW\,cm^{-2}}$ and 20 Hz, respectively (after [197])

The restoration of an image has been demonstrated using PC in amorphous $Ge_xSe_{100-x}$ thin films [198]. An unconventional DFWM process was used where no external counter propagating pump beam was required. The object to be conjugated was the word "Saasil," which means light in Mayan language. It was imprinted in a microscope slide with auto-adhesive letters. The aberrating element was a petri dish placed before the $Ge_xSe_{100-x}$ sample. Comparison of the original object (Fig. 4.18a) and the phase-conjugate image after passing through the aberrator (Fig. 4.18b) shows that the lettering is legible in the latter image. The image reflected on the conventional mirror is shown in Fig. 4.18c. As can be seen, the original object is completely unrecognizable. These results clearly show that $Ge_xSe_{100-x}$ thin films act as PC mirrors with the corresponding aberration correction properties. However,

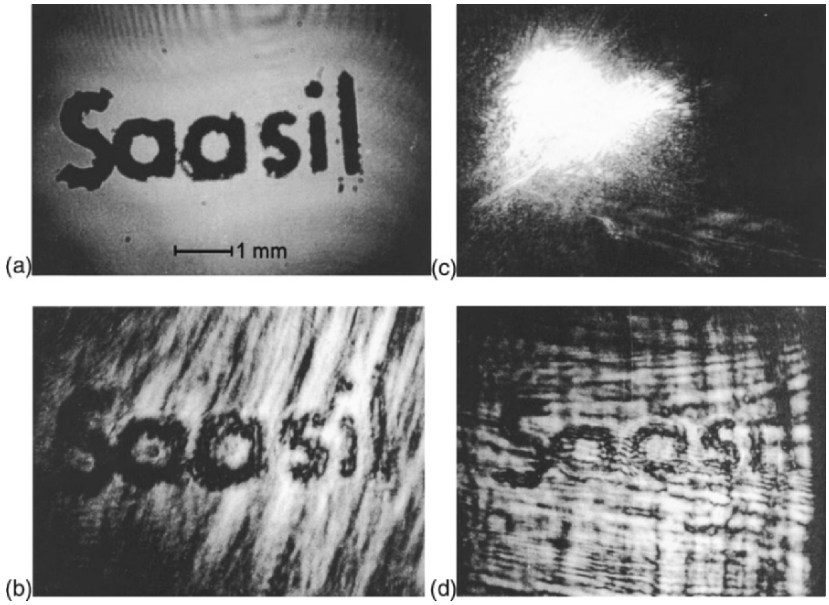


**Fig. 4.18.** (**a**) Original probe beam image, (**b**) phase-conjugate corrected image, (**c**) distorted image obtained from conventional reflection, and (**d**) phase-contrast image with crossed petri dishes as aberration element. Different $Ge_xSe_{100-x}$ chalcogenide films with $x$ between 1.5 and 20 were used as recording media (after [198])



the corrected image suffers from imperfections, in particular fuzzy lines stemming from the aberrator. These lines are present in the glass of petri dishes. So one of them was rotated by 90° to confirm that this was the origin of the pattern, as shown in Fig. 4.18d, where a set of perpendicular fuzzy lines is observed in the background. Fernandez-Guasti et al. [198] explain the presence of these lines as follows: Zones of the dishes with severe deformation deviate part of the probe beam into regions of the nonlinear film where the pump is not present or even move them away from the film. These high-spectral frequency components are obviously no longer conjugated and cause imperfections in the quality of image reconstruction.

Phase-conjugate signals with efficiencies ($I_{\mathrm{pc}}/I_{\mathrm{probe}}$) between 0.17% and 0.74% were obtained for films with selenium contents $x$ between 20 and 1.5. It was proposed that the counter-propagating pump was generated in the vicinity of the front surface air-film interface, which was consistent with the experimental results.

Electric poling using high electric fields ($1\,\mathrm{kV}\,\mu\mathrm{m}^{-1}$) at relatively high temperatures (e.g., 270°C) can be used to induce second-order nonlinearity and second-harmonic generation (SHG) in Ga–La–S and Pr-doped Ga–La–S glasses [199,200]. It has been shown that microcrystals are responsible for the

frequency-doubling process [199]. In the absence of microcrystals, there is no SHG signal. For low densities of micro-crystals, there is a preferential sample direction for the SHG interaction and the signal is polarization dependent. Second-harmonic generation conversion efficiencies as high as 0.02% have been achieved for GaLaS.

Kityk et al. [201] have studied photoinduced nonlinear optical phenomena in amorphous $As_2Te_3$–$CaCl_2$–$PbCl_2$ glasses using experimental (pump-probe technique) and theoretical (quantum-chemical and molecular-dynamics) methods. In particular, TPA and second-harmonic generation (SHG) were measured in the IR region from 5.5–21 μm. The measured intensity dependence of the photoinduced SHG at different laser powers and temperatures at a wavelength of 5.3 μm are presented in Fig. 4.19. It was found that, with increasing power of the pump CO-laser pulses, the SHG maximal output signal increases and achieves its maximum at photon fluxes within the range of 0.86–1.38 GW cm$^{-2}$ densities per pulse. The maximal output SHG signal

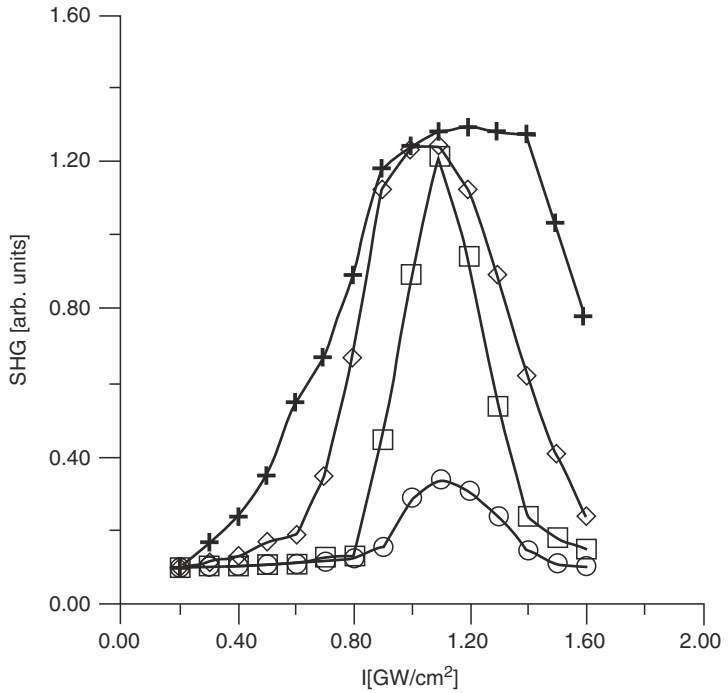


**Fig. 4.19.** Dependence of the photoinduced SHG at $\lambda = 5.3\,\mu m$, in arbitrary units, versus photoinducing CO laser power and temperature for $As_2Te_3$–$CaCl_2$–$PbCl_2$ glasses: (*plus*) 4.2 K, (*diamond*) 8.6 K, (*square*) 16.3 K, (*circle*) 22.4 K. All the measurements correspond to the time delay between the probe and the pump light of about 25 ps (after [201])

is observed for collinear polarizations of probe and pump light beams and incident angles lying within 3°–6°. They have also found that the maximal intensity of the output SHG is achieved for time delays of about 27 ps and at low temperatures below 20 K. By varying the time delay between the pump and probe beams, two TPA maxima (see Fig. 4.20) were observed. The first one occurs at a delay time range within 18–41 ps and continuously increases up to 10–48 ps with decreasing temperature down to liquid helium temperature. The second time-dependent TPA maximum is temperature (4.2–17 K) independent (within 62–99 ps).

The spectral dependence of the TPA signal was carried out in the spectral range 10–40 μm at different temperatures (see Fig. 4.21). One can see that the maximal TPA signal is achieved within the spectral range 21–24.5 μm at 22.4 K and its range increases up to 18–33 μm for $T = 4.2$ K. Kytik et al. [201] conclude that a good correlation between the TPA and SHG temperature dependencies exists and the key role of the vibrations and electron-vibration anharmonicity within the 8–22 μm range was revealed. The absolute SHG values were more than an order of magnitude less compared with ZnS crystals

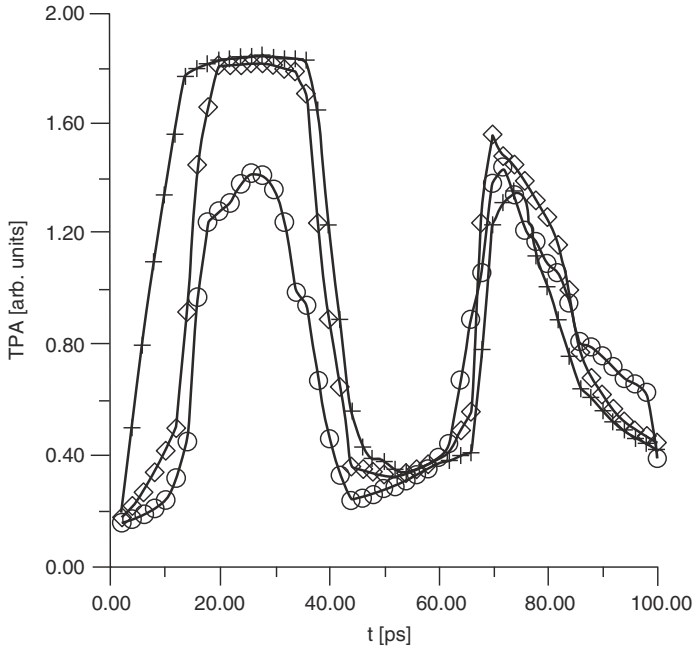


**Fig. 4.20.** Dependence of the photoinduced TPA at $\lambda = 5.3$ μm, in arbitrary units, versus pump-probe time delay at different temperatures for $As_2Te_3$–$CaCl_2$–$PbCl_2$ glasses: (*plus*) 4.2 K, (*diamond*) 8.6 K, (*square*) 16.3 K, and (*circle*) 22.4 K (after [201])

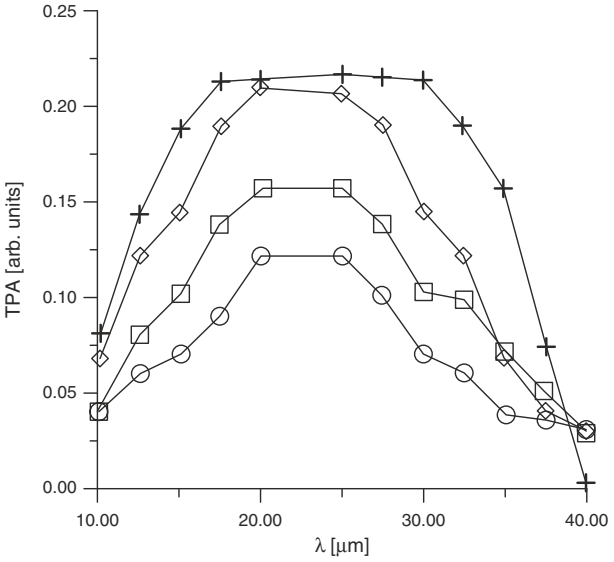


**Fig. 4.21.** Spectral dependence of the TPA, in arbitrary units, at different temperatures for $As_2Te_3$–$CaCl_2$–$PbCl_2$ glasses: (*plus*) 4.2 K, (*diamond*) 8.6 K, (*square*) 16.3 K, and (*circle*) 22.4 K (after [201])



in the case of the $\chi_{222}(\lambda = 10.6\,\mu\text{m})$ tensor components. They assert that their molecular-dynamics geometry optimization and quantum-chemical calculations unambiguously show that the photoinduced noncentrosymmetry is caused solely by the electron-quasiphonon anharmonic interaction within As–Te tetrahedra ($AsTe_4$). The dominant role of the As–Te cluster contributing to nonlinear optical susceptibilities was revealed theoretically, as well as by Fourier spectroscopy and ellipsometry measurements.

Liu et al. [202] have observed second-harmonic generation in $Ge_{20}As_{25}S_{55}$ chalcogenide glass irradiated by an electron beam. The second-harmonic intensity increased with increasing electron-beam current and accelerating voltage. They state that second-harmonic generation in $Ge_{20}As_{25}S_{55}$ glass was caused by the space-charge electrostatic field that was generated by irradiation with an electron beam. They obtained a second-order nonlinearity $\chi^{(2)}$ as great as $0.8\,\text{pm}\,\text{V}^{-1}$.

Figure 4.22 shows the Maker fringe pattern of $Ge_{20}As_{25}S_{55}$ glass, which shows a good symmetry. The SH intensity will have its peak value when the angle of incidence is $\pm 50^\circ - 60^\circ$, which is near the Brewster angle. The mechanism of SHG in $Ge_{20}As_{25}S_{55}$ glass was also studied by the method of thermally stimulated depolarization current (TSDC) [203]. The results of the measurements indicated that the glass was poled in thin layers at its surface (several micrometers) and that the nonlinearity was stable.

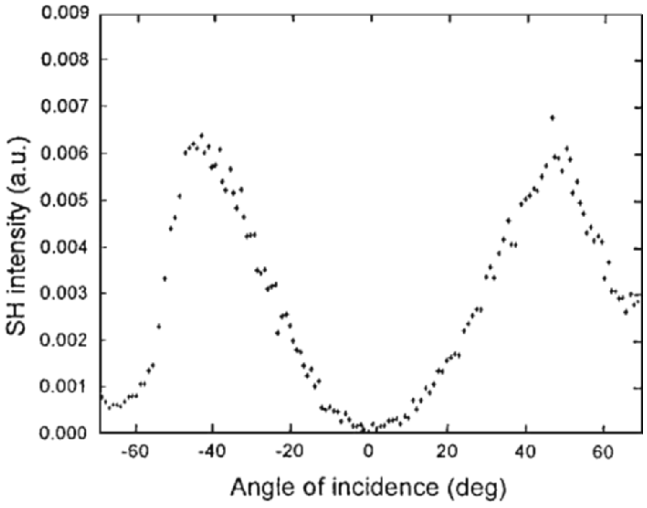


**Fig. 4.22.** Maker fringe pattern of $Ge_{20}As_{25}S_{55}$ glass. The accelerating voltage was 30 kV, beam current was 40 nA, and the irradiation time was 5 min (after [202])

## 4.5 Comparison of Chalcogenide Nonlinearities with Silica

Chalcogenide glasses based on S, Se, and Te have their IR cut-off in the 10–20 µm range but often suffer from small band-gap values, resulting in a poor transparency in the visible, which can be a real handicap to pump some rare earth elements. Most of these vitreous materials, for example $As_2S_3$, have a polymeric molecular character and do not easily accept doping cations in their framework [204]. However, some exceptional compositions based on $GeS_2.Ga_2S_3.Na_2S.La_2S_3$ combinations can be rare-earth doped without suffering too much from devitrification. Figure 4.23 illustrates the approximate position of the IR cut-off for several glasses, such as fluorides, chalcogenides, and tellurium halides (TeX) glasses.

Boling, Glass and Owyoung [166] (BGO) showed the following relation:

$$\chi^{(3)} \approx g[\chi^{(1)}]^2 f^3 / N_{\text{eff}} \hbar \omega_0 \tag{4.4}$$

can be generalized to a wide variety of solids, including some oxide glasses, where $\chi^{(1)}$ is the linear susceptibility, and $f$ is a local-field correction factor, which is usually taken to be the Lorentz local field:

$$f = (n^2 + 2)/3. \tag{4.5}$$

$N_{\text{eff}}$ is the oscillator strength or the number of effective oscillators and $\omega_0$ is the mean absorption frequency. The factor $g$ is the anharmonicity parameter and is a dimensionless quantity involving the properties of the ground state as well

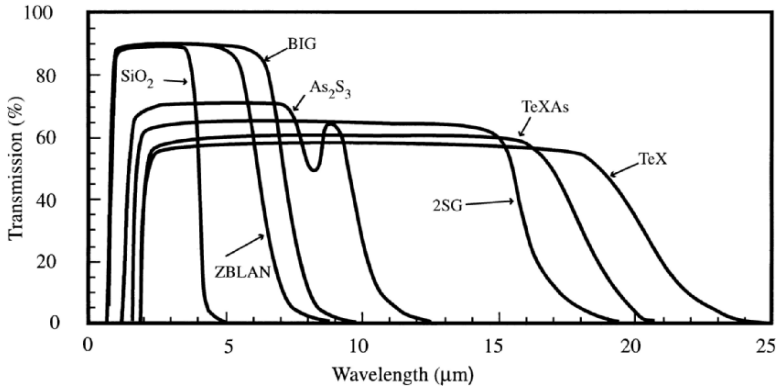


**Fig. 4.23.** Infrared transmission spectra of several glasses compared to silica. The two glasses ZBLAN and BIG are multicomponent fluoride glasses based on $ZrF_2$, and $BaF_2$ for the former and $BaF_2$, $InF_3$, $GaF_3$ for the latter. The glass 2SG is a selenium-based material containing Ga. The TeX glass is based on the combination of Te, Se, and $I_2$, while the TeX(As) is a similar glass with the addition of As (after [204])



as the excited states of the system. In the case that one polarizable constituent of the medium dominates, Boling et al. wrote the nonlinear refractive index in the low-frequency limit ($\omega \ll \omega_0$) as

$$n_2 = (gS)(n^2+2)^2(n^2-1)^2/48\pi n\hbar\omega_0(NS), \tag{4.6}$$

where $S$ is the effective oscillator strength and $N$ is the number of oscillators. The quantity $g$ is related to the anharmonic coefficient (the anharmonic force constant) $\mu$ as

$$g = \mu S\hbar/m{\omega_0}^2. \tag{4.7}$$

The refractive index can be written as [205]:

$$[(n^2-1)/4\pi][3/(n^2+2)] = (NS)\mathrm{e}^2/m({\omega_0}^2-\omega^2). \tag{4.8}$$

A large group of optical glasses were examined on this basis and a value for $gS$ of about 3 was found to give good agreement for all materials examined. Boling et al. [166] also proposed an expression connecting the nonlinear refractive index $n_2$ with optical parameters, such as $n_\mathrm{d}$ and the Abbe number $v_\mathrm{d}$, as follows:

$$n_2(10^{-13}\mathrm{esu}) = 68({n_\mathrm{d}}^2+2)^2(n_\mathrm{d}-1)/v_\mathrm{d}[1.52+\{({n_\mathrm{d}}^2+2)(n_\mathrm{d}+1)v_\mathrm{d}\}/6n_\mathrm{d}]^{1/2}. \tag{4.9}$$

The semi-empirical expressions for $n_2$ derived by Boling et al. [166] have been very useful as a guide for developing materials with relatively high values of

**Table 4.3.** Linear and nonlinear optical properties of typical glasses [205]

| optical glass | measurement technique ($\lambda, \mu$m) | refractive index $n$ ($\lambda, \mu$m) | $n_2$ ($10^{-20}$m$^2$ W$^{-1}$) | nonlinear susceptibility $\left\|\chi^{(3)}\right\|$ ($10^{-21}$m$^2$ V$^{-2}$) |
|---|---|---|---|---|
| $SiO_2$ | – | (1.456 (d)) | 2.73 | 0.392 |
| $As_2S_3$ | DFWM (1.06) | 2.48 (1.06) | – | 24.4 |
| $As_2S_3$ | Z (1.06) | 2.4 (1.06) | 1,400 | – |
| As–S–Se | THG (2) | 2.55 (2) | – | 197.4 |
| As–S–Se | – | 2.47 (10.6) | 175 (1.55) | – |
| Ge–As–Se–Te | – | 2.50 (10.6) | 140 (1.3) | – |
| $Ge_{10}As_{10}Se_{80}$ | Z (1.06) | – | 1,020 | – |
| $GeSe_4$ | Z (1.06) | – | 800 | – |
| $As_2Se_3$ | SRTBC (1.55) | 2.81 (1.55) | 2,300 | – |
| $Ga_{28}La_{12}S_{60}$ | Z (1.55) | 2.50 (10.6) | b | – |

d, d line; Z, Z-scan; DFWM, degenerate four-wave mixing; THG, third-harmonic generation; SRTBC, spectrally resolved two-beam coupling; b, not able to resolve the measurements; numbers in parentheses for $n_2$, measurement wavelength. Data for $As_2Se_3$ is from [178] and for $Ga_{28}La_{12}S_{60}$ is from [153]

$n_2$. The conclusion that can be drawn from these expressions is that high-index and high-dispersion materials should possess large nonlinearities. The expression with $gS = 3$ has been quite successful in predicting the nonlinear refractive indices for materials with small nonlinearities [166, 206]. Table 4.3 shows nonlinear indices and nonlinear susceptibilities of various optical glasses.

Systematic studies of the relationship of optical nonlinearities and glass compositions have also been conducted in many glass systems. In oxide glasses, for example, high linear and nonlinear refractive indices are found in systems containing large, polarizable cations such as Ti, Bi, Tl, Pb, Nb, or Te. The relationship between the linear and the nonlinear refractive indices is cation dependent. For instance, ions with an empty or unfilled d shell, such as Ti and Nb, contribute most strongly to the linear and nonlinear polarizabilities. In glasses that contain $TiO_2$ and $Nb_2O_3$, the linear refractive index is mainly determined by the total concentration of Ti and Nb, whereas the nonlinear index coefficient is much larger for glasses that contain $TiO_2$ than for those containing $Nb_2O_3$ [207]. The nonresonant type of optical nonlinearity is derived from the hyperpolarizabilities of the glass constituents, such as the heavy-metal cations ($Pb^{2+}$), transition-metal ions ($Ti^{4+}$ or $Ti^{3+}$) and $Te^{4+}$. The high nonlinearity of $Pb^{2+}$-containing glasses is attributed to the unusually large hyperpolarizabilities of the nonbonding lone-pair electrons. The filled inner electronic shells screen the outer electrons effectively from the nucleus, thus allowing large charge displacements to occur under the influence of an optical field. The anharmonic effects are therefore attributed to such large displacements [208]. The high nonlinear refractive indices of $TiO_2$ glass and

$TeO_2$ glass are attributed to the large number of low-lying, empty ($Ti^{4+}$) or sparsely occupied ($Ti^{3+}$) 3d electronic states, or to the empty 5d orbitals of the Te ions, respectively.

As seen in Table 4.3, chalcogenide glasses are found to have the largest nonresonant third-order nonlinearities reported to date [209]. In chalcogenide glasses, the minimum intrinsic absorption occurs at about $4-6\,\mu m$ compared to about $\sim 1\,\mu m$ in oxide glasses. Therefore, there should be some resonant contribution to the reported values of $\chi^{(3)}$ even at $2\,\mu m$. Hall [210] suggests that, in a four-wave mixing experiment, a large mixing signal may be due to a significant imaginary part of $\chi^{(3)}$, which is probably caused by the onset of resonant nonlinear processes, such as two-photon absorption. Pure $SiO_2$ has the smallest linear and nonlinear refractive indices of the oxide glasses. The introduction of modifiers into the silica network creates nonbridging oxygen bonds and specific structural units on a short-range scale of a few atomic distances. Adair et al. [211] show that $n_2$ increases with the fraction of nonbridging oxygen bonds if there are no polarizable cations present. In $SiO_2$, the top of the valence band is composed of lone-pair p-electron states of O atoms and the bottom of the conduction band is governed by anti-bonding character states 3p and 3d states of Si [212]. One-photon absorption occurs from the valence band to the conduction band. The fact that the two-photon spectrum lies at around half the energy of the optical gap ($E_g \sim 10\,eV$) suggests that two-photon transitions also occur from the valence to the conduction band.

# 5

# Optical Nonlinearities in Chalcogenide Fibres

## 5.1 Fabrication of Chalcogenide Fibers and Their Linear Optical Properties

Optical fibers are obtained by heating glass preforms fabricated via rod-in-tube type processes [213, 214] or by double-crucible processes [214–216].

Fabrication of single-mode chalcogenide optical fiber is essential for applications such as fiber amplifiers. The rod-in-tube technique has been the most popular process for fabrication of single-mode chalcogenide optical fibers [217, 218]. This technique involves many stretching and overjacketing steps that are not suitable for most glasses because of their thermal instability. To overcome this difficulty, a double-crucible technique has been used to produce single-mode optical fiber. A typical system consists of an inner quartz crucible (tube) concentrically positioned within an outer quartz crucible (tube). Each tube is connected individually to an inert gas source, flow meter, pressure controller, and pressure gauge. The outer diameter of the fiber and core/clad ratio can be controlled by adjusting the gas pressure in the inner and outer quartz tubes independently, by altering the drawing rate, and by adjusting the temperature. The core and cladding glasses are introduced into the inner and outer quartz tubes, respectively. Glasses are remelted, fined, and the temperature is then lowered quickly to the drawing temperature where fiber fabrication starts. Chalcogenide fibers with core diameters ranging from 2 to 400 µm and outer diameters from 50 to 500 µm can be fabricated by this technique under different fiber-drawing conditions. Figure 5.1 shows a typical double-crucible process.

Rod drawing from a preprepared preform has only been used to prepare gallium lanthanide sulfide (GLS) fibers. Core-clad fibers by this method were prepared by stretching (caning) a rod of glass to a smaller diameter, in the drawing tower, then inserting the cane into a tube of cladding glass before pulling to fiber. Figure 5.2 shows a typical rod-in-tube process. One of the main limitations of using the rod-in-tube method for producing core-clad fibers is

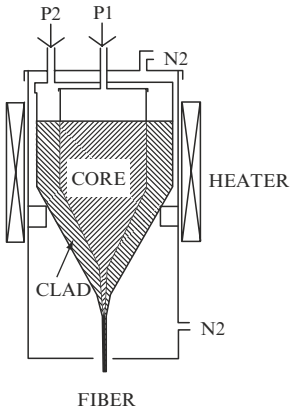


**Fig. 5.1.** Schematic diagram of fiberization by the double-crucible technique (after [220])

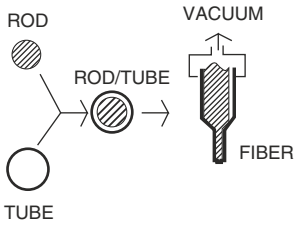


**Fig. 5.2.** Schematic diagram of fiber processing by the rod-in-tube technique (after [220])

the difficulty in making fibers with small core sizes. Therefore several collapses are required to achieve core diameters smaller than 15 µm. The fabrication of such fibers in GLS glasses, although possible, has proved difficult due to the thermal characteristics of the glass. Repeated heating leads to crystallization in the core, resulting in high optical-transmission losses.

The most effective fabrication technique uses a combination of extrusion, and the rod-in-tube method for manufacturing fiber preforms. The advantage of using extrusion to do this is that comparatively low temperatures could be used to fabricate the glass, which allows fabrication without crystallization [219].

### 5.1.1 Fabrication of Fibers by Extrusion

Through extrusion, it is possible to overcome the problems of devitrification and produce crystallite-free glasses. In the extrusion technique (Fig. 5.3) [221], high pressures are applied at elevated temperatures and the molten glass is forced through a die. The use of high pressures at reduced temperatures is the key to the success of this technique [222]. For the manufacture of relatively

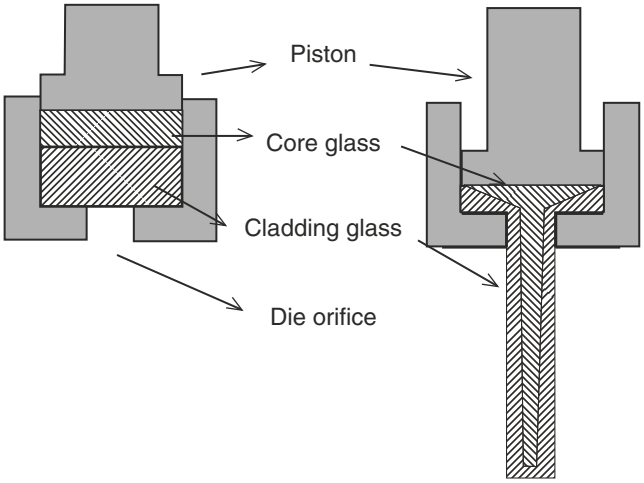


**Fig. 5.3.** Simple extrusion of two glass plates into a core-clad preform. Successful extrusion relies on radially nonuniform flow to produce the final fiber-preform geometry (after [221])

large cross-sections (>10 mm diameter) where high pressures, low temperatures and very slow draw speeds are required, a twin-rail traverse mechanism is used [222]. For fabricating small cross-sections in which moderate pressures and more rapid draw speeds are required, a tractor mechanism is used [222].

Since chalcogenide glasses are quenched liquids, normal laws of viscous liquids can be applied to them. Shearing forces applied to the glass above the transformation temperature induce flow. Successful extrusion is obtainable when the glass achieves a viscosity below approximately $10^9$ poise. The normal range of viscosity for glass extrusion is between $10^5$ and $10^{10}$ poise. Chalcogenide glasses have been extruded into a wide variety of sizes and shapes. Samples with a very high degree of polishing have been prepared for such applications as attenuated total internal reflection (ATR) [223], hollow glass waveguides [224], planar waveguides [225, 226] and mass-produced lenses of presized diameter and rod lenses. $As_2S_3$ and arsenic–germanium–selenium-based glasses have been extruded [222]. Typical pressures have ranged between 0.5 and 16 atmospheres. Feed rates range between 0.1 and 100 mm per minute. The final product must be annealed after extrusion to remove residual stresses.

### 5.1.2 Physical and Linear Optical Properties of Chalcogenide Fibers

Since chalcogenide glasses transmit to appreciably longer wavelengths in the IR than do silica and fluoride glasses, there are numerous potential applications in the civil, medical, and military areas. Table 5.1 lists some physical, mechanical, and optical properties of chalcogenide glasses used in making

**Table 5.1.** Selected physical properties of key fiber materials compared to conventional silica fiber (after [228])

| property | silica | ZBLAN | chalcogenide AsGeSeTe |
|---|---|---|---|
| glass transition, °C | 1175 | 265 | 245 |
| thermal conductivity, $\mathrm{W\,(m^{\circ}C)^{-1}}$ | 1.38 | 0.628 | 0.2 |
| thermal expansion coefficient, $10^{-6}$ per °C | 0.55 | 17.2 | 15 |
| Young's modulus, GPa | 70 | 58.3 | 21.5 |
| density, $\mathrm{g\,cm^{-3}}$ | 2.20 | 4.33 | 4.88 |
| refractive index, $n$ ($\lambda\,\mu$m) | 1.455 (0.7) | 1.49 (0.589) | 2.9 (10.6) |
| $\mathrm{d}n/\mathrm{d}T$, $10^{-5}$ per °C ($\lambda\,\mu$m) | +1.2 (1.06) | −1.5 (1.06) | +10 (10.6) |
| fiber transmission range, µm | 0.24–2.0 | 0.25–4 | 4–11 |
| loss at 2.94 µm, $\mathrm{dB\,m^{-1}}$ | ∼800 | 0.08 | 5 |
| loss at 10.6 µm, $\mathrm{dB\,m^{-1}}$ | NA | NA | 2 |

NA: Not applicable

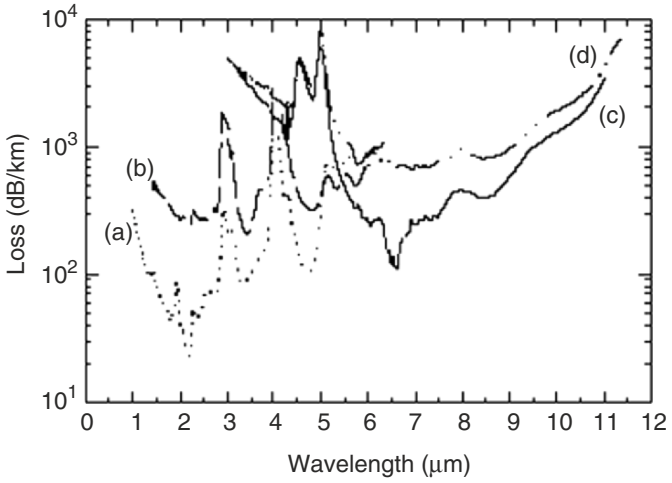


**Fig. 5.4.** Transmission loss spectra of (**a**) lowest loss sulfide ($As_{40}S_{60}$) fiber, (**b**) typical sulfide fiber, (**c**) lowest loss telluride ($\mathrm{Ge_{30}As_{10}Se_{30}Te_{30}}$) fiber, and (**d**) typical telluride fiber (after [229])

optical fibers. Compared to the more traditional oxide glasses, they can be described as having lower glass-transition temperatures ($T_\mathrm{g}$'s), higher coefficients of thermal expansion (CTE's), lower hardness, and higher indices of refraction [227]. The As–S fibers have received the most attention to date [229] and the loss routinely achieved is about 0.1–0.2 $\mathrm{dB\,m^{-1}}$ in fiber lengths of about 500 m. Purification and composition play an important role in making low-loss fibers. Figure 5.4 compares the losses routinely obtained for a couple

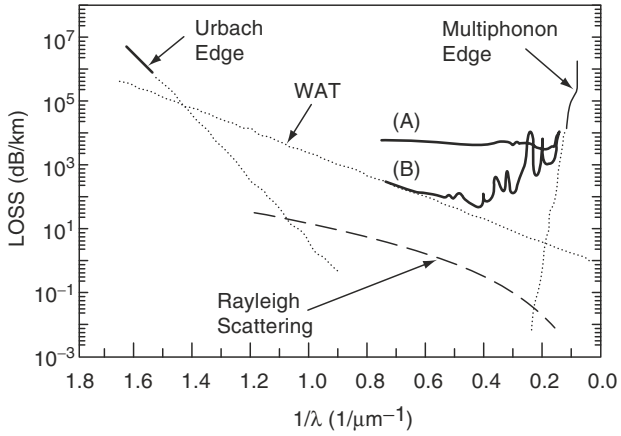


**Fig. 5.5.** Estimation of theoretical minimum loss in an arsenic sulfide fiber. A and B represent poor and high-quality glasses, respectively (after [232])



of chalcogenide glasses, along with the lowest losses reported in the literature [230, 231]. It is worthwhile to estimate the theoretical minimum loss in a sulfide fiber. This estimate has been done for an arsenic sulfide glass [232] and the results are shown in Fig. 5.5. The minimum loss is estimated to be about $4\,\mathrm{dB\,km^{-1}}$ at $5\,\mu\mathrm{m}$ [232]. The minimum loss obtained for a 400 ppm Dy-doped unclad selenide glass fiber was $0.8\,\mathrm{dB\,m^{-1}}$ at $6.6\,\mu\mathrm{m}$ and $3\,\mathrm{dB\,m^{-1}}$ at $1.3\,\mu\mathrm{m}$. Undoped samples have been fabricated into single-mode fibers with losses of $3\,\mathrm{dB\,m^{-1}}$ at $1.55\,\mu\mathrm{m}$.

In general, measured losses for rare-earth-doped chalcogenide glass fibers are $>0.5\mathrm{dB\,m^{-1}}$ and so improvements in purification and fiberization technology are still needed to reduce the measured optical losses. Since rare-earth-doped chalcogenide fibers emit in the 2–$5\,\mu\mathrm{m}$ region [233], they are an attractive alternative to blackbody sources for many applications. For example, arrays of such fibers can be used for infrared scene simulation (IRSS) for characterization of focal-plane-array detectors such as InSb [234].

Figure 5.6 shows the emission spectrum of a Pr-doped selenide glass fiber showing broadband emission between about 3 and $5\mu\mathrm{m}$. Hence, these fibers are capable of providing bright sources in the mid-IR.

## 5.2 Nonlinear Optical Properties of Fibers

### 5.2.1 Features of Chalcogenide Glass as a Nonlinear Material

Nonlinear materials can be categorized into resonant and nonresonant types [235]. The resonant-type material is used with a wavelength near its electronic

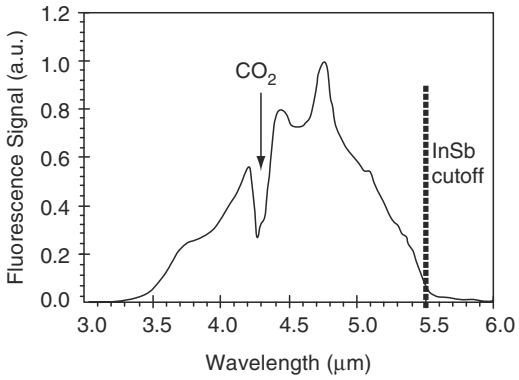


**Fig. 5.6.** The broadband mid-IR emission from a Pr-doped GeAsGaSe glass fiber (after [229])

absorption edge, so that its high resonant nonlinearity can be utilized. The problem with this type is that the response time is limited by the carrier relaxation time or slow thermal nonlinearity. However, the nonresonant-type material is used with a wavelength longer than its electronic absorption edge, so that ultrafast material response due to third-order electronic polarization is guaranteed. The drawback of this type is that its nonlinearity is relatively low, and thus a waveguide structure is necessary in order to keep a high power density within the long interaction length. Among the various kinds of materials, glass is the easiest material to use in fabricating a long-fiber-type waveguide. Due to its low loss characteristics, silica fiber has been one of the most commonly used nonresonant nonlinear media in all-optical switching [235]. However, the low nonlinearity of silica requires an extremely long fiber, for example a few kilometers in length. Glasses with higher nonlinearities are needed. Chalcogenide glasses show promise in this respect. Table 5.2 summarizes the nonlinear refractive index of some typical glasses with high nonlinearities.

### 5.2.2 Stimulated Light Scattering and Super-Continuum Generation

Stimulated Raman spectroscopy has attracted considerable attention. It provides a broad-band light amplification [236,237]. Stimulated Raman scattering can be regarded as a kind of nondegenerate two-photon processes. However, in the Raman scattering, one photon is absorbed by the virtual states and simultaneously one photon is emitted. When the incident light becomes intense, the Stokes-shifted light can be amplified. Most experiments have been done using optical fibers [236, 238] because of their long interaction length. Raman fiber amplifiers with 5–10 km lengths of silica can provide broad gains of $\sim$10 dB [239].

**Table 5.2.** Nonlinear refractive-index of typical nonlinear glasses: BK-7 is a borosilicate glass and SF-59 represents a lead-silicate glass

| glass composition | $n_2$ ($m^2\,W^{-1}$) |
|---|---|
| $SiO_2$ | $2 \times 10^{-20}$ |
| $BK-7$ | $3 \times 10^{-20}$ |
| SF-59 | $30 \times 10^{-20}$ |
| $As_2S_3$ | $200 \times 10^{-20}$ |
| $BeF_2$ | $0.8 \times 10^{-20}$ |

Super-continuum generation in silica fibers and other glasses is now extensively studied [240–244]. When pulsed or cw light propagates through a nonlinear medium, it may undergo spectral broadening [237]. For example a 350 m single-mode fiber, which is excited by a 2.22 W cw laser with a wavelength of 1.483 µm, can emit 2.1 W with a broad spectrum extending from 1.43 to 1.53 µm [241]. We should note that, different from stimulated light scattering, shorter-wavelength light is also generated in this process.

### 5.2.3 Second-Order Nonlinearity in Poled Glass

Since glass is an isotropic medium, generally it does not support second-order nonlinearity. However, it has been discovered that several kinds of poling methods can induce second-order nonlinearity in glass. Among different poling methods, the so-called optical poling was discovered [245] using optical fibers. It was found that an exposure of Ge-doped optical fibers with ∼1 m length to 70 kW Nd:YAG laser light for ∼1 h could induce a second-harmonic signal of 0.55 kW. This method can apply only to optical fibers, since the induced nonlinearity is relatively small $\chi^{(2)} \approx 10^{-4}\,pm\,V^{-1}$ [246]. The other poling method, so-called thermal poling, which is actually electro-thermal, was demonstrated in bulk $SiO_2$ [247]. The induced nonlinearity, $\sim 1\,pm\,V^{-1}$, evaluated from the second-harmonic signal of 1.06 µm laser light, is similar in magnitude to that of quartz. Since the nonlinearity is appreciably large, the method has been applied to other oxides [247–249] and chalcogenide glasses [250]. Liu et al. [251] have applied electron-beam poling to chalcogenide glasses, producing $\chi^{(2)} \sim 1\,pm\,V^{-1}$. An advantage of this technique is its high resolution, which could be promising for fabricating optical integrated circuits. Two possible poling mechanisms have been proposed [252]. One is that space charges produce a built-in electric field of $E_{dc} \sim 10^6\,V\,cm^{-1}$, which induces an effective $\chi^{(2)}$ given as $3E_{dc}\chi^{(3)}$ [246]. The other mechanism is that oriented defects, such as $E'$ centers (a kind of unpaired-electron dangling bond in oxide glasses) are responsible. It is reasonable to assume that UV excitation produces defective dipoles, which are oriented along an applied electric field. It should be noted that heating tends to enhance macroscopic ion migration, while enhancement of defect orientations is dominant in unheated poling methods.

## 5.3 Pulse Propagation in Fibers

### 5.3.1 Propagation of Optical Fields

The propagation of optical fields in fibers is governed by Maxwell's equations. In the SI system of units, these equations are:

$$\nabla \times E = -\partial B/\partial t \tag{5.1}$$

$$\nabla \times H = J + \partial D/\partial t \tag{5.2}$$

$$\nabla . D = \rho \tag{5.3}$$

$$\nabla . B = 0 \tag{5.4}$$

where $E$ and $H$ are electric and magnetic-field vectors, and $D$ and $B$ are corresponding electric and magnetic flux densities. In the absence of free charges in a medium such as optical fibers, $J = 0$ and $\rho = 0$, and $D$ and $B$ are related to $E$ and $H$ through:

$$D = \varepsilon_0 E + P, \tag{5.5}$$

$$B = \mu_0 H + M, \tag{5.6}$$

where $\varepsilon_0$ and $\mu_0$ are, respectively, the vacuum permittivity and permeability, and $P$ and $M$ are the induced electric and magnetic polarizations. For a nonmagnetic medium, such as optical fibers, $M = 0$.

By taking the curl of (5.1) and using (5.2), (5.5), and (5.6), one can find a relation between $E$ and $P$:

$$\nabla \times \nabla \times E = \frac{-1}{c^2}\frac{\partial^2 E}{\partial t^2} - \mu_0 \partial^2 P/\partial t^2, \tag{5.7}$$

where $c$ is the speed of light in vacuum and $\mu_0 \varepsilon_0 = 1/c^2$.

We can relate the induced polarization $P$ and the electric field $E$. In general, the evaluation of $P$ requires a quantum-mechanical approach. Such an approach is often necessary when the optical frequency is near a resonance of a medium. Far from such resonances, the relation between $P$ and $E$ is of the form:

$$P = \varepsilon(\chi^{(1)}.\, E + \chi^{(2)} : EE + \chi^{(3)} \vdots EEE + \cdots) \tag{5.8}$$

This is the case for optical fibers in the wavelength range of 0.5–2 µm that is of interest for the study of nonlinear effects.

For $\chi^{(3)}$ media, the induced polarization can be written as:

$$P(r,t) = P_{\mathrm{L}}(r,t) + P_{\mathrm{NL}}(r,t), \tag{5.9}$$

where:

$$P_{\mathrm{L}}(r,t) = \varepsilon_0 \int_{-\infty}^{\infty} \chi^{(1)}(t-t')\; E(r,t')\mathrm{d}t' \tag{5.10}$$

and

$$P_{\mathrm{NL}}(r,t) = \varepsilon_0 \iiint_{-\infty} \chi^{(3)}(t-t_1, t-t_2, t-t_3) \vdots E(r,t_1)E(r,t_2)E(r,t_3)\mathrm{d}t_1\mathrm{d}t_2\mathrm{d}t_3 \tag{5.11}$$

It should be remembered that (5.7), (5.9)–(5.11) provide a general formalism for studying third-order nonlinear effects in optical fibers. Several simplifying assumptions can be made. Firstly, $P_{\mathrm{NL}}$ in (5.9) is treated as a small perturbation to the total induced polarization. This is justified because the nonlinear effects are relatively weak in silica fibers. Considering $P_{\mathrm{NL}} = 0$ and writing (5.7) in the frequency domain, we have:

$$\nabla \times \nabla \times E(r,\omega) - \varepsilon(\omega)\frac{\omega^2}{c^2}E(r,\omega) = 0, \tag{5.12}$$

where $E(r,\omega)$ is the Fourier transform of $E(r,t)$ given by:

$$E(r,\omega) = \int_{-\infty}^{\infty} E(r,t)\exp(\mathrm{i}\omega t)\mathrm{d}t. \tag{5.13}$$

The dielectric constant in (5.12) is defined as:

$$\varepsilon(\omega) = 1 + \chi^{(1)}(\omega), \tag{5.14}$$

where

$\chi^{(1)}(\omega)$ is the Fourier transform of $\chi^{(1)}(t)$.

$\chi^{(1)}(\omega)$ is in general complex and its real and imaginary parts can be related to the refractive index $n(\omega)$ and the absorption coefficient $\alpha(\omega)$ as:

$$\varepsilon = (n + \mathrm{i}\alpha c/2\omega)^2. \tag{5.15}$$

So, from the above equations, one has:

$$n(\omega) = 1 + \frac{1}{2}\mathrm{Re}[\chi^{(1)}(\omega)] \tag{5.16}$$

$$\alpha(\omega) = \frac{\omega}{nc}\mathrm{Im}[\chi^{(1)}(\omega)]. \tag{5.17}$$

In order to solve (5.12), two further simplifications are normally made. First, because of low optical losses in fibers in the wavelength region of interest, the imaginary part of $\varepsilon(\omega)$ is small in comparison to the real part. So we can replace $\varepsilon(\omega)$ by $n^2(\omega)$ in (5.12) and include fiber losses later in a perturbative manner. Second, $n(\omega)$ is often independent of the spatial coordinates in both the core and the cladding of step-index fibers; therefore one can write:

$$\nabla \times \nabla \times E = \nabla(\nabla \cdot E) - \nabla^2 E = -\nabla^2 E. \tag{5.18}$$

Equation (5.12) takes the form:

$$\nabla^2 E + n^2(\omega)\frac{\omega^2}{c^2}E = 0, \tag{5.19}$$

which can be solved to find fiber modes.

### 5.3.2 Nonlinear Pulse Propagation

When short pulses with widths ranging from ∼10 ns to 10 fs propagate inside a fiber, both dispersive and nonlinear effects influence their shape and spectrum.

One can derive a basic equation that governs propagation of optical pulses in nonlinear dispersive fibers. Equation (5.7) can be written in the following form using (5.9) and (5.19):

$$\nabla^2 E - \frac{1}{c^2}\frac{\partial^2 E}{\partial t^2} = \mu_0 \frac{\partial^2 P_{\mathrm{L}}}{\partial t^2} + \mu_0 \frac{\partial^2 P_{\mathrm{NL}}}{\partial t^2}. \tag{5.20}$$

To solve (5.20), several simplifying assumptions can be made. First, $P_{\mathrm{NL}}$ is taken as a small perturbation to $P_{\mathrm{L}}$. This is justified because nonlinear changes in the refractive index are $<10^{-6}\, n$ in practice. Second, the polarization of the optical field along the fiber length is maintained so that a scalar approach is valid. The third assumption is that the optical field is quasimonochromatic, and has a spectral width such that $\Delta\omega/\omega_0 \ll 1$, where $\omega_0$ is the center of the pulse spectrum and $\Delta\omega$ is its pulse width. For $\omega_0 \sim 10^{15}\mathrm{s}^{-1}$, the last assumption is valid for pulses as short as 0.1 ps. If we adopt the slowly varying envelope approximation, we can write the electric field in the form:

$$E(r,t) = \frac{1}{2}\hat{x}[E(r,t)\exp(-\mathrm{i}\omega_0 t) + \mathrm{c.c.}], \tag{5.21}$$

where $\hat{x}$ is the polarization unit vector and $E(r,t)$ is a slowly varying function of time. We can also express $P_{\mathrm{L}}$ and $P_{\mathrm{NL}}$ as:

$$P_{\mathrm{L}}(r,t) = \frac{1}{2}\hat{x}[P_{\mathrm{L}}(r,t)\exp(-\mathrm{i}\omega_0 t) + \mathrm{c.c.}], \tag{5.22}$$

$$P_{\mathrm{NL}}(r,t) = \frac{1}{2}\hat{x}[P_{\mathrm{NL}}(r,t)\exp(-\mathrm{i}\omega_0 t) + \mathrm{c.c.}]. \tag{5.23}$$

By substituting (5.22) in (5.10), $P_{\mathrm{L}}$ can be obtained as:

$$\begin{aligned} P_{\mathrm{L}}(r,t) &= \varepsilon_0 \int_{-\infty}^{\infty} \chi_{xx}^{(1)}(t-t')E(r,t')\exp[\mathrm{i}\omega_0(t-t')]\mathrm{d}t' \\ &= \varepsilon_0/2\pi \int_{-\infty}^{\infty} \chi_{xx}^{(1)}(\omega)E(r,\omega-\omega_0)\exp[-\mathrm{i}(\omega-\omega_0)t]\mathrm{d}\omega, \end{aligned} \tag{5.24}$$

where $E(r,\omega)$ is the Fourier transform of $E(r,t)$.

By considering that the nonlinear response is effectively instantaneous, and by substituting (5.23) in (5.11), $P_{\mathrm{NL}}(r,t)$ reduces to:

$$P_{\mathrm{NL}}(r,t) = \varepsilon_0 \chi^{3}\vdots\, E(r,t)E(r,t)E(r,t). \tag{5.25}$$

It should be noted that the contribution of molecular vibrations to $\chi^{(3)}$ (the Raman effect) is neglected. For silica fibers, the vibrational or Raman response occurs over a time scale 60–70 fs. Hence (5.25) is approximately valid for pulse widths >1 ps.

When we substitute (5.21) in (5.25), there will be a term oscillating at $\omega_0$, as well as another term oscillating at $3\omega_0$. The latter term is generally negligible in optical fibers. If one uses (5.23), $P_{\mathrm{NL}}(r,t)$ is given by:

$$P_{\mathrm{NL}}(r,t) \approx \varepsilon_0 \varepsilon_{\mathrm{NL}} E(r,t), \tag{5.26}$$

where $\varepsilon_{\mathrm{NL}}$ is given by:

$$\varepsilon_{\mathrm{NL}} = \frac{3}{4}\chi^{(3)}_{xxxx} \left|E(r,t)\right|^2 . \tag{5.27}$$

In order to obtain the wave equation for a slowly varying amplitude $E(r,t)$, it is more convenient to work in the Fourier domain, but this is not possible because of the intensity dependence of $\varepsilon_{\mathrm{NL}}$. However, $\varepsilon_{\mathrm{NL}}$ can be treated as a constant during propagation [253, 254]. If we substitute (5.21) and (5.23) in (5.20), the Fourier transform $E(r, \omega - \omega_0)$ is found to satisfy the Helmholtz equation:

$$\nabla^2 E + \varepsilon(\omega) {K_0}^2 E = 0, \tag{5.28}$$

where $K_0 = \omega/c$ and

$$\varepsilon(\omega) = 1 + {\chi_{xx}}^{(1)}(\omega) + \varepsilon_{\mathrm{NL}}. \tag{5.29}$$

Since $\varepsilon_{\mathrm{NL}}$ is intensity dependent, both $n$ and $\alpha$ are also intensity dependent:

$$n = n + n_2 \left|E\right|^2 , \quad \alpha = \alpha + \alpha_2 \left|E\right|^2 . \tag{5.30}$$

Using $\varepsilon = (n + \mathrm{i}\alpha/2K_0)^2$ and (5.27) and (5.29), the nonlinear index coefficient $n_2$ and the two-photon absorption coefficient $\alpha_2$ are given by:

$$n_2 = \frac{3}{8n}\mathrm{Re}(\chi^{(3)}_{xxxx}), \tag{5.31a}$$

$$\alpha_2 = \frac{3\omega_0}{4nc}\,\mathrm{Im}(\chi^{(3)}_{xxxx}). \tag{5.31b}$$

Since $\alpha_2$ is relatively small for silica fibers, it is often ignored. We can use the method of separation of variables to solve (5.28) and assume a solution of the form:

$$E(r, \omega - \omega_0) = F(x,y) A(z, \omega - \omega_0) \exp(\mathrm{i}\beta_0 z), \tag{5.32}$$

where $A(z,\omega)$ is a slowly varying function of $z$ and $\beta_0$ is the wave number.

Equation (5.28) results in the following two equations:

$$\partial^2 F/\partial x^2 + \partial^2 F/\partial y^2 + [\varepsilon(\omega) K_0^2 - \beta^2]F = 0 \tag{5.33}$$

$$2\mathrm{i}\beta_0 \partial A/\partial z + (\beta^2 - \beta_0^2)A = 0. \tag{5.34}$$

Since $A(z,\omega)$ is assumed to be a slowly varying function of $z$, the second derivative $\partial^2 A/\partial z^2$ was neglected in obtaining (5.33). The dielectric constant $\varepsilon(\omega)$ can be approximated by:

$$\varepsilon = (n + \Delta n)^2 \approx n^2 + 2n\Delta n, \tag{5.35}$$

where $\Delta n$ is a small perturbation:

$$\Delta n = n_2 |E|^2 + \mathrm{i}\alpha/2K_0. \tag{5.36}$$

We can solve (5.33) using first-order perturbation theory [255]. The modal distribution $F(x, y)$ and the corresponding wave number $\beta(\omega)$ can be obtained by replacing $\varepsilon$ with $n^2$. We then include the effect of $\Delta n$ in (5.33). It should be noted that the electric field for the fundamental fiber mode is approximately given by [236]:

$$E(r, \omega) = \hat{x}\{A(\omega)F(x, y)\exp[\mathrm{i}\beta(\omega)z]\}$$

where $A(\omega)$ is a normalization constant. The transverse distribution $F(x, y)$ has a solution in terms of Bessel functions inside the core. Outside the core, $F(x, y)$ decays exponentially. In practice, however, $F(x, y)$ for the fundamental fiber mode is often approximated by a Gaussian distribution.

In first-order perturbation theory, the eigenvalue $\beta$ becomes:

$$\beta(\omega) = \beta(\omega) + \Delta\beta, \tag{5.37}$$

where

$$\Delta\beta = \frac{K_0 \int\int\limits_{-\infty} \Delta n |F(x, y)|^2 \,\mathrm{d}x\mathrm{d}y}{\int\int\limits_{-\infty} |F(x, y)|^2 \,\mathrm{d}x\mathrm{d}y}. \tag{5.38}$$

The electric field $E(r, t)$ can be written using (5.21) and (5.30) as:

$$E(r, t) = \frac{1}{2}\hat{x}\left\{F(x, y)A(z, t)\exp[\mathrm{i}(\beta_0 z - \omega_0 t)] + \mathrm{c.c.}\right\}. \tag{5.39}$$

The Fourier transform $A(z, \omega - \omega_0)$ of A(z,t) satisfies (5.33):

$$\partial A/\partial z = \mathrm{i}[\beta(\omega) + \Delta\beta - \beta_0]A, \tag{5.40}$$

where (5.37) was used and the approximation $\beta^2 - \beta_0^2 \approx 2\beta_0(\beta - \beta_0)$ was made.

One can give a physical meaning to (5.40). Each spectral component within the pulse envelope acquires a phase shift which is both frequency and intensity dependent.

One can go back to the time domain and use the inverse Fourier transform of (5.40) and obtain the propagation equation for $A(z, t)$.

$\beta(\omega)$ is normally expanded in a Taylor series about the carrier frequency $\omega_0$ as:

$$\beta(\omega) = \beta_0 + (\omega - \omega_0)\beta_1 + 1/2(\omega - \omega_0)^2\beta_2 + 1/6(\omega - \omega_0)^3\beta_3 + \cdots, \tag{5.41}$$

where

$$\beta_m = \left(\frac{\mathrm{d}^m\beta}{\mathrm{d}\omega^m}\right)_{\omega=\omega_0} \qquad (m = 1, 2, \ldots). \tag{5.42}$$

Cubic and higher-order terms in this expansion can be neglected in the spectral width $\Delta\omega \ll \omega_0$.

If $\beta_2 \approx 0$ for some specific values of $\omega_0$ (in the vicinity of the zero-dispersion wavelength of the fiber), it may be necessary to include the cubic term.

By taking the inverse Fourier transform of $A(z,\omega)$, we obtain:

$$A(z,t) = \frac{1}{2\pi}\int_{-\infty}^{\infty} A(z,\omega-\omega_0)\exp[-\mathrm{i}(\omega-\omega_0)t]\mathrm{d}\omega. \tag{5.43}$$

In the above, $\omega-\omega_0$ is replaced by the differential operator $\mathrm{i}(\partial/\partial t)$ and we obtain:

$$\partial A/\partial z = -\beta_1\partial A/\partial t + \mathrm{i}\beta_2\partial^2 A/\partial t^2 + \mathrm{i}\Delta\beta A. \tag{5.44}$$

It should be noted that the term in $\Delta\beta$ includes the effect of fiber loss and nonlinearity.

Using (5.36), (5.38), $\Delta\beta$ can be evaluated, and when substituted in (5.44) results in:

$$\frac{\partial A}{\partial z} + \beta_1\frac{\partial A}{\partial t} + \frac{\mathrm{i}\beta_2}{2}\frac{\partial^2 A}{\partial t^2} + \frac{\alpha}{2}A = \mathrm{i}\gamma\left|A\right|^2 A, \tag{5.45}$$

where $\gamma$, the nonlinear parameter, is defined as:

$$\gamma = \frac{n_2\omega_0}{cA_{\mathrm{eff}}}. \tag{5.46}$$

In the above, $|A|^2$ represents the optical power. The parameter $A_{\mathrm{eff}}$ is known as the effective core area and is defined as:

$$A_{\mathrm{eff}} = \frac{\left(\int\int_{-\infty} \left|F(x,y)\right|^2 \mathrm{d}x\mathrm{d}y\right)^2}{\int\int_{-\infty} \left|F(x,y)\right|^4 \mathrm{d}x\mathrm{d}y}. \tag{5.47}$$

It should be noted that $A_{\mathrm{eff}}$ depends on fiber parameters such as the core radius and the core-cladding index difference. For a Gaussian distribution of $F(x,y) \approx \exp[-(x^2+y^2)/w^2]$, $A_{\mathrm{eff}} = \pi w^2$, where $w$ is the width parameter.

$A_{\mathrm{eff}}$ can vary in the range 20–100 $\mu\mathrm{m}^2$ in the 1.5 $\mu$m region, depending on the fiber design. As a result, $\gamma$ takes values in the range 1–10 $\mathrm{W}^{-1}\,\mathrm{km}^{-1}$ if $n_2 \approx 2.6\times10^{-20}\,\mathrm{m}^2\,\mathrm{W}^{-1}$ is used. Equation (5.45) describes the propagation of picosecond optical pulses in single-mode fibers and is referred to as the nonlinear Schrödinger (NLS) equation. It includes the effects of fiber losses through $\alpha$, of chromatic dispersion through $\beta_1$ and $\beta_2$, and of fiber nonlinearity through $\gamma$. One can give a physical meaning to each of the above parameters.

The pulse envelope moves at the group velocity $\nu_{\mathrm{g}} \equiv 1/\beta_1$, while the effects of group-velocity dispersion (GVD) are governed by $\beta_2$. The GVD parameter $\beta_2$ can take positive or negative values, depending on whether the wavelength $\lambda$ is below or above the zero-dispersion wavelength $\lambda_{\mathrm{D}}$ of the fiber.

In standard silica fibers, $\beta_2 \sim 50\,\mathrm{ps}^2\,\mathrm{km}^{-1}$ in the visible region but becomes close to $-20\,\mathrm{ps}^2\,\mathrm{km}^{-1}$ near wavelengths of $\sim 1.5\,\mu\mathrm{m}$, the change in sign occurring in the vicinity of $1.3\,\mu\mathrm{m}$ [236]. The group-velocity dispersion of $As_2S_3$ glass is given by [256]. The zero-dispersion wavelength of this material is about $5\,\mu\mathrm{m}$ so that it has a large normal dispersion around the communication wavelength (1.3–$1.55\,\mu\mathrm{m}$). The GVD at $1.55\,\mu\mathrm{m}$ is as large as $400\,\mathrm{ps\,km}^{-1}\,\mathrm{nm}^{-1}$. Thus, unlike conventional silica fiber, it is difficult to control the GVD of the fiber by changing the fiber structure, and the GVD of the chalcogenide fiber is determined by material dispersion.

### 5.3.3 Higher-Order Nonlinear Effects

The propagation equation (5.45) has been successful in explaining a large number of nonlinear effects [236]. However, some modifications should be made, depending on the experimental conditions. For example, (5.45) does not include the effects of stimulated inelastic scattering effects such as stimulated Raman scattering (SRS) and stimulated Brillouin scattering (SBS). If the peak power of the incident pulse is above a threshold level, both SRS and SBS can transfer energy from the pulse to a new pulse, which may propagate in the same or the opposite direction. The two pulses interact with each other through the Raman or Brillouin gain and cross-phase modulation (XPM).

For ultrafast optical pulses, whose width is close to or less than 1 ps, (5.45) should be modified. Because of the large spectral width of such pulses, several approximations made in the derivation of (5.45) become questionable, one of these being the neglect of the Raman effect. For pulses with a wide spectrum ($> 0.1\,\mathrm{THz}$), the Raman gain can amplify the low-frequency components of a pulse by transferring energy from the high-frequency components of the same pulse, so-called intrapulse Raman scattering. As a result of this phenomenon, the pulse spectrum shifts toward the low-frequency (red) side as the pulse propagates inside the fiber. This phenomenon is called the self-frequency shift [257] and is related to the delayed nature of the Raman response [258]. It should be emphasized that (5.45) is the simplest nonlinear equation for studying third-order nonlinear effects in optical fibers. When the peak power of the optical pulse becomes so large that it is necessary to include the fifth and higher-order terms in (5.8), one needs to modify the NLS equation. One way to achieve this modification is to replace the nonlinear parameter in $\gamma$ in (5.45) by:

$$\gamma = \frac{\gamma_0 A}{1 + b_\mathrm{s} |A|^2} \approx \gamma_0 (1 - b_\mathrm{s} |A|^2), \tag{5.48}$$

where $b_\mathrm{s}$ is the saturation parameter related to the power level at which the nonlinearity starts to saturate. For silica fibers, $b_\mathrm{s} |A|^2 \ll 1$ in most practical situations, and (5.48) can be used. For power levels of $\approx 1\,\mathrm{GW\,cm}^{-2}$, the approximation $\gamma = \gamma_0 (1 - b_\mathrm{s} |A|^2)$ in (5.48) can be used.

The resulting equation involves both the third and fifth powers of the amplitude $A$, and is called the quintic NLS equation. It is also referred to as the cubic-quintic NLS equation. Fibers made of materials with large values of $n_2$ (silicate and chalcogenide fibers) are likely to show saturation effects at lower power levels and hence (5.48) is more relevant for such fibers.

## 5.4 Group-Velocity Dispersion Compensation by Fiber Gratings

In Sect. 5.3, the nonlinear Schrödinger (NLS) equation was obtained that governs the propagation of optical pulses inside single-mode fibers. For pulse widths $> 5\,\mathrm{ps}$, we can use (5.45) and write it as:

$$\mathrm{i}\frac{\partial A}{\partial z} = -\mathrm{i}\frac{\alpha}{2}A + \frac{\beta}{2}\frac{\partial^2 A}{\partial t^2} - \gamma\left|A\right|^2 A, \tag{5.49}$$

where $A$ is the slowly varying amplitude of the pulse envelope and $T$ is measured in a frame of reference moving with the pulse at the group velocity $\nu_\mathrm{g}$ ($T = t - z/\nu_\mathrm{g}$)

The three terms on the right-hand side of (5.49) show the effects of fiber losses, dispersion, and nonlinearity on pulses propagating inside optical fibers. Depending on the initial width $T_0$ and the peak power $P_0$ of the incident pulse, either dispersive or nonlinear effects may dominate along the fiber.

Two scale lengths, $L_\mathrm{D}$(dispersion length) and $L_\mathrm{N}$(nonlinear length), can be defined and pulses evolve differently depending on their values:

$$L_\mathrm{D} = T_0^2/\left|\beta_2\right|, \quad L_\mathrm{NL} = 1/\gamma P_0, \tag{5.50}$$

where the fiber length is such that $L \ll L_\mathrm{NL}$ and $L \ll L_\mathrm{D}$, the fiber maintains the pulse shape during propagation. This regime is useful for optical communication systems to allow for distortion-free transmission. If the fiber length is such that $L \ll L_\mathrm{NL}$, but $L \sim L_\mathrm{D}$, the pulse evolution is then governed by GVD, and nonlinear effects play a relatively minor role. The effect of GVD is to broaden the pulse during propagation along the fiber.

When the fiber length is such that $L \ll L_\mathrm{D}$ but $L \sim L_\mathrm{NL}$, pulse evolution in the fiber is governed by SPM that leads to spectral broadening of the pulse.

When the fiber length is longer or comparable to both $L_\mathrm{D}$ and $L_\mathrm{NL}$, dispersion and nonlinearity act together as the pulse propagates along the fiber. In the anomalous-dispersion regime ($\beta_2 < 0$), the fiber can support solitons. In the normal-dispersion regime ($\beta_2 > 0$), the GVD and SPM effects can be used for pulse compression.

It is sometimes necessary to include the third-order term proportional to $\beta_3$ in (5.41). This happens if the pulse wavelength nearly coincides with the zero-dispersion wavelength $\lambda_\mathrm{D}$,$\beta_2 \approx 0$; the $\beta_3$ term then provides the dominant contribution to the GVD effects [259]. Also, for ultrashort pulses

(width $T_0 < 1\,\mathrm{ps}$), it is necessary to include the $\beta_3$ term even when $\beta_2 \neq 0$. In a fiber-optic communication system, information is transmitted along a fiber using a coded sequence of optical pulses whose width is determined by the bit rate, $B$, of the system. Dispersion-induced broadening of pulses is undesirable because it interferes with the detection process and leads to errors if the pulse spreads outside its allocated bit slot ($T_\mathrm{B} = 1/B$).

Clearly, GVD limits the bit rate for a fixed transmission distance $L$ [260]. There are several schemes to compensate for GVD dispersion. First, modern fiber-optic communication systems operating near $1.55\,\mu\mathrm{m}$ reduce the GVD effects using dispersion-shifted fibers designed such that the minimum-loss wavelength and the zero-dispersion wavelength nearly coincide. Although operation at the zero-dispersion wavelength is most desirable, other considerations may preclude such a design, because at most one channel can be located at the zero-dispersion wavelength in a wavelength-division-multiplexed (WDM) system. The technique of dispersion management provides a solution to this problem. It consists of combining fibers with different characteristics such that the average GVD of the entire fiber link is quite low.

When the bit rate of a single channel exceeds $100\,\mathrm{Gb\,s^{-1}}$, ultrashort pulses (width $\sim 1\,\mathrm{ps}$ ) would be used in each bit slot. In this case, the pulse spectrum becomes broad enough that it is difficult to compensate GVD over the entire bandwidth of the pulse. The solution to this problem is provided by fibers, or other devices, designed such that both $\beta_2$ and $\beta_3$ are compensated simultaneously [261–275]. Fiber gratings, liquid–crystal modulators, and other devices can also be used for this purpose [267–273]. When both $\beta_2$ and $\beta_3$ are nearly compensated, propagation of femtosecond optical pulses is limited by the fourth-order dispersion effect governed by the parameter $\beta_4$. Compensation of dispersion up to fourth-order has been achieved [275].

## 5.5 Applications

Various kinds of third-order nonlinear optical materials have been studied for their suitability of use in all-optical switching [276], and pulse compression [277]. Among them, glass fibers offer the advantage of reduced operating power because of the long interaction length.

Silica fibers have been extensively studied because of their low losses [278]. However, their nonlinearity is weak and they require very long fibers ($>100\,\mathrm{m}$). So other highly nonlinear glasses are needed. Third-harmonic generation (THG) measurements have revealed that $As_2S_3$ glass has a $\chi^{(3)}$ two orders of magnitude higher than that of silica glass [279]. A very efficient optical Kerr effect in $As_2S_3$-based chalcogenide glass fiber has been observed [280] and efficient all-optical switching using a small-core fiber only a few meters long has been demonstrated [281]. For practical applications, some other nonlinear properties of $As_2S_3$ glass, such as the response time, are needed. It should be noted that enhancement of third-order nonlinear effects other than the optical

Kerr effect, such as stimulated Raman scattering (SRS) and two-photon absorption (TPA), would be predicted. In silica fibers, it is well known that SRS can lead to delayed nonlinear response [258, 282]. Also, TPA limits the transmittable gate power and thereby limits the obtainable phase shift [283, 284]. The third-order nonlinear properties of $As_2S_3$-based glass fibers have been studied at a wavelength of around 1.55 µm [285]. An ultrafast response less than 100 fs was obtained by time-resolved pump-probe measurements and spectrum broadening due to SPM. It was claimed that SRS was observed in a fiber for the first time. The Stokes shift was in good agreement with the spontaneous Raman data and the Raman-gain coefficient was $4.4 \times 10^{-12}$m W$^{-1}$, which is two orders of magnitude higher than that of silica fiber. As expected, the Raman gain led to a retarded nonlinear response, with a relaxation time of about 97 fs. A weak transmission change due to TPA was observed and the TPA coefficient was estimated to be $6.2 \times 10^{-15}$m W$^{-1}$. It was asserted that, from the results obtained, $As_2S_3$-based glass fibers offer an ultrafast response and low TPA characteristics, and are therefore appropriate for nonlinear optical media at communication wavelengths.

All-optical switching using $As_2S_3$-based fiber was demonstrated in the Kerr-shutter and in a nonlinear optical loop mirror (NOLM) configuration. In the first demonstration of the Kerr shutter using a 50-cm-long fiber at 1.3 µm, the switching power was 14 W. Afterward, the switching power was reduced to 3 W in a 1-m-long small-core fiber, using laser diode driving sources and assistance of an erbium-doped fiber amplifier (EDFA) at 1.55 µm. The switching power was reduced to 0.4 W using a 4-m-long low-loss fiber in NOLM [256].

One of the simplest ways to reduce further the switching power is to increase the interaction length by using a longer fiber. However, the large GVD of an $As_2S_3$ fiber causes walk-off between the gate and the signal, which limits the effective interaction length. To overcome this limitation of the switching power or switching speed due to GVD, some kind of compensation technique is needed. Chirped gratings in particular can be used for dispersion compensation [286].

Since glasses lack a center of inversion symmetry, and thus have no second-order nonlinear susceptibility, they should not show SHG. However, undoped and Pr-doped GaLaS glasses have exhibited SHG [287]. This SHG may be due to crystallization or the effect of frozen-in electric fields. Electric poling has been successfully used to obtain SHG in silica-based fiber systems [288]. It is not unreasonable to expect similar results in chalcogenide fibers except that, since the electrical conductivity is lower for chalcogenide glasses, the (breakdown) electric field will be lower.

Dixit et al. [289] have investigated a Fabry–Perot (FP) filter and a nonlinear fiber-loop mirror (NFLM) for their suitability as photonic switching devices. They have found from their analysis that fibers made of doped chalcogenide glasses hold promise for applications. The advantage is seen to be more in the case of FP filters than in NFLM. It is seen that Se-based chalcogenide

glass fibers are a better choice in Fabry–Perot switching devices even with attenuation levels of $\alpha = 170\,\mathrm{dB\,m^{-1}}$. This is because the switching power is 7.5 W for a length of 2 mm, in contrast to 23 kW for conventional silica glass with a length of 2 cm. If $\alpha$ is reduced to values such as $3\,\mathrm{dB\,m^{-1}}$, as in $As_2S_3$-based glass fibers, the switching power can be brought down to 442 W, with a device length of 2 cm. These authors state that, in contrast, chalcogenide glass fiber may not be a better option for NFLM unless the present loss values of the order of $3\,\mathrm{dB\,cm^{-1}}$ in this material are reduced to a greater extent. The present values of loss coefficients in these glasses necessitate the use of very small loop lengths ($\sim$15 cm). If the loss can be decreased to a value of $0.2\,\mathrm{dB\,m^{-1}}$, then the improved figure of merit would bring down the switching power with increased lengths ($\sim$2 m), thus adding to its advantages. If fluctuations in composition and density, which normally lead to large attenuation levels, can be controlled, thus leading to materials with higher values of nonlinear coefficient and lower values of $\alpha$, the overall figure of merit can be improved.

In recent years, great interest has been generated by the development of holey or microstructured optical fibers [290]. The large and controllable variations of transverse refractive index offered by these fibers provide new opportunities for the control and guidance of light [291, 292]. To date, holey fibers are usually made from conventional silica glasses. The significant advantage for novel glasses is that different core and cladding glass compositions are no longer required. This relaxes the fabrication difficulties associated with core and cladding glasses with differing thermal properties. It has been difficult in the past to fabricate low-loss single-mode compound glass fibers due to problems arising from the different physical properties of the core and cladding materials. The varied heating steps required to fabricate single-mode compound fiber leads to the promotion of crystallization, and hence inducing of losses. Holey fibers can be made using a single heating step, reducing crystallization problems, and significantly reducing the fiber loss. Hence, holey fibers provide a new route toward the successful development of low-loss single-mode compound glass optical fibers.

Planar channel waveguide devices based on the GLS glass system have the potential for use in glass waveguide lasers, wavelength multiplexers, and optical switching/splitting in the IR [290]. Further potential for optical couplers (such as directional couplers) in the IR would allow the important applications of power division and wavelength demultiplexing to be realized. Further devices can be derived from the higher index contrast possible with GLS holey fibers allowing for fibers with very high numerical aperture NA (well in excess of unity). As a result of improvement in pump confinement, tight focusing and shorter devices and lower thresholds are possible.

Third-order Kerr nonlinearities and Raman gain have been studied experimentally in high-purity $As_2Se_3$ optical fibers for wavelengths near 1.55 µm [293]. Raman-gain measurements on the same fiber used for the $n_2$ measurements were carried out with a CW pump at a wavelength of 1,540 nm. Raman

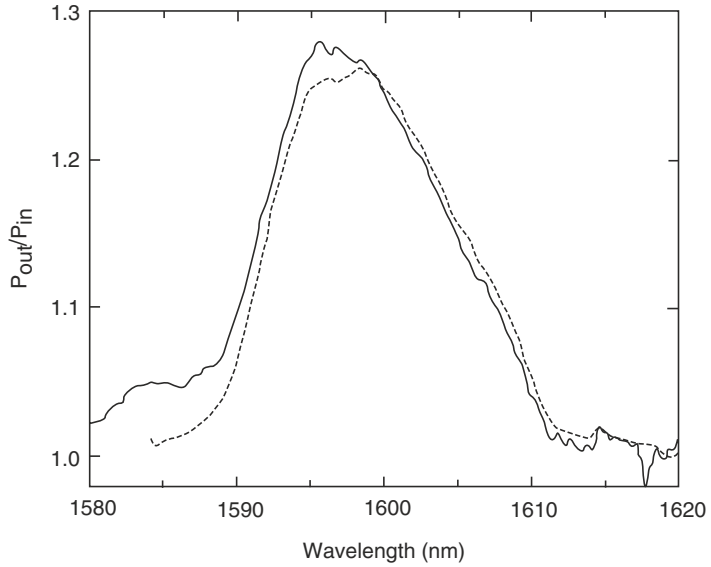


**Fig. 5.7.** Raman-gain spectra measured in an 85-cm-long As–Se fiber (*solid curve*) compared with the Raman spectrum for the bulk material (*dotted curve*). The ratio of the power output to the power input, normalized to the ratio well removed from the Raman-gain region, is shown as a function of wavelength (after [293])

gain was expected at the Raman frequency shift of $830\,\mathrm{cm}^{-1}$, corresponding to a wavelength shift of 65 nm from the pump and a Raman-gain peak near 1,605 nm. The ratio of the output to input signal levels normalized to the ratio at wavelengths outside the Raman-gain spectral region is shown in Fig. 5.7 for an average pump power in the fiber of 190 mW. We define the Raman gain by:

$$I_{\mathrm{out}} = I_{\mathrm{in}} \exp(g_R I_{\mathrm{p}} L), \tag{5.51}$$

where $g_R$ is the Raman gain in meters per watt, $I_{\mathrm{p}}$ is the pump intensity in watts per square meter, $L$ is the fiber length in meters, and $I_{\mathrm{in}}$ and $I_{\mathrm{out}}$ are the input and output signal intensities, respectively. A value of $g_R \approx 5.1 \times 10^{-11}\,\mathrm{m\,W}^{-1}$, which is nearly 780 times the value for silica, is obtained. The linear Raman spectrum measured for bulk $As_2\,Se_3$ is shown in Fig. 5.7 as the dotted curve.

Since the gain is small (<1), we expect the spectral shapes of the gain spectrum and the linear scattering spectrum to be nearly identical. One of the primary applications envisioned for these As–Se fibers is a compact, low-cost, low-pump-power Raman amplifier that would be tunable over a broad range in the optical communications band between 1.2 and 1.6 μm wavelengths. For a 20-dB Raman amplifier gain and a reasonably low pump power of 100 mW in a fiber with a $40\,\mu\mathrm{m}^2$ effective core area, the As–Se fiber would need to be 29 m long. If the fiber were drawn down to an effective area of $2\ \mu\mathrm{m}^2$,

the required fiber length would only be 1.4 m long. As an example of an application that uses the Kerr nonlinearity, the optical regenerator based on SPM proposed by Mamyshev [294] and Westbrook [295] can be considered. Optical regenerators are important for maintaining signal-to-noise ratios over long-distance optical–communications links in future all-optical systems. The Mamyshev regenerator is attractive since it can be implemented in an all-fiber configuration. It relies on spectral broadening in a highly nonlinear fiber to distinguish between the high optical signal level associated with 1's and the low-level noise in the 0's of the data stream. A bandpass filter with its center frequency shifted by at least the linear optical bandwidth is used to separate the strongly self-phase modulated 1's from the 0's. The phase shift for the 1's level was found to be optimal at a nonlinear phase shift of $7.6\pi$ [294]. If we assume a 10 m length of As–Se fiber with less than 1 dB of linear loss, a regenerator fiber length of 10 m is formed. For achieving $7.6\pi$ phase shift, the peak power in the 1's must be $\sim 1$ W. At $40\,\mathrm{Gb\,s^{-1}}$ data rates, by use of a return to zero (RZ) data format with a 30 % duty factor, this corresponds to a pulse length $\tau = 7$ ps and an average power in the fiber of 300 mW.

Ogusu et al. [296] have estimated the values of $g_B$, the Brillouin gain coefficient, and the phonon lifetime for typical $As_2S_3$ and $As_2Se_3$ chalcogenide glasses. Stimulated Brillouin Scattering (SBS) is one of the most important effects of third-order nonlinearities in various liquids, gases, and solids. SBS can be detrimental to the performance of coherent optical–communication systems. Moreover, it sometimes suppresses the operation of nonlinear fiber devices such as bistable devices and switching devices. SBS is useful for applications such as fiber sensors, Brillouin lasers, Brillouin amplifiers, pulse compressors, and phase conjugates. Although organic crystals have been found to exhibit high-Brillouin gain [297, 298], there is no high-gain material that can be drawn to be an optical fiber. Because chalcogenide glasses are transparent in the infrared region and have high third-order nonlinearity, they are considered to be potential materials for functional optical fibers. Three important parameters (Brillouin-gain coefficient $g_B$, phonon lifetime $T_B$ and Brillouin shift $\nu_B$) should be considered when studying SBS. The parameters of SBS materials are closely related to those of acousto-optical materials, which are applicable to modulators, deflectors, scanners, converters, etc. In these two effects, an excited acoustic wave causes periodic density variations in the direction of propagation, and an optical wave incident normally or obliquely with respect to the moving grating is reflected or deflected, respectively. In acousto-optical devices, the acoustic wave is usually excited by a transducer, whereas the acoustic wave for inducing Brillouin scattering is coherently excited by a pump optical field via an electrostriction coefficient of the material. Therefore, it is possible to estimate the magnitude of the Brillouin-gain coefficient from known values of acoustic material parameters. It should be noted that the most suitable figure of merit, independent of device configuration used to determine the diffraction efficiency of acousto-optical devices, is given by [299, 300]:

$$M_1 = \frac{n^7 p_{12}^2}{\rho v_A}, \tag{5.52}$$

where $n$ is the refractive index, $p_{12}$ is the longitudinal photoelastic constant of the material, $\rho$ is the density of the material, and $\nu_A$ is the velocity of sound. Using $M_1$, one can express the Brillouin-gain coefficient $g_B$ as [236]:

$$g_B = \frac{2\pi n^7 p_{12}^2}{c\lambda^2 \rho \nu_A \Delta\nu_\mathrm{B}} = \frac{2\pi^2}{c\lambda^2} M_1 T_\mathrm{B}, \tag{5.53}$$

where $c$ is the speed of light, $\lambda$ is the free-space wavelength of the pump wave, and $\Delta\nu_\mathrm{B}$ is the full-width half-maximum of the Brillouin-gain spectrum. The spectral width $\Delta\nu_\mathrm{B}$ is related to the damping time of acoustic waves or the phonon lifetime $T_\mathrm{B}$ by:

$$\Delta\nu_\mathrm{B} = \frac{1}{\pi T_\mathrm{B}}. \tag{5.54}$$

One can estimate the phonon lifetime $T_\mathrm{B}$ from data for the attenuation coefficient $\alpha_\mathrm{A}$ and from the velocity $\nu_\mathrm{A}$ of acoustic waves [296]:

$$T_\mathrm{B} = \frac{1}{\alpha_\mathrm{A} \nu_\mathrm{A}}. \tag{5.55}$$

Values of $g_B$ and $T_\mathrm{B}$ have been calculated for fused silica, $As_2S_3$ and $As_2Se_3$ and are shown in Table 5.3 [296]. For fused silica, the calculated values of $g_B$ and $T_\mathrm{B}$ agree well with the reported values of $g_B = 3.5 - 3.8 \times 10^{-11}\,\mathrm{m\,W^{-1}}$ and $T_\mathrm{B} = 4\,\mathrm{ns}$ at $1.06\,\mu\mathrm{m}$ [298]. The calculated magnitude of $g_B$ for $As_2S_3$ and $As_2Se_3$ glasses is $48.2 \times 10^{-11}$ and $53.2 \times 10^{-11}\,\mathrm{m\,W^{-1}}$, respectively, which are $\approx 20 - 25$ times that of fused silica. The calculated phonon lifetime $T_\mathrm{B}$ of both chalcogenide glasses is $\approx 1\,\mathrm{ns}$. The application of SBS is limited to pump pulses shorter than $T_\mathrm{B}$ because its generation is suppressed on such a time scale.

Thielen et al. [304] have given a computer model using a finite-element technique to model the behavior of a fiber Raman laser. The model demonstrates the feasibility of a mid-infrared fiber Raman laser pumped at $5.59\,\mu\mathrm{m}$ by a carbon monoxide laser and operating at a wavelength of $6.46\,\mu\mathrm{m}$. This

**Table 5.3.** Calculated Brillouin-gain coefficient $g_\mathrm{B}$ and phonon lifetime $T_\mathrm{B}$ of $SiO_2$, $As_2S_3$, $As_2Se_3$ glasses at $\lambda = 1.06\,\mu\mathrm{m}$ (after [296])

| material | n | $\rho$ ($\mathrm{g\,cm^{-3}}$) | $v_\mathrm{A}$ ($\mathrm{m\,s^{-1}}$) | $p_{12}$ | $\Gamma_\mathrm{A}$ ($\mathrm{dB\,cm^{-1}\,GHz^{-2}}$) | $\nu_\mathrm{B}$ (GHz) | $T_\mathrm{B}$ (ns) | $g_B$ ($\mathrm{m\,W^{-1}} \times 10^{-11}$) |
|---|---|---|---|---|---|---|---|---|
| $SiO_2$ | 1.45 | 2.20[a] | 5,960[a] | 0.286[b] | 12[a] | 16.3 | 4.57 | 2.24 |
| $As_2S_3$ | 2.48[c] | 3.20[a] | 2,600[c] | 0.299[d] | 170[a] | 12.2 | 1.33 | 48.2 |
| $As_2Se_3$ | 2.81[e] | 4.64[a] | 2,250[c] | 0.266[f] | 280[a] | 11.3 | 0.969 | 53.2 |

[a][300], [b][297], [c][301], [d][299], [e][302], [f][303]

wavelength may be of interest in surgical applications since it corresponds to the amide II absorption. It was shown that slope efficiencies (the slope of calculated Raman laser, output versus pump laser input power) approaching 80% with moderate threshold powers can be achieved. Reducing the loss of the fiber is one way to increase the efficiencies and reduce the threshold powers. Other methods include, for example, increasing the numerical aperture NA of the fiber, which will further reduce the mode field radius yielding a higher gain in the fiber. If a large NA is not desirable for beam-divergence considerations, then making a tapered fiber is also possible. In this case, a low-NA fiber is tapered down, providing an adiabatic transition from a large-core low-NA fiber to a small-core large-NA fiber. This technique yields high intensities in the fiber while maintaining a low-NA output [304].

Asobe et al. [305] have demonstrated laser-diode-driven all-optical switching with an $As_2S_3$-based glass fiber only 2 m long with assistance from an erbium-doped fiber amplifier. If a mode-locked Nd:YAG laser used as the gate pulse source for an optical Kerr shutter switch in $As_2S_3$-based fiber at 1.3 μm [306] were replaced with a laser diode, it would stabilize switching (depending primarily on the stability of the laser system), reduce timing jitter between the gate and the signal pulses (which would substantially increase the operating speed), and simplify optical-signal processing. A distributed-feedback laser diode (DFB-LD) with a wavelength of 1.552 μm was used as the gate pulse source. Gain switching of the laser with an electrical-pulse generator yielded an 18-ps-wide (FWHM) pulse with a repetition rate of 100 MHz. The resulting pulse was compressed using a 270 m-long fiber with a normal dispersion of 70 ps (km nm)$^{-1}$ and amplified with a diode-pumped 120 m-long EDFA with an erbium concentration of 880 p.p.m. With a gate pulse 8.2 ps wide, a peak power of 13.9 W was obtained. Using the 2 m-long $As_2S_3$ chalcogenide fiber, they achieved high repetition-rate switching with multiplexed signal pulses. Ultrafast switching with a repetition rate as high as 80 GHz was successfully demonstrated.

# 6

# Optical Switching in Chalcogenide Glasses

## 6.1 Criteria of Material Properties for All-optical Switching

One of the key problems in developing all-optical switches is to obtain high switching speeds by using purely electronic nonlinearities. To have an efficient switching process, there should be no generation of real populations or carriers which would limit the switching recovery speed. There should also be no loss involved in the process of switching. There are therefore a set of material constraints or figures of merit to be considered. It is helpful to examine first the effects of linear and nonlinear absorption in a waveguide. In order to have an optical-switching operation, a pump or control pulse must produce a sufficiently large nonlinear phase shift. The integral of the intensity over the device length gives the total phase shift accumulated in the waveguide.

Let us first consider that two-photon absorption is negligible and consider only the effect of linear absorption, for which the transmitted intensity is given by:

$$I(z) = I_0 \mathrm{e}^{-\alpha z}. \tag{6.1}$$

The total nonlinear phase shift is increased by increasing either the incident intensity or the device length. When the effect of two-photon absorption is considered, we notice that it has a limiting effect on the maximum transmitted intensity through the waveguide [307, 308]. The intensity as a function of length is given by:

$$I(z) = \frac{I_0 \mathrm{e}^{-\alpha z}}{1 + \beta I_0 (1 - \mathrm{e}^{-\alpha z})/\alpha}. \tag{6.2}$$

The two-photon absorption increases with increasing incident intensity and, in the limit of high peak intensities or large two-photon absorption, the output of the waveguide approaches a value that is independent of the incident intensity, given by:

$$I_{\max} = \alpha \mathrm{e}^{-\alpha z}/\beta(1 - \mathrm{e}^{-\alpha z}). \tag{6.3}$$

As a result of linear as well as nonlinear absorption, and hence a reduction in the intensity, the total accumulated phase shift decreases. Absorption also produces carriers which, once excited, limit the switching recovery time.

In order to obtain high-speed optical switching, it is desirable to maximize the integrated area underneath the $I$ versus $l$ (waveguide length) curve and minimize the total absorption.

To investigate explicitly the role of the linear and nonlinear optical constants in determining a figure of merit, let us consider the total phase shift produced by a control pulse of duration $\tau$. The phase change over a length $l$ is given by:

$$\Delta\Phi = \frac{2\pi}{\lambda} n_2 \int_0^l I(z)\,\mathrm{d}z + \frac{2\pi}{\lambda}\left(\frac{\partial n}{\partial N}\right)\frac{1}{h\nu}\int_0^\tau [I_0 - I(t)]\,\mathrm{d}t, \tag{6.4}$$

where the first term describes the phase change produced by the instantaneous nonlinearity $n_2$, while the second term describes the effects of carrier generation on the nonlinear index. For the case of negligible two-photon absorption, the total nonlinear phase shift is given by:

$$\Delta\Phi = \frac{2\pi}{\lambda} n_2 I_0 \left(\frac{1 - \mathrm{e}^{-\alpha l}}{\alpha}\right). \tag{6.5}$$

We may define a figure of merit to describe the role of nonlinear index and linear absorption as:

$$\text{Figure of merit} = \frac{n_2}{\alpha}. \tag{6.6}$$

In the case when two-photon absorption is present, the nonlinear phase shift may be calculated by substituting (6.2) in (6.4) and we obtain:

$$\Delta\Phi = \frac{2\pi}{\lambda} n_2 \frac{1}{\beta} \ln\left(1 + \frac{\beta}{\lambda} I_0 [1 - \mathrm{e}^{-\alpha l}]\right). \tag{6.7}$$

We can obtain the incident intensity necessary to produce a $\pi$ phase shift:

$$I_\pi = \frac{[e^{\lambda\beta/2n_2} - 1]}{\beta}\left(\frac{1 - \mathrm{e}^{-\alpha l}}{\alpha}\right). \tag{6.8}$$

When $\lambda\beta/n_2$ is large, (6.8) predicts that the intensity $I_\pi$ required for a $\pi$ phase shift increases without bound. A second figure of merit relates two-photon absorption and the nonlinear index:

$$\text{Figure of merit} = \frac{2n_2}{\lambda\beta}. \tag{6.9}$$

This figure of merit must be maximized in order to obtain switching with negligible two-photon absorption. We can now consider the limiting effect of carrier generation as a result of two-photon absorption.

Consider a square pulse of intensity $I$ and duration $\tau$. The total number of carriers generated depends on the time integral of the absorption and scales as the pulse duration $\tau$. We can obtain the nonlinear phase shift produced by the excited carriers as:

$$\Delta\Phi = \frac{2\pi}{\lambda}\frac{(\partial n)}{(\partial N)}\frac{1}{h\nu}[I_0 - I(l)]\tau. \tag{6.10}$$

The above equation shows that shorter pulses are more desirable, since they generate a smaller excited population. The above points show the complexity of the problem of developing materials for all-optical switching. In order to have a successful switch, other points should also be taken into account. These include the wavelength of operation, dispersion of the nonlinear properties, pulse intensities and duration.

## 6.2 Design Issues for All-Optical Switching

In order to develop a viable all-optical switch, other design issues should also be taken into account. The basic problem is that the switching pulses are not left invariant by the switching operation. The complication arises since the phase is varying dynamically because the control-pulse intensity is time dependent. Spectral broadening and pulse reshaping change the switching pulse. Since the pulse intensity is a function of time, the phase shift is also time dependent. The effect of a time-varying phase or phase modulation is to induce a frequency chirp on the signal pulse. Increasing the bandwidth can significantly enhance the effects of pulse broadening from dispersion. The problems of spectral broadening and pulse reshaping are in fact complementary. We should note that pulse reshaping results in a shortened pulse being generated.

One of the most promising approaches for all-optical switching which addresses a number of these problems is the use of solitons which allows dispersionless propagation. Here, self-phase modulation-frequency broadening balances negative group-velocity dispersion.

The use of solitons and soliton-collision schemes has been an active area of investigation for all-optical switching [309–312].

## 6.3 All-Optical Switching in Chalcogenide Glasses

### 6.3.1 All-Optical Switching using Chalcogenide Glass Fibers

All-optical switching using an $As_2S_3$-based fiber was first shown by a Kerr-shutter experiment [313]. The polarization of the signal and gate pulses is offset by 45°. A gate pulse induces a phase-shift difference between two signal components whose polarizations are parallel and perpendicular to that of the gate. When the phase-shift difference reaches $\pi$, the polarization of the

signal is switched by 90°. In the optical-Kerr effect, the nonlinear phase shift induced by an intense pump beam (gate) is used to change the transmission of a weak probe (signal) through a nonlinear medium [314]. This effect can be used to make an optical shutter with picosecond response times [315]. The operating principle of a Kerr shutter can be understood in the following way. The pump and probe beams are linearly polarized at the fiber input with an angle of 45° between their directions of polarization. A crossed polarizer at the fiber output blocks probe transmission in the absence of the pump beam. When the pump is turned on, the refractive indices of the parallel and perpendicular components of the probe change slightly due to pump-induced birefringence. The phase difference between the two components at the fiber output manifests as a change in the probe polarization, and a portion of the probe intensity is transmitted through the polarizer. The probe transmissivity depends on the pump intensity and can be controlled simply by changing it. In particular, a pulse at the pump wavelength opens the Kerr shutter only during its passage through the fiber.

The most successful implementation of nonlinear interference effects to switching has been with the NOLM. In this case (Fig. 6.1), both beams follow the same fiber path, but they propagate in opposite directions. The relative beam powers are determined by the coupling ratio $r : (1 - r)$ at the coupler. After one round trip, the beams both encounter the coupler again and a part ($p_r$) of the total signal is reflected back to the incidence channel, and the remainder is transmitted ($p_o$). If $r \neq 0.5$, the more intense of the two counterpropagating beams experiences a larger nonlinear phase shift and the differential phase shift is [316]:

$$\Delta\phi^{\mathrm{NL}} = k_0 n_2 L[p_1 - p_2]/A_{\mathrm{eff}}, \tag{6.11}$$

where $p_1$ and $p_2$ are the powers of the counterpropagating beams and

$$p_i = p_1 + p_2. \tag{6.12}$$

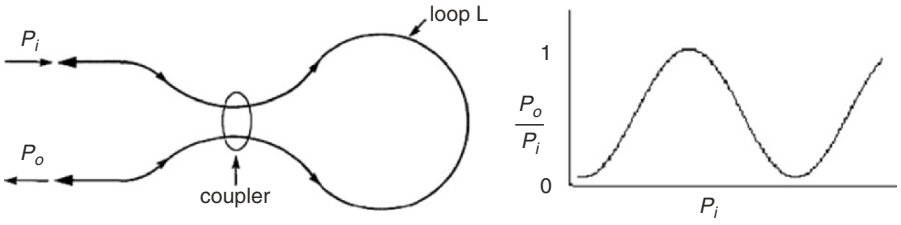


**Fig. 6.1.** Schematic representation of an NOLM and its typical response (after [316])

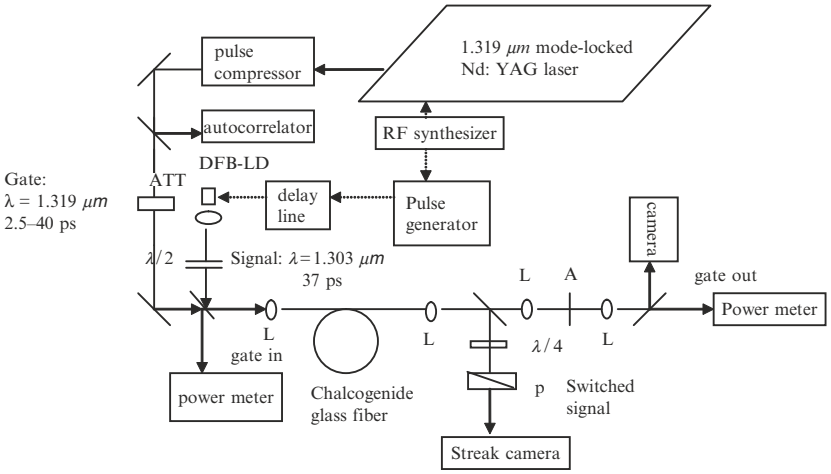


**Fig. 6.2.** Experimental layout of an optical Kerr-shutter configuration. ATT: attenuator, $\lambda/2$: half plate, $\lambda/4$: quarter-wave plate, L: lens, A: variable aperture, p: polarizer (after [317])



As a result, the interference condition at the coupler is changed when the two counterpropagating beams meet. This gives the response function:

$$p_t = p_i(1 - 2r(1 - r)\,[1 + \cos([1 - 2r]\Delta\beta_o p_i L)]). \tag{6.13}$$

To investigate the potential of chalcogenide fibers for all-optical switches, an optical Kerr-shutter experiment was constructed [317]. A schematic of the experimental set up is shown in Fig. 6.2. The gate pulse was generated from a mode-locked Nd:YAG laser operating at a wavelength of 1.319 µm, with a repetition of 100 MHz. Short pulses were obtained using a pulse compressor which consisted of a fiber and a grating pair [318]. Gate pulses of 2.5 ps to 40 ps width with an assumed Gaussian profile were obtained.

A distributed feedback (DFB) laser diode operating at a wavelength of 1.303 µm was used as the signal source. The gate and signal beams were combined with a dichroic mirror and focused into the chalcogenide fiber. The gate power to the fiber was monitored using the gate beam reflected by the dichroic mirror. The polarization of the gate pulses was coincident with the optical axes of the fiber. There was a difference of 45° in the polarization between the gate and signal. The transmitted signal pulses having elliptical polarization were linearly polarized by a quarter-wave plate and analyzed by a polarizer. "Normally on" and "Normally off" states could be obtained by adjusting the polarizer. The temporal waveform of the switched signal pulses was observed with a streak camera.

The switching time and $n_2$ value were estimated using an approximation where the nonlinear refractive effect is instantaneous within the time scale of

the gate pulse, the gate pulses have a Gaussian profile, gate pulse broadening due to self-phase modulation (SPM) and GVD is neglected, and the peak-power depletion of the gate pulse is caused only by the linear loss of the fiber. The phase-shift difference $\Delta\phi(t)$ between two orthogonal polarization modes caused by cross-phase modulation (XPM) is given by [313]:

$$\Delta\phi(t) = \frac{2}{3}\frac{4\pi n_2}{\lambda_s A_{\text{eff}}} I_g(0,0) L f(t) \tag{6.14}$$

where $L$ is the fiber length, $\lambda_{\text{s}}$ is the signal wavelength, $A_{\text{eff}}$ is the effective core area, $I_{\text{g}}(t,z)$ is the gate-pulse profile, and $f(t)$ is the normalized phase shift.

It can be shown [317] that the signal transmission is given by:

$$T(t) = \sin^2 \frac{\Delta\phi(t)}{2}. \tag{6.15}$$

Regarding the operating wavelength, 1.55 μm is the common wavelength for optical communication. In addition, the erbium-doped fiber amplifier (EDFA) works in this region and hence it is easy to obtain an intense optical pulse from a laser diode. As a result, laser-diode driven ultrafast all-optical switching becomes possible by using an $As_2S_3$-based glass fiber and with the assistance of an EDFA. A schematic of the experimental set up is shown in Fig. 6.3.

An optical Kerr-shutter configuration was used for simplicity. A distributed-feedback laser diode (DFB-LD) with a wavelength of 1.552 μm was used as the gate-pulse source. Gain switching of the laser with an electrical-pulse generator yields an 18 ps-wide (FWHM) pulse with a repetition rate of

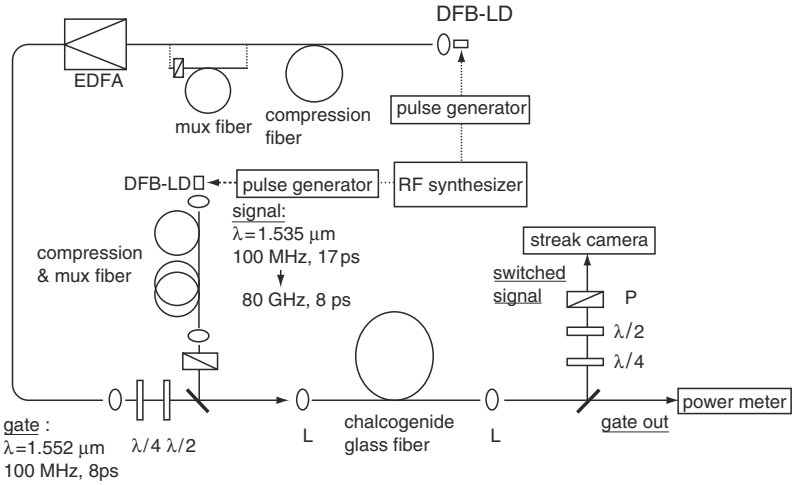


**Fig. 6.3.** Experimental setup of laser-diode driven ultrafast all-optical switching. L, lens; P, polarizer; mux, multiplexing; DFB-LD, distributed-feedback laser diode (after [319])

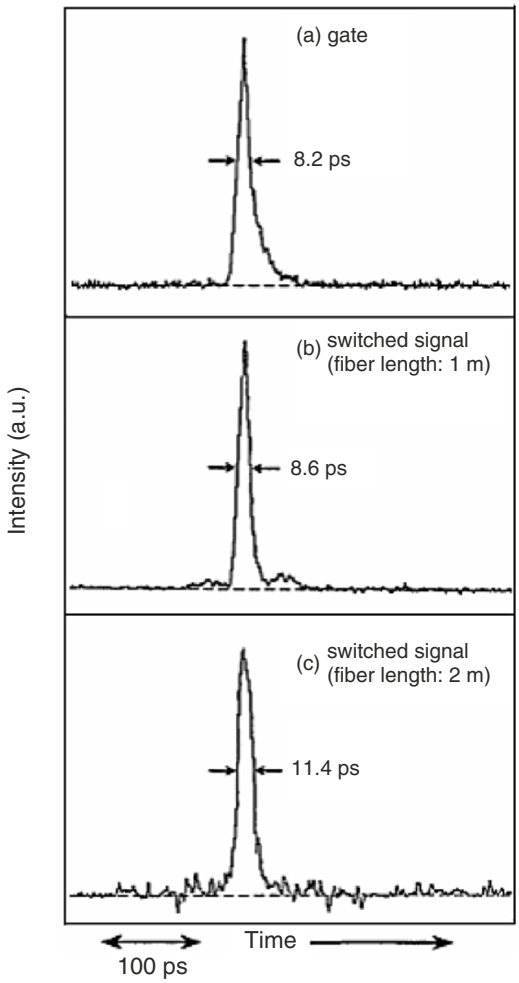


**Fig. 6.4.** (**a**) Gate pulse and (**b**), (**c**) switched signal waveforms with different fiber lengths using an $As_2 S_3$-based glass fiber (after [319])

100 MHz. The resulting pulse was compressed with a 270-m-long fiber with a normal dispersion of 70 ps (km nm)$^{-1}$ and amplified with a diode-pumped 120-m-long EDFA. With a gate pulse of 8.2 ps, a peak power of 13.9 W was obtained. Figures 6.4a and b show the waveform of the gate pulse and the switched signal pulse, respectively, for a 1-m-long $As_2 S_3$ fiber. The switched signal pulse was observed to be 8.6 ps wide. This value is close to the gate pulse width and confirms that the nonlinear index change is instantaneous within the time scale of the gate pulse width. Figure 6.4c shows the waveform of the switched signal for a 2-m-long fiber, corresponding to a phase shift of $0.6\pi$. A switching time of 11.4 ps was observed, which is very close to the 11.0 ps that is calculated from the phase-shift profile [319].

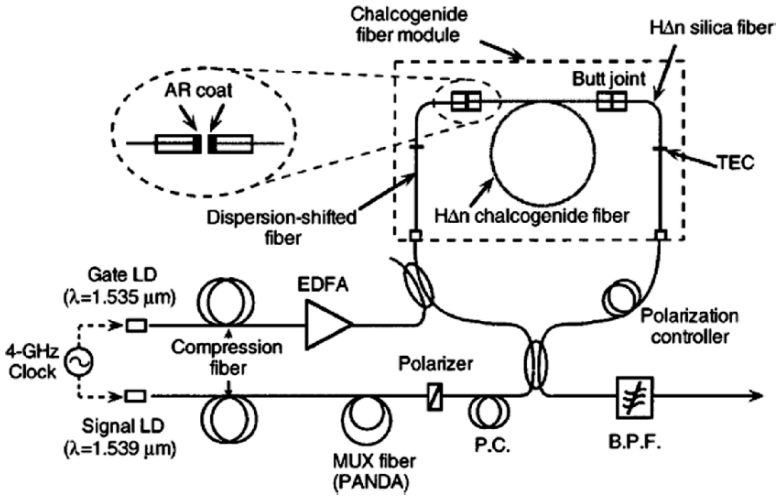


**Fig. 6.5.** Experimental setup for all-optical switching with NOLM using an $As_2S_3$-based fiber (after [321]). P.C.; polarization controller, $H\Delta n$ fiber; fiber with a large effective refractive index between core and cladding, PANDA; polarization-maintaining fiber, TEC; thermally diffused expanded core



The optical Kerr shutter is useful in checking the extent of nonlinearity, but it does not necessarily provide the lowest switching power. By comparison, an NOLM utilizes the difference in phase shift between two signal beams which propagate in the fiber in the same and the opposite direction as the gate pulse [320]. Thus the NOLM configuration is advantageous in reducing the signal power. Switching with NOLM using an $As_2S_3$-based fiber has been demonstrated [321]. Figure 6.5 shows the schematic experimental set up.

A chalcogenide fiber module consisting of a 4-m-long $As_2S_3$-based fiber, small-core silica-based fiber, and a conventional dispersion-shifted fiber (fiber core is silica with small amounts of dopants such as $GeO_2$ and $P_2O_5$) was fabricated. In order to prevent Fresnel reflection from the interface between the silica-based fiber and the $As_2S_3$-based glass fiber, the edges of both fibers were antireflection coated (AR) and butt-jointed. The small-core silica-based fiber was spliced to the conventional dispersion-shifted fiber using TEC (thermally diffused expanded core) technology. The NOLM consisted of a 30 dB fiber coupler, the chalcogenide fiber module, and a polarization controller (PC). Gate and signal pulses were generated by gain switching of the DFB laser diodes and compression with a positive dispersion fiber. The gate pulse was amplified with an EDFA. The signal pulse was multiplexed using polarization dispersion in a polarization-maintaining (PANDA) fiber. The switching power was reduced to 0.4 W using the NOLM configuration with a low-loss fiber. Figure 6.6 shows the results of the demultiplexing experiment.

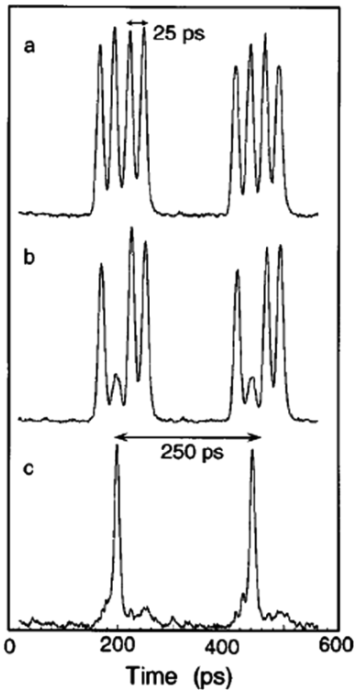


**Fig. 6.6.** Temporal waveforms of (**a**) input signal and (**b**, **c**) switched signals in an all-optical demultiplexing experiment (after [321])



The input signal had a pulse period of 25 ps, which corresponds to 40 GHz. Asobe et al. [321] were able to extract one of the multiplexed pulses at a gate repetition of 4 GHz.

### 6.3.2 All-Optical Switching in Thin Chalcogenide Films

#### Modeling of an NLDC Switch

The demands for higher-data rate communication systems are stimulating research into new techniques for enhancing the capabilities of tomorrow's systems. Although wavelength-division-multiplexing techniques show great promise for upgrading existing systems, there is a simultaneous effort focused on enhancing system functionality and network flexibility through the use of fast optical switching and signal-processing techniques, and recent multi-terabit transmission demonstrations have involved both wavelength- and time-division multiplexed systems [322]. Fast switching on the timescale of picoseconds cannot be performed with electronic devices and researchers

are investigating the use of all-optical components for ultra-fast operations such as switching, and time-division multiplexing and demultiplexing.

The requirement for operating times to be significantly faster than those possible with electronics means that these optical components must operate in the picosecond or subpicosecond range. Compact devices will require large optical nonlinearities, so that switching can be effected at modest power levels. Another desirable feature relates to the integrability of these ultra-fast switching components with other optoelectronic components, such as lasers and detectors. Although normal III–V semiconductor materials exhibit large optical nonlinearities near the band edge (with photon excitation having energies equal to or near the optical gap energy), they have a relatively slow (nanosecond) response due to slow recombination times for the optically-excited carriers [322].

The small size of these switching elements, combined with their integrability and low power requirements, provide considerable promise for practical applications.

The potential applications of nonlinear directional couplers (NLDC) in all-optical processing have attracted a great deal of research since they were first introduced by Jensen in 1982 [323]. Usually, these devices can be used as optical switches, optical limiters and logic gates. When they are used as switching devices, NLDC can be self-switching devices. A directional coupler consists of two identical single-mode waveguides (bar and cross) placed in closed proximity to permit coupling between the evanescent fields. It is well known that a two-waveguide NLDC with suitable length behaves as an optical switch. For use as a self-switch device, couplers with Kerr nonlinearity are considered. When the optical power in a directional coupler is high enough that the nonlinearity in the coupler becomes important, power switching between the two waveguides becomes dependent on the optical power.

Chalcogenide glasses have an ultrafast response time, low linear and nonlinear losses, high nonlinear Kerr coefficients, low noise and straightforward manufacturing with existing planar waveguide technology [324]. Hence they are a good candidate for making all-optical switches, especially NLDC switches. By depositing chalcogenide glass thin films on silica substrates using pulsed laser deposition (PLD), single-mode channel waveguides [325] have been fabricated. Waveguides can also be written directly by means of selective photo-bleaching the chalcogenide film (by illuminating the material with above-band-gap light). Normally, illumination of chalcogenide glasses with above-band-gap light causes photo-darkening to occur in these glasses. In the case of GeAsSe however, photo-bleaching occurs as a result of glass illumination. Illuminated areas have lower refractive indices and can be used as cladding for the waveguide. Finally, by means of two such waveguides parallel and near to each other, a nonlinear directional coupler (NLDC) is constructed. By using the nonlinear properties of chalcogenide films, Zakery et al. [326] studied the switching characteristic of NLDC. They used exactly the same equation used by Yang, Villeneuve, and Stegeman [327] but Zakery et al. [326]

considered both two- and three-photon absorption mechanisms and neglected group-velocity dispersion and free-carrier absorption. The equation governing the complex amplitudes $A_1$ and $A_2$ in the two waveguides of NLDC are given by [327].

$$\mathrm{i}\frac{\partial A_{1,2}}{\partial z} + \frac{2\pi a_2 n_2}{\lambda}\left(1 + \frac{\mathrm{i}T}{8\pi}\right)|A_{1,2}|^2 A_{1,2} + \frac{\mathrm{i}\beta_3 a_3}{2}|A_{1,2}|^4 A_{1,2} + KA_{2,1} = 0. \tag{6.16}$$

Here $z, \lambda, K$ are the propagation coordinate, wavelength and linear coupling coefficient, respectively. The 2PA figure of merit $T$ is given by $T = 2\beta_2\lambda/n_2$ and $n_2, \beta_2, \beta_3$ are the nonlinear refractive index, 2PA, and 3PA coefficients, respectively. $a_2$ and $a_3$ represent overlap integrals over the modal profiles in the waveguides for the third- and fifth-order nonlinearities, respectively. By using the normalized parameters $\zeta = z/L_\mathrm{c}$ and $q_{1,2} = (2\pi a_2 n_2 L_\mathrm{c}/\lambda)^{1/2}$, with $L_c = \pi/2K$ representing one half-beat length, (6.16) becomes

$$\mathrm{i}\frac{\partial q_{1,2}}{\partial \varsigma} + \left(1 + \frac{\mathrm{i}T}{8\pi}\right)|q_{1,2}|^2 q_{1,2} + \frac{\mathrm{i}V}{8\pi}|q_{1,2}|^4 q_{1,2} + \frac{\pi}{2}q_{2,1} = 0 \tag{6.17}$$

Here $V = I_\mathrm{c}\lambda\beta_3 a_3/(a_2 n_2)$, $I_\mathrm{c}$ being the cw critical intensity for switching, given by $\lambda/(a_2 n_2 L_\mathrm{c})$. In (6.17), $V$ is the figure of merit associated with 3PA, which is dependent not only on material parameters ($n_2$ and $\beta_3$) but also on device design. The effect of 3PA on switching operation was widely studied in [327] and in the absence of 2PA, $V$ must be smaller than 0.68. Fortunately, the 3PA in chalcogenide glasses is very low but not negligible [328], especially at high input powers. Because $V$ is also design dependent, a suitable value would be $V = 0.1$ [327]. From their experimental results on chalcogenide films prepared by PLD, Zakery et al. [326] obtained $T = 0.2$. By using this parameter, they studied the NLDC switch. Suppose the input power ($P_\mathrm{in}$) enters the bar state (the switch has two input states called the bar and cross states) of the NLDC. They studied the switching behavior by solving numerically the coupled differential equations (6.17) and used a Runge-Kutta method by taking into account two- and three-photon absorption coefficients. Figure 6.7 plots the normalized output power (fraction of the output power to the input power) from the bar state versus normalized distance for various input powers. For comparison with the actual value ($T = 0.2$ and $V = 0.1$) that they chose from experimental data, they also plotted normalized output power in the ideal case ($T = 0$ and $V = 0$ means two- and three-photon absorption are zero). In Fig. 6.7 for the ideal case, complete switching occurs at the half-beat length ($\zeta = 1$) which means that at the half-beat length for low input powers, the output power from the bar state is zero while for high input powers, the output power from the bar state is 100% of the input power. This shows that the NLDC at the half-beat length behaves as a self-switch. On the other hand, in the same figure (Fig. 6.7) for the actual case ($T = 0.2$ and $V = 0.1$) at the half-beat length there is no difference between the ideal and actual cases when input power is low, but for high input powers two- and

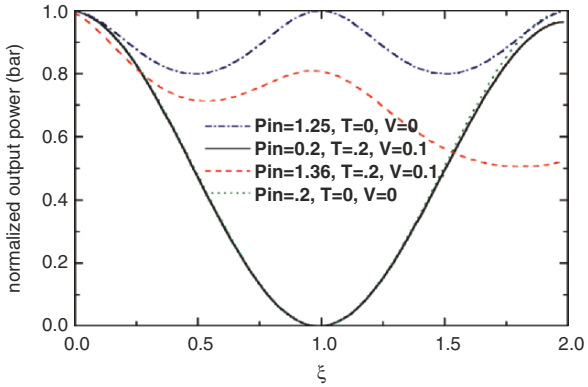


**Fig. 6.7.** Normalized output power from the bar state versus normalized distance (with respect to the half-beat length) $\varsigma$ for various normalized input powers. For low input powers and at half-beat length ($\varsigma = 1$), all of the power is in the cross state and for high input powers, output power goes only into the bar state (after [326])

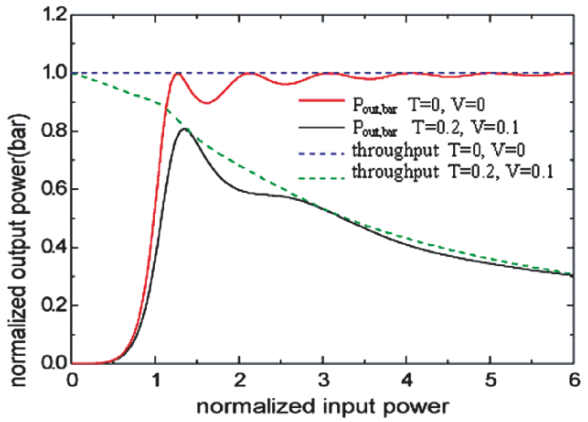


**Fig. 6.8.** Normalized output power (with respect to normalized input power) in the bar state and throughput (sum of normalized output powers from the bar and cross states) versus normalized input power at half-beat length for the actual (lower *curves*) and ideal cases (upper *curves*) (after [326])

three-photon absorption affects the output power and reduces it to 80% of the input power. This result shows that, although operation of the switch is not complete, switching occurs and is good enough for applications.

For a more complete study of the switching behavior, Zakery et al. [326] plotted normalized output power in the bar state versus the input power at half-beat length in the ideal and actual cases. As seen in Fig. 6.8, by increasing the normalized input power, the normalized output power in the bar state also increases until it reaches the maximum normalized output power, as expected.

For the ideal case, the maximum output power was 100% and for the actual case it was 80%. An important point to note in Fig. 6.8 is that the maximum output power does not occur at the same normalized input power for the ideal and actual cases. For the ideal case, the first maximum occurs at 1.25 but for the actual case it increases to 1.36 times the normalized input power.

After the first maximum in the ideal case, we have another maximum, which suggests that the switching can occur at higher normalized input powers, but for the actual case we have only one maximum after the first maximum and throughput decreases and switching does not occur above 1.36 times the normalized input power.

Figures 6.9 and 6.10 are similar to Fig. 6.8 but we plotted output power (not normalized with respect to the input power) for the ideal and actual cases at half-beat length, respectively. We see the behavior of the switch at low powers and also we observe that switching occurs at a normalized input power of 1.25 for the ideal and 1.36 for the actual case. Also, we see that in the ideal case for input powers above 1.25, switching occurs and the output power is the same as the input power. For the actual case for powers above 1.36, we observe that the output power remains roughly constant, which suggests that, with increasing the input power, the output power does not change and hence the input power does not affect the output power. This result may be used in other applications.

Zakery et al. [329] have also modeled the behavior of the nonlinear directional switch by taking into account the effect of group-velocity dispersion

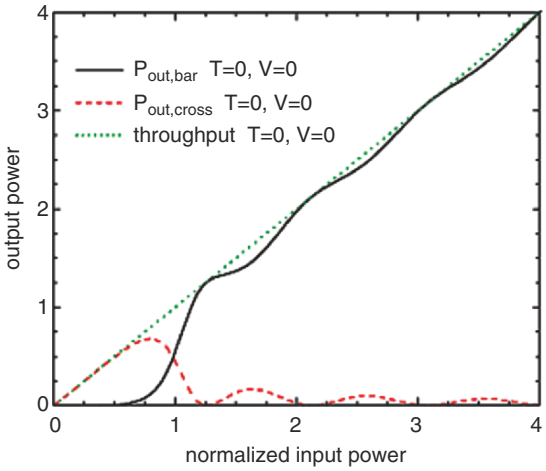


**Fig. 6.9.** Output power in the bar state and throughput (sum of output powers from the bar and cross states) versus normalized cw input power at half-beat length for the ideal case. For low input power, the output power in the bar state is very nearly proportional to input power (after [326])

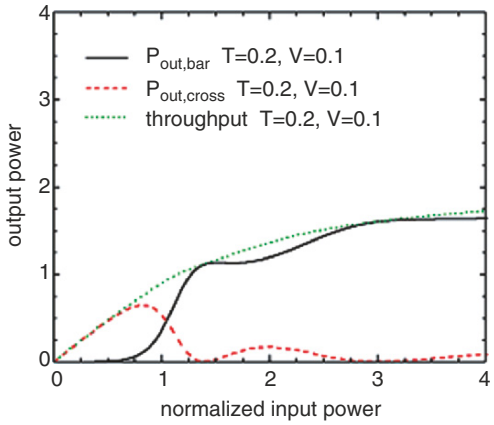


**Fig. 6.10.** Output power in the cross state and throughput (sum of output powers from the bar and cross states) versus normalized cw input power at half-beat length for the actual case. For low input powers, the output power from the cross state is proportional to input power. For high input powers, contrary to the ideal case, the output power remains constant (after [326])

GVD on pulse propagation. An equation of the form below is obtained which can be solved using Fourier series analysis techniques (FSAT) [330].

$$\mathrm{i}\frac{\partial q_{1,2}}{\partial \varsigma} - H\frac{\partial^2 q_{1,2}}{\partial t'^2} + \left(1 + \frac{\mathrm{i}T}{8\pi}\right)|q_{1,2}|^2 q_{1,2} + \frac{\mathrm{i}V}{8\pi}|q_{1,2}|^4 q_{1,2} + \frac{\pi}{2}q_{2,1} = 0 \quad (6.18)$$

$$H = B_2\pi/4K$$

$$t' = t - z/v_\mathrm{g},$$

where $v_\mathrm{g}$ is the group velocity, t is time, $B_2$ is GVD, and $K$ is the usual coupling coefficient (between field amplitudes in two waveguides) as previously defined in (6.16). For the ideal case, where two-and three-photon absorption coefficients are zero, the switch performance was studied when an input pulse is entered the bar state. As Fig. 6.11 shows, for pulses with low input intensities in the bar state, the performance of the switch is complete and efficient coupling is taking place. The effect of GVD is to broaden the pulse, as expected.

For higher input pulse intensities, i.e., Fig. 6.12 and for the case of $A = 2$, switching is still taking place but high nonlinearity starts to show its effect by narrowing of the pulse, as is seen at long enough $\zeta$ (normalized distance in the waveguide). If we increase the input pulse intensity still further, as seen in Fig. 6.13, although the switching is still taking place, its performance is not satisfactory. The pulse shape changes and is chirped; moreover, higher nonlinearities lead to further narrowing of the pulse. It seems that if some higher

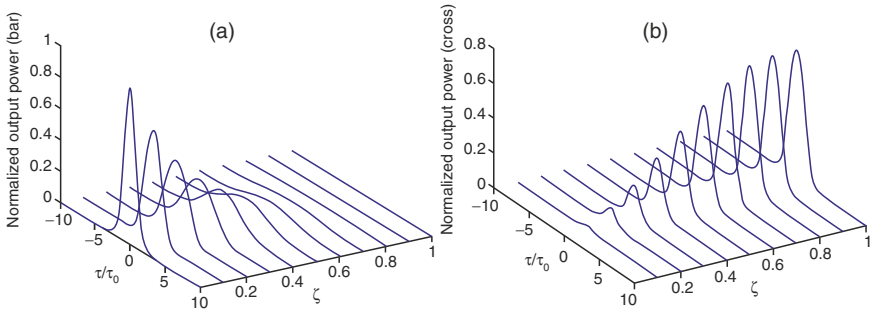


**Fig. 6.11.** Normalized output power for pulse propagation in (**a**) bar state (**b**) cross state of NLDC versus normalized distance $\zeta$ and normalized time $\tau/\tau_0$ for low input intensities in the bar state. $H = 1$ and $A = 0.3$ (after [329]). $H$ is proportional to the ratio of GVD and the coupling coefficient, and $A$ represents the input pulse intensity

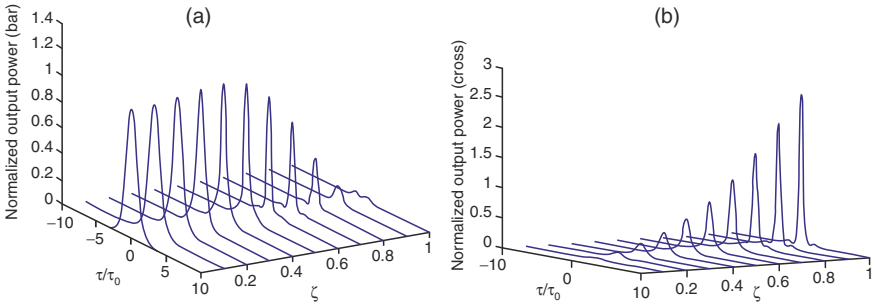


**Fig. 6.12.** Normalized output power for pulse propagation in (**a**) bar state (**b**) cross state of NLDC versus normalized distance $\zeta$ for medium input intensities in the bar state. $H = 1$ and $A = 2$ (after [329])

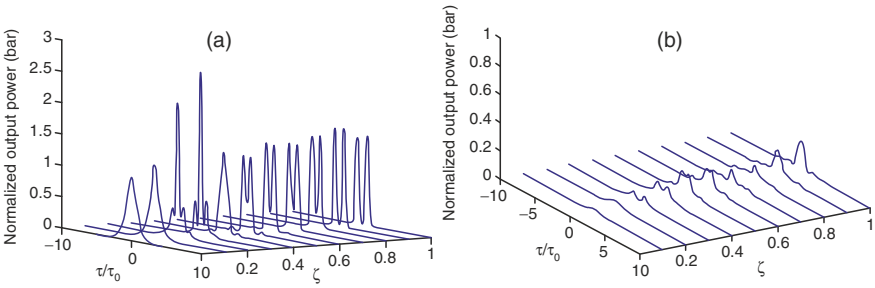


**Fig. 6.13.** Normalized output power for pulse propagation in (**a**) bar state (**b**) cross state of NLDC versus normalized distance $\zeta$ for high input intensities in the bar state. $H = 1$ and $A = 4$ (after [329])

GVD can be tolerated, a good performance of the switch can be expected even at high input pulse intensities.

### Fabrication and Characterization of NLDC Switches Made in Chalcogenide Films

At present, investigations of integrated NLDCs for switching applications are focused on semiconductor materials such as AlGaAs and GaInAs [331, 332] because of their easy fabrication by conventional integrated-circuit processes. However, two-photon absorption can significantly attenuate signals in these materials when operating at 1.55 µm, and hence can reduce power efficiency.

Chalcogenide glasses possessing high third-order optical nonlinearity (up to 27,000 times that of silica) [333] and having generally a good nonlinear figure of merit are attractive candidates for all-optical processing applications. The application of single-mode $As_2S_3$ fibers at sub-watt powers in all-optical switching has already been demonstrated [319]. Ruan et al. [334] have also fabricated $As_2S_3$ rib waveguides with losses as low as $0.2\,dB\,cm^{-1}$ at 1.55 µm using standard photolithography and ICP etching [334]. Another attractive feature of chalcogenide waveguides is their very small mode area due to a large refractive-index contrast between the chalcogenide core and a polymer or air clad. As a result, the optical-field intensity is enhanced significantly in the chalcogenide waveguide. Furthermore, nonlinear phase shifts as large as $4.7\pi$ have been observed in a 6-cm long $As_2S_3$ waveguide with an effective mode area $\sim 4.2\,\mu m^2$ [335]. Ruan et al. [336] have reported the design, fabrication and characterization of an NLDC in an $As_2S_3$ glass based on their ICP etching processes. On the whole, a satisfactory all-optical switching process was observed. The schematic structure of the directional coupler (DC) is illustrated in Fig. 6.14. The DC consisted of two parallel waveguides. A series of DCs with different structures were designed and laid out in a mask.

$As_2S_3$ films of about 2.6 µm thick were deposited using ultrafast pulsed-laser deposition onto oxidized silicon wafers. The $As_2S_3$ rib waveguides were etched using ICP etching [334,335]. The whole length of the device was 6.2 cm. For characterization of the devices fabricated, a low repetition (1.5 MHz) and

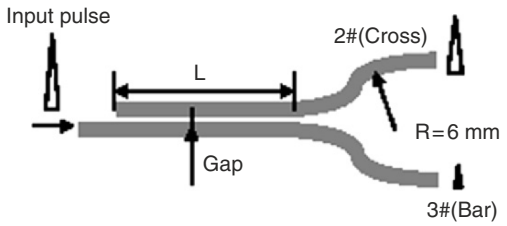


**Fig. 6.14.** Schematic view of the fabricated $As_2S_3$ directional coupler, where $R$ is the s-bend radius at the output, 2# and 3# are samples 2 and 3 (after [336])

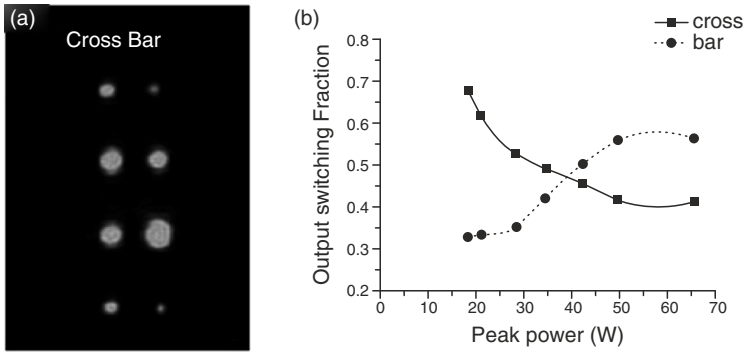


**Fig. 6.15.** (**a**) The recorded switching process for $As_2S_3$ films, (**b**) measured switching curve of $As_2S_3$ films as a function of peak power (after [336])

high peak power (1,300 W) pulsed laser was employed. The operating wavelength was 1.53 µm, while the pulse duration was about 7 ps.

Figure 6.15a shows the recorded images of the two output channels of one of the samples used. The peak power in the waveguide increased from a low value to a high level and then reduced to a low value again with a change in the input intensity. It can be seen from Fig. 6.15a that, at low intensity, the cross channel had the higher output. When the intensity increased, the output ratio started changing, and more power was coupled back to the bar channel. When the average power increased to about 0.7 mW, the intensities of the two spots switched, with a higher output in the bar channel. When the power decreased to a low level, the output ratio switched back and therefore a reversible switching behavior was observed.

Figure 6.15b shows a plot of the normalized output transmission of the cross and bar states as a function of the peak power in the waveguide. A switching effect is clearly indicated. Ruan et al. [336] defined the switching power as the peak power which produces the highest extinction ratio. As seen in Fig. 6.15b, the extinction ratios reached their maximum value when the peak power was 55 W and remained almost constant even when the peak power was further increased. Therefore, the switching power was considered to be about 55 W, corresponding to an intensity of $0.9\,\mathrm{GW\,cm^{-2}}$. Complete switching was not, however, possible due to pulse breakup, which occurred when the response time of the nonlinearity was shorter than the pulse duration [337].

## 6.4 All-Optical Switches, AND Gate, NOR Gate, etc.

### 6.4.1 Introduction

The concept of all-optical switching is shown schematically in Fig. 6.16. We can inject information in the form of a stream of optical pulses into one input

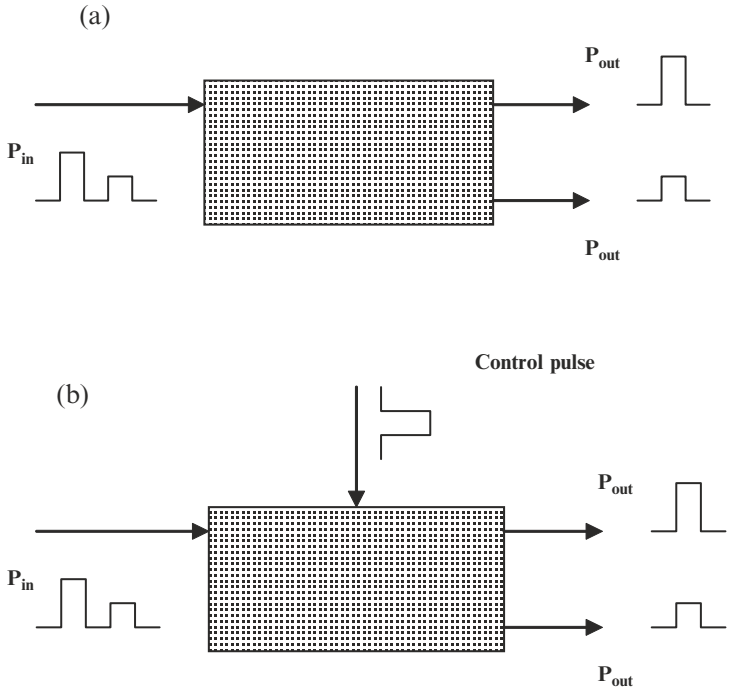


**Fig. 6.16.** Schematic of the operation of an all-optical switch for (**a**) self-switching based on input power, and (**b**) for control-pulse-induced switching

channel and the output channel is determined either by the power of the input signal, or the simultaneous presence of a control signal. One can write the intensity-dependent refractive index as:

$$n(I) = n_0 + \Delta n(I), \tag{6.19}$$

where $I$ is the local intensity. Many physical mechanisms can lead to $\Delta n(I)$. Index changes in semiconductors can be induced by carrier generation, exciton bleaching, optical Stark effect, bound electrons and absorption-induced thermal effects [338]. However, for ultrafast switching, it is necessary that the index changes on a subpicosecond time scale in response to an optical beam. This means that instantaneously responding (<1 ps) Kerr nonlinearities associated with electronic transitions in matter, for example nonresonant bound electrons in semiconductors or other materials, are needed and we can write :

$$\Delta n(I) = n_2 I. \tag{6.20}$$

We should also note that the index change is local, i.e., it occurs only at the point where the light intensity exists.

Waveguide media in the form of fibers or channels are attractive since $I$ = Power/Area, and it is possible to maximize the intensity by minimizing

the beam cross-sectional area, typically in waveguides to the wavelength of light squared (the beam cross-section in the waveguide is of the order of the wavelength of light). Therefore, switching with low or moderate power levels is allowed.

Switching in fibers is far more advanced than in integrated optical structures [339]. Although the nonlinearity in silica (a typical glass) is very small, the attenuation-limited propagation distance $\alpha^{-1}$ is larger than one kilometer. If one measures the nonlinear phase shift:

$$\Delta\Phi^{\mathrm{NL}} = \frac{2\pi\Delta n}{\alpha\lambda}, \tag{6.21}$$

a large phase shift ($\sim 100\,\pi$) can be induced. For structures based on planar integrated optics, materials with a combination of nonlinearity and loss to produce a nonlinear phase shift of several $\pi$ over one attenuation length are needed. Chalcogenide glasses with high nonlinearities (a few hundred times that of silica) and small losses offer great potential in these applications.

### 6.4.2 Nonlinear Interferometric Devices

Devices based on power-dependent interference between two guided-wave beams provide the simplest phenomenon that leads to all-optical switching.

In a nonlinear Mach-Zehnder interferometer [340], the input beam is divided into two by a beam-splitting coupler, and the two beams propagate along independent paths and are recombined by a second beam-combining coupler.

The relative phase between the two beams is obtained from:

$$\Delta\Phi^{\mathrm{NL}} = k_0 n_2 \left[ \frac{P_1}{A_{1,\mathrm{eff}}} L_1 - \frac{P_2}{A_{2,\mathrm{eff}}} L_2 \right] \tag{6.22}$$

and can be changed optically by increasing the input power or by using different values for the effective area $A$ or lengths $L$ in the two arms.

When $\Delta\Phi^{\mathrm{NL}} = \pi$ is induced, the output can switch from 0 to $P_i$, or vice versa.

The other interferometric device using nonlinear interference effects for switching is the NOLM [309, 341] mentioned in Sect. 6.3.

### 6.4.3 Nonlinear Beam-Coupling Devices

In these devices, the exchange of energy between two modes, either in neighboring channels or in the same waveguide, is controlled with optical power. The beams can travel in the same direction as in a nonlinear directional coupler (NLDC), or in opposite directions as in a nonlinear distributed feedback grating.

The linear directional coupler consists of two parallel, identical channels (or two fiber cores) which are spaced close enough so that the fields associated with the guided modes overlap in space. As a result there is a coupling of energy from one guide to the other with propagation distance, and vice versa.

### 6.4.4 Polarization Switching Devices

In this class of devices, the polarization of a signal beam is varied by changing the incident guided-wave power.

Rocking filter fibers were developed to rotate the plane of polarization of the incident light through some chosen angle [342]. The fibers are moderately birefringent with beat lengths (the distance at which the whole power is coupled back to the original channel) of typically a few centimeters. As they are pulled from the preform, the preform is rocked periodically in a twisting motion, imparting a periodic twist and therefore strain (period = $L_t$) to the fiber. The twist angle is small. As a result, the polarization axis is twisted periodically with distance down the fiber. If $L_t = L_{bir}$, the polarization rotations in each period are cumulative and the plane of polarization rotates with distance. Since $L_{bir} \propto \lambda$, synchronism between the birefringence and twist periods occurs at only one wavelength. On synchronism, the plane of polarization rotates by $\pi$ after one beat length, which is 10–100 twist periods long. If the fiber is truncated after a rotation of $\pi/2$, the output is nulled between parallel polaroids, and is a maximum between crossed polarizers.

### 6.4.5 Soliton Switching Devices

There are a number of switching devices utilizing the special properties of temporal solitons. These include trapping of two copropagating, orthogonally polarized solitons and another resulting from soliton collisions.

Isolated solitons in a birefringent fiber travel at different velocities, but, when two orthogonally polarized solitons of the same frequency are launched simultaneously, the index changes produced via cross-phase modulation can alter their relative motion. The presence of one pulse produces an attractive potential for the orthogonally polarized pulse. This locks the two pulses together. The center frequency of the two pulses is shifted on propagation so that their group velocities are equal. Therefore, the arrival time of any one soliton at the end of the fiber depends on whether the second soliton is present or not.

This phenomenon can be used to implement logic gates, either by utilizing the time differential or the frequency shift. By blocking only the frequency-shifted pulses with a Fabry–Perot etalon and transmitting the incident frequency, a signal is obtained when only one signal is input (XOR gate) [343]. The absence of signal corresponds to an AND gate.

The NOR gate pioneered by Islam [344] is based on the effect that two pulses on a birefringent fiber attract each other so that they tend to equalize

their velocities. If the enable-E pulse travels by itself through the fiber, it arrives at the output in a certain time slot. Arrival of the E-pulse in the designated time slot is taken as a one. If an orthogonally polarized single pulse A is injected, it attracts the E-pulse and tries to impart its own speed to it. The E-pulse emerges in a different time slot, an event interpreted as a zero [344].

## 6.5 Limitations of All-Optical Switches

Minimum values of the switching energy $E$ and the switching time $T$ of all-optical switches are governed by the following fundamental physical limits.

The only fundamental limit on the minimum switching time arises from energy-time uncertainty [345]. In fact, optical pulses of a few femtoseconds (a few optical cycles) are readily generated. Such speeds cannot be obtained by semiconductor electronic switches (and are also beyond the present capabilities of Josephson devices). Subpicosecond switching speeds have been demonstrated in a number of optical-switching devices. Switching energies can also, in principle, be much smaller than in semiconductor electronics. Limits on the size of photonic switches are governed by diffraction effects, which make it difficult to couple optical power to and from devices with dimensions smaller than the wavelength of light.

The primary limitation on all-optical switching is a result of the weakness of the nonlinear effects in currently available materials, which makes the required switching energy rather large. Another important practical limit is related to the difficulty of thermal transfer of the heat generated by the switching process. This limitation is particularly severe when the switching is performed repetitively. If a minimum switching energy $E$ is used in each switching operation, a total energy $E/T$, where $T$ is the switching time, is used every second. For very short switching times, the power can be quite large. The maximum rate at which the dissipated power must be removed sets a limit, making the combination of very short switching times and very high switching energies untenable. Note, however, that thermal effects are less restrictive if the device is operated at less than the maximum repetition rate; i.e., the energy of one switching operation has more than a bit time to be dissipated.

## 6.6 Summary

Requirements of materials used for efficient optical switches are given. Limitations of two-photon absorption on the performance of a switch are introduced. All-optical switching using chalcogenide fibers by different techniques such as optical Kerr-shutter (OKS) technique and NOLM configuration are presented. Fabrication of nonlinear directional couplers (NDCs) in chalcogenide

films and their use as an optical switch is given. It is shown that fabricated NDCs can be used as efficient switches and can easily be fabricated for use in all-optical integrated circuits. Modeling of an NDC switch is presented and the performance of the switch is investigated in some detail. Optical switches based on interferometric techniques, polarization-switching devices, soliton-switching devices and their use as elements in logic circuits are discussed. Finally, limitations of all-optical switching, such as switching time, energy, size, and their practical limitations are presented.

# 7

# Issues and Future Directions

## 7.1 Optical Limiting

The investigation performed by Kwak et al. [346] demonstrated that amorphous chalcogenide thin films, including $As_2S_3$ films, offer promise as materials for optical limiters. The optical-limiting effects are of special interest in nonlinear optics and optoelectronics owing to their possible application for the protection of eyes and sensitive detectors against intense radiation. The mechanisms responsible for optical limiting are of different nature. Reverse saturable absorption, which is associated with a large cross-section of absorption from excited levels, brings about optical-limiting effects in colloidal metals [347], fullerenes [348], and phthalocyanines [349]. The optical limiting in organic clusters is caused by strong nonlinear refraction [350], whereas the optical limiting in semiconductor structures is governed by two-photon absorption (2PA) [351].

Ganeev et al. [352] investigated nonlinear optical characteristics and optical limiting in $As_2S_3$, $As_{20}S_{80}$, $2As_2S_3/As_2Se_3$, and $3As_2S_3/As_2Se_3$ chalcogenide films. They used a standard procedure for calculating the Z-scan with a limiting aperture in order to evaluate the optical limiting caused by Kerr-type nonlinearities in chalcogenide films. The film position was fixed in the region corresponding to a minimum transmittance (ahead of the focal point in the case of self-focusing and behind the focal point in the case of self-defocusing) where 2PA processes are of little significance. As in the case of nonlinear absorption, the experimental investigation of the optical limiting in semiconductors was performed using the scheme with an open aperture. The sample position corresponds to a minimum transmittance; i.e., the sample is located at the focal point. In this case, the optical limiting is due to 2PA. Their investigations demonstrated that chalcogenide films, such as $2As_2S_3/As_2Se_3$, $3As_2S_3/As_2Se_3$, hold promise for use as intracavity elements for the compression of picosecond pulses. The nonlinear refractive indices and the 2PA coefficients of these films were measured using the Z-scan technique at the wavelengths of a picosecond Nd:YAG laser ($\lambda = 1,064$ and 532 nm).

The optical limiting associated with the Kerr-type nonlinearities was analyzed for the amorphous chalcogenide films. It was demonstrated that the $2As_2S_3/As_2Se_3$ film is characterized by a 12.5-fold optical limiting. The optical limiting due to 2PA was investigated experimentally. It was found that the $As_2S_3$ film exhibits a 25-fold optical limiting.

Troles et al. [353] have studied the optical-limiting behavior of three chalcogenide glasses from the Ge–As–Se ternary system: $As_2Se_3$, $GeAsSe_7$, which is the stochiometric mixing of the $GeSe_4$ and $AsSe_3$ glasses, i.e. $(GeSe_4)_{1/2}(AsSe_3)_{1/2}$ and $GeAs_2Se_2$, which is a low-content selenium glass. They have also studied two glasses from the $PbI_2$–$As_2S_3$–$Sb_2S_3$–$Bi_2S_3$ family, one composition without lead iodide, $(As_2S_3)_{45}(Sb_2S_3)_{45}(Bi_2S_3)_{10}$ referred to as Pb-0, and a second one containing 30% of lead iodide, $(PbI_2)_{30}(As_2S_3)_{30}(Sb_2S_3)_{30}(Bi_2S_3)_{10}$, referred to as Pb-30. For all the above glasses, they have measured the transmitted intensity versus the incident intensity when this intensity increased from 0.1 up to 6 GW cm$^{-2}$ using an Nd:YAG pulsed laser at 1.064 µm. Results are shown in Fig. 7.1. The straight line corresponds to linear transmission of these high-linear-index glasses without nonlinear effects. When the input intensity increases, different samples show the same behavior, where the transmitted intensities exhibit a clear decrease compared to the reference transmittance line. We can see, for the glasses tested, that the transmitted intensity moves away from the reference line when the input intensity increases. This indicates for the above glasses a real behavior of optical limiters. The best optical-limiting properties were

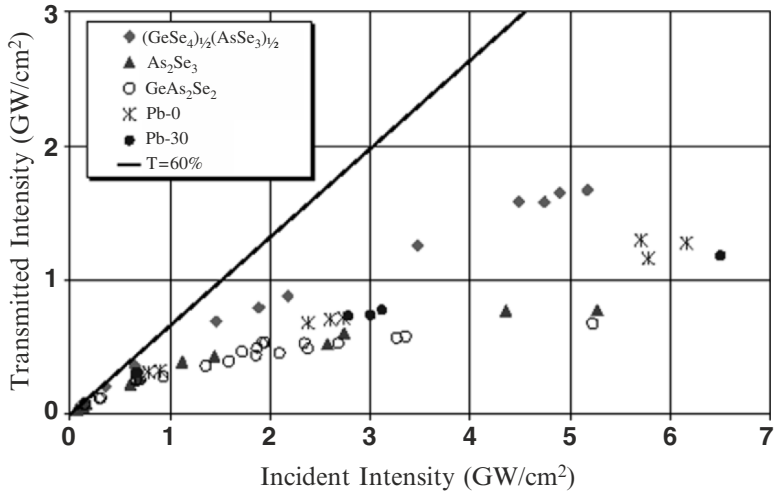


**Fig. 7.1.** Optical-limiting behavior of $(GeSe_4)_{1/2}(AsSe_3)_{1/2}$ (*diamond*), $As_2Se_3$ (*triangle*), $GeAs_2Se_2$ (*open circle*), Pb-0 (*star*), and Pb-30 (*filled circle*). The sample thicknesses were, respectively, 1.18, 1.44, 1.26, 1.88, and 0.94 mm (after [353])

observed for the two glasses $As_2Se_3$ and $GeAs_2Se_2$. From a comparison of calculated and experimental transmittance measurements, Troles et al. [353] assert that the optical-limiting behavior is mainly induced by 2PA. The optical limiting of chalcogenide glasses is of interest for application in the protection of infrared detectors.

## 7.2 Second-Harmonic Generation and Electro-Optic Effects

The process of second-harmonic generation (SHG) is related to the second-order susceptibility $\chi^{(2)}$ and is only allowed in noncentrosymmetric materials. Since glasses are macroscopically isotropic, SHG is not expected to be an efficient process in optical fibers. Aside from the electric-dipole process, which is described by $\chi^{(2)}$, there is the possibility that SHG may result from magnetic dipole or quadrupole moments, but these are predicted to be very weak effects [354]. Indeed, very weak SHG is observed in unirradiated fibers [355, 356]. In 1987, however, Osterberg and Margulis [357, 358] found that a Ge–P doped fiber that had been irradiated for several hours with a very intense laser beam at 1.06 µm (mode-locked, Q-switched Nd–YAG laser with a peak power of 50 kW) showed a strong second-harmonic signal which grew exponentially with the time of irradiation. The second-harmonic efficiency was as high as 5% and the second-harmonic beam was intense enough to pump a dye laser [357]. Although there is still no fully satisfactory macroscopic or microscopic model available, many experimental results have generated various ideas about the photoinduced SHG taking place in the fiber. Since photoinduced SHG has only been reported for Ge–P or Ge-doped silica fibers, the conclusion has been made that Ge-related defects play an important role in the formation of the second-harmonic-generation process. Possible defects include oxygen-deficient sites, such as Ge–Si and Ge–Ge bonds, and GeO centers [359–361]. One of the most important experimental observations was reported by Stolen and Tom [362], who found that the time necessary to induce the SHG in the fiber could be substantially reduced when, in addition to the very strong infrared beam, the fiber was simultaneously exposed to a weak green beam at 532 nm, obtained by doubling part of the infrared light with a frequency-doubling crystal. The green light is only present during the preparation process (seeding); during probing of the SHG, only the infrared beam is coupled into the fiber. On the basis of their results, Stolen and Tom proposed a model for the photoinduced SHG with two main ingredients (1) a nonlinear interaction between the infrared and green beams leading to a direct-current polarization via a $\chi^{(3)}$ mechanism, which is allowed in the unirradiated fiber, that is

$$P_{\mathrm{DC}} = \chi^{(3)} E_{2\omega} E_{\omega} E_{\omega} \tag{7.1}$$

and (2) a direct-current polarization permanently orienting defects in the fiber and giving rise to an effective $\chi^{(2)}$. Because of the fact that a nonlinear

interaction between the infrared and the green preparation beams is responsible for the creation of the direct-current polarization, this polarization will also be periodic with exactly the periodicity that is required to achieve phase matching during the subsequent probing of the induced SHG. As a test for the above model, experiments have been carried out in which an external direct-current field was applied to orient the defects [363–367] with fields of several $1,000\,\mathrm{V\,cm^{-1}}$ applied to Ge–P doped silica core glass preforms and fibers; no permanent $\chi^{(2)}$ could be obtained [363, 364]. However, when a fiber was irradiated with blue laser light during the application of the field, a permanent $\chi^{(2)}$ was observed [365–367]. This experiment indicates the importance of photoexcitation of the defect centers.

Qiu et al. [368] reported on photoinduced SHG in chalcogenide glasses. Fundamental and second-harmonic waves from a nanosecond pulsed Nd:YAG laser were used to induce second-order nonlinearity in chalcogenide glasses. The magnitude of SHG in $Ge_{20}As_{20}S_{60}$ glass was $10^4$ times larger than that of a telluride glass. Moreover, no apparent decay of the photoinduced SHG in $Ge_{20}As_{20}S_{60}$ glass was observed after optical poling at room temperature. It was suggested that the large and stable value of $\chi^{(2)}$ is due to the induced defect structures and large $\chi^{(3)}$ of the chalcogenide glasses.

Second-order nonlinear optical effects, such as SHG and linear electro-optics (LEO), in the midinfrared spectral range (5–15 μm) were experimentally observed [369] for the first time. It was found that the novel $As_2Te_3$–$BaBr_2$–$BiCl_3$ chalcogenide glasses, possessing transmission windows within the 3–45 μm spectral range, have both photoinduced SHG equal to $0.0012\,\mathrm{pm\,V^{-1}}$ and comparable values of photoinduced electro-optic effect at a wavelength of excitation ($\lambda = 10.6\,\mu\mathrm{m}$). The photoinduced anharmonic electron–phonon interaction plays a major role in the observed phenomena. A good correlation between the IR-induced nonlinear optical susceptibilities and the photoinduced anharmonic electron–quasi–phonon interaction was demonstrated.

Pruneri et al. [370] have investigated second-harmonic generation in gallium–lanthanum–sulfide (Ga:La:S) and germanium sulfide + Ga:La:S glasses. It was shown that microcrystals of Ga:La:S and the $\alpha$ phase of gallium sulfide ($\alpha - Ga_2S_3$), whose presence in the glass matrix was revealed by energy-dispersive spectroscopy and X-ray-diffraction analysis, are responsible for the frequency-doubling process. These results suggest that Ga:La:S-based glasses, free of crystalline phases, should not show second-order nonlinearity. Therefore, for optical-amplifier applications, where microcrystalline features have to be in any case absent in order to keep the scattering losses at low levels, second-order nonlinear processes should not constitute a major problem.

Li et al. [371] have studied third-order nonlinear susceptibilities of zinc niobium tellurite glasses ZnO–$Nb_2O_5$–$TeO_2$ and measured their optical nonlinearities by using forward DFWM. The bistability for the $(ZnO)_{15}$–$(Nb_2O_5)_{20}(TeO_2)_{65}$ glass sample was observed in a Fabry–Perot (F–P)

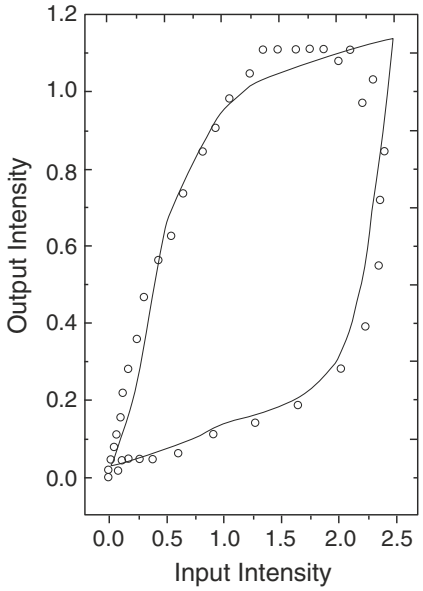


**Fig. 7.2.** The bistability for $15ZnO–20Nb_2O_5–65TeO_2$ glass sample: (*solid line*) approximate correction curve; (*open circles*) experimental results (after [371])



cavity. Figure 7.2 shows the bistability behavior for this sample. The incident laser light was of wavelength 532 nm from a nanosecond YAG laser with a repetition rate of 10 Hz. The hysteresis loop in Fig. 7.2 displays the character of the bistability in the glass sample. A good bistability was observed with a glass with a high content of ZnO dopant. This was probably due to an increase in the transparency of the glass with an increase in ZnO content. The results show that this kind of tellurite glass can have promising applications in the realm of nonlinear optical devices and photonic materials.

## 7.3 Fabrication of Rib and Ridge Waveguides and of Fiber Gratings

Fabrication and characterization of low-loss rib chalcogenide waveguides has been achieved [372]. A number of chalcogenide rib waveguides with widths ranging from 1 to 7 μm and depths from 0 to 4 μm were fabricated [373] using dry etching in $As_2S_3$ films prepared by pulsed laser deposition techniques.

Dry-etching systems employed in this work were either a helicon plasma source [374] or an Oxford instruments RIF-100 ICP etcher. When etching using the helicon system, the RF power was fixed at 600 W in order to achieve

a high enough plasma density, while the gas ratio and bias voltage were varied and optimized. It was found that $CF_4$ gas alone etched the chalcogenide films slowly but the etch rate could be significantly increased using a $CF_4/O_2$ gas mixture. Both the substrate bias voltage and the gas ratio were found to affect the sidewall angle. The etch rate of $As_2S_3$ waveguides was about $250\,\mathrm{nm\,min^{-1}}$. Ruan et al. [372] also successfully used the Oxford Instruments ICP (inductively coupled plasma) system to etch chalcogenide waveguides. Their experiments indicated that the high-density ICP plasma etcher resulted in very similar etching behavior to the helicon plasma etcher. However, the etching rate for the chalcogenide glasses was about an order of magnitude higher when using the same RF power and bias voltage, while the etch rate of the photoresist was unchanged. An $As_2S_3$ waveguide etched by the ICP system using a photoresist mask is shown in Fig. 7.3a. In this case, the waveguide width was almost identical to the mask width as, for example, shown in Fig. 7.3b where the mask width was $2\,\mu\mathrm{m}$. So, it proved easier to obtain narrower waveguides and to control their width and profile using the ICP etcher.

Propagation-loss measurements were performed using the cut-back method using waveguides of lengths between 12 and 50 mm. A high-quality polysiloxane coating ($n = 1.53$) at $1.55\,\mu\mathrm{m}$ was applied to the top of the waveguide as a cladding during characterization. The high-index contrast ensured that light was tightly confined in the core layer. A high numerical aperture (NA) fiber with mode field (the extent of the electric field of the fiber mode inside the fiber) diameter of $4.2\,\mu\mathrm{m}$ at $1.55\,\mu\mathrm{m}$ wavelength was used as both input and output fiber to reduce the mode mismatch to the waveguides. Although simulation showed that these deeply etched waveguide structures supported multiple modes at 1.31 and $1.55\,\mu\mathrm{m}$, higher order modes generally had high losses due to stronger coupling of the propagating field to the sidewalls. As a result, only the fundamental mode was observed to propagate along these waveguides. The results of measurements of the transmission coefficient as a function of

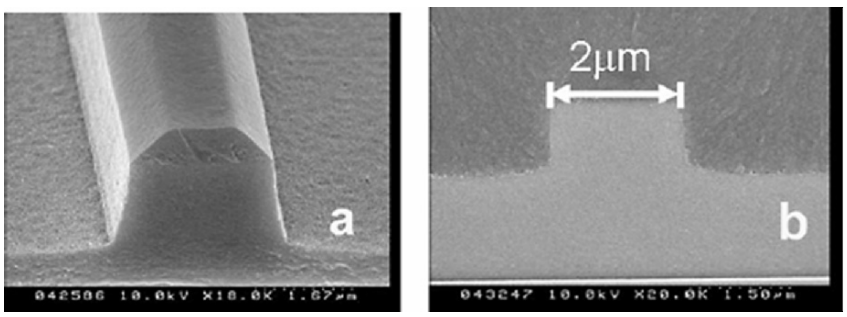


**Fig. 7.3.** SEM micrograph showing the profile of $As_2S_3$ waveguides etched by ICP (Inductively Coupled Plasma) using a photoresist mask (**a**) $As_2S_3$ waveguide with a photoresist mask, (**b**) coating with polysiloxane cladding, its width is well controlled as required (after [372])

the length gave the smallest loss of $0.25\,\mathrm{dB\,cm^{-1}}$ at 1,550 nm for the 4 and 5 µm wide waveguides, increasing to about $0.5\,\mathrm{dB\,cm^{-1}}$ for the 3 µm wide guides. This was due to the increased coupling of the fundamental mode to the sidewall as the waveguide became narrower. Se-based chalcogenide waveguides with similar dimensions were also characterized and a higher loss ($1.6\,\mathrm{dB\,cm^{-1}}$) was, however, found at 1.55 µm.

To test the nonlinear properties of the chalcogenide waveguides, Ruan et al. [372] measured spectral broadening due to self-phase modulation (SPM) for pulses propagating through a 50 mm long and 5 µm wide waveguide. They showed that a 8 ps duration input pulses at 1,573 nm were nearly transform-limited and were obtained from a KTP optical parametric oscillator (OPO). The power from the OPO was coupled into a SMF-28 single-mode fiber with a 3 mm long section of high-NA fiber thermally expanded and spliced to its output end. The use of this short length of high, NA fiber allowed high-peak power to be delivered to the chalcogenide waveguide without any fiber-induced phase shift. A standard SMF-28 fiber was employed to collect a small fraction of the transmitted light and couple it to an optical spectrum analyzer. The measured spectral broadening indicated that a phase shift of $\approx\pi$ was obtained [375]. Figure 7.4 shows the spectrum of the broadened signal passed through a $As_2S_3$ waveguide. The peak pulse power in the waveguide was obtained from the high-NA fiber after correction of the coupling loss (about $1.8\,\mathrm{dB\,cm^{-1}}$ for one end) and waveguide loss, and was estimated to be 40 W. The effective area of the fundamental mode of the waveguide was modeled and found to be about $8\,\mu\mathrm{m}^2$. The calculated third-order nonlinearity based on the nonlinear phase shift was $3.05 \times 10^{-18}\,\mathrm{m^2W^{-1}}$, very close to the value of $2.92 \times 10^{-18}\,\mathrm{m^2\,W^{-1}}$ measured by the Z-scan technique for bulk samples of the glasses [376].

It should be noted that the Z-scan for $As_2S_3$ indicates that the nonlinear figure of merit (FOM) ($T = \beta\lambda/n_2$, where $\beta$ is the 2PA coefficient) is <0.1

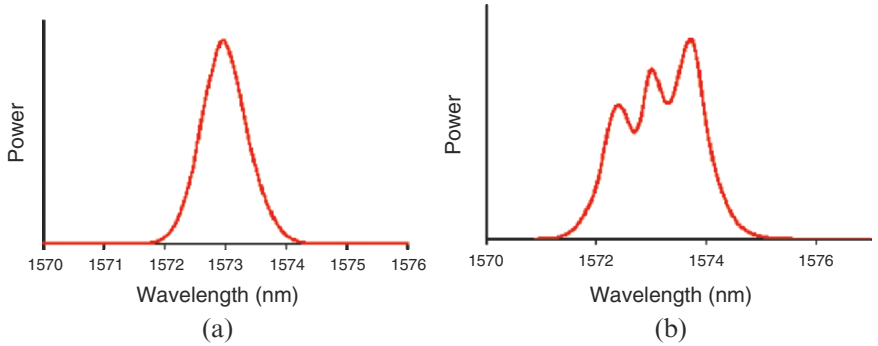


**Fig. 7.4.** (**a**) Spectrum of input signal at 1,573 nm, (**b**) spectral broadening corresponding to $\pi$ phase shift and peak power 40 W in an $As_2S_3$ waveguide (after [372])

at 1,550 nm [376]. It is consistent with the data of [373], where $T = 0.009$, and hence 2PA is expected to be negligible in these experiments [377]. They conclude that subwatt switching can be achieved in a 5 cm long structure, assuming that the coupling loss can be held at <1 dB.

Vallee et al. [378] have presented a real-time observation of Bragg grating formation in amorphous $As_2S_3$ ridge waveguides. The result of a typical recording is presented in Fig. 7.5, with a total writing intensity of $I_w = 1.1\,\mathrm{mW\,mm^{-2}}$. Figure 7.5 actually shows the grating transmission spectrum evolution for a TE mode probe for several exposure times. The time evolution of the grating formation has a nonmonotonic behavior with a strong initial growth followed by a slow decrease due to the saturation of the refractive index of the material.

The experimental set-up allowed them to monitor and control in situ the key parameters describing the Bragg diffraction, i.e., its reflectivity, resonant wavelength, and FWHM. It was shown that the relatively small reflectivities of recorded Bragg gratings are not related to the small amplitude of refractive-index modulation, which could result from e.g., mechanical vibrations of their holographic set-up. They have shown that the induced refractive-index modulations in reality are large. Other detrimental factors, such as multimode character of their channel waveguides and the spatial inhomogeneity of the induced refractive-index changes in them, actually prevented the achievement of higher grating reflectivities.

Low-loss shallow-rib waveguides were fabricated [379] using $As_2Se_3$ chalcogenide glass and polyamid–imide polymer. Waveguides were patterned directly in the $As_2Se_3$ layer by photodarkening followed by selective wet etching. Theory predicted a modal effective area of 3.5–4 $\mu m^2$, and this was supported by near-field modal measurements. The F–P technique was used to estimate propagation losses as low as $0.25\,\mathrm{dB\,cm^{-1}}$. First-order Bragg gratings near 1,550 nm were holographically patterned in some waveguides. The Bragg gratings exhibited an index modulation on the order of 0.004. They were used as a means to assess the modal effective indices of the waveguides. It was asserted that small-core $As_2Se_3$ waveguides with embedded Bragg gratings have the potential for the realization of all-optical Kerr-effect devices.

The creation of microchannels in a photosensitive material ($As_2S_3$), has been reported [380]. It was shown that microchannels are created through

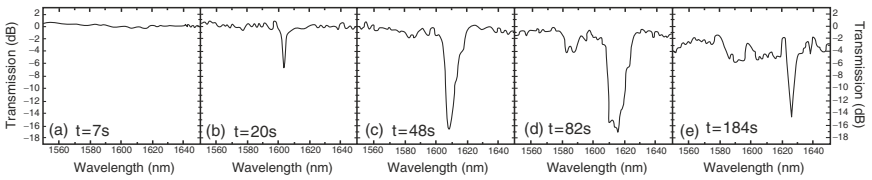


**Fig. 7.5.** Sequence of normalized transmission optical spectra for five exposure times for a TE mode probe in a 10 μm wide ridge waveguide of length $L = 2$ mm (after [378])

the process of self-writing and are very sensitive to the photosensitivity of the material, the quality of the incident wavefront and the light intensity. The very large photosensitivity of $As_2S_3$ allows for the self-written waveguide to become much smaller than the incident beam. It can indeed be as small as 1 µm wide. A numerical analysis based on the nonlinear Schrödinger equation accounts well for the diversity of the microchannels experimentally observed. It was also shown that microchannels can actually guide light efficiently. A variety of microchannel creation processes was observed in an $As_2S_3$ slab exposed to radiation at 800 nm. It was shown that clean wavefronts lead to single microchannels, but noisy wave fronts lead to multiple microchannels that are created at the interface. As the intensity is increased, the sensitivity to imperfections in the cleave grows, so that very erratic microchannels can be created. Also, at high intensities, it was possible to saturate strongly the refractive-index increase, leading to very large microchannels. The model, based on the nonlinear Schrödinger equation and a dependence of the refractive index on the absorbed energy by TPA, could account for all the previous microchannel formation. It was asserted that the microchannel process is thus the continuation of the waveguide self-writing process under the conditions that the photosensitive material is allowing for substantial index variation so that saturation does not occur at an early stage. $As_2S_3$ is such a material, where the index variation is sufficiently large to allow for this process.

Gallium–lanthanum–sulfide (Ga:La:S) optical glass is an interesting material for both fiber and planar technologies, as it offers possibilities for a wide array of devices suitable for use in both nonlinear applications and as IR lasers [381]. Direct laser writing into this glass has yielded low-loss single-mode channel waveguides. Samples were exposed to above-band gap illumination of focused UV ($\lambda$ =244 nm) light at varying intensities ($I_{UV}$ = 1.5–90 kW cm$^{-2}$) and scan velocities ($V_{SCAN}$ = 0.005–0.067 m s$^{-1}$). The exposed regions were evaluated through atomic force microscopy (AFM), and a surface compaction (0.3–3.6 µm) was observed. Sample topography was examined using a scanning electron microscope (SEM) with analysis of chemical changes within the exposed regions performed with energy-dispersive X-ray microscopy (EDAX). Waveguide attenuation was measured to be $0.2 \pm 0.1$ dB cm$^{-1}$ at 1.3 µm with a positive change in refractive index ($\Delta n = 10^{-3}$). The chemical mechanism for these photoinduced changes with resulting photodensification has been correlated with a relative increase in the lanthanum content within the waveguide core. It was asserted that advancement in purification techniques to reduce metallic and nonmetallic impurities in the glass matrix will ultimately lead to higher quality bulk glass, thereby reducing residual losses in the glass. Furthermore, optimizing write parameters and the bulk glass composition will yield devices for use in a wide range of applications. Doped optical devices for communications systems, highly nonlinear optical waveguides, IR sensor systems, and lasers could also be eventually achieved.

Chalcogenide thin films ($As_2S_3$ and $As_{24}S_{38}Se_{38}$) have been deposited upon unheated $SiO_2$/Si substrates [382]. A 2 µm-thick $SiO_2$ layer was present

to isolate optically the chalcogenide layers from the higher refractive index of the Si substrate. The deposition rate monitored with a quartz-crystal monitor was of the order of $3.5\,\mathrm{nm\,s^{-1}}$. Typical thicknesses of about 1 or $2\,\mu\mathrm{m}$ were deposited. Samples were annealed at 130°C for several hours in order to improve physical and thermal properties. Annealed $As_2S_3$ and $As_{24}S_{38}Se_{38}$ films generally have propagation losses of about $1\,\mathrm{dB\,cm^{-1}}$ at 1,000 and 1,300 nm. Unannealed samples exhibit more often losses twice these measured values. The surface of the chalcogenide films was affected by the external environment and a degradation of the propagation losses was observed for older films (5 months after deposition), in which $\sim 3\,\mathrm{dB\,cm^{-1}}$ was measured at 1,000 nm; hence suitable packaging would be needed. A standard photolithographic process was employed to fabricate 1–10 μm wide straight channel waveguides [382]. Although the 1 μm guides were more lossy, they propagated the light over a few cm, indicating the good quality of their fabrication process. A multilayer $As_{24}S_{38}Se_{38}/As_2S_3$ directional coupler, with 6 μm spacing between the lines was also fabricated. A laser-writing technique was also used to create efficient 3D channel waveguides in thin films, in both As–S, As–S–Se glasses and multilayer films. A photoinduced channel waveguide has been written by 10 mW Ar-ion laser beam exposure at 514 nm, which induced a refractive-index change of about 1%.

The feasibility of a planar channel waveguide amplifier and laser made of praseodymium ($Pr^{3+}$) doped chalcogenide glass, based on the binary composition $GeS_2$, was investigated by means of an appositely implemented computer code [383]. The buried channel waveguide amplifier, having both core and substrate doped with a dopant concentration $N = 3,000$ ppm, showed gain close to $G = 7$ dB for an input signal power of $P_\mathrm{s} = 1\,\mu\mathrm{W}$ at the wavelength $\lambda_\mathrm{s} = 1,310$ nm and a pump power of $P_\mathrm{p} = 200$ mW at the wavelength $\lambda_\mathrm{p} = 1,020$ nm. The F–P laser, based on the aforesaid buried channel waveguide terminated by an input mirror having reflectivity $R_1 = 98\%$ and an output mirror having reflectivity $R_2 = 41\%$, exhibited a threshold pump power $P_\mathrm{th} = 16$ mW and a slope efficiency (for the graph of the laser output power versus the launched pump power) of $S = 8\%$.

Waveguide structures were written using a train of femtosecond pulses at 850 nm in $As_{40}S_{60}$ glasses [384]. A breakage of As–S bonds with the formation of As–As and S–S bonds and an increase of the disorder of the glass structure, leading to a photomodification of glass optical properties, were observed using micro-Raman spectroscopy. These results were verified by comparison with reference to arsenic-rich, and sulfur-rich glasses which contained the corresponding homopolar bonds. The resulting index difference between the core-exposed and surrounding cladding (unexposed) regions was measured to have increased ($\Delta n = 5 \times 10^{-4}$), consistent with the index changes seen in self-written planar waveguides written in the same material. Similarities in resulting photoinduced structural modification between band-gap exposure and high-intensity subband-gap exposure have been shown [384]. Two mechanisms of nonlinear absorption have been discussed as the origin

of the chemical changes during waveguide formation. The structural change produced may prove to be very promising for the control and the optimization of the waveguide-writing procedure.

The combination of high nonlinearity and photosensitivity raises the exciting possibility of all-optical devices, such as regenerators, based on a combination of nonlinear propagation and either linear filtering or dispersion management [385, 386]. For these applications, however, the requirements for grating filtering performance, in terms of strength, uniformity, and apodisation (elimination of sidelobes) are very high. Shokooh-Saremi et al. [387] state that, while there have been many reports recently of Bragg gratings written in chalcogenide glass fibers and waveguides, they have not been of adequate quality for advanced application. They claim the first demonstration of ultrastrong, near-perfect, raised-apodised Bragg gratings in $As_2S_3$ chalcogenide rib waveguides using a modified Sagnac holographic writing set-up [387].

A cross-section of the $As_2S_3$-based rib waveguide is shown in Fig. 7.6a.

The $As_2S_3$ layer was deposited on a silica-on-silicon wafer by ultrafast pulsed-laser deposition (PLD) and patterned by photolithography followed by a dry-etching process [372]. A polymer overcladding layer was then deposited to protect the chalcogenide layer. The widths of the rib waveguides varied from 3.2 to 6.2 µm. These waveguides support multiple modes in each orthogonal polarisation (TE and TM). The propagation loss was typically 0.1–0.5 dB cm$^{-1}$ for the wider waveguides. Figure 7.6b shows the layout of the grating writing set-up. Sokooh-Saremi et al. [387] used a modified Sagnac interferometer, because of its stability and tunability (Bragg wavelength), in combination with a CW, frequency-doubled, diode-pumped Nd:YAG laser at $\lambda = 532$ nm, with a maximum available power at the sample of 50 mW. The (linearly polarised) beam was expanded, focused, and split using a phase mask ($\Lambda_m = 10,633$ nm). The $+1$ and $-1$ diffracted orders (from the phase mask) were reflected from a pair of mirrors and interfered at the surface of the waveguide sample with a spot size at the writing plane of $5.5 \times 0.6$ mm$^2$. The laser's short coherence length (∼4 mm) limited the length of the interference pattern, resulting in a nearly ideally apodised (constant average photoinduced index change) grating ∼4 mm in length. The gratings were characterized with an unpolarized high-power EDFA-ASE source, butt-coupled into the waveguide via a high-NA fiber. A second high-NA fiber coupled the transmitted output to an optical spectrum analyzer with 60 pm resolution to measure the transmission spectra. Figure 7.7 shows the transmission spectra for two orthogonal polarizations of a grating written on a 3.2 µm wide waveguide of $As_2S_3$ with high-exposure conditions, resulting in a spectrally wide (4.0 nm) deep grating.

The measured grating strength of $-27$ dB was limited by the measurement capability, due primarily to a combination of birefringence splitting and limited control of the degree of polarisation [387]. As seen from Fig. 7.7, the very low-sidelobe levels are a clear indication of achieving near-perfect apodisation.

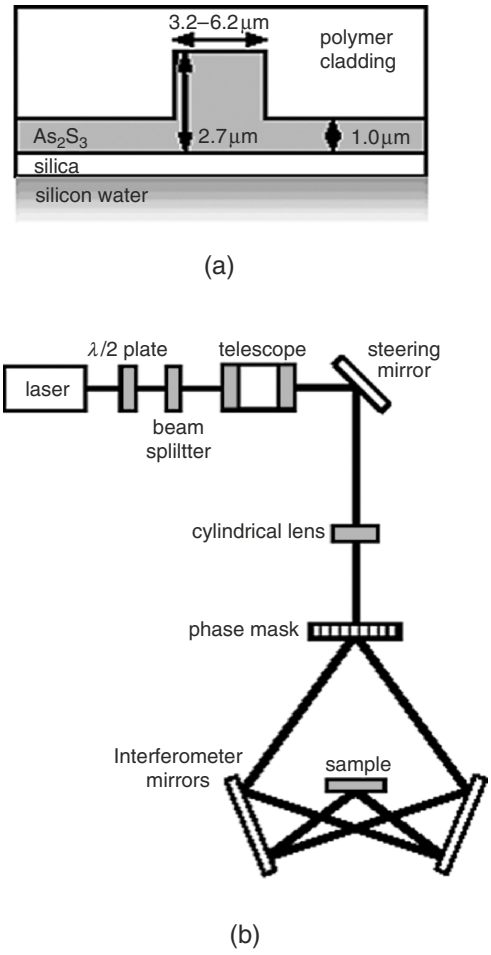


**Fig. 7.6.** Schematic views of structure and writing set-up. (**a**) Waveguide structure. (**b**) Writing set-up based on a modified Sagnac interferometer (after [387])



An index change of 0.006 was estimated from the spectral width of the grating. Figure 7.7 also shows the transmission spectra for the TM polarisation calculated using the transfer-matrix method for thin-film filters [388], showing good agreement with experiment.

Ta'eed et al. [389] reported a fully integrated, passive, all-optical regenerator capable of terabit per second operation, based on a highly nonlinear chalcogenide ($As_2S_3$) glass rib waveguide followed by an integrated Bragg grating bandpass filter. They demonstrated a clear nonlinear power-transfer curve with 1.4 ps optical pulses, capable of improving the signal-to-noise ratio

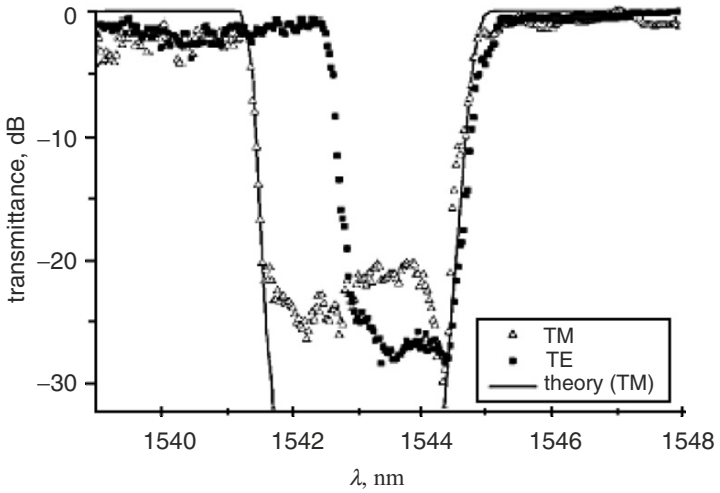


**Fig. 7.7.** Grating transmission spectra for TE and TM polarizations of a grating written in an $As_2S_3$ thin film. Numerical simulation of TM polarisation is obtained using the transfer-matrix method (after [387])



and reducing the bit-error rate (BER) for digital signals. This regenerator operates on a principle proposed by Mamyshev [390], producing a nonlinear power-transfer curve through a combination of spectral broadening via SPM in a straight nonlinear waveguide segment, followed by linear spectral filtering by an integrated waveguide Bragg grating filter. Figure 7.8 illustrates the principle of operation of the device reported in [390]. A straight nonlinear rib waveguide is followed by a waveguide Bragg grating filter, with the grating passband offset from the signal wavelength by more than the signal optical bandwidth, so that, at low intensities, the optical signal is blocked by the filter. At higher intensities, the pulses undergo SPM-induced spectral broadening so that a portion of the spectrum overlaps with the transmission bandpass filter and consequently is transmitted. At still higher intensities, the signal experiences significant broadening, and the power within the transmission pass band saturates. The resulting S-shaped nonlinear power-transfer curve (Fig. 7.8c) has the effect of reducing noise on both the "0" and "1" signals, improving both the optical signal-to-noise ratio and, for bits that contain information, the BER [391]. The chalcogenide waveguides were fabricated by pulsed laser deposition of a 2.4 µm thick $As_2S_3$ film, with a refractive index of 2.38, followed by photolithography and reactive-ion etching to form a 5 cm long, 4 µm wide rib waveguide with a rib height of 1.1 µm, and then overcoated with a polymer film transparent in the visible.

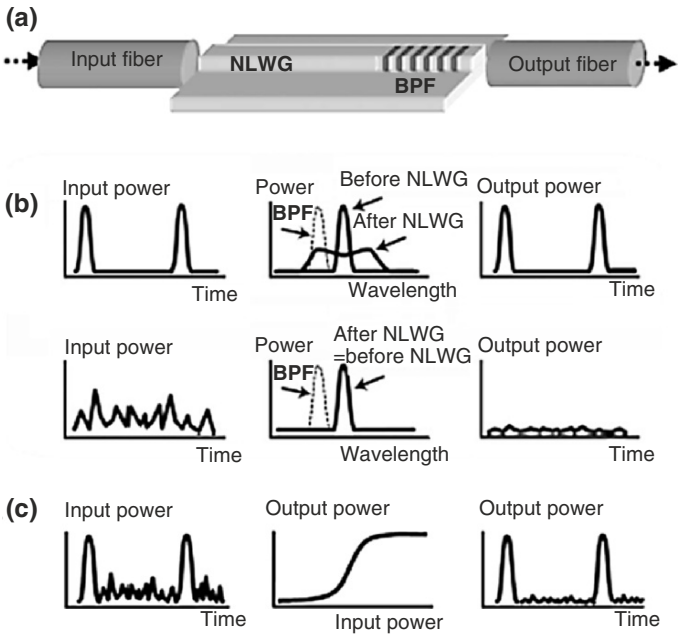


**Fig. 7.8.** Principle of device (a fully integrated, passive, all-optical regenerator) operation. (**a**) The optical regenerator consists of a 5 cm-long nonlinear $As_2S_3$ rib waveguide (NLWG) where SPM-induced spectral broadening occurs, followed by an integrated Bragg-grating bandpass filter (BPF), offset from the signal frequency, near the exit facet. (**b**) Input noise experiences less SPM spectral broadening than does the signal, and hence is attenuated more than the signal after filtering. (**c**) This produces a nonlinear power-transfer curve and results in both optical signal-to-noise ratio and BER improvement (after [389])

Waveguide gratings were written near the exit facet of the waveguide by using a Sagnac interferometer along with a CW 532 nm doubled Nd:YAG laser having a coherence length of ∼4 mm, which provided compensated refractive-index apodization. The sample was exposed with 10 mW for 60 s, resulting in an extremely high quality of the gratings in terms of both grating spectral width (>6 nm each at 3 dB), and in-band rejection ((>25 dB) at the grating center), as well as very low sidelobe level which was critical for the successful performance of the regenerator. The device performance was demonstrated with 1.4 ps pulses from a mode-locked laser, with the light passed through a polarization controller and then an optical amplifier (designed to minimize excess spectral broadening), resulting in 8.75 MHz repetition rate pulses at peak powers up to 1.2 kW, nearly transform limited with a spectral width of 1.9 nm, tunable from 1,530 to 1,560 nm. The output of the amplifier was butt coupled into the waveguide by using a short 20 cm length of standard single-mode fiber followed by 5 mm of high-NA fiber spliced on the end to improve coupling efficiency to the waveguide. The output of the waveguide

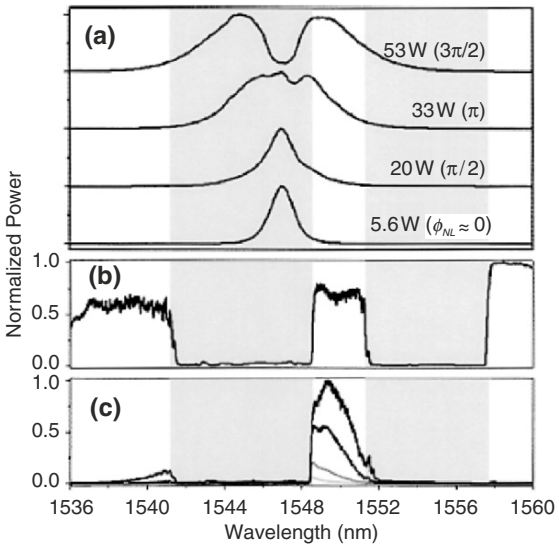


**Fig. 7.9.** (**a**) Evolution of pulse spectra versus power through a bare waveguide of $As_2S_3$ with no grating filter, showing spectral broadening due to nonlinear SPM. (**b**) Transmission spectrum of the bandpass filter (formed by two sequential offset gratings for TE polarized light, showing a passband of 2.8 nm near 1,555 nm, offset by 3 nm from the carrier wavelength. (**c**) Sliced SPM broadened output spectra after the filter (after [389])

was then directed into a power-meter, an optical spectrum analyzer, or an optical autocorrelator.

Figure 7.9a shows the pulse spectra for 1.8 ps pulses after they have passed through a bare waveguide of $As_2S_3$, showing significant broadening with increasing input power. The maximum peak power in the waveguide was 53 W, corresponding to a maximum intensity of $\sim$1.0 GW cm$^{-2}$. Ta'eed et al. [389] state that they did not observe any nonlinear effects due to 2PA at the power levels in their experiments, and estimated a minimum value for a FOM >10, consistent with previous measurements [372]. Figure 7.9b shows the transmission spectrum of the waveguide Bragg grating for TE polarization. The grating in fact consisted of two gratings, offset from each other to produce an overall rejection bandwidth of 16.3 nm with a 2.8 nm wide passband in the middle.They could launch TE-polarized pulses to better than a 20 dB extinction ratio by adjusting the polarization controller before the amplifier. As seen in Fig. 7.9c, this resulted in low transmission at low-input powers, since the filter rejection bandwidth was much wider than the spectral bandwidth of the input pulse. As the input pulse power was increased, SPM broadened the spectrum so that the power was transmitted through the passband of the grating. Figure 7.10 shows the autocorrelation of the input and output pulses at high power, indicating that input pulses were broadened slightly to $\sim$3 ps.

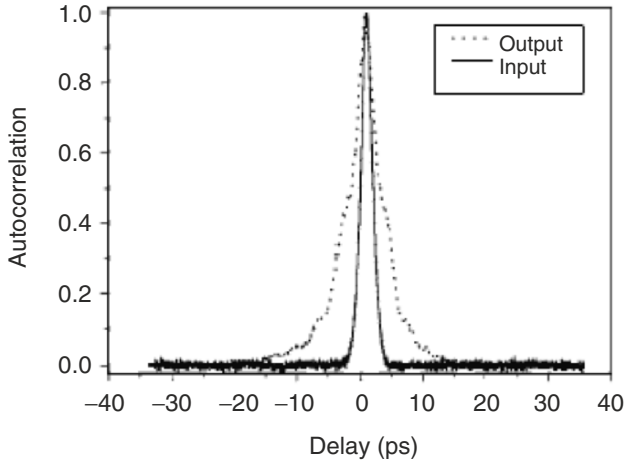


**Fig. 7.10.** Autocorrelation of input (*solid*) and output (*dotted*) pulses incident on a waveguide fiber grating at high power. Pulses broaden from an inferred Gaussian width of 1.4–3.3 ps, because of grating-edge dispersion and pulse-filter mismatch (after [389])

This broadening is not due to either waveguide dispersion or material dispersion but is due mainly to the grating dispersion near the edge of the stop band [392]. Optimizing the grating passband shape and width is expected to reduce this broadening and can provide flexibility, even tenability, for reconfigurable regeneration.

The above regenerator operates at peak powers up to 55 W with low-duty-cycle optical pulses. However, practical devices would need to operate at subwatt power levels and with high-duty-cycle optical pulses. Ta'eed et al. [389] state that, by increasing the device length to 50 cm through the use of serpentine or spiral structures, increasing the material nonlinearity (by using $As_2Se_3$ rather than $As_2S_3$, and by decreasing the waveguide area by a factor of 10 (to $1\,\mu m^2$), a reduction in operating power by 2 orders of magnitude should be achievable, resulting in subwatt power-level operation.

## 7.4 All-Optical Nonlinear Integrated Circuits

Progress in the integrated-optics field has traditionally been hindered by the lack of a single material that can provide all of the desired functionalities and/or incompatibilities between different materials. Chalcogenide glasses might address some of these challenges, for two reasons. First, chalcogenide-glass thin films can be deposited on room-temperature substrates and typically do not require postdeposition annealing at high temperature. This potentially enables monolithic integration of chalcogenide glass devices with other functional materials and devices. Second, chalcogenide glasses can enable

diverse passive and active functionality. They can be directly patterned on a submicron scale, which is required for realization of waveguides, gratings, and holographic elements. Moreover, they combine good laser-glass properties (when doped with rare-earth elements) with high nonlinearities, which might enable the fabrication of complex devices such as integrated pulsed laser sources [393, 394]. Ponnampalam et al. [379] have fabricated waveguides based on $As_2Se_3$ chalcogenide glass, a promising material for nonlinear integrated optics at 1,550 nm. Commercial polymers were used as upper and lower claddings. Good quality evaporated chalcogenide filmswere prepared and smooth waveguide facets could be realized directly by wafer cleaving. The waveguide losses measured at 980 nm were typically in the $\sim$1 dB cm$^{-1}$ range [395]. Waveguides with rib widths ranging from 3.8 to 4.2 μm and lengths ranging from 5 to 20 mm were used in F–P measurements of propagation loss [396, 397]. The measurement employed a narrow line-width 1,530 nm semiconductor DFB laser source. By varying the temperature of the laser source, the emission wavelength was varied. The normalized output power was plotted as a function of time as the laser temperature was ramped. A typical F–P fringe pattern is shown in Fig. 7.11a. Fringe quality was generally excellent and results were highly repeatable. From the data shown in Fig. 7.11a (representative of the best waveguides realized), for a waveguide length of $\sim$1.75 cm, transmission loss is estimated as 0.26 dB cm$^{-1}$. Figure 7.11b shows representative data for a set of 8 waveguides lying on the same chip. Predicted losses were generally in the 0.25–2 dB cm$^{-1}$ range, reflecting the experimental nature of the fabrication process [379]. It was believed that the loss was overestimated in many cases, due to the presence of two waveguide modes or possibly due to the inconsistent waveguide facet quality. The scattered light streak images (inset to Fig. 7.11a) and overall insertion losses exhibited less variation.

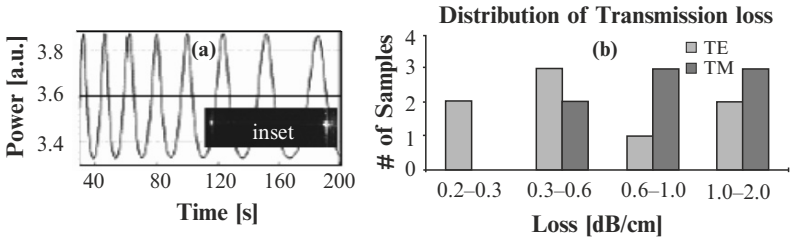


**Fig. 7.11.** (**a**) A typical F–P fringe pattern. Output intensity normalized to the input intensity is plotted against time (as the laser temperature and emission wavelength are ramped in time). The variation of wavelength with time was not linear, so the fringes do not exhibit a regular spacing. (**b**) Bar chart showing distribution of losses for 8 waveguides of $As_2Se_3$ within a single sample. Inset: typical scattered light streak image (after [379])

## 7.5 Inclusion of Metal Nanoparticles to Enhance Nonlinearity

Glasses which contain nanoparticles of metals [398, 399] or semiconductors [400] have attracted considerable interest due to their unique third-order nonlinearities. A variety of physical and chemical methods such as melt-quenching, sputtering, sol-gel, and ion implantation have been used to prepare nanodispersed glasses. With regards to the mechanisms of nonlinearity, it should be said that, when the particle is a semiconductor such as CuCl and CdSSe, excitons are responsible [401]. The exciton in semiconductor particles can be treated as a two-level system, and at the resonance frequency, $\left|\chi^{(3)}\right|$can be written as:

$$\left|\chi^{(3)}\right| \approx \mathrm{Im}\chi^{(3)} \propto \left|\mu^4\right| NT_1T_2^2, \tag{7.2}$$

where $\mu$ is the dipole moment of excitons, $N$ is the number of particles, $T_1$ is the exciton lifetime ($\approx$100 ps) and $T_2$ is the dephasing term. An enhancement by a factor of $10^3$ when compared to the bulk value is estimated for $\left|\chi^{(3)}\right|$ of closely packed CuCl particles with a radius of 40 nm [402].

For metal particles, such as spherical Au particles in a glass matrix, local-field enhancement and plasmon effects can be envisaged [398, 399]. In this case, $\chi^{(3)}$can approximately be given by:

$$\chi^{(3)} = P_{\mathrm{m}}{\chi_{\mathrm{m}}}^{(3)} \left|3\varepsilon_h/(\varepsilon_{\mathrm{m}} + 2\varepsilon_{\mathrm{h}})\right|^2 \left[3\varepsilon_{\mathrm{h}}/(\varepsilon_{\mathrm{m}} + 2\varepsilon_{\mathrm{h}})\right]^2 \tag{7.3}$$

where $P_{\mathrm{m}}$ is the volume fraction of metal particles, ${\chi_{\mathrm{m}}}^{(3)}$ is the bulk nonlinearity of the metal and $\varepsilon_{\mathrm{h}}$ and $\varepsilon_{\mathrm{m}}$ are linear dielectric constants of the host (glass) and the metal, respectively.

Other parameters such as size, size distribution, shape, and concentrations may affect the nonlinearity [403]. A narrow size distribution is preferred, while the shape may be spherical, ellipsoidal, rod-like, and so forth [404]. When the concentration of particles within the matrix increases, particle–particle electric interaction becomes important [405] and then the particles eventually percolate [406]. Particles can be arrayed to produce photonic structures with novel nonlinear properties such as light confinement [400]. Generation of second-harmonic signals from oriented ellipsoidal Ag nanoparticles in silica has been reported [407]. The oriented-particle structure has been produced through a kind of mechanical poling (tensile deformation and simultaneous heating.). Table 7.1 presents nonlinear properties of silica glass when doped with different metallic dopants.

In order to use nanoparticle-embedded systems efficiently in optical communication applications, two problems need to be overcome. First, linear absorption and scattering should be reduced and secondly, the resonant wavelengths should be shifted to the 1.3–1.5 μm spectral region.

Ogusu et al. [417] have prepared $\mathrm{Ag}_x(\mathrm{As}_{0.4}\mathrm{Se}_{0.6})_{100-x}$ chalcogenide glasses by a melt-quenching method and measured their linear and nonlinear properties to evaluate their potential applications to all-optical ultrafast switching devices. Their nonlinear refraction and absorption were measured by the

**Table 7.1.** Nonlinear properties of silica glass doped with metal nanoparticles (after [409–416])

| dopant | matrix | diam. (nm) | process | measurement ($\lambda$, nm) | $\lvert\chi^{(3)}\rvert$ ($m^2\,V^{-2}$) | $\tau$ (ps) | $\chi_m^{(3)}$ ($m^2\,V^{-2}$) | ref. |
|---|---|---|---|---|---|---|---|---|
| Au | $SiO_2$ | 5.5 | SPT | DFWM (532) | $1.82(10^{-15})$ | – | | [408] |
| Au | $SiO_2$ | 5.8 | IP | DFWM (532) | $1.68(10^{-15})$ | – | $11.2(10^{-16})$ | [409] |
| Au | $SiO_2$ | 8.8 | MQH | DFWM (532) | $\sim 3.5(10^{-19})$ | – | $9.8(10^{-16})$ | [410] |
| Au | $SiO_2$ | 1.4–6 | SG | DFWM (532) | $\sim 10.8(10^{-17})$ | – | $1.4(10^{-15})$ | [411] |
| Au | $SiO_2$ | 3–80 | SPT | DFWM (532) | $3.5(10^{-14})$ | – | – | [412] |
| Ag | $SiO_2$ | 2–5 | SPT | TBSD (400) | $2.24(10^{-16})$ | – | – | [413] |
| Cu | $SiO_2$ | 2–28 | IP | ZS (532) | $n_2'' = \sim 2.3(10^{-7})$ ($cm^2\,W^{-1}$) | <5 | | [414] |
| Cu | $SiO_2$ | 12–28 | SPT | DFWM (532) | $5.6(10^{-17})$ | – | – | [415] |
| Cu | $SiO_2$ | 5.2–12.6 | IP | ZS (570) | $n_2'' = \sim 6(10^{-10})$ ($cm^2\,W^{-1}$) | – | – | [412] |

MQH, melt-quench and heat treatment; SPT, sputtering; IP, ion implantation; SG, sol-gel process.
DFWM, Degenerate four-wave mixing; TBSD, two beam self-diffraction; ZS, z-scan technique.

Z-scan method at 1.05 µm. The addition of Ag to $As_2Se_3$ glass led to an increase in the nonlinear refractive index without introducing an increase in the nonlinear absorption coefficient. The glass with an Ag content of $x = 20$ at.% revealed a high nonlinearity, ranging from 2,000–27,000 times that of fused silica, depending on the incident optical intensity. Ogusu et al. [417] state that, although the figure of merit $F = 2\lambda\beta/n_2$ of the samples tested at 1.05 µm does not satisfy a standard criterion ($F < 1$), it can be expected to decrease at the telecommunication wavelengths of 1.3 and 1.55 µm. They believe that Ag–As–Se glass is one of the most promising materials for all-optical switching devices at 1.55 µm.

## 7.6 Other Applications

Binary phase-Dammann gratings (a type of binary phase grating which is designed in such a way that it generates a two-dimensional array of equally spaced and equal intensity spots in the output plane) are promising optical fan-out elements for applications to lightwave communications and digital optical computing systems [418]. Kwak et al. present a simple technique for fabricating Dammann gratings and have demonstrated $9 \times 9$ array generation utilizing the property of the photoinduced anisotropy of amorphous chalcogenide semiconductor thin films. The principles of Dammann gratings in conjunction with the photoinduced anisotropy, which is described in terms of third-order nonlinear polarization, were presented. Experimental results show that photoanisotropic amorphous $As_2S_3$ thin film is capable of generating a binary $(0, \pi)$ phase grating.

Broadly tunable near and midinfrared lasers are of interest for a variety of applications, including high-resolution spectroscopy, meterology, pumping of nonlinear optical frequency converters such as OPOs and standoff chemical sensing [419]. Tunable laser sources in the 2–3 μm region include $Cr^{2+}$-doped chalcogenide lasers; cryogenic systems, such as color-center lasers; limited tunability devices, such as Tm and Ho lasers, gas or chemical lasers, and diode lasers; and nonlinear optical devices such as OPOs. Transition-metal-doped chalcogenide lasers are of great interest because of their high versatility, broad room-temperature wavelength tunability, high optical efficiencies, and their potential to be scaled to high powers via direct diode or fiber laser pumping. To date, continuous-wave (CW), gain-switched, Q-switched and mode-locked laser operation has been demonstrated in a $Cr^{2+}$doped ZnSe medium [420]. Material advantages include broad absorption and emission bands, high fluorescence quantum efficiencies at room temperature, high-gain cross-sections, and minimal loss mechanisms, such as excited-state absorption or up-conversion. Additionally, the materials can be produced by a variety of methods, including several direct growth techniques and diffusion doping. The principal material disadvantages include a relatively large change in refractive index with temperature (large $dn/dt$), which can induce thermal lensing, and a short, microsecond, energy-storage time. Fundamental material properties, the current state-of-the-art of CW and pulsed $Cr^{2+}$doped chalcogenide lasers, have been reviewed by Carrig et al. [419].

Three-dimensional (3D) holographic recording in $As_2S_3$ glass using 800 nm wavelength, 150 fs duration pulses has been reported [421]. A diffractive beam splitter was used to generate 2–5 beams which were then focused for recording by an objective lens of NA (=0.75). The recorded 3D hologram was read out by diffraction of 632 nm He–Ne laser beam confirming the expected pattern of holograms. The mechanism of photodarkening and optical damage of $As_2S_3$ glass and dielectrics in general was discussed. The 2PA cross-section, $\sigma_2 = 74.6 \times 10^{-50}\,\mathrm{cm}^4\,\mathrm{s}^{-1}$, was determined by transmission for pulses of 150 fs and 800 nm wavelength. Also, it was demonstrated that the optical-damage threshold scales as the band gap energy for fluorides ($CaF_2, SrF_2, BaF_2, MgF_2$). Nano-/microstructuring of $As_2S_3$ glass by ablation in air was also demonstrated. High fluence($>5\,\mathrm{J\,cm}^{-2}$) irradiation of the 800 nm wavelength, 150 fs duration pulses was used to ablate $As_2S_3$ glass [421]. Self-organized growth of fibers, rods, and microsphere-type structures was observed. The composition of the nano/microstructured material was close to that of the source $As_2S_3$ glass (with up to 20% surplus of sulfur in nanorods). Straight rods as thin as 20 nm in diameter and over 1 μm long were obtained [421].

Among the family of chalcogenide glasses, $As_2S_3$ and $As_2Se_3$ are important (IR) transparent materials for a variety of applications such as IR sensors, waveguides, and photonic crystals. With the promise of accessibility to any wavelengths between 3.5 and 16 μm using tunable quantum cascade lasers (QCL) and chalcogenides with IR properties that can be compositionally

adjusted, ultrasensitive, solid-state, photonic-based chemical sensing in the midwave IR region is now possible [422]. Pacific Northwest National Laboratory (PNNL) has been developing QCLs, chalcogenides, and all other components for an integrated approach to chemical sensing. Significant progress has been made in glass formation and fabrication of different structures at PNNL. Three different glass-forming systems, As–S, As–S–Se, and As–S–Ag have been examined for this application. Purification of constituents from contaminants and thermal history are two major issues in obtaining defect-free glasses. Sundaram et al. [422] have shown how the optical properties can be systematically modified by changing the chemistry in the As–S–Se system. Different fabrication techniques need to be employed for different geometries and structures. They have successfully fabricated periodic arrays and straight waveguides using laser-writing and characterized the structures. Wet-chemical lithography has been extended to chalcogenides and challenges identified. They have also demonstrated holographic recording or diffraction gratings in chalcogenides [422].

Fabrication of 3D woodpile photonic band gap crystals from photosensitive chalcogenide glass with the help of interference lithography and layer-by-layer construction has been presented [423]. The alignment method is described, which is scalable to the extremely small feature sizes required for photonic crystals in the visible region (see Fig. 7.12). The observation and preliminary studies of photoinduced self-developing relief modulation gratings in $As_2S_3$ has been reported [424]. They were excited with near-band gap light of a CW argon laser at 488 nm. The surface of the chalcogenide film was expanded in the illuminated regions. These modulations demonstrate a strong memory effect and can be erased by heating. Galstyan et al. [424] have separated the surface and volume (scalar and vector) excitations, using different light intensity and polarization states.

Results of this study may play an important role, both in the fundamental understanding of photostructural changes, and in photonic applications of the different chalcogenide materials. Of particular practical interest is the photofabrication of periodic microstructures, e.g., Bragg filters (Bragg gratings) in infrared chalcogenide waveguides.

The pulsed plasma-deposition technique [425, 426] has been used to deposit layered structures of $SiO_2$ and $GeS_x$ glasses. High-quality, essentially hydrogen-free films were prepared. Results were presented [426] that suggest that these films could have useful properties in the production of both passive optical filters and active optical devices. In particular, the comparatively low-laser power density that is required to observe a nonlinear optical response in these materials ($<10\,\mathrm{kW\,cm^{-2}}$), the fast response of the effect ($< 250\,\mathrm{ps}$), and the ability to select the band gap, could make these materials important in the production of all-optical logic gates.

Rosenblum et al. [427] have studied both the "after-pulse effect" and the dynamic characteristics of photostructural transformations induced in

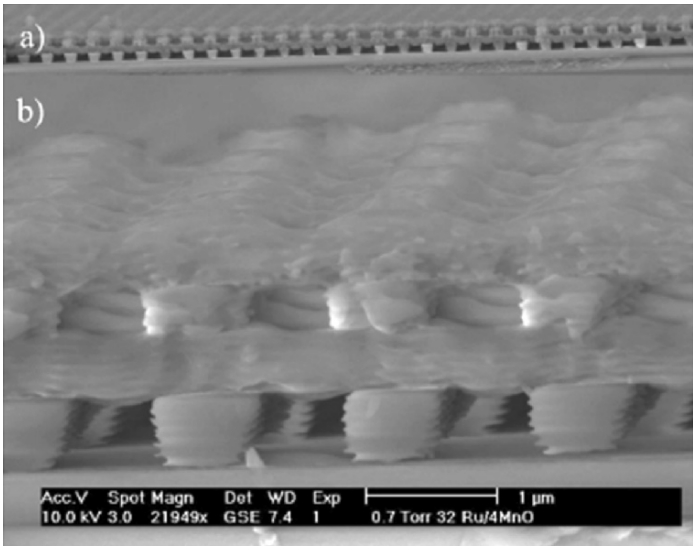


**Fig. 7.12.** A scanning electron microscope image of a four-layer $As_2S_3$ simple cubic layer-by-layer photonic crystal: (**a**) Low-magnification image and (**b**) Unit-cell structure (after [423])



glassy $As_{0.5}Se_{0.5}$ films by nanosecond pulsed 532 nm excitation. The dynamic characteristics of photostructural transformations were investigated by the transient-grating method [428]. The laser writing beam was separated into two equal intensity beams that interfere on the sample, writing a grating of period $\sim$1.5 µm. A weak CW He–Ne laser beam was sent normal to the sample in order to probe the grating formation. A high-speed photomultiplier ($\sim$ns response time) detected the probe light diffracted by the grating. The after-pulse effect investigation demonstrated more than a $10^3$times increase of the photosensitivity in the case of pulsed excitation. Dynamic characteristics (Fig. 7.13) showed a dual timescale behavior and different intensity dependence of transient and long-timescale signals. A sharp and short peak with a timescale of a few tens of nanoseconds (the "transient pulse") was followed by a slow (a few microseconds) increase of the signal that asymptotically reached a constant value (the after-pulse value).

The obtained data indicate that the strong increase of photosensitivity following short intense pulsed light excitation is due to a two-photon effect that aids the process of structural rearrangement. It was asserted that, if two photons are absorbed close to each other that weaken or break the neighboring interatomic bonds of the chalcogenide glass, the process of structural rearrangement proceeds with a much larger probability and this process can be realized only at large enough writing beam intensities. Based on their

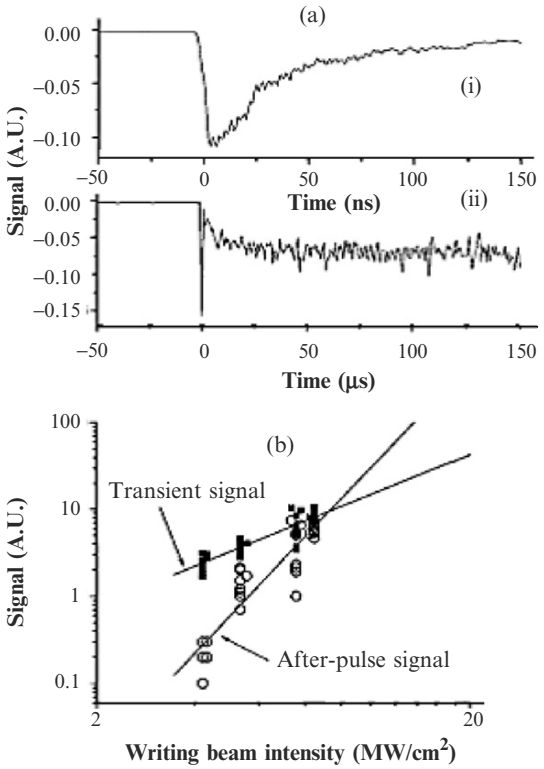


**Fig. 7.13.** (**a**) Typical diffracted signal, a few tens of nanoseconds transient (i) was followed by a slow asymptotic response, the after-pulse effect (ii). The transient started with the exciting pulse, within their experimental error of 1 ns. (**b**) Diffracted signal as a function of the writing beam intensity (after [427])



results, they propose that chalcogenide photoresists are materials of choice for pulsed holography.

Heebner et al. [429] have used sequences of optical microresonators to construct densely integrated structures that display slow group velocity, ultrahigh or low dispersion of controllable sign, enhanced SPM, and nonlinear optical switching. Microresonators confine light to circulate within and among compact photonic structures. Fabrication technology has advanced such that high-bandwidth microresonators are readily constructed from either high dielectric constant "photonic wires" [430] or photonic crystals [431] for the enhancement of nonlinearities [432, 433]. Both guiding structures have the ability to confine light to small dimensions. The use of artificial media composed of sequences of microresonators is a promising approach to the construction of photonic waveguides with engineerable optical properties. Their exotic

nonlinear properties result from a combination of increased effective path lengths and coherent intensity buildup. Heebner et al. [429] propose that these nonlinear properties can be exploited to construct optical switches, optical limiters, pulse compressors, pulse imagers [434], and other nonlinear photonic devices relying on the interplay with group-velocity dispersion. Heebner et al. [429] expect microresonator-based structures to become essential components for integrated nonlinear photonic applications. By using linear and nonlinear refractive indices of Se-based chalcogenide glasses, they estimate that a $\pi$ nonlinear phase shift is obtainable with a 1 ps, 1 pJ pulse by use of a single ultracompact microresonator of moderate finesse (see Fig. 7.14).

Bright soliton switching has been observed in materials with negative GVD [435–437]. Hence for chalcogenide glasses with a positive GVD, we expect dark soliton switching to take place. Dark solitons are more stable in the presence of noise and spread more slowly in the presence of loss compared to bright solitons in optical-communication systems. These properties provide the means for potential applications of dark solitons in optical communication systems [438, 439]. The design of an efficient switch requires a low-nonlinear absorption coefficient relative to the nonlinear refractive index, as is clear from the FOM [FOM $= \alpha_2\lambda/n_2$ with $n(I) = n_0 + n_2 I$ and $\alpha = \alpha_0 + \alpha_2 I$]. For Mach–Zehnder-based all-optical switching, the necessary condition is FOM$<$ 0.2. Fortunately, chalcogenide glasses have a small FOM, i.e. smaller than 0.2, because of their low-optical losses. Optical properties of chalcogenide glass have been used to design an NLDC switch showing dark-soliton switching [440]. The high nonlinearity of chalcogenide glass can reduce the switch length. The group-velocity dispersion of chalcogenide glass

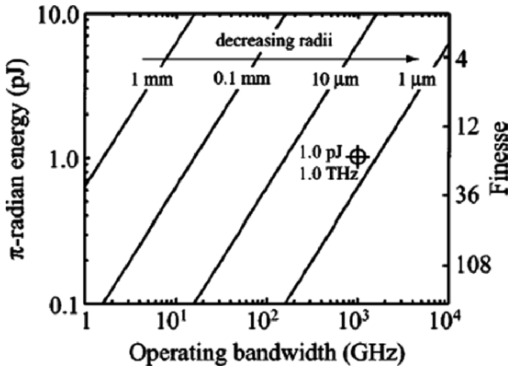


**Fig. 7.14.** Inherent trade-off between bandwidth and energy required to achieve a $\pi$ nonlinear phase shift per resonator in a single-channel SCISSOR (side-coupled integrated spaced sequence resonators) structure. The diagonal lines correspond to constant resonator diameter for AlGaAs or Se-based chalcogenide systems near 1.55 µm. Increasing finesse is directly proportional to decreasing energy (after [429])

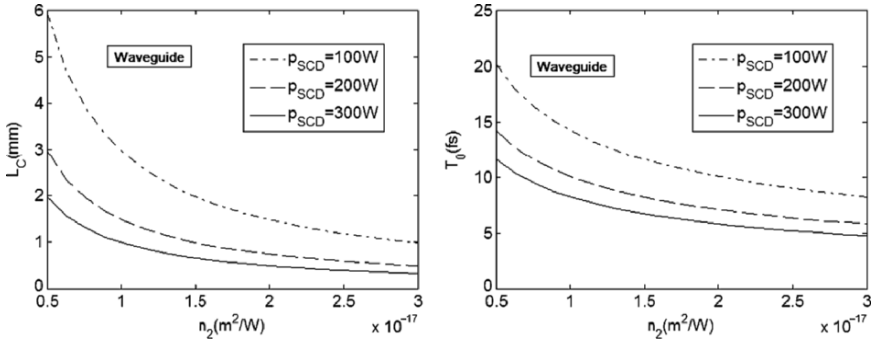


**Fig. 7.15.** Variation of the length of nonlinear directional coupler switch (**a**) and the input pulse width $T_0$ (**b**) versus the nonlinear refractive index of chalcogenide glasses for different switching powers (after [440])

at 1.55 µm is about $+545\,\mathrm{ps^2\,km^{-1}}$ [441] and its $n_2$ value is from 10 to about 1,000 times that of silica glass. The results [440] show that if we have a chalcogenide glass with a nonlinear refractive index of about $2.5 \times 10^{-17}\,\mathrm{cm^2\,W^{-1}}$, by choosing a dark switching power of $P_{\mathrm{DS}} = 100\,\mathrm{W}$, the length of the coupler must be about $L_{\mathrm{C}} = 1.2\,\mathrm{mm}$ and the input pulse width should be about 10 fs.

Hatami also considered 2PA in his simulation and studied its effect on dark-soliton switching. His results showed that for figures of merit smaller than unity, switching was possible but the pulse width increased. For FOM smaller than 0.2, it seems that there is no appreciable effect of 2PA on dark-soliton switching. Many chalcogenide glasses have a FOM<0.2. Therefore, it is possible to design an NLDC switch with 1.2 mm length for a dark-soliton pulse of width of about 10 fs and a power of about 100 W (see Fig. 7.15).

These results indicate that, by a combination of very short coupler lengths and ultra-fast switching, fabrication of integrated optical switches on a small scale is possible, which can be used in ultra-fast terabit optical computation applications.

## 7.7 Summary

Different applications of chalcogenide glasses based on their optical nonlinearities have been described. Optical limiters and their behavior for use as a filter for protection of IR detectors have been mentioned. Generation of second-harmonic signals using different poling methods in chalcogenide glasses has been presented and their electro-optic properties were introduced. Bistability observed in chalcogenide glasses has been discussed and promising applications in nonlinear photonic devices were mentioned. Fabrication of rib and ridge waveguides and of fiber gratings and their use in optical regenerators has been presented. The feasibility of fabrication of integrated

all-optical nonlinear circuits is shown and discussed. It is shown that, by introducing metal nanoparticles in the chalcogenide glass matrix, its nonlinearity is enhanced, which is promising news for practical applications. Other devices, such as binary phase gratings, broadly tunable sources in the near and midinfrared, 3D holographic gratings, 3D photonic band gap structures, and dark-soliton switching devices are introduced and proposed for applications.

# References

## Chapter 1


1. A.B Seddon, J. Non-Cryst. Solids **184**, 44 (1995)
2. J.S. Sanghera, I.D. Aggarwal, J. Non-Cryst. Solids **256–257**, 6 (1999)
3. V.K. Tikhomirov, J. Non-Cryst. Solids **256–257**, 328 (1999)
4. A. Zakery, S.R. Elliott, J. Non-Cryst. Solids **330**, 1 (2003)
5. W.H. Zachariasen, J. Am. Ceram. Soc. **54**, 3841 (1932)
6. S.R. Elliott, J. Non-Cryst. Solids **81**, 71 (1986)
7. P. Colomban, J. Corset (eds.) in *Special Issue: Raman (Micro) Spectrometry and Materials Science*, J. Raman Spectrosc. (1999)
8. W.H. Weber, R. Merlin (eds.), *Raman Scattering in Materials Science* (Springer, Berlin Heidelberg New York, 2000)
9. A. Schulte, K.A. Richardson, in *Near-Infrared Raman Spectroscopy of Chalcogenide Glasses for Integrated Optics*, Recent Research Developments in Non-Crystalline Solids (Transworld Research Network, P.O. 36/248 (1) Vallakkadavu, Trivandrum-695008, Kerala, India, 2001)
10. K. Richardson, T. Cardinal, M. Richardson, A. Schulte, S. Seal, in *Engineering Glassy Chalcogenide Materials for Integrated Optics Applications*, ed. by A.V. Kolobov, Photoinduced Metastability in Amorphous Semiconductors (Wiley-VCH, Weinheim 2003)
11. A. Apling, A.J. Leadbetter, A.C. Wright, J. Non-Cryst Solids **23**, 369 (1977)
12. C. Rivero, A. Schulte, C. Lopez, K. Richardson, K. Turcotte, V. Hamel, A. Villeneuve, T. Galstian, in *OSA Topical Meeting on Nonlinear Guided Waves* (Cleanwater, FL, 2001)
13. A. Schulte, C. Rivero, K. Richadrson, K. Turcotte, J. Laniel, V. Hamel, A. Villeneuve, A. Saliminia, T. Galstian, Opt. Commun. **198**, 125 (2001)
14. C. Rivero, P. Sharek, G. Nootz, C. Lopez, W. Li, K. Richardson, A. Schulte, G. Braunstein, R. Erwin, V. Hamel, K. Turcotte, E. Knystautas, Thin Solid Films **425**, 59 (2003)
15. C.A. Rivero, P.S. Sharek, G. Nootz, C. Lopez, K.A. Richardson, A. Schulte, R.B. Irwin, T. Galstian, V. Hamel, K. Turcotte, A. Villeneuve, R. Valee, Proc. Soc. Photo. Opt. Instrum. Eng. **4468**, 47 (2001)
16. S. Seal, K.A. Richardson, C. Lopez, A. Graham, D.K. Verma, A. Saliminia, T. Galstian, A. Villeneuve, Phys. Chem. Glasses **43**, 59 (2002)

17. R. Asal, P.E. Rivers, H.N. Rutt, J. Phys. Condens. Mater **9**, 6217 (1997)
18. S. Benazeth, M.H. Tuilier, A.M. Loireau-Lozac'h, H. Dexpert, P. Lagarde, J. Flahaut, J. Non-Cryst. Solids **110**, 89 (1989)
19. G. Lucazeau, S. Barnier, A.M. Loireau-Lozac'h, Mater. Res. Bull. **12**, 437 (1977)
20. K. Tanaka, in *Sub-Gap Photo-Induced Phenomena in Chalcogenide Glasses*, ed. by A.V. Kolobov, Photoinduced Metastability in Amorphous Semiconductors (Wiley-VCH, Weinheim, 2003)
21. D. Monroe, M.A. Kastner, Phys. Rev. B **33**, 8881 (1986)
22. R.B. Barclay, J. Phys. Condens. Mater **6**, L431 (1994)
23. M. Kastner, D. Adler, H. Fritzsche, Phys. Rev. Lett. **34**, 1346 (1975)
24. D. Vanderbilt, J.D. Joannopoulos, Phys. Rev. Lett. **49**, 823 (1982)
25. A. Kolobov, M. Kondo, R. Durny, M. Matsuda, K. Tanaka, Phys. Rev. B **56**, R485 (1998)
26. M. Popescu, in *Structure, Defects and Electronic Properties of Amorphous Semiconductors*, ed. by A.V. Kolobov, Photoinduced Metastability in Amorphous Semiconductors (Wiley-VCH, Weinheim, 2003)
27. K. Tanaka, J. Optoelectron. Adv. Mater. **4**, 505 (2001)
28. K. Tanaka, A. Odajima, J. Non-Cryst. Solids **46**, 259 (1981)
29. S.R. Elliott, in *Chalcogenide Glasses*, ed. by J. Zarzycki. Materials Science and Technology, vol. 9 (VCH, Weinheim 1991), p. 375
30. K. Tanaka, S. Nakayama, Jpn. J. Appl. Phys. Part 1 **38**, 3986 (1999)
31. K. Tanaka, T. Gotoh, N.Y. Yoshida, S. Nonomura, J. Appl. Phys. **91**, 125 (2002)
32. K. Tanaka, S. Nakayama, J. Optoelectron. Adv. Mater. **2**, 5 (2000)
33. D. Goldschmidt, J. Opt. Soc. Am. A **1**, 275 (1984)
34. A. Zakery, Y. Ruan, A.V. Rode, M. Samoc, B. Luther-Davies, J. Opt. Soc. Am. B **9**, 1844 (2003)
35. L. Tichy, H. Ticha, P. Nagels, R. Callaerts, R. Mertens, M. Vlcek, Mat. Lett. **39**, 122 (1999)
36. G. Lenz, J. Zimmermann, T. Katsufuji, M.E. Lines, H.Y. Hwang, S. Spalter, R.E. Slusher, S.W. Cheong, J.S. Sanghera, I.D. Aggarwal, Opt. Lett. **25**, 254 (2000)
37. E.M. Vogel, M.J. Weber, D.M. Krol, Phys. Chem. Glasses **32**, 231 (1991)
38. S. Ramachandran, S.G. Bishop, Appl. Phys. Lett. **74**, 13 (1999)
39. C.W. Slinger, A. Zakery, P.J.S. Ewen, A.E. Owen, Appl. Opt. **1**, 2490 (1992)
40. A. Zakery, PhD Thesis, Edinburgh University, 1991
41. A. Saliminia, A. Villeneuve, T.V. Galgtian, S. LaRochell, K. Richardson, J. Lightwave Technol. **17**, 837 (1999)
42. K.A. Richardson, J.M. McKinley, B. Lawrence, S. Joshi, A. Villeneuve, J. Opt. Mater. **10**, 155 (1998)
43. A. Zoubir, L. Shah, K. Richardson, M. Richardson, in *Proceedings of the Society of Photo-Optical Instrumentation Engineers*, 4760-5, 2 High Power Laser Ablation in Materials (Taos, NM, 2002)
44. A. Mori, Y. Ohishi, T. Kanamori, S. Sudo, Appl. Phys. Lett. **70**, 1230 (1997)
45. T. Schweizer, B.N. Samson, R.C. Moore, D.W. Hewak, D.N. Payne, Electron. Lett. **33**, 414 (1997)
46. Y.D. West, T. Schweizer, D.J. Brady, D.W. Hewak, Fiber Integr. Opt. **19**, 229 (2000)

47. B. Cole, L.B. Shaw, P.C. Pureza, R. Mossadegh, T.S. Sanghera, I.D. Aggarwal, J. Non-Cryst. Solids **256–257**, 253 (1999)
48. T. Schweizer, D.J. Brady, D.W. Hewak, Research Review, Optoelectronic Research Centre, University of Southampton (1996)
49. L.B. Shaw, D. Schaafsma, J. Moon, B. Harbison, J. Sanghera, I.D. Aggarwal, in *OSA Technical Digest Series*, vol. 11 (Optical Society of America, Washington, DC, 1997) p. 255
50. J. Nishii, S. Morimoto, I. Inagawa, R. Iizuka, T. Yamashita, T. Yamagishi, J. Non-Cryst. Solids **140**, 199 (1992)
51. M. Asobe, T. Kanamori, K. Naganuma, H. Itoh, T. Kaino, J. Appl. Phys. **77**, 5518 (1995)
52. L.E. Busse, J.A. Moon, J.S. Sanghera, I.D. Aggarwal, Laser Focus World **32**, 143 (1996)
53. L. Busse, J. Moon, J.S. Sanghera, I.D. Aggarwal, J. Harrington, K.K. Lum, in *Proceeding of the 1995 IRIS Speciality Group on Materials* (Erim, Ann Arbor, MI, 1995) p. 237
54. I.D. Aggarwal, L.E. Busse, L.B. Shaw, B. Cole, J.S. Sanghera, in *Proceedings of the Diode Laser Technology Review* (Albuquerque, NM, 1998)
55. J.S. Sanghera, I.D. Aggarwal, in *Proceedings of the 18th International Congress on Glass*, (San Francisco, CA) 5–10 July 1998
56. G. Edwards, Research at Vanderbilt, Fall, 1996
57. J. Heo, M. Rodrigues, S. Saggese, G.H. Sigel Jr., Appl. Opt. **30**, 3944 (1991)
58. J.S. Sanghera, F.H. Kung, L.E. Busse, P.C. Pureza, I.D. Aggarwal, J. Am. Ceram. Soc. **78**, 2198 (1995)
59. X.H. Zhang, M.V. Duhamel, H.L. Ma, C. Blanchetiere, J. Lucas, J. Non-Cryst. Solids **161**, 547 (1993)
60. M. Druy, in *Infrared Fiber Optics*, Ch. 8, ed. by J.S. Sanghera, I.D. Aggarwal (CRC, Boca Raton, FL, 1998)
61. **P. Melling, Commercial Literature, Rempec Inc
62. M. Saito, Technology Digest First Workshop on Optical Fiber Sensors, Jpn. Soc. Appl. Phys. 113 (1985)
63. G. Nau, F. Bucholtz, K.J. Ewing, S.T. Vohra, J.S. Sanghera, I.D. Aggarwal, Proc. Soc. Photo. Opt. Instrum. Eng. **2883**, 682 (1996)
64. B. Rigas, P.T.T. Wong, Cancer Res. **52**, 84 (1992)
65. T. Ueda, K. Yamad, T. Sugita, J. Eng. Ind. **114**, 317 (1992)
66. N.S. Kapany, R.J. Simms, Infrared Phys. **5**, 69 (1996)
67. M. Saito, M. Takizawa, S. Sakuragi, F. Tanei, Appl. Opt. **24**, 2304 (1985)
68. J. Nishii, T. Yamashita, T. Yamagishi, C. Tanaka, H. Stone, Appl. Phys. Lett. **59**, 2639 (1991)
69. **Raytheon IR Center of Excellence. Product 256 × 256 InSb VISMIR FPA. Company literature
70. H. Suto, Infrared Phys. Technol. **38**, 93 (1997)
71. D.T. Schaafsma, R. Mossadegh, J.S. Sanghera, I.D. Aggarwal, J.M. Gilligan, N.H. Tolk, M. Luce, R. Generosi, P. Perfetti, A. Cricenti, G. Margaritondo, Ultramicroscopy **77**, 77 (1999)
72. A.G. Antipenko, N.V. Artem'ev, A.A. Betin, V.R. Kamenskii, V.P. Novikov, V.G. Plotnichenko, I.V. Skripanchev, G.E. Snopatin, Quantum Electron. **25**, 498 (1995)
73. K. Petkov, G. Kozhuharova, in *2nd East-West Surface Science Workshop, EWSSW'96* (Pamporowo, Bulgaria, 1996) p. 284

74. K. Petkov, P.J.S. Ewen, J. Non-Cryst. Solids **249**, 150 (1999)
75. M. Guittard, A.M. Loireaulozach, F. Berguer, S. Barnier, J. Flahaut, J. Solid State Chem. **62**, 191 (1986)
76. P.A. Young, J. Phys. C **4**, 93 (1971)
77. R. Swanepoel, J. Phys. E **16**, 214 (1983)
78. K.A. Cerqua-Richardson, J.M. McKinley, B. Lawrence, S. Joshi, A. Villeneuve, Opt. Mater. **10**, 155 (1998)
79. X.F, Wang, X.J. Zhao, Z.W. Wang, H.T. Guo, S.X. Gu, J.G. Yu, C.L. Liu, Q.H. Gong, Mater. Sci. Eng. B **1**(10), 38 (2004)
80. S. Cherukulappurath, M. Guignard, C. Marchand, F.S. Smektala, G. Boudebs, Optics Commun. **242**, 213 (2004)
81. J.M. Harbold, F.O. Ilday, F.W. Wise, J.S. Sanghera, V.Q. Nguyen, L.B. Shaw, I.D. Aggarwal, Opt. Lett. **27**, 119 (2002)
82. D. Marchese, M. De Sario, A. Jha, A.K. Kar, E.C. Smith, Opt. Soc. Am. B **15**, 2361 (1998)
83. D.S. Gill, R.W. Eason, C. Zaldo, H.N. Rutt, N.A. Vainos, J. Non-Cryst. Solids **191**, 321 (1995)
84. J. Laniel, J.M. Menard, A. Villeneuve, R. Vallee, C. Lopez, K.A. Richardson, Proc. Soc. Photo. Opt. Instrum. Eng. **4833**, (2002)
85. A.V. Rode, B. Luther-Davies, E.G. Gamaly, J. Appl. Phys. **85**, 4213 (1999)
86. A.V. Rode, B. Luther-Davies, E.G. Gamaly, J. Appl. Phys. **85**, 4222 (1999)
87. A.V. Rode, A. Zakery, M. Samoc, R.B. Charters, E.G. Gamaly, B. Luther-Davies, Appl. Surf. Sci. **197–198**, 481 (2002)
88. A. Zakery, J. Phys. D: Appl. Phys. **35**, 2909 (2002)
89. D. Tsu, J. Vac. Sci. Technol. A **17**, 1854 (1999)
90. A.E. Owen, A.P. Firth, P.J.S. Ewen, Philos. Mag. B **52**, 347 (1985)
91. P.J.S. Ewen, A.E. Owen, in *High Performance Glasses*, ed. by M. Cable, J.M. Parker (Blackie, London, 1992) Chap. 14
92. K. Tanaka, Phys. Rev. B **57**, 5163 (1998)
93. J. Qiu, J. Si, K. Hirao, Opt. Lett. **26**, 914 (2001)
94. J.F. Viens, C. Meneghini, A. Villeneuve, T.V. Galstian, E.J. Knystautas, M.A. Duguay, K.A. Richardson, T. Cardinal, J. Lightwave Technol. **17**, 1184 (1999)

## Chapter 2

95. A. Yariv, *Quantum Electronics*, 3rd edn. (Wiley, New York, 1989)
96. M. Born, E. Wolf, *Principles of Optics*, 7th edn. (Cambridge University Press, 1999)
97. A. Yariv, P. Yeh, *Optical Waves in Crystals* (Wiley, New York, 1984)
98. R.W. Boyd, *Nonlinear Optics*, 2nd edn. (Academic, New York, 2003)
99. L.F. Mollenauer, R.H. Stolen, J.P. Gordon, Phys. Rev. Lett. **45**, 1095 (1980)
100. B.L. Lawrence, M. Cha, J.U. Kang, W. Toruellas, G. Stegeman, G. Baker, J. Meth, S. Etemad, Electron. Lett. **30**, 447 (1994)
101. R.W. Helwarth, J. Opt. Soc. Am. **67**, 1 (1977)
102. A. Yariv, D.M. Pepper, Opt. Lett. **1**, 16 (1977)
103. W. Kaiser, M. Maier, in *Laser Handbook*, ed. by F.T. Arecchi, E.O. Schulz-DuBois (North-Holland, Amsterdam, 1972)

104. A. Yariv, R.A. Fisher, in *Optical Phase Conjugation*, ed. by R.A. Fisher (Academic, New York, 1983)
105. U. Simon, F.K. Tittel, in *Methods of Experimental Physics*, vol. 3, ed. by R.G. Hulet, F.B. Dunning (Academic, San Diego, 1994)
106. J.F. Reintjes, *Nonlinear Optical Parametric Process in Liquids and Gases* (Academic, New York, 1984)
107. P.N. Prasad, D.J. Williams, *Introduction to Nonlinear Optical Effects in Molecules and Polymers* (Wiley, New York, 1991)

## Chapter 3

108. R.L. Sutherland, *Handbook of Nonlinear Optics*, 1st edn. (Marcel Dekker, New York, 1996)
109. A. Samoc, M. Samoc, M. Woodruff, B. Luther-Davies, *Poly (p-phenylenevinylene): An Attractive Material for Photonic Applications*, ed. by D.L. Wise, G.E. Wnek, D.J. Trantolo, T.M. Cooper, J.D. Gresser. Photonic Polymer Systems (Marcel Dekker, New York, 1998)
110. H.J. Eichler, P. Guenther, D.W. Pohl, *Laser-induced Dynamic Gratings*. Springer Series in Optical Sciences, vol. 50 (Springer, Berlin Heidelberg New York, 1986)
111. G.M. Carter, J. Opt. Soc. Am. B **4**, 1018 (1987)
112. Y. Peng, M. Samoc, P.N. Prasad, J. Chem. Phys. **94**, 5282 (1991)
113. F.P. Strohkendl, L.R. Dalton, R.W. Hellwarth, H.W. Sarkas, Z.H. Kafafi, J. Opt. Soc. Am. B **14**, 92 (1997)
114. H. Kanbara, S. Fujiwara, K. Tanaka, H. Nasu, K. Hirao, Appl. Phys. Lett. **70**, 1925 (1997)
115. R. Adair, L.L. Chase, S.A. Payne, J. Opt. Soc. Am. B **4**, 875 (1987)
116. M. Sheik-bahae, A.A. Said, T.H. Wei, D.J. Hagan, E.W. Van Stryland, IEEE J. Quant. Electron. **26**, 760 (1989)
117. M. Samoc, A. Samoc, B. Luther-Davies, Z. Bao, L. Yu, B. Hsieh, U. Scherf, J. Opt. Soc. Am. B **15**, 817 (1998)
118. J.T. Gopinath, M. Soljacic, E.P. Ippen, V.N. Fuflyigin, W.A. King, M. Shurgalin, J. Appl. Phys. **96**, 6931 (2004)
119. H. Nasu, K. Kubodera, M. Kobayashi, M. Nakamura, K. Kamiya, J. Am. Ceram. Soc. **73**, 1794 (1990)
120. P.N. Prasad, D.J. Williams, *Introduction to Nonlinear Optical Effects in Molecules and Polymers* (Wiley, New York, 1991)
121. X.F. Wang, Z.W. Wang, J.G. Yu, C.L. Liu, X.J. Zhao, Q.H. Gong, Chem. Phys. Lett. **399**, 230 (2004)
122. G.P. Agrawal, *Nonlinear Fiber Optics*, 3rd edn. (Academic, New York, 2001)
123. R.R. Alfano, *The Super-Continuum Laser Source* (Springer, Berlin Heidelberg New York, 1989)
124. M. Asobe, K. Suzuki, T. Kanamori, K. Kubodera, Appl. Phys. Lett. **60**, 1153 (1992)
125. K.A. Cerqua-Richardson, J.M. McKinley, B. Lawrence, S. Joshi, A. Villeneuve, Opt. Mater. **10**, 155 (1998)
126. I. Kang, T. Krauss, F. Wise, Opt. Lett. **22**, 1077 (1997)

127. S. Smolorz, I. Kang, F. Wise, B.G. Aitken, N.F. Borrelli, J. Non-Cryst. Solids **256–257**, 310 (1999)
128. J.M. Harbold, F.O. Ilday, F.W. Wise, J.S. Sanghera, V.Q. Nguyen, L.B. Shaw, I.D. Aggarwal, Opt. Lett. **27**, 119 (2002)
129. G. Boudebs, F. Sanches, J. Troles, F. Smektala, Opt. Commun. **199**, 425 (2001)
130. F. Smektala, J. Troles, P. Houizot, T. Jouan, G. Boudebs, S. Cherukulappurath, V. Couderc, P.A. Champert, Proc. Soc. Photo. Opt. Instrum. Eng. **5451**, 347 (2004)

## Chapter 4

131. K. Tanaka, Appl. Phys. Lett. **80**, 177 (2002)
132. H. Kanbera, S. Fujiwara, K. Tanaka, H. Nasu, K. Hirao, Appl. Phys. Lett. **70**, 925 (1997)
133. Z.H. Zhou, T. Hashimoto, H. Nasu, K. Kamiya, J. Appl. Phys. **84**, 2380 (1998)
134. M. Asobe, T. Kanamori, K. Kubodera, IEEE Photon. Technol. Lett. **P1L4**, 362 (1992)
135. M. Asobe, K. Suzuki, T. Kanamori, K. Kubodera, Appl. Phys. Lett. **60**, 1153 (1992)
136. M. Asobe, T. Kanamori, K. Kubodera, IEEE J. Quantum Electron. **29**, 2325 (1993)
137. M. Asobe, Opt. Fiber Technol. **3**, 142 (1997)
138. M. Sheik-Bahae, D.C. Hutchings, D.J. Hagan, E.W. Van Stryland, IEEE J. Quantum Electron. **27**, 1296 (1991)
139. H. Nasu, K. Kubodera, H. Kobayashi, M. Nakamura, K. Kamiya, J. Am. Ceram. Soc. **4**, 1794 (1990)
140. Z.H. Zhou, H. Nasu, T. Hashimoto, K. Kamiya, J. Ceram. Soc. Jpn. **105**, 1079 (1997)
141. J.M. Harbold, F.O. Ilday, F.W. Wise, J.S. Sanghera, V.Q. Nguyen, L.B. Shaw, I.D. Aggarwal, Opt. Lett. **27**, 119 (2002)
142. G. Lenz, J. Zimmerman, T. Katsufuji, M.E. Lines, H.Y. Hwang, S. Spalter, R.F. Slusher, S.W. Cheong, J.S. Sanghera, I.D. Aggarwal, Opt. Lett. **25**, 254 (2000); J.M. Harbold, F.O. Ilday, F.W. Wise, J.S. Sanghera, V.Q. Nguyen, L.B. Shaw, I.D. Aggarwal, Opt. Lett. **27**, 119 (2002)
143. J. Harbold, F.O. Ilday, F.W. Wise, B.G. Aitken, IEEE Photon. Technol. Lett. **14**, 822 (2002)
144. C. Quemard, F. Smetkala, V. Couderc, A. Barthelemy, J. Lucas, J. Phys. Chem. Solids **62**, 1435 (2001)
145. T.I. Kosa, R. Rangel-Rojo, E. Hajto, P.J.S. Ewen, A.E. Kar, B.S. Wherrett, J. Non-Cryst. Solids **164–166**, 1219 (1993)
146. A. Zakery, M. Hatami, J. Opt. Soc. Am. B **22**, 591 (2005)
147. A. Zakery, Y. Ruan, A.V. Rode, M. Samoc, B. Luther-Davies, J. Opt. Soc. Am. B **20**, 1844 (2003)
148. A. Zakery, J. Phys. D: Appl. Phys. **35**, 2909 (2002)
149. K.S. Bindra, H.T. Bookey, A.K. Kar, B.S. Wherrett, X. Liu, A. Jha, Appl. Phys. Lett. **79**, 1939 (2001)
150. F. Smektala, C. Quemard, L. Leneindre, J. Lucas, A. Barthelemy, C. De Angelis, J. Non-Cryst. Solids **239**, 139 (1998)

151. T. Cardinal, K.A. Richardson, H. Shim, A. Schulte, R. Beatty, K. Le Foulgoc, C. Meneghini, J.F. Viens, A. Villeneuve, J. Non-Cryst. Solids **256–257**, 353 (1999)
152. S. Spalter, H.Y. Hwang, J. Zimmermann, G. Lenz, T. Katsufuji, S.-W. Cheong, R.E. Slusher, Opt. Lett. **27**, 363 (2002)
153. K.A. Cerqua-Richardson, J.M. McKinley, B. Lawrence, S. Joshi, A. Villeneuve, Opt. Mat. **10**, 155 (1998)
154. S. Smolorz, I. Kang, F. Wise, B.G. Aitken, N.F. Borrelli, J. Non-Cryst. Solids **256–257**, 310 (1990)
155. K. Petkov, P.J.S. Ewen, J. Non-Cryst. Solids **249**, 150 (1999)
156. X.F. Wang, Z.W. Wang, J.G. YU, C.L. Liu, X.J. Zhao, Q.H. Gong, Chem. Phys. Lett. **399**, 230 (2004)
157. F. Smektala, J. Troles, V. Couderc, A. Barthelemy, G. Boudebs, F. Sanchez, H. Zeghlache, G. Martinelli, Y. Quiquempois, S. Bailleux, Proc. Soc. Photo. Opt. Instrum. Eng. **4628**, 30 (2002)
158. H. Nasu, J. Matsuoka, K. Kamiya, J. Non-Cryst. Solids **178**, 23 (1994)
159. G. Boudebs, Proc. Soc. Photo. Opt. Instrum. Eng. **5212**, 23 (2003)
160. R. Rangel Rojo, E.H. Poniatowski, A. Munoz Flores, Proc. Soc. Photo. Opt. Instrum. Eng. **2730**, 397 (1996)
161. S.Y. Kim, M.J. Kang, S.Y. Choi, Mat. Res. Soc. Proc. **803**, 259 (2004)
162. M. Munzar, L. Tichy, H. Ticha, Curr. Appl. Phys. **2**, 181 (2002)
163. R.C. Miller, Appl. Phys. Lett. **5**, 17 (1964); J.J. Wynne, Phys. Rev. **178**, 1295 (1969)
164. H. Kobayashi, H. Kanbara, M. Koga, K. Kubodera, J. Appl. Phys. **74**, 3683 (1993)
165. K. Petkov, R. Todorov, D. Kozhuharova, L. Tichy, E. Cernoskova, P.J.S. Ewen, J. Mat. Sci. **39**, 961 (2004)
166. N.I. Boling, A.T. Glass, A. Owyoung, IEEE J. Quantum Electron. **QE-14**, 601 (1978)
167. S.H. Wemple, M. Di Domenico, Phys. Rev. B **3**, 1338 (1971)
168. R.A. Ganeev, A.I. Ryasnyansky, M.K. Kodirov, T. Usmanov, J. Opt. A: Pure Appl. Opt. **4**, 446 (2002)
169. R.A. Ganeev, A.I. Ryasnyansky, R.I. Tugushev, T. Usmanov, J. Opt. A: Pure Appl. Opt. **5**, 409 (2003)
170. L. Tichy, H. Ticha, P. Nagels, R. Callaerts, R. Mertens, M. Vleek, Mat. Lett. **39**, 122 (1999)
171. S. Cherukulappurath, M. Guignard, C. Marchand, F. Smektala, G. Boudebs, Opt. Commun. **242**, 313 (2004)
172. K. Ogusu, J. Yamasaki, S. Maeda, M. Kitao, M. Minakata, Opt. Lett. **29**, 265 (2004)
173. F. Smektala, C. Quemard, V. Couderc, A. Barthelemy, J. Non-Cryst. Solids **274**, 232 (2000)
174. J. Troles, F. Smektala, G. Boudebs, A. Monteil, Opt. Mat. **22**, 335 (2003)
175. C.H. Kwak, Y.L. Lee, S.G. Kim, J. Opt. Soc. Am. B **16**, 600 (1999)
176. R.E. Slusher, G. Lenz, J. Hodelin, J.S. Sanghera, L.B. Shaw, I.D. Aggarwal, J. Opt. Soc. Am. B **21**, 1146 (2004)
177. A. Zakery, S.R. Elliott, J. Non-Cryst. Solids **330**, 1 (2003)
178. J.M. Harbold, F.O. Ilday, F.W. Wise, J.S. Sanghera, V.Q. Nguyen, L.B. Shaw, I.D. Aggarwal, Opt. Lett. **27**, 119 (2002)

179. K. Tanaka, J. Non-Cryst. Solids **338–340**, 534 (2004)
180. A. Jha, X. Liu, A.K. Kar, H.T. Bookey, Curr. Opin. Solid State Mater Sci. **5**, 475 (2001)
181. M. Asobe, T. Kanamori, K. Naganumi, H. Itoh, T. Kaino, J. Appl. Phys. **77**, 5518 (1995)
182. F. Sanchez, G. Boudebs, S. Cherukulappurath, H. Leblond, J. Troles, F. Smektala, J. Nonlinear Opt. Phys. Mat. **13**, 7 (2004)
183. J. Singh, K. Shimakawa, in *Advances in Amorphous Semiconductors* (Taylor & Francis, London, 2003)
184. S.R. Elliott in *Materials Science and Technology*, vol. 9, ed. by J. Zarzycki, (Wiley-VCH, Weinheim, 1991)
185. J. Requejo-Isidro, A.K. Mairaj, V. Pruneri, D.W. Hewak, M.C. Netti, J.J. Baumberg, J. Non-Cryst. Solids **317**, 241 (2003)
186. M. Sheik-Bahae, J.J. Hagan, E.W. Van Stryland, Phys. Rev. Lett. **65**, 96 (1990)
187. J.I. Pankov, *Optical Processes in Semiconductors* (Dover, New York, 1971)
188. M. Huang, L. Ouyang, W.Y. Ching, Phys. Rev. B **59**, 3540 (1999)
189. M. Sheik-Bahae, E.W. Van Stryland, in *Semiconductors and semimetals*, vol. 58, ed. by E. Garmire, A. Kost (Academic, San Diego, CA, 1999)
190. G. Boudebs, S. Cherukulappurath, M. Guignard, J. Troles, F. Smektala, F. Sanchez, Opt. Commun. **232**, 417 (2004)
191. J.M. Harbold, F.O. Ilday, F.W. Wise, IEEE Photon. Technol. Lett. **14**, 822 (2000)
192. J. Troles, F. Smektala, G. Boudebs, A. Monteil, Opt. Mater. **22**, 335 (2003)
193. E. Haro-Poniatowski, M. Fernandez-Guasti, S. Camacho-Lopez, F. Ruiz, Physica A **207**, 329 (1994)
194. A. Monteil, G. Boudebs, F. Sanchez, C. Duverger, B. Boulard, J. Troles, F. Smektala, Proc. Soc. Photo. Opt. Instrum. Eng. **4829**, 109 (2003)
195. Y. Quiquempois, A. Villeneuve, D. Dam, K. Turcotte, J. Maier, G. Stegeman, S. Lacroix, Electron. Lett. **36**, 733 (2000)
196. T. Yoko, K. Kamiya, H. Yamada, K. Tanaka, J. Am. Ceram. Soc. **71**, C70 (1988)
197. J. Qiu, J. Si, K. Hirao, Opt. Lett. **26**, 914 (2001)
198. M. Fernandez-Guasti, R.F. Alonso-Pinzon, E. Haro-Poniatowski, Opt. Commun. **221**, 37 (2003)
199. V. Pruneri, P.G. Kazansky, D. Hewak, J. Wang, H. Takebe, D.N. Payne, Appl. Phys. Lett. **70**, 155 (1997)
200. M.T. De Araujo, M.V.V. Vermelho, A.S. Gouveia-Neto, S.B. Sombra, J.A. Medeiros-Neto, IEEE Photon. Technol. Lett. **8**, 821 (1998)
201. I.V. Kityk, B. Sahroui, Phys. Rev. B **60**, 942 (1999)
202. Q. Liu, F. Gan, X. Zhao, K. Tanaka, A. Narazaki, K. Hirao, Opt. Lett. **26**, 1347 (2001)
203. H.D. Jannek, D.E. Day, J. Am. Ceram. Soc. **64**, 227 (1981)
204. J. Lucas, Curr. Opin. Solid State Mater. Sci. **4**, 181 (1999)
205. M. Yamane, Y. Asahara, *Glasses for Photonics* (Cambridge University Press, Cambridge, 2000)
206. A.J. Glass, Laser Program Annual Report-1974 (Lawrence Livermore Laboratory, 1975) p. 256
207. E.M. Vogel, S.G. Kosinski, D.M. Krol, J.L. Jackel, S.R. Friberg, M.K. Oliver, J. Non-Cryst. Solids **107**, 244 (1989)

208. X. Zhu, Q. Li, N. Ming, Z. Meng, Appl. Phys. Lett. **71**, 867 (1997)
209. H. Nasu, Y. Ibara, K. Kubodera, J. Non-Cryst. Solids **110**, 229 (1989)
210. D.W. Hall, M.A. Newhouse, N.F. Borrelli, W.H. Dumbaugh, D.L. Weidman, Appl. Phys. Lett. **54**, 1293 (1989)
211. R. Adair, L.L. Chaseand, S.A. Payne, J. Opt. Soc. Am. B **4**, 875 (1987)
212. K. Tanaka, *Group VIb Amorphous Materials and Applications*, ed. by G. Lucovsky, M. Popescu, Non-Crystalline Materials for Optoelectronics, Optoelectronic Materials and Devices, vol. 1 (INOE Bucharest, 2004) Chap. 3.

## Chapter 5

213. J. Nishii, T. Yamashita, T. Yamagishi, Appl. Opt. **28**, 5122 (1989)
214. J.S. Sanghera, I.D. Aggarwal, L. Busse, P. Pureza, V. Nguyen, R. Miklos, F. Kung, R. Mossadegh, Proc. Soc. Photo. Opt. Instrum. Eng. **2396**, 71 (1995)
215. T. Kanamori, Y. Terunuma, S. Takahashi, T. Miyashita, J. Lightwave Technol. **2**, 607 (1984)
216. A.V. Vasil'ev, G.G. Devyatykh, E.M. Dianov, A.N. Gur'yanov, A. Yu. Laptev, V.G. Plotnichenko, Yu. N. Pyrkov, G.E. Snopatin, I.V. Skripachev, M.F. Churbanov, V.A. Shipunov, Quant. Electron. **23**, 89 (1993)
217. D.W. Hewak, R.C. Moore, T. Schweizer, J. Wang, B. Samson, W.S. Brocklesby, D.N. Payne, E.J. Tarbox, Electron. Lett. **32**, 384 (1996)
218. A. Mori, Y. Ohishi, T. Kanamori, S. Sudo, Appl. Phys. Lett. **70**, 1230 (1997)
219. Y.D. West, T. Scheweizer, D.J. Brady, D.W. Hewak, Fiber Integr. Opt. **19**, 229 (2000)
220. J.S. Sanghera, L.B. Shaw, L.E. Busse, V.Q. Nguyen, P.C. Pureza, B.C. Cole, B.B. Harbison, I.D. Aggarwal, R. Mossadegh, F. Kung, D. Talley, D. Roselle, R. Miklos, Fiber Integr. Opt. **19**, 251 (2000)
221. D.J. Gibson, J.A. Harrington, J. Appl. Phys. **95**, 3895 (2004)
222. T.J. Loretz, A.R. Hilton Sr., A.R. Hilton Jr., J. McCord, Proc. Soc. Photo. Opt. Instrum. Eng. **2977**, 14 (1997)
223. L. Baylor, S. Nave, in *Fiber Optic Sensing*, Meas. Control, 93 (1996); J. Heo, M. Rodrigues, S. Saggese, G.H. Sigel Jr., Appl. Opt. **30**, 3944 (1991)
224. T. Abel, J. Hirsch, J. Harrington, Proc. Soc. Photo. Opt. Instrum. Eng. **2131**, 11 (1994)
225. S.Q. Gu, S. Ramachandran, E.E. Reuter, D.A. Turnbull, J.T. Verdeyen, S.G. Bishop, Appl. Phys. Lett. **66**, 670 (1995)
226. S.Q. Gu, S. Ramachandran, E.E. Reuter, D.A. Turnbull, J.T. Verdeyen, S.G. Bishop, J. Appl. Phys. **77**, 3365 (1995)
227. J.S. Sanghera, I.D. Aggarwal, in *Infrared Fiber Optics*, ed. by J.S. Sanghera and I.D. Aggarwal (CRC, Boca Raton 1998) p. 325
228. J.A. Harrington, *Infrared Fibers and Their Applications*, vol. 135 (SPIE Press Monograph PM, 2004)
229. I.D. Aggarwal, J.S. Sanghera, J. Optoelectron. Adv. Mater. **4**, 665 (2002)
230. J.S. Sanghera, V.Q. Nguyen, P.C. Pureza, F.H. Kung, R. Miklos, I.D. Aggarwal, J. Lightwave Technol. **12**, 737 (1994)
231. M.F. Churbanov, J. Non-Crystal. Solids **140**, 324 (1992)
232. J.S. Sanghera, I.D. Aggarwal, J. Non-Cryst. Solids **213–214**, 63 (1997)

233. L.B. Shaw, B. Cole, P. Thielen, J.S. Sanghera, I.D. Aggarwal, IEEE J. Quantum Electron. **37**, 1127 (2001)
234. J. Moon, B.B. Harbison, J.S. Sanghera, I.D. Aggarwal, in *Proceedings of the Photonics*, Madras, India, 9–13 December 1996
235. S. Kawanishi, H. Takara, K. Uchiyama, M. Saruwatari, T. Kitoh, Electron. Lett. **29**, 2211 (1993)
236. G.P. Agrawal, *Nonlinear Fiber Optics*, 3rd edn. (Academic, San Diego, 2001)
237. R.W. Boyd, *Nonlinear Optics*, 2nd edn. (Academic, San Diego, 2003)
238. G.I. Stegeman, R.H. Stolen, J. Opt. Soc. Am. B **6**, 652 (1989)
239. J. Bromage, J. Lightwave Technol. **22**, 79 (2004)
240. R.L. Sutherland, *Handbook of Nonlinear Optics*, 2nd edn. (Marcel Dekker, New York, 2003)
241. A. Zheltikov, Appl. Phys. B: Laser Opt. **77**, 143 (2003)
242. A.K. Abeeluck, C. Headley, Appl. Phys. Lett. **85**, 4863 (2004)
243. Y. Ni, Q. Wang, X. Liu, J. Peng, B. Zhou, Appl. Phys. Lett. **85**, 3384 (2004)
244. X.H. Ni, C. Wang, X.C. Liang, M. Al-Rubaiee, R.R. Alfano, IEEE J. Select. Topic. Quant. Electron. **10**, 1229 (2004)
245. U. Osterberg, W. Margulis, Opt. Lett. **11**, 516 (1986)
246. R.H. Stolen, H.W.K. Tom, Opt. Lett. **12**, 585 (1987)
247. Y. Luo, A. Biswas, A. Frauenglass, S.R. Brueck, Appl. Phys. Lett. **84**, 4935 (2004)
248. B. Ferreira, E. Fargin, J.P. Manaud, G. Le Flem, V. Rodriguez, T. Buffeteau, J. Non-Cryst. Solids **343**, 121 (2004)
249. G.S. Murugan, T. Suzuki, Y. Ohishi, Y. Takahashi, Y. Benino, T. Fujiwara, T. Komatsu, Appl. Phys. Lett. **85**, 3405 (2004)
250. M. Guignard, V. Nazabal, J. Troles, F. Smektala, H. Zeghlache, Y. Quiquempois, A. Kudlinski, G. Martinelli, Opt. Exp. **13**, 789 (2005)
251. Q.M. Liu, F.X. Gan, X.J. Zhao, K. Tanaka, A. Narazaki, K. Hirao, Opt. Lett. **26**, 1347 (2001)
252. Y. Quiquempois, P. Niay, M. Dounay, B. Poumellec, Curr. Opin. Solid State Mater. Sci. **7**, 89 (2003)
253. G.P. Agrawal, in *Supercontinuum Laser Source*, ed. by R.R. Alfano (Springer, Berlin Heidelberg New York, 1989) Chap. 3
254. H.A. Haus, *Waves and Fields in Optoelectronics* (Prentice-Hall, Englewood Cliffs, 1984) Chap. 10
255. P.M. Morse, H. Feshbach, in *Methods of Theoretical Physics* (McGraw-Hill, New York, 1953) Chap. 9
256. M. Asobe, Opt. Fiber Technol. **3**, 142 (1997)
257. F.M. Mitschke, L.F. Mollenauer, Opt. Lett. **11**, 659 (1986)
258. J.P. Gordon, Opt. Lett. **11**, 662 (1986)
259. A.W. Snyder, J.D. Love, *Optical Waveguide Theory* (Chapman & Hall, London, 1983) Chaps. 12–15
260. G.P Agrawal, *Fiber-Optic Communication Systems* (Wiley, New York 1997) Chap. 2
261. C.C. Chang, A.M. Weiner, A.M. Vengsarakar, D.W. Peckham, Opt. Lett. **21**, 1141 (1996)
262. S. Kawanishi, H. Takara, O. Kamatani, T. Morioka, M. Saruwatari, Electron. Lett. **32**, 470 (1996)
263. S. Kawanishi, H. Takara, T. Morioka, O. Kamatani, K. Takiguchi, T. Kitoh, M. Saruwatari, Electron. Lett. **32**, 916 (1996)

264. K. Takiguchi, S. Kawanishi, H. Takara, K. Okamoto, Y. Ohmori, Electron. Lett. **32**, 755 (1996)
265. C.C. Chang, A.M. Weiner, IEEE J. Quantum Electron. **33**, 1455 (1997)
266. M. Durkin, M. Ibsen, M.J. Cole, R.I. Laming, Electron. Lett. **23**, 1891 (1997)
267. C.C. Chang, H.P. Sardesai, A.M. Weiner, Opt. Lett. **23**, 283 (1998)
268. K. Takiguchi, S. Kawanishi, H. Takara, A. Himeno, K. Hattori, J. Lightwave Technol. **16**, 1647 (1998)
269. T. Imai, T. Komukai, M. Nakazawa, Electron. Lett. **34**, 2422 (1998)
270. H. Tsuda, K. Okamoto, T. Ishii, K. Naganuma, Y. Inoue, H. Takenouchi, T. Kurokawa, IEEE Photon. Technol. Lett. **11**, 569 (1999)
271. S. Shen, A.M. Weiner, IEEE Photon. Technol. Lett. **11**, 827 (1999)
272. F. Futami, K. Taira, K. Kikuchi, A. Suzuki, Electron. Lett. **35**, 2221 (1999)
273. T. Komukai, T. Inui, M. Nakazawa, IEEE J. Quantum Electron. **36**, 409 (2000)
274. T. Yamamoto, E. Yoshida, K.R. Tamura, K. Yonenaga, M. Nakazawa, IEEE Photon. Technol. Lett. **12**, 353 (2000)
275. M.D. Pelusi, F. Futami, K. Kikuchi, A. Suzuki, IEEE Photon. Technol. Lett. **12**, 795 (2000)
276. G.I. Stegeman, E.M. Wright, N. Finlayson, R. Aznoni, C.T. Seaton, J. Lightwave Technol. **6**, 953 (1988)
277. M. Yamashita, K. Torizuka, T. Uemiya, T. Shimada, Appl. Phys. Lett. **58**, 2727 (1991)
278. N.J. Doran, D. Wood, Opt. Lett. **13**, 56 (1988)
279. H. Nasu, K. Kubodera, H. Kobayashi, M. Nakamura, K. Kamiya, J. Am. Ceram. Soc. **73**, 1794 (1990)
280. M. Asobe, T. Kanamori, K. Kubodera, IEEE J. Quantum Electron. **29**, 2325 (1993)
281. M. Asobe, H. Itoh, T. Miyazawa, T. Kanamori, Electron. Lett. **29**, 1966 (1993)
282. R.H. Stolen, J.P. Gordon, W.J. Tomlinson, H.A. Haus, J. Opt. Soc. Am. B **6**, 1159 (1989)
283. V. Mizrahi, K.W. Delong, G.I. Stegeman, M.A. Saifi, M.J. Andrejco, Opt. Lett. **14**, 1140 (1989)
284. M. Sheik-Bahae, D.C. Hutchings, D.J. Hagan, E.W. Van Stryland, IEEE J. Quantum Electron. **27**, 1296 (1991)
285. M. Asobe, T. Kanamori, K. Naganuma, H. Itoh, T. Kaino, J. Appl. Phys. **77**, 5518 (1995)
286. F. Quellette, Opt. Lett. **16**, 303 (1989)
287. M.T. de Aruajo, M.V.D. Vermelho, A.S. Gouveia-Net, A.S.B. Sombra, J.A. Medeiros Neto, IEEE Photon. Technol. Lett. **8**, 821 (1996)
288. S.J. Russell, H. Takabe, J. Lightwave Technol. **15**, 1484 (1997)
289. N. Dixit, R. Vijaya, Proc. Soc. Photo. Opt. Instrum. Eng. **4417**, 477 (2001)
290. A.K. Mairaj, M.N. Petrovich, Y.W. West, A. Fu, D.W.J. Harwood, L.N. Ng, T.M. Monro, N.G. Broderick, D.W. Hewak, Proc. Soc. Photo. Opt. Instrum. Eng. **4204**, 278 (2001)
291. T.M. Monro, D.J. Richardson, N.G.R. Broderick, P.J. Bennett, J. Lightwave Technol. **17**, 1093 (1999)
292. R.F. Cregan, B.J. Mangan, J.C. Knight, T.A. Birks, P.St.J. Russell, P.J. Roberts, D.C. Allan, Science **285**, 1537 (1999)
293. R.E. Slusher, G. Lenz, J. Hodelin, J.S. Sanghera, L.B. Shaw, I.D. Aggarwal, J. Opt. Soc. Am. B **21**, 1146 (2004)

294. P.V. Mamyshev, in *Proceedings of the European Conference on Optical Communications*, vol. 1 (ECOC, Madrid, 1998), p. 475
295. P.S. Westbrook, T.H. Her, B.J. Eggleton, S. Hunsche, G. Raybon, Electron. Lett. **38**, 1193 (2002)
296. K. Ogusu, H. Li, M. Kitao, J. Opt. Soc. Am. B **21**, 1302 (2004)
297. G.W. Faris, L.E. Jusinski, A.P. Hickman, J. Opt. Soc. Am. B **10**, 587 (1993)
298. H. Yoshida, M. Nakatsuka, H. Fujita, T. Sasaki, K. Yoshida, Appl. Opt. **36**, 7783 (1997)
299. D.A. Pinnow, IEEE J. Quantum Electron. **QE-6**, 223 (1970)
300. N. Uchida, N. Niizeki, Proc. IEEE **61**, 1073 (1973)
301. H. Nasu, New Glass **4**, 13 (1990)
302. K. Ogusu, J. Yamasaki, S. Maeda, M. Kitao, M. Minakata, Opt. Lett. **29**, 265 (2004)
303. Y. Ohmachi, N. Uchida, J. Appl. Phys. **43**, 1709 (1972)
304. P.A. Thielen, L.B. Shaw, J.S. Sanghera, I.D. Aggarwal, Opt. Express **11**, 3248 (2003)
305. M. Asobe, H. Kobayashi, H. Itoh, T. Kanamori, Opt. Lett. **18**, 1056 (1993)
306. M. Asobe, T. Kanamori, K. Kubodera, IEEE Photon. Technol. Lett. **4**, 362 (1992)

## Chapter 6

307. T.F. Boggess, Jr., A.L. Smirl, S.C. Moss, I.W. Boyd, E.W. Van Stryland, IEEE J. Quantum Electron. **QE-21**, 488 (1985)
308. E.W. Van Stryland, Y.Y. Wu, D.J. Hagan, M.J. Soileau, K. Mansour, J. Opt. Soc. Am. B **5**, 1980 (1988)
309. K.J. Blow, N.J. Doran, B.K. Nayar, Opt. Lett. **14**, 754 (1989)
310. M.N. Islam, E.R. Sunderman, R.H. Stolen, W. Pleibel, J.R. Simpson, Opt. Lett. **14**, 811 (1989)
311. M.N. Islam, Opt. Lett. **15**, 417 (1990)
312. J.D. Moores, K. Bergman, H.A. Haus, E.P. Ippen, Opt. Lett. **16**, 138 (1991)
313. M. Asobe, T. Kanamori, K. Kubodera, IEEE Photon. Technol. Lett. **4**, 362 (1992)
314. M.A. Duguay, J.W. Hansen, Appl. Phys. Lett. **15**, 192 (1969)
315. M.A. Duguay, in *Progress in Optics*, ed. by E. Wolf, vol. 14 (North-Holland, Amsterdam, 1976) p. 163
316. G.I. Stegeman, in *Ultrafast All-optical Waveguide Switching in Non-linear Optics and Optical Physics*, ed. by I.C. Khoo, J.F. Lam, F. Simoni (World Scientific, Singapore, 1994) p. 234
317. M. Asobe, T. Kanamori, K. Kubodera, IEEE J. Quantum Electron. **29**, 2325 (1993)
318. W.J. Tomlinson, R.H. Stolen, C.U. Shank, J. Opt. Soc. Am. B **1**, 139 (1984)
319. M. Asobe, H. Kobayashi, H. Itoh, Opt. Lett. **18**, 1056 (1993)
320. V. Mizrahi, K.W. Delong, G.I. Stegeman, M.A. Saifi, M.J. Andrejco, Opt. Lett. **14**, 1140 (1989)
321. M. Asobe, T. Ohara, I. Yokohama, T. Kaino, Electron. Lett. **32**, 1396 (1996)
322. P.W.E. Smith, Proc. Soc. Photo. Opt. Instrum. Eng. **3491**, 3 (1998)
323. S.M. Jensen, IEEE J. Quantum Electron. **QE-18**, 1850 (1982)

324. G. Lenz, J. Zimmermann, T. Katsufuji, M.E. Lines, H.Y. Hwang, S. Spalter, R.E. Slusher, S.W. Cheong, J.S. Sanghera, I.D. Aggarwal, Opt. Lett. **25**, 254 (2000)
325. A. Zakery, Y. Ruan, A.V. Rode, M. Samoc, B. Luther-Davies, J. Opt. Soc. Am. B **20**, 1844 (2003)
326. A. Zakery, M. Hatami, J. Opt. Soc. Am. B **22**, 591 (2005)
327. C.C. Yang, A. Villeneuve, G.I. Stegeman, Opt. Lett. **17**, 710 (1992)
328. A. Zakery, S.R. Elliott, J. Non-Cryst. Solids **330**, 1 (2003)
329. A. Zakery, Int. J. Optoelectron. Advanced Mater. **7**, 1143 (2005)
330. H. Ghafouri-Shiraz, P. Sahumet, M. Nagata, IEEE J. Quantum Electron. **31**, 190 (1995)
331. T. Takizawa, A. Uchino, T. Shimizu, Y. Takeuchi, S. Arai, Jpn. J. Appl. Phys. Part 2 **36**(2A), L110 (1997)
332. K. Alhemyari, A. Villeneuve, J.U. Kang, J.S. Aitchison, C.N. Ironside, G.I. Stegeman, Appl. Phys. Lett. **63**, 3562 (1993)
333. K. Ogusu, J. Yamasaki, S. Maeda, M. Kitao, M. Minakata, Opt. Lett. **29**, 265 (2004)
334. Y. Ruan, W. Li, R. Jarvis, N. Madsen, A. Rode, B. Luther-Davies, Opt. Express **12**, 5140 (2004)
335. Y. Ruan, B. Luther-Davies, W. Li, A. Rode, V. Kolev, S. Madden, Opt. Lett. **30**, 2605 (2005)
336. Y. Ruan, B. Luther-Davies, A. Rode, V. Kolev, W. Krolikowski, in *Lasers and Electro-Optic Society, LEOS 2005*. The 18th Annual Meeting of the IEEE (2005) p. 609
337. R. Hoffe, J. Chrostowski, Opt. Commun. **57**, 34 (1986)
338. N. Peyghamberian, S.W. Koch, in *Semiconductor Nonlinear Materials*, ed. by H.M. Gibbs et al. Nonlinear Photonics (Springer, Berlin Heidelberg New York, 1990) p. 7
339. G.P. Agrawal, *Nonlinear Fiber Optics* (Academic, San Diego, 1989)
340. B.K. Nayar, N. Finlayson, N.J. Doran, S.T. Davey, D.L. Williams, J.W. Arkwright, Opt. Lett. **16**, 408 (1991)
341. N.J. Doran, D. Wood, Opt. Lett. **13**, 56 (1988)
342. R.H. Stolen, A. Ashkin, W. Pliebel, Opt. Lett. **9**, 300 (1984)
343. M.N. Islam, Opt. Lett. **14**, 1257 (1989)
344. M.N. Islam, Opt. Lett. **15**, 417 (1990); M.N. Islam, in *Ultrafast all-optical soliton fiber switching*, Conference on Lasers and Electro-Optics (Anaheim, CA, 1990) Paper CMD1
345. Bahaa E.A. Saleh, M.C. Teich, *Fundamentals of Photonics* (Wiley, New York, 1991)

## Chapter 7

346. C.H. Kwak, Y.I. Lee, S.G. Kim, J. Opt. Soc. Am. B **16**, 600 (1999)
347. R.A. Ganeev, A.I. Ryasnyansky, S.R. Kamalov, et al., J. Phys. D: Appl. Phys. **34**, 1602 (2001)
348. R.A. Ganeev, A.I. Ryasnyansky, M.K. Kodirov, T. Usmanov, Opt. Commun. **185**, 473 (2000)
349. L.W. Tutt, A. Kost, Nature **356**, 224 (1992)

350. Z.R. Chen, H.W. Hou, X.Q. Xin, et al. J. Phys. Chem. **99**, 8717 (1995)
351. M. Sheik-Bahae, A.A. Said, T. Wei, et al., IEEE. J. Quantum Electron. **26**, 760 (1990)
352. R.A. Ganeev, A.I. Ryasnyansky, T. Usmanov, Phys. Solid State **45**, 207 (2003)
353. J. Troles, F. Smektala, G. Boudebs, A. Monteil, B. Bureau, J. Lucas, Opt. Mater. **25**, 231 (2004)
354. E.M. Vogel, M.J. Weber, D.M. Krol, Phys. Chem. Glasses **32**, 231 (1991)
355. Y. Fujii, B.S. Kawasaki, K.O. Hill, D.C. Johnson, Opt. Lett. **5**, 48 (1980)
356. Y. Sasaki, Y. Ohmori, Appl. Phys. Lett. **39**, 466 (1981)
357. U. Osterberg, W. Margulis, Opt. Lett. **11**, 516 (1986)
358. U. Osterberg, W. Margulis, Opt. Lett. **12**, 57 (1987)
359. H. Kawazoe, J. Non-Cryst. Solids **71**, 231 (1985)
360. E.J. Friebele, D.L. Griscom, Mater. Res. Soc. Symp. Proc. **61**, 319 (1986)
361. L.N. Skuja, A.N. Trukhin, A.E. Plaudio, Phys. Status Solidi, A **84**, K153 (1984)
362. R.H. Stolen, H.W.K. Tom, Opt. Lett. **12**, 585 (1987)
363. V. Mizrahi, U. Osterberg, J.E. Sipe, G.I. Stegeman, Opt. Lett. **13**, 279 (1988)
364. V. Mizrahi, U. Osterberg, C. Krautschik, G.I. Stegeman, Opt. Lett. **53**, 557 (1988)
365. M.V. Bergot, M.C. Farries, M.E. Fermann, L. Li, L.J. Poyntz-Wright, P.St.J. Russell, A. Smithson, Opt. Lett. **13**, 592 (1988)
366. M.E. Fermann, L. Li, M.C. Farries, D.N. Payne, Electron. Lett. **24**, 894 (1988)
367. M.E. Fermann, L. Li, M.C. Farries, L.J. Poyntz-Wright, L. Dong, Opt. Lett. **14**, 748 (1989)
368. J. Qiu, J. Si, K. Hirao, Opt. Lett. **26**, 914 (2001)
369. I.V. Kityk, B. Sahraoui, J. Chem. Phys. **114**, 8105 (2001)
370. V. Pruneri, P.G. Kazansky, D. Hewak, J. Wang, H. Takebe, D.N. Payne, Appl. Phys. Lett. **70**, 155 (1997)
371. J. Li, Z. Sun, X. Zhu, H. Zeng, Z. Xu, Z. Wang, J. Lin, W. Huang, R.S. Armstrong, P.A. Lay, Opt. Mat. **25**, 401 (2004)
372. Y. Ruan, W. Li, R. Jarvis, N. Madsen, A. Rode, B. Luther-Davies, Opt. Express **12**, 5140 (2004)
373. M. Asobe, T. Kanamori, K.Naga Numa, H. Itoh, J. Appl. Phys. **77**, 5518 (1995)
374. A.J. Perry, D. Vender, R.W. Boswel, J. Vac. Sci. Technol. B **9**, 310 (1991)
375. G.P. Agrawal, in *Nonlinear Fiber Optics*, ed. by P.L. Kelley, I.P. Kaminow, G.P. Agrawal (Academic, New York, 2001)
376. Y. Ruan, B. Luther-Davies, W. Li, A. Rode, M. Samoc, ACTA Optica Sinica **23**(Suppl. 363), 363 (2003)
377. R.E. Slusher, B.J. Egelton, in *Nonlinear Photonic Crystals*, ed. by R.E. Slusher, B. Eggeleton (Springer, Berlin Heidelberg New York, 2003)
378. R. Vallee, S. Frederick, K. Astaryan, M. Fischer, T.V. Galstian, Opt. Commun. **230**, 301 (2004)
379. N. Ponnampalam, R.G. DeCorby, H.T. Nguyen, P.K. Dwivedi, C.J. Haugen, J.N. McMullin, S.O. Kasap, Opt. Express **12**, 6270 (2004)
380. N. Ho, J. Laniel, R. Vallee, A. Villeneuve, Proc. Soc. Photo. Opt. Instrum. Eng. **4833**, 762 (2002)
381. A. Mairaj, P. Hua, H.N. Rutt, D.W. Hewak, J. Lightwave Technol. **20**, 1578 (2002)
382. J-F. Viens, A. Villeneuve, K. Le Foulgoc, K. Richardson, T. Cardinal, Proc. Soc. Photo. Opt. Instrum. Eng. **3491**, 366 (1998)

383. A. D'Orazio, M. De Sario, L. Mescia, V. Petruzzelli, F. Prudenzano, A.P. Caricato, G. Leggieri, M. Martino, Proc. Soc. Photo. Opt. Instrum. Eng. **4645**, 174 (2002)
384. O.M. Efimov, L.B. Glebov, S.H. Park, K.A. Richardson, E. Van Stryland, T. Cardinal, M. Couzi, J.L. Bruneel, Proc. Soc. Photo. Opt. Instrum. Eng. **4347**, 469 (2001)
385. M. Asobe, Opt. Fiber Technol. **3**, 142 (1997)
386. B.J. Eggleton, R.E. Slusher, C.M. deSterke, P.A. Krug, J.E. Sipe, Phys. Rev. Lett. **76**, 627 (1996)
387. M. Shokooh-Saremi, V.G. Ta'eed, I.C.M. Littler, D.J. Moss, B.J. Eggleton, Y. Ruan, B. Luther-Davies, Electron. Lett. **41**, 738 (2005)
388. P. Yeh, *Optical Waves in Layered Media* (Wiley, New York, 1988)
389. V.G. Ta'eed, M. Shokooh-Saremi, L. Fu, D.J. Moss, M. Rochette, I.C.M. Littler, B.J. Eggleton, Y. Ruan, B. Luther-Davies, Opt. Lett. **30**, 2900 (2005)
390. P.V. Mamyshev, in *24th European Conference on Optical Communication* (IEEE, 1998) p. 475
391. M. Rochette, J.N. Kutz, J.L. Blows, D. Moss, J.T. Mok, B.J. Eggleton, IEEE Photon. Technol. Lett. **17**, 908 (2005)
392. G. Lenz, B.N.J. Eggleton, C.R. Giles, C.K. Madsen, R.E. Slusher, IEEE J. Quantum Electron. **34**, 1390 (1998)
393. J. Fick, E.J. Knystautas, A. Villeneuve, F. Schiettekatte, S. Roorda, K.A. Richardson, J. Non-Cryst. Solids **272**, 200 (2000)
394. G. Lenz, S. Spalter, in *Chalcogenide Glasses*, ed. by R.E. Slusher, B.J. Eggleton. Nonlinear Photonic Crystals (Springer, Berlin Heidelberg New York, 2003)
395. R.M. Bryce, H.T. Nguyen, P. Nakeeran, R.G. DeCorby, P.K. Dwivedi, C.J. Haugen, J.N. McMullin, S.O. Kasap, J. Vac. Sci. Technol. A **22**, 1044 (2004)
396. R.G. Walker, Electron. Lett. **23**, 154 (1973)
397. L.S. Yu, Q.Z. Liu, S.A. Pappert, P.K.L. Yu, S.S. Lau, Appl. Phys. Lett. **64**, 536 (1994)
398. F. Gonella, P. Mazzoldi, in *Handbook of Nanostructured Materials and Nanotechnology*, vol. 4, ed. by H.S. Nalwa (Academic, San Diego, 2000) Chap. 2
399. V.M. Shalaev, *Nonlinear Optics of Random Media* (Springer, Berlin Heidelberg New York, 2000)
400. M. Ajgaonkar, Y. Zhang, H. Grebel, C.W. White, Appl. Phys. Lett. **75**, 1532 (1999)
401. G. Banfi, V. Degiorgio, D. Ricard, Adv. Phys. **47**, 510 (1998)
402. Y. Li, M. Takata, A. Nakamura, Phys. Rev. B **57**, 9193 (1998)
403. P.D. Persans, T.M. Hayes, L.B. Lurio, J. Non-Cryst. Solids **349**, 315 (2004)
404. J.L. Gu, J.L. Shi, G.J. You, L.M. Xiong, S.X. Qian, Z.L. Hua, H.R. Chen, Adv. Mater. **17**, 557 (2005)
405. Y. Hamanaka, K. Fukuta, A. Nakamura, L.M. Liz-Marzan, P. Mulvaney, Appl. Phys. Lett. **84**, 4938 (2004)
406. R. Del Coso, J. Requejo-Isidro, J. Solis, J. Gonzalo, C.N. Afonso, J. Appl. Phys. **95**, 2755 (2004)
407. A. Podlipensky, J. Lange, G. Seifert, H. Graener, I. Gravetchi, Opt. Lett. **28**, 716 (2003)
408. H. Wakabayashi, H. Yamanaka, K. Kadono, T. Sakaguchi, M. Miya, in *Proceedings of the International Conference on Science and Technology of New Glass* (Ceramic Society of Japan, Tokyo, 1991) p. 412

409. K. Fukumi, A. Chayahara, K. Kadono, T. Sakaguchi, Y. Horino, M. Miya, J. Hayakawa, M. Satou, Jpn. J. Appl. Phys. **30**, L742 (1991)
410. K. Kadono, T. Sakaguchi, H. Wakabayashi, T. Fukimi, H. Yamanaka, M. Miya, H. Tanaka, Mat. Res. Soc. Symp. Proc. Mater. Res. Soc. **282**, 903 (1993)
411. J. Matsuoka, R. Mizutani, S. Kaneko, H. Nasu, K. Kamiya, K. Kadono, et al. J. Ceram. Soc. Jpn. **101**, 53 (1993)
412. H.B. Liao, R.F. Xiao, J.S. Fu, P. Yu, G.K.L. Wong, P. Sheng, Appl. Phys. Lett. **70**, 1 (1997)
413. I. Tanahashi, M. Yoshida, Y. Manabe, T. Tohda, S. Sasaki, T. Tokizaki, A. Nakamura, Jpn. J. Appl. Phys. **33**, L1410 (1994)
414. R.H. Magruder, R.F. Haglund, Jr., L. Yang, J.E. Wittig, K. Becker, and R.A. Zuhr, Mat. Res. Soc. Symp. Proc. Mater. Res. Soc. **224**, 369 (1992)
415. T. Akai, K. Kadono, H. Yamanaka, T. Sakaguchi, M. Miya, H. Wakabayashi, J. Ceram. Soc. Jpn. **101**, 105 (1993)
416. M. Yamane, Y. Asahara, *Glasses for Photonics* (Cambridge University Press, Cambridge, 2000)
417. K. Ogusu, J. Yamasaki, S. Maeda, M. Kitao, M. Minakata, Opt. Lett. **29**, 265 (2004)
418. C.H. Kwak, S.Y. Park, H.M. Kim, E.H. Lee, C.M. Kim, Opt. Commun. **88**, 265 (1992)
419. T.J. Carrig, G.J. Wagner, W.J. Alford, A. Zakel, Proc. Soc. Photo. Opt. Instrum. Eng. **5460**, 265 (2004)
420. T.J. Carrig, J. Electron. Mater **31**, 759 (2002)
421. S. Juodkazis, T. Kondo, A. Rode, S. Matsuo, H. Misawa, Proc. Soc. Photo. Opt. Instrum. Eng. **5662**, 179 (2004)
422. S.K. Sundaram, B.R. Johnson, M.J. Schweiger, J.E. Martinez, B.J. Riley, L.V. Saraf, N.C. Anheier, Jr., P.J. Allen, J.F. Schultz, Proc. Soc. Photo. Opt. Instrum. Eng. **5359**, 234 (2004)
423. F. Feigel, Z. Kotler, B. Sfez, A. Arsh, M. Klebanov, V. Lyubin, Mat. Res. Symp. Proc. **692**, 675 (2002); A. Feigel, M. Veinger, B. Sfez, A. Arsh, M. Klebanov, V. Lyubin, Appl. Phys. Lett. **83**, 4480 (2003)
424. T.V. Galstyan, J.-F. Viens, A. Villeneuve, K. Richardson, M.A. Duguay, J. Lightwave Technol. **15**, 1343 (1997)
425. G.A. Scarsbrook, I.P. Llewellyn, S.M. Ojha, R. Heinecke, Vacuum **38**, 627 (1988)
426. I.P. Llewellyn, G. Scarsbrook, R.A. Heinecke, Proc. Soc. Photo. Opt. Instrum. Eng. **1148**, 84 (1989)
427. G. Rosenblum, B.G. Sfez, Z. Kotler, V. Lyubin, M. Klebanov, Appl. Phys. Lett. **75**, 3294 (1999)
428. Y. Aoyagi, Y. Segawa, S. Namba, T. Suhara, H. Nishihara, H. Gamo, Phys. Status Solidi A **67**, 669 (1981)
429. J.E. Heebner, P. Chak, S. Pereira, J.E. Sipe, R.W. Boyd, J. Opt. Soc. Am. B **21**, 1818 (2004)
430. J.P. Zhang, D.Y. Chu, S.L. Wu, S.T. Ho, W.G. Bi, C.W. Tu, R.C. Tiberio, Phys. Rev. Lett. **75**, 2678 (1995)
431. S. Fan, P.R. Villeneuve, J.D. Joannopoulos, H.A. Haus, Opt. Express **3**, 4 (1998)
432. M.D. Rahn, A.M. Fox, M.S. Skolnick, T.F. Krauss, J. Opt. Soc. Am. B **19**, 716 (2002)

433. S. Mingaleev, Y. Kivshar, J. Opt. Soc. Am. B **19**, 2241 (2002)
434. C.W. Bennett, B.H. Kolner, Opt. Lett. **24**, 783 (1999)
435. P.L. Chu, B.A. Malomed, G.-D. Peng, J. Opt. Soc. Am. B **10**, 1379 (1993)
436. K.S. Chiang, Opt. Soc. Am. B **14**, 1437 (1997)
437. Y. Wang, W. Wang, Appl. Phys. B **79**, 51 (2004)
438. G.P. Agrawal, *Nonlinear Fiber Optics*, 3rd edn. (Academic, California, 2001) pp. 159–164
439. Y.S. Kivshar, G.P. Agrawal, *Optical Solitons*, 1st edn. (Academic, California, 2003) pp. 133–140
440. M. Hatami, PhD Thesis, Shiraz University (2006); A. Zakery, M. Hatami, J. Phys. D: Appl. Phys. **40**, 1010 (2007).
441. A. Zakery, J. Optoelectron. Advanced Mater. **7**, 1143 (2005)

# Index

Springer Series in

# OPTICAL SCIENCES

Volume 1

1 **Solid-State Laser Engineering**
By W. Koechner, 5th revised and updated ed. 1999, 472 figs., 55 tabs., XII, 746 pages

Published titles since volume 100

100 **Quantum Interference and Coherence**
Theory and Experiments
By Z. Ficek and S. Swain, 2005, 178 figs., XV, 418 pages

101 **Polarization Optics in Telecommunications**
By J. Damask, 2005, 110 figs., XVI, 528 pages

102 **Lidar**
Range-Resolved Optical Remote Sensing of the Atmosphere
By C. Weitkamp (Ed.), 161 figs., XX, 416 pages

103 **Optical Fiber Fusion Splicing**
By A.D. Yablon, 2005, 137 figs., XIII, 306 pages

104 **Optoelectronics of Molecules and Polymers**
By A. Moliton, 2005, 229 figs., 592 pages

105 **Solid-State Random Lasers**
By M. Noginov, 2005, 131 figs., XII, 238 pages

106 **Coherent Sources of XUV Radiation**
Soft X-Ray Lasers and High-Order Harmonic Generation
By P. Jaeglé, 2006, 332 figs., XIII, 416 pages

107 **Optical Frequency-Modulated Continuous-Wave (FMCW) Interferometry**
By J. Zheng, 2005, 137 figs., XVIII, 254 pages

108 **Laser Resonators and Beam Propagation**
Fundamentals, Advanced Concepts and Applications
By N. Hodgson and H. Weber, 2005, 587 figs., XXVI, 794 pages

109 **Progress in Nano-Electro Optics IV**
Characterization of Nano-Optical Materials and Optical Near-Field Interactions
By M. Ohtsu (Ed.), 2005, 123 figs., XIV, 206 pages

110 **Kramers–Kronig Relations in Optical Materials Research**
By V. Lucarini, J.J. Saarinen, K.-E. Peiponen, E.M. Vartiainen, 2005,
37 figs., X, 162 pages

111 **Semiconductor Lasers**
Stability, Instability and Chaos
By J. Ohtsubo, 2005, 169 figs., XII, 438 pages

112 **Photovoltaic Solar Energy Generation**
By A. Goetzberger and V.U. Hoffmann, 2005, 139 figs., XII, 234 pages

113 **Photorefractive Materials and Their Applications 1**
Basic Effects
By P. Günter and J.P. Huignard, 2006, 169 figs., XIV, 421 pages

114 **Photorefractive Materials and Their Applications 2**
Materials
By P. Günter and J.P. Huignard, 2006, 370 figs., XVII, 640 pages

115 **Photorefractive Materials and Their Applications 3**
Applications
By P. Günter and J.P. Huignard, 2007, 316 figs., X, 366 pages

116 **Spatial Filtering Velocimetry**
Fundamentals and Applications
By Y. Aizu and T. Asakura, 2006, 112 figs., XII, 212 pages

Springer Series in

# OPTICAL SCIENCES

117 **Progress in Nano-Electro-Optics V**
Nanophotonic Fabrications, Devices, Systems, and Their Theoretical Bases
By M. Ohtsu (Ed.), 2006, 122 figs., XIV, 188 pages

118 **Mid-infrared Semiconductor Optoelectronics**
By A. Krier (Ed.), 2006, 443 figs., XVIII, 751 pages

119 **Optical Interconnects**
The Silicon Approach
By L. Pavesi and G. Guillot (Eds.), 2006, 265 figs., XXII, 389 pages

120 **Relativistic Nonlinear Electrodynamics**
Interaction of Charged Particles with Strong and Super Strong Laser Fields
By H.K. Avetissian, 2006, 23 figs., XIII, 333 pages

121 **Thermal Processes Using Attosecond Laser Pulses**
When Time Matters
By M. Kozlowski and J. Marciak-Kozlowska, 2006, 46 figs., XII, 217 pages

122 **Modeling and Analysis of Transient Processes in Open Resonant Structures**
New Methods and Techniques
By Y.K. Sirenko, N.P. Yashina, and S. Ström, 2007, 110 figs., XIV, 353 pages

123 **Wavelength Filters in Fibre Optics**
By H. Venghaus (Ed.), 2006, 210 figs., XXIV, 454 pages

124 **Light Scattering by Systems of Particles**
Null-Field Method with Discrete Sources: Theory and Programs
By A. Doicu, T. Wriedt, and Y.A. Eremin, 2006, 123 figs., XIII, 324 pages

125 **Electromagnetic and Optical Pulse Propagation 1**
Spectral Representations in Temporally Dispersive Media
By K.E. Oughstun, 2007, 74 figs., XX, 456 pages

126 **Quantum Well Infrared Photodetectors**
Physics and Applications
By H. Schneider and H.C. Liu, 2007, 153 figs., XVI, 250 pages

127 **Integrated Ring Resonators**
The Compendium
By D.G. Rabus, 2007, 243 figs., XVI, 258 pages

128 **High Power Diode Lasers**
Technology and Applications
By F. Bachmann, P. Loosen, and R. Poprawe (Eds.) 2007, approx. 535 figs., VI, 546 pages

129 **Laser Ablation and its Applications**
By C.R. Phipps (Ed.) 2007, approx. 300 figs., XX, 586 pages

130 **Concentrator Photovoltaics**
By A. Luque and V. Andreev (Eds.) 2007, approx. 242 figs., XV, 298 pages

131 **Surface Plasmon Nanophotonics**
By M.L. Brongersma and P.G. Kik (Eds.) 2007, approx. X, 298 pages

132 **Ultrafast Optics V**
By S. Watanabe and K. Midorikawa (Eds.) 2007, approx. 303 figs., XII, 520 pages

133 **Frontiers in Surface Nanophotonics**
Principles and Applications
By D.L. Andrews and Z. Gaburro (Eds.) 2007, approx. 89 figs., X, 250 pages

134 **Strong Field Laser Physics**
By T. Brabec, 2007, approx. 150 figs., XV, 500 pages

135 **Optical Nonlinearities in Chalcogenide Glasses and their Applications**
By A. Zakery and S.R. Elliott, 2007, approx. 102 figs., IX, 199 pages